



**HAL**  
open science

# Development of ultra-high field CEST technics for studying brain metabolism

Solène Bardin

► **To cite this version:**

Solène Bardin. Development of ultra-high field CEST technics for studying brain metabolism. Imaging. Université Paris-Saclay, 2022. English. NNT : 2022UPAST172 . tel-03985070

**HAL Id: tel-03985070**

**<https://theses.hal.science/tel-03985070>**

Submitted on 13 Feb 2023

**HAL** is a multi-disciplinary open access archive for the deposit and dissemination of scientific research documents, whether they are published or not. The documents may come from teaching and research institutions in France or abroad, or from public or private research centers.

L'archive ouverte pluridisciplinaire **HAL**, est destinée au dépôt et à la diffusion de documents scientifiques de niveau recherche, publiés ou non, émanant des établissements d'enseignement et de recherche français ou étrangers, des laboratoires publics ou privés.

Development of ultra-high field CEST  
technics for studying brain metabolism  
*Développement de techniques CEST à ultra-haut champ  
pour l'étude du métabolisme cérébral*

**Thèse de doctorat de l'université Paris-Saclay**

École doctorale n° 575, electrical, optical, bio : physics and engineering  
(EOBE)

Spécialité de doctorat: Imagerie et Physique Médicale

Graduate School : Sciences de l'ingénierie et des systèmes. Référent :  
Faculté des sciences d'Orsay

Thèse préparée dans l'unité de recherche BAOBAB (Université Paris-Saclay,  
CEA, CNRS), France, sous la direction de **Luisa CIOBANU**, Directrice de  
recherche, NeuroSpin, CEA, la co-direction de **Fawzi BOUMEZBEUR**, Directeur  
de recherche, NeuroSpin, CEA.

**Thèse soutenue à Paris-Saclay, le 14 décembre 2022, par**

**Solène BARDIN**

**Composition du jury**

Membres du jury avec voix délibérative

<b>Vincent LEBON</b> Professeur des universités - praticien hospitalier, CEA-Service Hospitalier Frédéric Joliot Université Paris-Saclay	Président
<b>Guilhem PAGÈS</b> Chargé de recherche-HDR, AgroRésonance, INRAE Université Clermont-Auvergne	Rapporteur & Examineur
<b>Jean-Philippe RANJEVA</b> Professeur, CRMBM Université Aix-Marseille	Rapporteur & Examineur
<b>Cornelius FABER</b> Professeur associé, Université de Münster	Examineur



**Titre:** Développement de techniques CEST à ultra-haut champ pour l'étude du métabolisme cérébral  
**Mots clés:** CEST, métabolisme cérébral, IRM, IRM fonctionnelle, ultra-haut champ

L'imagerie RMN de transfert de saturation par échange chimique (IRM CEST) est un outil puissant pour l'imagerie métabolique. L'IRM CEST permet de détecter indirectement des métabolites avec une sensibilité et des résolutions temporelle et spatiale accrues par rapport à la spectroscopie RMN (SRM), via la réduction du signal de l'eau après l'application d'un module de présaturation à la fréquence du métabolite. Grâce à l'avènement des champs magnétiques intenses pour l'IRM, l'IRM CEST suscite un intérêt croissant. Des avancées significatives ont été rapportées aussi bien dans les stratégies d'acquisition que les chaînes de traitement permettant la détection de nombreux métabolites dont le glucose, le glutamate, le myo-inositol, le lactate ou la créatine, et des applications prometteuses dans différentes disciplines (oncologie, sciences musculo-squelettiques, physiologie ou neurosciences) ont été proposées. Cependant, il reste difficile d'étudier les effets CEST plus faibles provenant de métabolites moins concentrés, en échange lent ou de détecter des changements CEST rapides. Cette thèse de doctorat visait à développer des techniques CEST à ultra-haut champ pour étudier le métabolisme cérébral *in vivo*. D'abord, l'avantage des ultra-hauts champs magnétiques pour l'imagerie CEST a été démontré *in vitro* par l'étude de trois neurométabolites majeurs : glucose, lactate et glutamate à différents champs magnétiques (9.4, 11.7 et 17.2 T). L'influence des changements de température et de pH sur la réponse CEST a également été étudiée. Puis, le développement et l'implémentation d'une nouvelle approche d'IRM CEST ultra-rapide sont présentés : la séquence "CEST-linescan". Cette méthode est adaptée à la détection des effets CEST ténus générés par des métabolites moins concentrés ou en échange lent. Grâce à sa rapidité, ce protocole d'acquisition offre une meilleure stabilité du signal tout en maintenant un rapport contraste/bruit similaire aux séquences CEST standards. Pour le traitement des

données, un outil d'analyse (PEAKIT) spécifiquement dédié à la caractérisation de contributions CEST a été développé au sein de notre équipe. PEAKIT estime la hauteur, la surface et la significativité statistique du pic CEST en se basant sur l'estimation de la ligne de base locale autour de la contribution CEST d'intérêt et est donc peu affecté par la forme globale des données CEST. Ces deux outils dédiés ont permis, pour la première fois, la détection *in vivo* (dans le muscle squelettique et dans le cerveau du rat) de la carnosine, un dipeptide endogène doté d'importantes fonctions antioxydantes et connu pour être impliqué notamment dans la réponse cellulaire à des niveaux élevés d'inflammation. Deux autres dérivés de la carnosine (anserine et homocarnosine) ont également été étudiés. Enfin, nous avons adapté le CEST-linescan ultrarapide afin d'étudier les changements métaboliques dynamiques dans le cerveau du rat. Une étude préliminaire a consisté à détecter les changements du contraste CEST induits par une variation contrôlée du pH. Nous avons ensuite étudié les changements métaboliques induits par l'activation neuronale déclenchée par une stimulation électrique de la patte avant chez le rat. Nous avons adapté la séquence et mis en œuvre diverses stratégies d'acquisition afin de minimiser les effets BOLD et maintenir la sensibilité et la spécificité (biochimique) du contraste CEST fonctionnel. Même si les résultats obtenus ne nous ont pas permis de détecter des changements significatifs dans les contributions CEST spécifiques pendant la tâche fonctionnelle, nous concluons que les protocoles d'imagerie développés demeurent prometteurs. En employant des paradigmes de stimulation optimisés pour des réponses d'activation plus stables et en augmentant le nombre d'animaux pour une plus grande puissance statistique, nous espérons être en mesure d'identifier les changements métaboliques transitoires induits par l'activité neuronale.

**Title:** Development of ultra-high field CEST technics for studying brain metabolism  
**Keywords:** CEST, cerebral metabolism, MRI, functional MRI, ultra-high field

Chemical exchange saturation transfer Magnetic Resonance Imaging (CEST MRI) is a powerful tool for metabolic imaging. Detection of specific neurometabolites can be performed using CEST MRI with enhanced sensitivity, and temporal and spatial resolution compared to NMR Spectroscopy (MRS), by measuring the reduction in bulk water signal after application of a dedicated presaturation module. With the increased availability of high and ultra-high magnetic fields, CEST MRI techniques gained a lot of attention. Significant advancements have been reported in both the acquisition strategies and processing pipelines which allowed the *in vivo* detection of numerous brain metabolites including glutamate, glucose, myo-inositol, lactate, creatine and promising applications in different disciplines (e.g. oncology, musculoskeletal sciences, physiology or neurosciences) have been demonstrated. Yet, it remains challenging to investigate weaker CEST effects from molecules with lower concentrations or slower exchange rates or detect rapid CEST changes. This PhD thesis aimed at the development of ultra-high field CEST technics for studying brain metabolism *in vivo*. In this project, the advantage of ultra-high magnetic fields for CEST imaging was first demonstrated *in vitro* through an investigation of the CEST detection of three major neurometabolites: glucose, lactate and glutamate at different high magnetic fields (9.4, 11.7 and 17.2 T). The influence of temperature and pH changes on the CEST response was also investigated. In the second part of this thesis, the development and implementation of a new ultrafast CEST MRI approach are presented: the "CEST-linescan" sequence. This method is adapted to the detection of the tenuous CEST effects generated by metabolites with very low concentrations and very low exchange rates. Due to its rapidity, this acquisition protocol is offering a better signal stabil-

ity while maintaining a contrast-to-noise ratio similar to that of standard CEST sequences. For processing, we used an analysis tool (PEAKIT) developed in our team specifically for characterizing CEST contributions. PEAKIT estimates the CEST peak height, area and statistical significance based on the estimation of the local baseline around the CEST contribution-of-interest and is therefore minimally impacted by the global shape of the CEST data. These two CEST-related tools enabled, for the first time, the *in vivo* detection (in the skeletal muscle and in the brain of rats) of carnosine, an endogenous dipeptide with important antioxidant functions known to be involved notably in the cellular response to high levels of inflammation. Two other derivatives of carnosine (anserine and homocarnosine) were also studied. In the last part of the project, we focused on adapting the ultrafast CEST-linescan sequence for the investigation of dynamic metabolic changes in the rat brain. A preliminary study consisted in detecting changes in the CEST contrast induced by a controlled pH decrease. We were then focused on monitoring metabolic changes induced by neuronal activation triggered by an electrical forepaw stimulation in rats. We made several sequence modifications and implemented various acquisition strategies in order to minimize the BOLD effects and maintain the sensitivity and (biochemical) specificity of the CEST signal changes. Even though the results obtained did not allow us to detect significant changes in specific CEST contributions during the functional task, we conclude that the imaging protocols developed are promising. By employing stimulation paradigms optimized for stable activation responses and increasing the number of animals for higher statistical power, we expect to be able to pinpoint transient metabolic changes driven by neuronal activity.



# Remerciements

Ces travaux de thèse n'auraient probablement jamais abouti sans l'aide et le soutien d'un grand nombre de personnes que j'ai eu la chance d'avoir à mes côtés pendant ces trois années.

Merci à l'ensemble des membres de mon jury de thèse pour le temps et l'intérêt que vous avez accordés à la lecture de mon manuscrit et pour la richesse des échanges que nous avons eus au cours de ma soutenance.

Merci Luisa pour ton accompagnement très poussé tout au long du projet. J'ai beaucoup admiré ta curiosité, ta persévérance, ton envie d'aller de l'avant tout le temps et sur tous les plans, ton efficacité, ta capacité à changer de stratégie quand ceci était utile. J'espère pouvoir faire preuve d'autant d'application dans mes prochains projets. Merci d'avoir été présente à tout instant, d'avoir répondu à mes questions, et de m'avoir emmenée au bout de ma thèse.

Merci Fawzi pour ta disponibilité, ta bienveillance et le recul que tu as apportés sur chaque étape de ma thèse. C'est vrai qu'après ton passage, il fallait souvent changer plein de choses mais c'était toujours pertinent et précieux pour la suite. Merci également d'avoir répondu présent dans les moments les plus tendus du projet, je pense en particulier à la rédaction de ce manuscrit et la préparation de la soutenance pour lesquelles tu m'as apporté un soutien sans failles, jusqu'à la dernière seconde.

Merci Erwan de m'avoir toujours aidée, d'avoir été flexible et disponible même quand tu gérais plusieurs manips en même temps. Tu m'as fait gagner beaucoup de temps et tu as contribué à rendre ces nombreuses expériences moins pesantes pour moi. Merci également de m'avoir écoutée quand j'en avais besoin. Et merci aussi, pour tes « blagues mythiques », sinon c'est pas drôle.

Merci à l'ensemble des membres permanents de l'équipe de CIEL pour l'aide que vous m'avez apportée sur divers sujets et à différents instants de mon parcours, merci Davide, Françoise, Sébastien, Benoît, Tom, Clément.

Merci aux différents collaborateurs qui avez fait un bout de route avec nous, vous m'avez permis de pousser mon sujet un peu plus loin : Cornelius, Henriette, Daniel et Verena sur le projet BAMBOO et Patrick, Céline, Giancarlo et Giovanna sur le projet de carnosine CEST.

Un très grand merci à l'ensemble des étudiants (doctorants ou post-doctorants) qui ont constitué mon entourage direct au sein de NeuroSpin pendant mes trois années de thèse. Merci Roxane d'avoir été mon acolyte en début d'aventure, ton départ anticipé à mi-parcours m'a montré à quel point j'avais eu besoin de ton soutien. Merci Laura, Pauline, Jacques, Riccardo, Julia de m'avoir accueillie et de m'avoir montré le chemin ! Merci à l'ensemble de l'équipe Ginkgo, votre bonne humeur rayonnait jusqu'à mon bureau. Merci Marie d'avoir partagé avec moi ces discussions, ces repas, ces trajets. Mention spéciale au Palaiseau squad pour cette régularité incontestable au sushi, bravo et merci Adrien d'avoir réussi à égaler

mon engouement déraisonnable pour ce restaurant. Merci Ioana pour ta douceur et tes attentions.

Et merci bien sûr à l'équipage final de l'équipe CIEL : Paul, Marianne, Thaddée (sur toi seul repose l'esprit du bureau du cringe à présent), Gaelle, Clémentine, Corentin, Koven, Mélanie, El Arbi, Quentin. Merci pour le rire, le soutien, les échanges, les réponses plus ou moins pertinentes, merci aussi pour les Kinder Bueno, les yaourts aux marrons, les M&M's et autres aliments indispensables à la réussite d'une thèse. Vous avez clairement rendu la fin de mon aventure beaucoup plus agréable.

Au-delà des collègues de travail, je tiens à remercier l'ensemble des grimpeurs que j'ai eu la chance de rencontrer à Arkose Massy, vous retrouver sur les tapis de grimpe m'a permis de garder le moral au beau fixe : merci Charlotte, Suzanne, Solène, Marc, Ivan, Dim, Stéphane, KyLuc, Kyvinh, Thibault, Nico, Daphné, Gauthier, Thomas, Lucas, Benoît, Corentin, Javi, Juliette et Daniel.

Merci à tous les copains venus de divers horizons qui m'avez encouragée et soutenue, je vous dois beaucoup : merci Iris, Sarah, Gaëtan, Benjamin, Thibault, Jo, Eline, Elena, Alizé, Ayoub, Solia, Héloïse, Mélanie, Ibtissame, Baptiste, le CIPPIL, la BrBi family et autres anciens Supop.

Merci aux habitants de la coloc vauhallanaise, différents suivants les années, je me suis toujours sentie bien en votre compagnie, malgré l'absence du mon nom sur le bail.

Merci tout particulier à Pidel, tu m'as assuré la meilleure gestion technique de soutenance que je pouvais espérer, le cœur sur la main, comme à ton habitude.

Merci les voisins Rémi et Lauriane, vous avez suivi de près les étapes successives de ma thèse et ensoleillé chaque instant de partage au Val.

Merci à ma famille, proche et plus éloignée, pour votre soutien, vos attentions et votre présence à ma soutenance. Merci également à la famille de Pierre pour votre implication, qui m'a beaucoup touchée.

Enfin merci à toi Pierre, je n'aurais pas pu avoir meilleur soutien direct que toi. Tu as toujours su apporter un début de réponse à tous mes problèmes, mes moments de panique, mes interrogations, mes colères et mes doutes. Ta positivité quotidienne, ton soutien sur tous les plans et ta volonté de toujours proposer une solution m'ont aidée à prendre chaque fois un peu plus confiance en moi et dans ce projet. Merci pour tout.

# Table of contents

<b>Remerciements</b>	<b>iii</b>
<b>Table of contents</b>	<b>v</b>
<b>Résumé de la thèse en français</b>	<b>ix</b>
0.1 Introduction à l'imagerie métabolique basée sur le CEST	ix
0.2 Développement d'une nouvelle méthodologie CEST	x
0.2.1 Exploration des contrastes CEST à 17.2 T	xi
0.2.2 Séquence d'acquisition CEST ultra-rapide	xii
0.2.3 Développement d'un outil d'analyse de Z-spectres	xiv
0.3 Application à la détection de métabolites faiblement concentrés	xv
0.4 Application à la détection des changements métaboliques transitoires pendant l'activation neuronale	xvii
0.5 Conclusion	xxi
<b>List of figures</b>	<b>xxiii</b>
<b>List of tables</b>	<b>xxvii</b>
<b>List of symbols and abbreviations</b>	<b>xxix</b>
<b>1 Introduction to metabolic imaging using CEST MR</b>	<b>1</b>
1.1 Introduction to metabolic imaging	3
1.2 Chemical Exchange Saturation Transfer : Origin and theory	4
1.2.1 The emergence of CEST	4
1.2.2 Slow-to-intermediate exchange condition	7
1.2.3 Saturation Transfer	10
1.2.4 Sensitivity enhancement mechanism	13
1.2.5 Saturation transfer signal Characterization	14
1.3 Applications	15
1.3.1 Overview of all the applications	15
1.3.2 Different CEST contrasts	16
1.3.3 Conclusion	21
<b>2 Material and Methods</b>	<b>23</b>
2.1 Imaging systems	24
2.1.1 Magnets and gradients	24
2.1.2 Radio-Frequency (RF) coils	25
2.1.3 Adjustments	27
2.2 Phantoms	28

2.3	Animal experimentation . . . . .	30
2.3.1	Animals . . . . .	30
2.3.2	Experimentation protocols . . . . .	31
<b>3</b>	<b>Development of a new CEST MR methodology</b>	<b>37</b>
3.1	Exploration of CEST contrasts in phantoms at 17.2 T . . . . .	39
3.1.1	Z-spectra of lactate, glucose and glutamate at high fields . . . . .	39
3.1.2	Optimization of the $B_{1,sat}$ saturation power, influence of the $B_0$ static field and of the temperature . . . . .	41
3.1.3	Influence of the pH . . . . .	44
3.1.4	Selectivity towards a specific metabolite . . . . .	45
3.1.5	Conclusion . . . . .	48
3.2	Ultra-fast CEST MR acquisition sequence . . . . .	49
3.2.1	On the importance of a fast CEST MR sequence . . . . .	49
3.2.2	Principle and sequence pulse diagram . . . . .	49
3.2.3	Data analysis . . . . .	51
3.2.4	Conclusion . . . . .	53
3.3	Development of a Z-spectrum analysis tool . . . . .	54
3.3.1	Principle of the PEAKIT software tool . . . . .	55
3.3.2	Demonstration . . . . .	59
3.3.3	Conclusion, discussion and perspective . . . . .	62
<b>4</b>	<b>Applications to the detection of low concentrated metabolites</b>	<b>63</b>
4.1	Carnosine and its derivatives: roles and bio-distribution . . . . .	65
4.2	<i>In vitro</i> study . . . . .	66
4.2.1	Experimental protocol . . . . .	66
4.2.2	Results . . . . .	66
4.3	<i>In vivo</i> study . . . . .	68
4.3.1	Experimental protocol . . . . .	68
4.3.2	Data analysis . . . . .	69
4.3.3	Results . . . . .	70
4.4	Conclusion, discussion and perspectives . . . . .	74
<b>5</b>	<b>Applications to the detection of transient metabolic changes during neuronal activation</b>	<b>77</b>
5.1	State-of-the-art . . . . .	79
5.2	Assessment of CEST changes due to a controlled pH decrease . . . . .	80
5.2.1	Experimental protocol . . . . .	80
5.2.2	Results . . . . .	81
5.3	Modification of the CEST-LS sequence and acquisition strategy to minimize BOLD confound . . . . .	84
5.3.1	Challenge of CEST detection in the context of neuronal activity . . . . .	84
5.3.2	Presentation of the principle of the $grad_{opp}$ CEST-LS sequence . . . . .	86
5.3.3	Summary . . . . .	89
5.3.4	Convention and graphical codes . . . . .	89
5.4	Experimental protocols . . . . .	89
5.4.1	Neuronal activation induced by forepaw electrical stimulation . . . . .	90
5.4.2	CEST-LS $grad_{opp}$ implementation . . . . .	91
5.4.3	Processing . . . . .	99

*TABLE OF CONTENTS*

---

5.5	Results . . . . .	99
5.5.1	Results for experiment 1.1 and 1.2 . . . . .	100
5.5.2	Experiment 2 . . . . .	105
5.5.3	Conclusion . . . . .	107
<b>6</b>	<b>Conclusion and perspectives</b>	<b>109</b>
6.1	General conclusion . . . . .	110
6.2	Perspectives . . . . .	112
6.2.1	CEST quantification . . . . .	112
6.2.2	Human scanners and clinical perspectives . . . . .	113
6.2.3	Conclusion . . . . .	116
<b>7</b>	<b>List of publications</b>	<b>119</b>
<b>8</b>	<b>Bibliography</b>	<b>121</b>



# Résumé de la thèse en français

L'objectif du travail présenté dans ce mémoire était de développer et de mettre en œuvre de nouvelles techniques de Transfert de Saturation par Échange chimique (CEST, en anglais) à très haut champ magnétique afin de repousser les limites en terme de sensibilité et de résolution temporelle notamment des techniques CEST à l'état de l'art.

## 0.1 Introduction à l'imagerie métabolique basée sur le CEST

Il existe aujourd'hui une grande variété de techniques d'imagerie médicale qui permettent, dans leur utilisation la plus courante, d'accéder à des informations anatomiques ou structurelles sur des tissus solides (tomodensitométrie) ou mous (Imagerie par Résonance Magnétique (IRM), imagerie par ultrasons (échographie, US). Dans un cadre plus spécifique, ces techniques permettent également de sonder les propriétés fonctionnelles, mécaniques, vasculaires voire moléculaires de notre corps.

L'imagerie moléculaire est une branche dynamique de l'imagerie médicale dont l'objectif est de détecter, quantifier et imager les processus biologiques et les biomarqueurs de pathologie *in vivo*. Les méthodes les plus communes comme la tomographie par émission de positons (TEP) ou la tomographie par émission monophotonique (TEMP) utilisent des radio-traceurs qui ciblent spécifiquement une molécule (transporteur, protéine) ou un processus biologique d'intérêt. L'imagerie métabolique par résonance magnétique est probablement l'approche la plus polyvalente, non-invasive et non-radioactive. L'approche canonique pour l'IRM métabolique est la spectroscopie RMN *in vivo* (SRM) et en particulier l'imagerie spectroscopique (ISRM).

Le CEST s'est révélé être une technique très puissante pour détecter ou imager les métabolites endogènes avec une sensibilité accrue et de meilleures résolutions temporelles et spatiales, dans certaines conditions, que celles de la détection directe par SRM ou ISRM. Son principe est basé sur la détection indirecte d'un métabolite d'intérêt possédant des protons en échange chimique avec l'eau. En effet, l'application d'un module de présaturation à la fréquence des protons échangeables du métabolite en question, une réduction du signal de l'eau peut être observée avec une amplification dépendante des taux d'échange et de l'intensité de la saturation. La figure 1 schématise le principe du CEST avec un système comprenant deux groupes de protons : ceux de l'eau libre ("pool A") et ceux du métabolite, ici appelé soluté ("pool B").

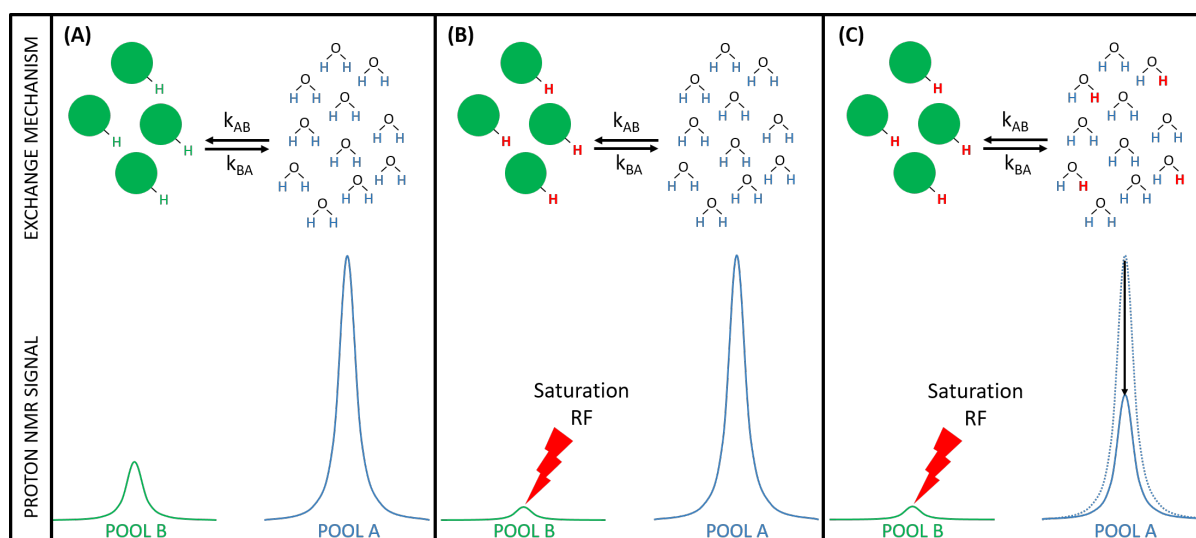


Figure 1: Représentation schématique de l'effet CEST entre le groupe de protons de l'eau (pool A) et un groupe de protons du soluté (pool B). (A) Situation avant la saturation radiofréquence (RF). Le signal RMN montre un petit pic pour les protons du pool B à faible concentration et un pic plus important pour les protons du pool A (pas à l'échelle). (B) Les protons échangeables du soluté sont labellisés (en rouge) en saturant leurs protons échangeables par une irradiation RF sélective (appliquée à leur fréquence de résonance). Le signal RMN montre une diminution du pic du soluté. (C) Les protons saturés sont transférés du pool B au pool A et l'impulsion RF continue de saturer les protons du soluté. Le signal RMN de l'eau est partiellement saturée et cette réduction correspond au contraste CEST.

Grâce à l'avènement des champs magnétiques intenses pour l'IRM, l'IRM CEST suscite un intérêt croissant. Des avancées significatives ont été rapportées aussi bien dans les stratégies d'acquisition que les chaînes de traitement permettant la détection de nombreux métabolites dont le glucose, le glutamate, le myo-inositol, le lactate ou la créatine, et des applications prometteuses dans différentes disciplines (oncologie, sciences musculo-squelettiques, physiologie ou neurosciences) ont été proposées.

## 0.2 Développement d'une nouvelle méthodologie CEST

Cette section résume le chapitre 3 qui présente nos développements dans le domaine de la RMN CEST, les travaux réalisés *in vitro* et nos résultats ultérieurs. Une première section propose une exploration générale du contraste CEST en analysant les réponses CEST de trois métabolites typiques dans différentes conditions expérimentales. Les avantages du haut champ magnétique et la sélectivité du signal CEST sont discutés et illustrés par quelques expériences. La section suivante décrit le principe d'une nouvelle méthode d'acquisition CEST ultrarapide. Enfin, nous introduisons et présentons un outil logiciel conçu pour l'analyse des contributions CEST. Ces deux outils ont été développés et optimisés pour les expériences CEST présentées en préparation des chapitres suivants (chapitres 4,5).

### 0.2.1 Exploration des contrastes CEST à 17.2 T

Dans cette section, toutes les acquisitions ont été réalisées en utilisant un fantôme à quatre compartiments composé de solutions de lactate, de glucose, de glutamate et d'un mélange des trois. Le même fantôme a été étudié à l'aide de trois scanners à trois champs magnétiques différents : 9,4, 11,7 et 17,2 T. Les acquisitions ont été réalisées à la température ambiante (21°C) et à la température du corps (37°C).

Dans l'ensemble, la puissance de saturation optimale de  $B_{1,sat}$  pour chaque métabolite s'est avérée être globalement indépendante de l'intensité du champ  $B_0$  et de la température de l'échantillon pour la gamme de  $B_0$  et  $T^\circ$  explorées dans ce travail. Pour tous les métabolites et pour la température considérée, une augmentation de  $B_0$  conduit à une augmentation du contraste CEST. Il y a deux raisons principales à cette sensibilité CEST accrue à champs magnétiques plus élevés : (i) les temps de relaxation  $T_1$  plus longs qui participent à une saturation plus efficace et (ii) le fait que la condition d'observabilité CEST est mieux satisfaite en raison de la meilleure résolution spectrale aux champs magnétiques plus élevés, en particulier pour les métabolites dont l'échange chimique est relativement lent. L'augmentation d'une température ambiante (21 °C) à une température physiologique (37 °C) entraîne une augmentation des taux d'échange et donc des contrastes CEST.

Le développement de séquences CEST pour la détection *in vivo* n'est cependant pas triviale car la réponse CEST d'un seul métabolite dépend non seulement de nombreux paramètres expérimentaux ( $B_{1,sat}$ ,  $t_{sat}$ ,  $\delta$  ... ) mais varie également en fonction des caractéristiques du tissu *in vivo* analysé ( $T_1, T_2$ ) et des propriétés physiologiques ( $T$ , pH) . De plus, la réponse CEST de la molécule d'intérêt est toujours entremêlée à d'autres contributions CEST provenant de molécules possédant des protons échangeables dont les fréquences de résonance sont dans la même plage fréquentielle (auxquelles s'ajoutent les éventuels contrastes MT et NOE). Bien qu'il soit possible de sélectionner les paramètres de séquence qui optimisent la réponse CEST d'une certaine molécule par rapport aux autres effets CEST pour des conditions physiologiques données, la sélection des contributions CEST spécifiques et leur quantification restent le principal défi auquel les études CEST doivent faire face. De nombreuses stratégies d'analyse des données ont été proposées pour relever ce défi.

La dépendance du profil  $MTR_{asym}$  du glucose vis-à-vis de  $B_0$  est présenté à titre d'exemple dans la figure 2. La caractérisation de la réponse CEST d'un métabolite et l'optimisation de l'intensité du module de présaturation  $B_1$  sont des étapes nécessaires avant de tenter de détecter un métabolite *in vivo*. L'utilisation de conditions proches du contexte physiologique ( $37 \pm 1$  °C et pH  $7 \pm 0.1$ ) permet de rendre l'optimisation plus précise. Cependant, en raison de toutes les autres contributions CEST, cette étape doit toujours être complétée par une optimisation *in vivo* dans laquelle il est possible de sélectionner un certain contraste CEST en réglant le pouvoir de saturation  $B_1$ .

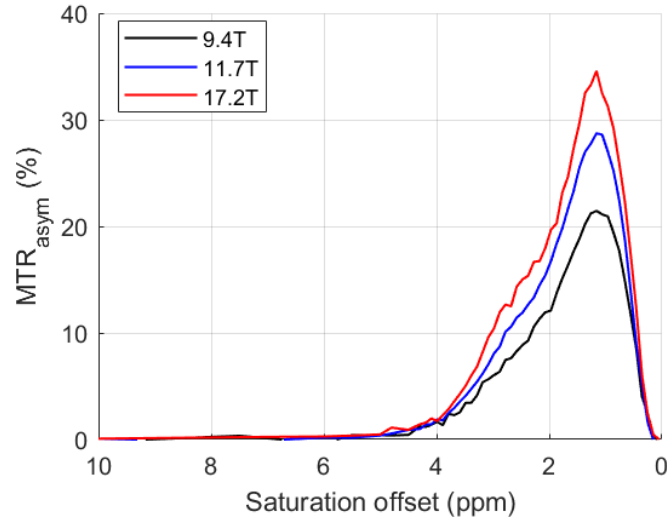


Figure 2: Glucose à température ambiante (21 °C) avec une puissance de saturation optimisée de  $B_{1,sat}$  à trois champs statiques (9.4 T, 11.7 T et 17.2 T)

### 0.2.2 Séquence d'acquisition CEST ultra-rapide

Dans la perspective de limiter les instabilités du signal au cours du temps dues aux dérives de fréquence et au bruit d'origine physiologique, une nouvelle séquence appelée CEST-linescan (CEST-LS) basée sur une méthode proposée dans [X. Xu, J.-S. Lee, and Jerschow 2013] a été développée. Pour construire la séquence CEST-LS, nous sommes partis d'une séquence CEST traditionnelle et nous avons ajouté une paire de gradients pendant le module de saturation et le module de lecture, nous avons éliminé l'encodage de phase et nous avons ajouté des bandes de saturation pour sélectionner un faisceau (Figure ??).

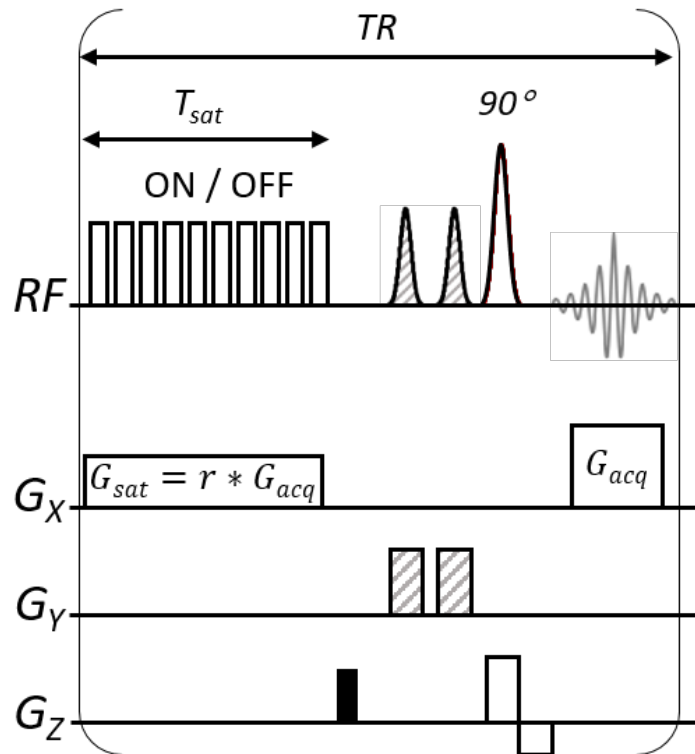


Figure 3: Chronogramme des impulsions de la séquence CEST-LS. Le module de saturation CEST a été placé devant une séquence d'écho de gradient standard dans laquelle le gradient de codage de phase a été supprimé. Des spoilers de gradient ont été appliqués sur la direction  $z$  (rectangle noir plein). Des bandes de saturation FOV ont été ajoutées pour éliminer le signal en dehors du ROI souhaité (motif hachuré). Les impulsions de saturation CEST sont activées et désactivées (amplitude à zéro) pour générer des profils saturés ou de référence, respectivement. L'axe des  $X$  est également appelé le sens de lecture.

Des exemples d'acquisitions et de traitement de données CEST-LS *in vitro* ont été présentés. Avec ce nouveau concept, l'acquisition d'un spectre-Z ne nécessite que deux TR. Cette méthode très rapide ouvre la porte à une résolution temporelle plus élevée qui peut être utile dans des expériences statiques mais surtout dynamiques. Dans le cas d'une expérience statique (mesure d'un Z-spectre constant), cette résolution temporelle plus élevée permet une meilleure stabilité du signal car elle rend la détection CEST moins sensible aux variations de fréquence et aux dérives physiologiques dans le temps (respiration, pulsation, mouvements inopinés). Dans le cas d'expériences dynamiques (avec des changements métaboliques/physiologiques attendus), la possibilité d'acquérir rapidement un spectre-Z permet de détecter d'éventuels changements fonctionnels du contraste CEST en temps réel.

Le principe d'acquisition et d'analyse d'un spectre-Z est illustré en figure 4.

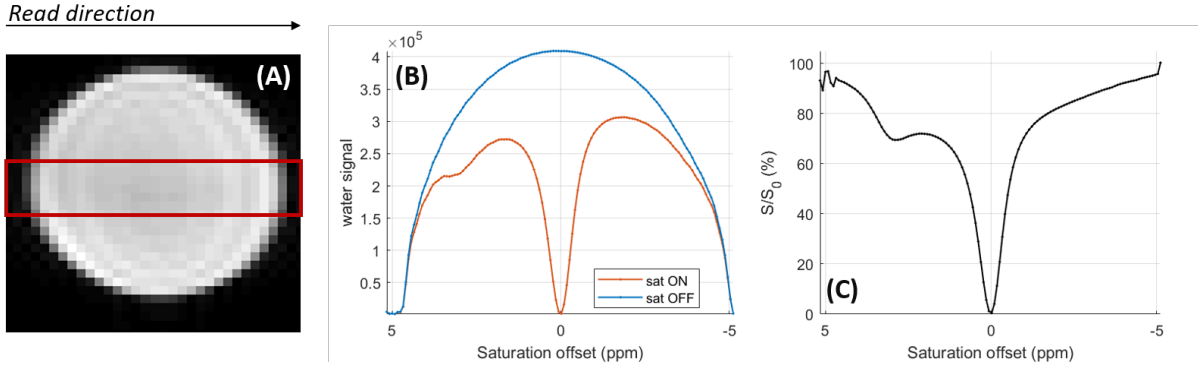


Figure 4: Analyse CEST-LS pour les données acquises dans un échantillon de glutamate 20 mM montré dans (A). La boîte rouge montre le voxel dans lequel les données ont été acquises. (B) Moyenne des profils d'eau saturée et de référence. (C) Rapport entre le profil saturé et le profil de référence.

### 0.2.3 Développement d'un outil d'analyse de Z-spectres

Parallèlement à la mise en œuvre de la séquence CEST-LS, le développement et le test d'un outil d'analyse appelé PEAKIT ont été réalisés. Ce travail a été réalisé en collaboration avec Michele Lecis, un étudiant en thèse de master dans notre équipe. PEAKIT est un outil logiciel conçu pour la détection et la caractérisation des pics CEST présents dans un Z-spectre. Comparé aux autres outils similaires, PEAKIT a l'avantage de ne pas nécessiter d'hypothèses concernant le décalage en fréquence des pics, leur forme ou l'allure locale de la ligne de base sous-jacente. Après une estimation de la ligne de base basée sur la régression du processus gaussien, PEAKIT fournit les décalages des déplacements chimiques, les surfaces, les hauteurs et la significativité statistique des pics. La performance de l'outil a été démontrée et évaluée par l'analyse des données CEST in vitro et in vivo acquises en utilisant la séquence CEST-LS. La figure 5 propose une représentation schématique du principe de fonctionnement de l'algorithme PEAKIT.

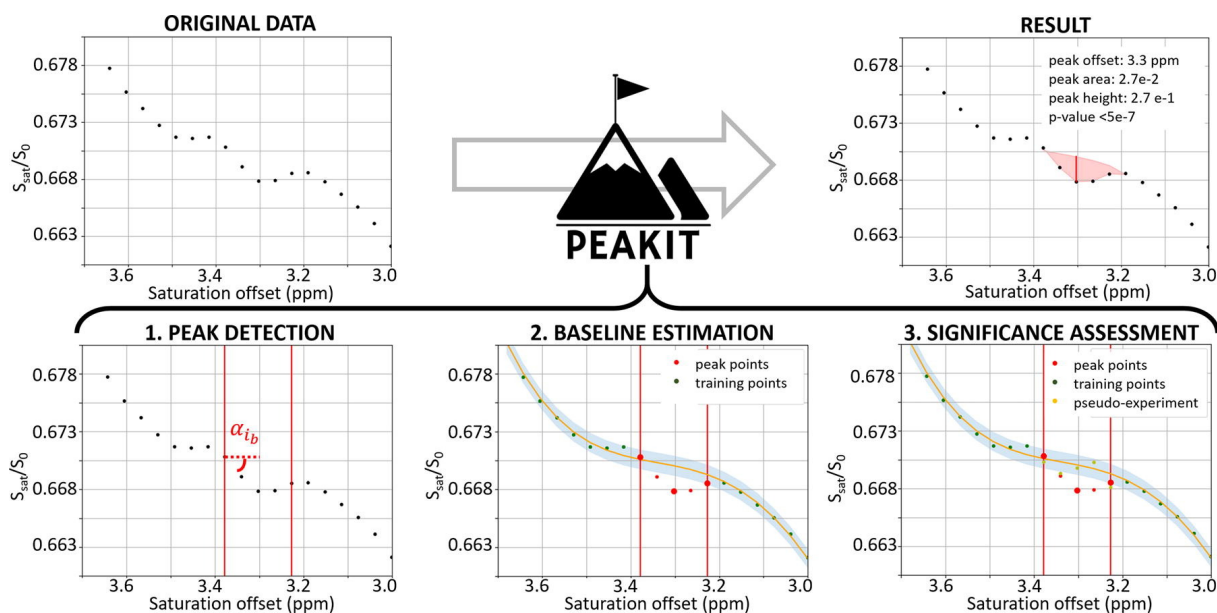


Figure 5: Principe de fonctionnement de PEAKIT décomposé en trois phases : la détection du pic, l'estimation de la ligne de base et l'estimation de la significativité.

### 0.3 Application à la détection de métabolites faiblement centrés

A l'aide de ces deux outils d'acquisition et d'analyse spécifiquement conçus pour la détection des effets CEST ténus, nous avons démontré, pour la première fois, la détection *in vivo* de la carnosine et de ses dérivés (Chapitre 4). La carnosine est un dipeptide endogène ayant d'importantes fonctions antioxydantes connues pour être impliquées notamment dans la réponse cellulaire à des niveaux élevés d'inflammation. Les effets CEST de la carnosine, de l'ansérine et de l'homocarnosine ont été caractérisés pour la première fois dans des fantômes, démontrant la possibilité de séparer leurs contributions individuelles en utilisant une haute résolution spectrale (0,005 ppm) et une faible puissance de saturation CEST (0,15  $\mu\text{T}$ ) (Figure 6).

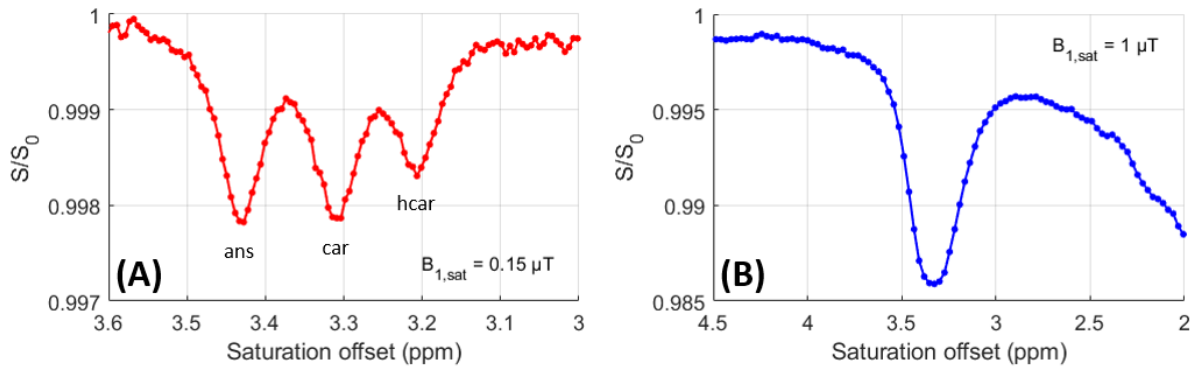


Figure 6: Résultats du CEST-LS sur l'échantillon contenant de l'ansérine, de la carnosine et de l'homocarnosine. (A) Z-spectre CEST-LS obtenu avec  $B_{1,sat} = 0.15 \mu T$  et une résolution de 0.005 ppm. Les pics de l'homocarnosine, de la carnosine et de l'ansérine sont clairement visibles et distincts. (B) Z-spectre CEST-LS obtenu avec  $B_{1,sat} = 1 \mu T$  et une résolution de 0,03 ppm. Les Z-spectres en A et B ont été moyennés sur 10 et 18 répétitions, respectivement.

Grâce à l'utilisation d'une résolution spectrale et d'une intensité de saturation adaptée, la signature CEST de ces peptides a ensuite été mise en évidence, *in vivo*, dans le cerveau (Figure 8) et les muscles (Figure 7) squelettiques du rat.

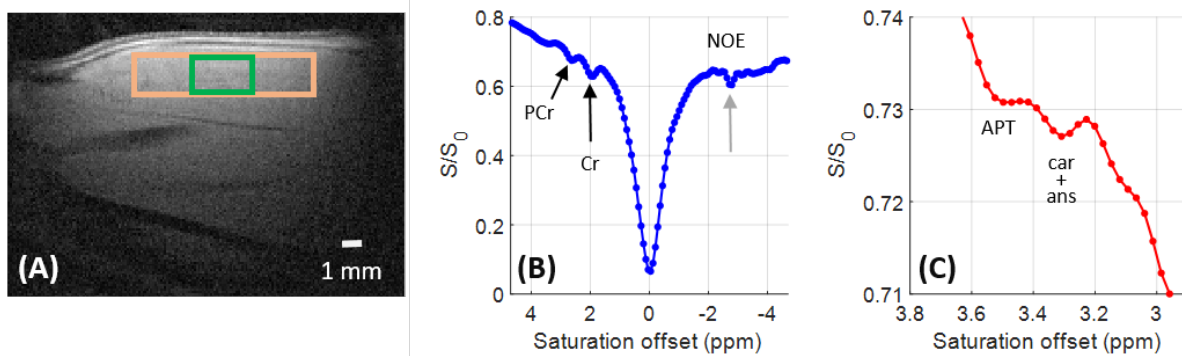


Figure 7: Résultats CEST-LS sur un muscle squelettique de jambe de rat (A) Image anatomique d'un muscle de la jambe inférieure d'un rat montrant le ROI utilisé pour le CEST-LS en orange et le voxel pour la spectroscopie H-RMN en vert. (B) Z-spectre à faible résolution montrant la créatine (Cr) et la phospho-créatine (PCr). Le pic net indiqué par une flèche grise à -2,7 ppm correspond à la graisse (C) Zoom montrant les pics combinés de car + ans et APT. Tous les Z-spectres ont été acquis avec  $B_{1,sat}=1 \mu T$ .

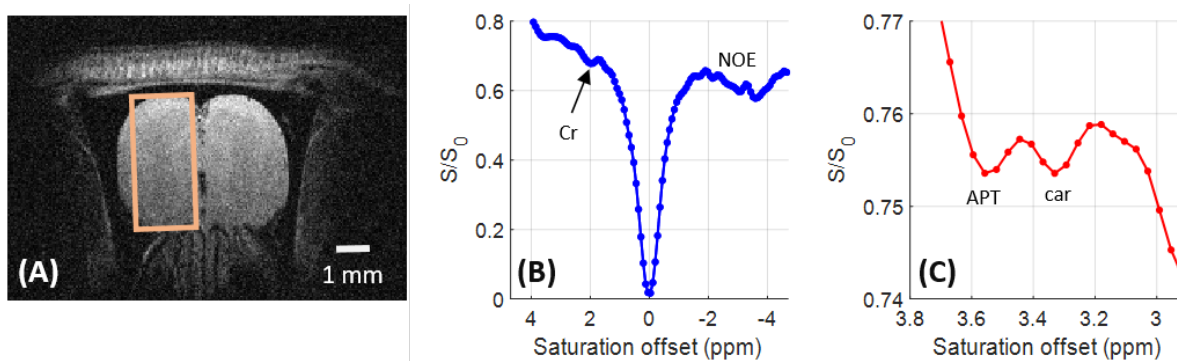


Figure 8: Résultats CEST-LS sur un bulbe olfactif de rat. (A) Image anatomique d'un bulbe olfactif de rat montrant la ROI utilisé pour les acquisitions CEST-LS (B) Z-spectre à basse résolution montrant le pic de Cr (C) Z-spectre à haute résolution montrant les pics de Car et APT. Tous les Z-spectres ont été acquis avec  $B_{1,sat}=1 \mu T$ .

La présence de carnosine et d'ansérine dans le muscle a été corroborée par la spectroscopie  $^1H$ -RMN localisée *in vivo*. Cependant, la sensibilité de la SRM était insuffisante pour détecter la carnosine et l'homocarnosine dans le cerveau. Les quantités absolues de carnosine et de dérivés dans les tissus étudiés ont été déterminées par chromatographie en phase liquide avec ionisation par électro-ébulisisation couplée à la spectroscopie de masse en utilisant des méthodes standard de dilution isotopique et ceux-ci étaient en accord avec les contrastes CEST observés. La robustesse de l'approche CEST-linescan et les conditions favorables au CEST à champ magnétique ultra-élevé, combinées aux grandes performances de caractérisation de l'outil d'analyse PEAKIT, ont permis pour la première fois la détection *in vivo* par CEST de la carnosine et des peptides apparentés dans le muscle squelettique et dans le cerveau (bulbe olfactif et néocortex).

#### 0.4 Application à la détection des changements métaboliques transitoires pendant l'activation neuronale

Dans la dernière partie de ce projet (chapitre 5), nous nous sommes concentrés sur l'adaptation de la séquence CEST-LS ultrarapide pour l'étude des changements métaboliques dynamiques dans le cerveau du rat. A travers une étude préliminaire, nous avons démontré la possibilité de détecter des changements dans le contraste CEST pendant l'induction d'une diminution contrôlée du pH avec une expérience d'hypercapnie (Figure 9). L'analyse avec PEAKIT a permis de conclure qu'une diminution du pH entraîne une diminution du contraste APT-CEST et une augmentation du contraste CEST des amines.

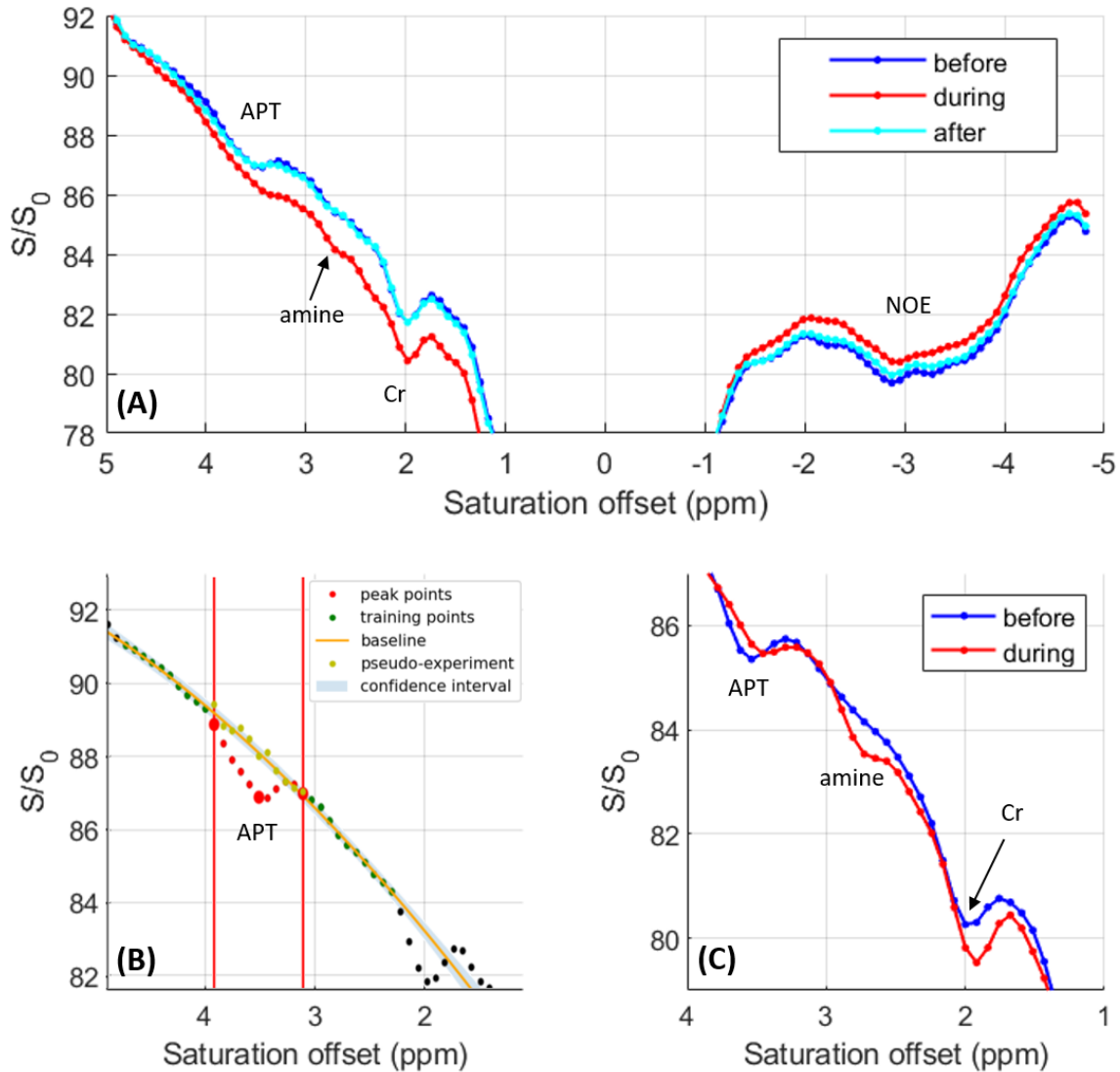


Figure 9: (A) Z-spectre zoomé pour les trois périodes de temps chez le rat 1 (avant (bleu foncé), pendant (rouge) et après (bleu clair) l'administration de  $\text{CO}_2$ ). On reconnaît l'APT, l'amine, la créatine et le NOE. Les changements de base dus à l'augmentation de la perfusion cérébrale sont visibles (B) Exemple d'analyse PEAKIT du pic APT d'un Z-spectre avant l'administration de  $\text{CO}_2$  (C) Évolution du signal CEST amide et amine pour le rat 2 avant et après l'administration de  $\text{CO}_2$ .

Nous avons ensuite concentré nos travaux sur le suivi des changements métaboliques induits par l'activation neuronale. Nous avons apporté plusieurs modifications à la séquence et mis en œuvre diverses stratégies d'acquisition afin de minimiser la contribution BOLD et d'améliorer la sensibilité et la spécificité biochimique du signal CEST. Entre autres ajustements, un protocole expérimental impliquant un nouveau module CEST a été proposé et mis en œuvre. La nouvelle version de la séquence CEST-LS a été appelée CEST-LS grad<sub>opp</sub> et est basée sur le calcul du rapport entre le signal de l'eau obtenu à un certain décalage de saturation divisé par le signal de l'eau obtenu au décalage de saturation opposé. Par ailleurs, Le module de lecture est passé de l'écho de gradient à l'écho de spin afin de réduire le contraste BOLD. L'utilisation de l'écho de spin est rendue possible par le long TR employé dans la détection CEST et confère un meilleur SNR que les séquences d'écho de gradient. Le TE

a été réduit à 5 ms, ce qui a également contribué à réduire le contraste BOLD. La figure 10 présente un parallèle entre la séquence CEST-LS classique et sa version adaptée à la détection de changement métaboliques dûs à l'activation neuronale.

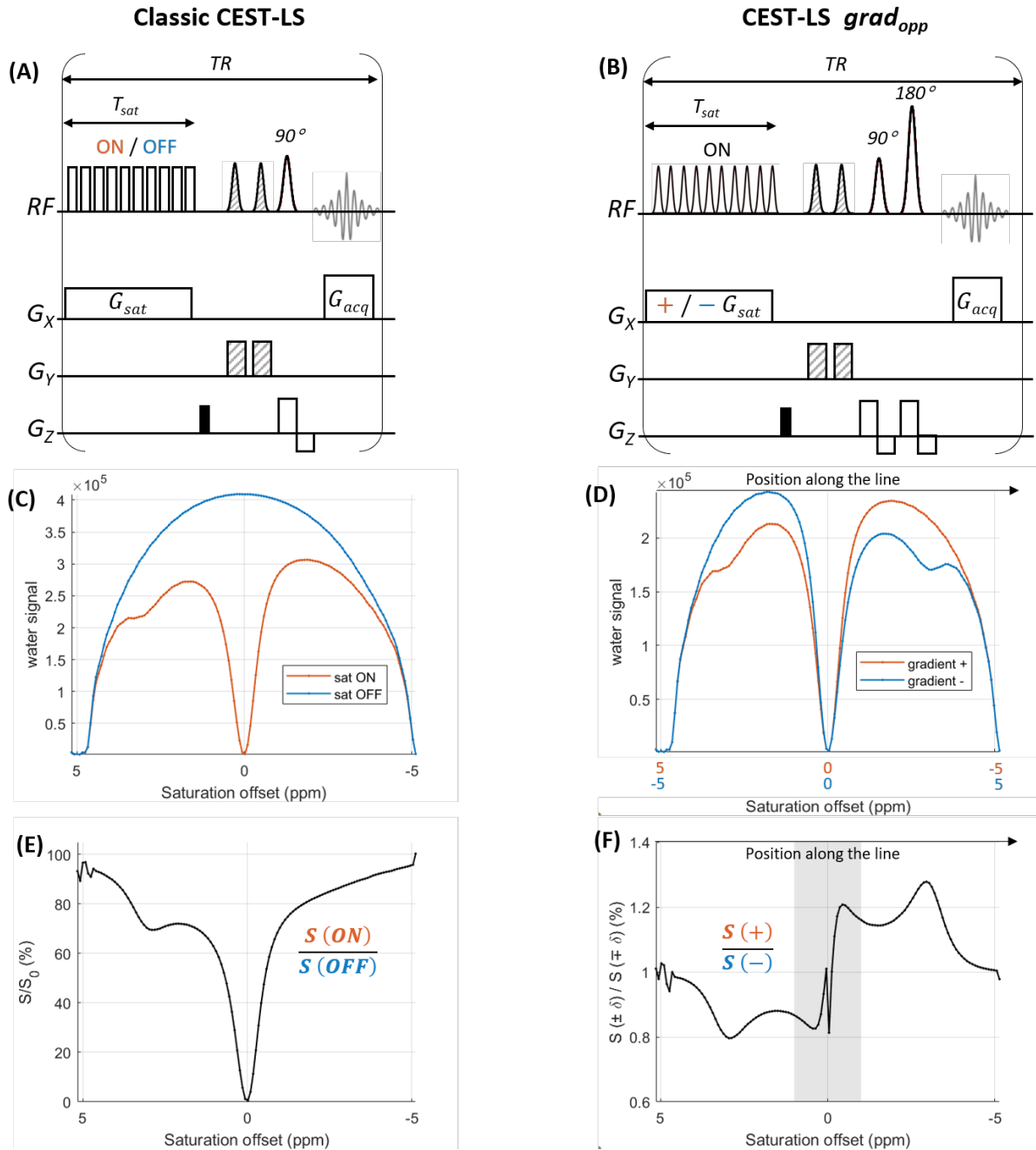


Figure 10: Transition de la séquence CEST-LS vers la version CEST-LS  $grad_{opp}$ . Chronogramme des séquences CEST-LS "classique" (A) et CEST-LS  $grad_{opp}$  (B). Des gradients "spoilers" sont appliqués selon la direction z (rectangle noir plein). Des bandes de saturation FOV sont ajoutées pour éliminer le signal externe à la ROI souhaitée (motif hachuré). En (A), les impulsions de saturation sont alternativement activées et désactivées et le gradient de saturation  $G_{sat}$  est maintenu constant. En (B), le module de saturation est toujours activé et le signe du gradient de saturation  $G_{sat}$  alterne à chaque TR. Le signal est lu en utilisant un GE dans (A) et un SE dans (B). Deux types de profils obtenus avec deux répétitions consécutives de CEST-LS classique (C) et de CEST-LS  $grad_{opp}$  (D). (C) montre un profil obtenu avec le module de saturation activé (orange) et un profil de référence obtenu avec le module de saturation désactivé (bleu). (D) montre un profil obtenu avec un gradient de saturation positif  $G_{sat}$  (orange) et un profil obtenu avec le gradient de saturation opposé  $G_{sat}$  (bleu). (E) montre le Z-spectre donné par le rapport entre les deux profils générés par le CEST-LS classique. (F) montre le R-spectre défini par le rapport entre les profils avec  $G_{sat}$  positif et  $G_{sat}$  négatif. Dans cet exemple, les données ont été obtenues à partir d'un échantillon de glutamate 20 mM à pH 7,0.

Nous avons étudié les changements métaboliques induits par l'activation neuronale déclenchée par une stimulation électrique de la patte avant chez le rat. Le voxel CEST-LS a été positionné de manière à ce que la moitié de la ligne couvre l'activation maximale et que l'autre moitié ne couvre pas du tout l'activation (Figure 11).

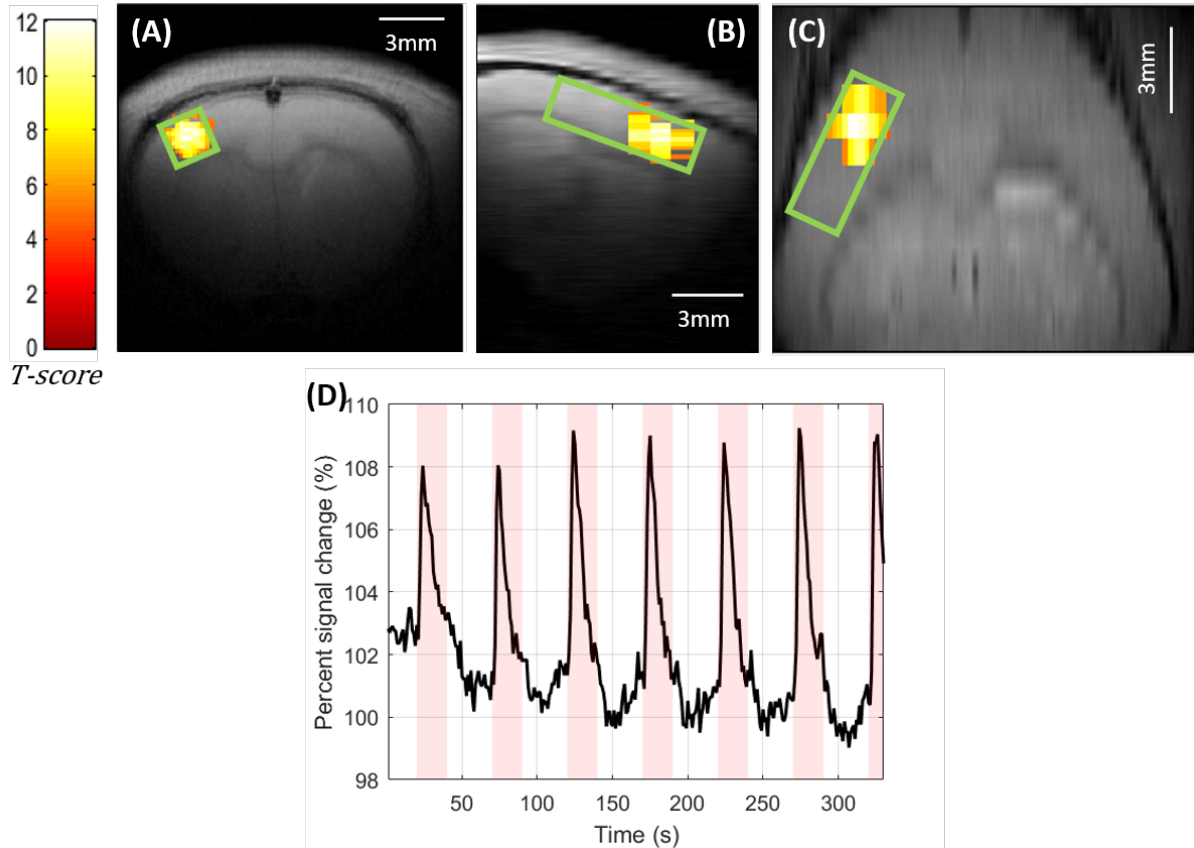


Figure 11: Effet BOLD obtenu avec une stimulation électrique de la patte avant (gauche) représentée. Cartes d'activation "T-scores" recalées à la référence anatomique selon une vue axiale (A), sagittale (B) ou coronale (C). Le voxel vert représente la position de la ligne dans laquelle les données CEST sont acquises. (D) Évolution temporelle du signal BOLD recueilli dans une région incluse dans la zone d'activation (obtenue pour un schéma de stimulation de 20 s ON, 30 s OFF).

Même si les résultats obtenus ne nous ont pas permis de détecter des changements significatifs dans les contributions CEST spécifiques pendant la tâche fonctionnelle, les protocoles d'imagerie développés restent prometteurs. En utilisant des paradigmes de stimulation optimisés pour des réponses d'activation stables et en augmentant le nombre d'animaux pour une plus grande puissance statistique, nous espérons être en mesure d'identifier les changements métaboliques transitoires induits par l'activité neuronale.

## 0.5 Conclusion

Dans l'ensemble, ce projet a démontré que les approches d'imagerie métabolique et fonctionnelle basées sur le CEST sont prometteuses en particulier à champs magnétiques ultra-

hauts mais des développements méthodologiques restent nécessaires pour permettre leur pleine exploitation en neurosciences et recherche biomédicale. La poursuite de ces développements a le potentiel d'offrir de nouvelles perspectives dans l'étude du métabolisme en conditions normales et pathologiques du rongeur à l'homme.

# List of Figures

1	Représentation schématique de l'effet CEST entre le groupe de protons de l'eau et un groupe de protons du soluté. . . . .	x
2	Glucose à température ambiante (21 °C) avec une puissance de saturation optimisée de $B_{1,sat}$ à trois champs statiques (9.4 T, 11.7 T et 17.2 T) . . . . .	xii
3	Chronogramme des impulsions de la séquence CEST-LS . . . . .	xiii
4	Analyse CEST-LS pour les données acquises dans un échantillon de glutamate 20 mM . . . . .	xiv
6	CEST-LS results on sample n° 11 containing anserine, carnosine and homocarnosine . . . . .	xvi
7	Résultats CEST-LS sur un muscle squelettique de jambe de rat . . . . .	xvi
8	Résultats CEST-LS sur un bulbe olfactif de rat . . . . .	xvii
9	Évolution du Z-spectre avec l'administration de CO <sub>2</sub> et estimation de la contribution CEST . . . . .	xviii
10	Transition de la séquence CEST-LS vers la version CEST-LS grad <sub>opp</sub> . . . . .	xx
11	Effet BOLD obtenu avec une stimulation électrique de la patte avant . . . . .	xxi
1.1	Schematic representation of a standard saturation transfer sequence . . . . .	5
1.2	Schematic representation of the CEST effect between a bulk water protons pool and solute protons pool . . . . .	6
1.3	Spectra representing the spin systems of pool A and B under several exchange regimes . . . . .	10
1.4	<i>In vitro</i> and <i>in vivo</i> Z-spectrum and $MTR_{asym}$ . . . . .	14
1.5	Conventional and APT MR images of a patient with lung cancer metastasis and a patient with stroke at 5 days postonset . . . . .	17
1.6	gluCEST maps of a wild-type mouse and a transgenic model of AD . . . . .	18
1.7	CrCEST and LATEST MRI of muscle metabolism before and after exercise . . . . .	19
1.8	Applications of glucoCEST in preclinical and clinical studies . . . . .	20
2.1	Pictures of the four pre-clinical scanners . . . . .	24
2.2	The Faraday cage surrounding the 17.2 T pre-clinical scanner . . . . .	25
2.3	Volume coils . . . . .	26
2.4	Surface coils . . . . .	26
2.5	Schematic representation of coil combination n°5 . . . . .	27
2.6	Phantom containers . . . . .	29
2.7	Temperature probe inserted in a phantom . . . . .	30
2.8	Experimental setup for animal scanning . . . . .	31
2.9	Example of a mask used for <i>in vivo</i> experiments . . . . .	32
2.10	Temperature and breathing rate monitoring . . . . .	32
2.11	Heating system . . . . .	33

2.12	Air and gas anesthesia delivery system . . . . .	33
2.13	Infusion pump . . . . .	34
2.14	The temperature probe inserted in the phantoms . . . . .	35
3.1	3D representation of the chemical structure of lactate, glucose and glutamate. . . . .	39
3.2	Schematic representation and anatomical image of the quadruple phantom . . . . .	40
3.3	Z-spectrum of lactate, glucose and glutamate with their corresponding $MTR_{asym}$ . . . . .	41
3.4	Example of $B_{1,sat}$ optimization experiment on 20 mM glutamate . . . . .	42
3.5	Glucose at room temperature (21 °C) with optimized $B_{1,sat}$ saturation power at three static fields (9.4 T, 11.7 T and 17.2 T) . . . . .	43
3.6	$MTR_{asym}$ spectra of glucose at RT and 37 °C for two static fields (9.4 T, 17.2 T) with optimized $B_{1,sat}$ power . . . . .	44
3.7	Z-spectrum and corresponding $MTR_{asym}$ of glutamate at pH 7.0 and pH 7.2, at 37 °C . . . . .	45
3.8	Z-spectrum and corresponding $MTR_{asym}$ of glucose at pH 6.0 . . . . .	45
3.9	Z-spectrum and $MTR_{asym}$ of lactate, glucose, glutamate and a mixture of all three at 7 and 17 T . . . . .	46
3.10	CEST contrast selection on a cherry tomato . . . . .	47
3.11	CEST-LS pulse sequence . . . . .	50
3.12	Simplified representation of one repetition of the CEST-LS pulse sequence . . . . .	50
3.13	Simplified pulse designs of the CEST-LS sequence . . . . .	51
3.14	CEST-LS analysis . . . . .	52
3.15	CEST-LS Z-spectrum and $MTR_{asym}$ of hydrogen peroxide . . . . .	53
3.16	Schematic representation of the peak detection process . . . . .	57
3.17	Baseline estimation using GP . . . . .	58
3.18	Examples of PEAKIT analysis of Z-spectra acquired on carnosine phantoms . . . . .	60
3.19	PEAKIT analysis of a Z-spectrum acquired <i>in vivo</i> on a rat leg muscle . . . . .	61
4.1	3D representation of the chemical structure of carnosine, anserine and homocarnosine . . . . .	65
4.2	CEST-LS results on sample n° 11 containing anserine, carnosine and homocarnosine . . . . .	67
4.3	Model $^1\text{H-NMR}$ spectra of homocarnosine, carnosine and anserine . . . . .	68
4.4	CEST-LS results on a rat leg skeletal muscle . . . . .	71
4.5	CEST-LS results on a rat olfactory bulb . . . . .	71
4.6	CEST-LS results on a rat neocortex . . . . .	72
4.7	$^1\text{H-NMR}$ spectrum on a rat leg . . . . .	73
5.1	CEST-LS sequence with the saturation module alternatively turned on and off . . . . .	81
5.2	Influence of the $\text{CO}_2$ administration on the profiles baseline . . . . .	82
5.3	Z-spectrum evolution with $\text{CO}_2$ administration and CEST contribution estimation . . . . .	83
5.4	BOLD signal enhancement dependence on echo time with gradient-echo (filled symbols) and spin-echo (open symbols) EPI at 3 T. . . . .	85
5.5	Functional CEST simulations results . . . . .	86
5.6	From classic CEST-LS to CEST-LS $\text{grad}_{opp}$ . . . . .	88
5.7	BOLD signal obtained with forepaw electrical stimulation . . . . .	91
5.8	CEST-LS $\text{grad}_{opp}$ profiles and $R$ -spectrum acquired in the cortex . . . . .	93

5.9	CEST-LS $\text{grad}_{\text{opp}}$ positive and negative profiles temporal analysis through activation . . . . .	95
5.10	Different version of the CEST-LS $\text{grad}_{\text{opp}}$ sequence . . . . .	97
5.11	Timelines associated with all three experiments . . . . .	98
5.12	Typical data obtained with experiment 1.1 . . . . .	100
5.13	CEST-LS $\text{grad}_{\text{opp}}$ results obtained with experiment 1.1 . . . . .	101
5.14	Illustration of the problem faced in experiment 1.1 and 1.2 . . . . .	103
5.15	CEST-LS $\text{grad}_{\text{opp}}$ results obtained with experiment 1.2 . . . . .	104
5.16	Schematic representation of the principle used in CEST-LS $\text{grad}_{\text{opp}}$ with block in experiment 2 . . . . .	106
5.17	Temporal BOLD signal collected in the activated area during experiment 2 . . . . .	107
6.1	Simulated $MTR_{\text{asym}}$ for a 10 mM carnosine solution at four different $B_0$ magnetic fields: 3 T, 7 T, 11.7 T and 17.2 T. . . . .	115



# List of Tables

2.1	Characteristics of the four MRI scanners . . . . .	24
2.2	Characteristics of the different RF coils . . . . .	25
2.3	List of phantoms and brief description . . . . .	28
2.4	List of animals used for the experiments and their characteristics . . . . .	31
3.1	Chemical shifts and exchange rates at 37 °C for lactate, glucose and glutamate .	41
3.2	Optimized $B_{1,sat}$ saturation power ( $\mu$ T) at 3 static fields (9.4 T, 11.7 T, 17.2 T) at two temperatures (21 °C and 37 °C) for lactate, glucose and glutamate . . . . .	42
3.3	CEST contrast (%) obtained with optimal $B_{1,sat}$ saturation power at three static field (9.4 T, 11.7 T, 17.2 T) at two temperatures ( 21 °C and 37 °C) for lactate, glucose and glutamate . . . . .	43
3.4	Evolution of the " exchange rate (at 37 °C) to chemical shift " ratio across our three static magnetic field strengths (9.4 T, 11.7 T, 17.2 T) for lactate, glucose and glutamate . . . . .	43
3.5	PEAKIT output obtained on the Z-spectrum of a rat leg muscle . . . . .	62
4.1	Parameters for <i>in vivo</i> CEST-LS acquisitions . . . . .	69
4.2	LC-ESI-MS/MS results . . . . .	73
5.1	Hypercapnia protocol . . . . .	81
5.2	PEAKIT analysis of amide (3.5-3.6 ppm) and amine (2.7-2.8 ppm) CEST signals	84
5.3	Experimental parameters for the three different experiments . . . . .	96
6.1	Advantages and drawbacks of human scanners for the CEST detection of metabolic changes induced by neuronal activation . . . . .	116



# List of symbols and abbreviations

**AD** Alzheimer's disease

**APT** Amide Proton Transfer

**BOLD** Blood Oxygen Level Dependent

$BW_{acq}$  CEST-LS acquisition bandwidth

$BW_{sat}$  CEST-LS saturation range

$B_0$  Static magnetic field

$B_{1,sat}$  Field strength of the RF pulse used in the saturation module of a CEST sequence

**CBF** Cerebral Blood Flow

**CEST** Chemical Exchange Saturation Transfer

**CEST-LS** CEST-linescan sequence

**CEST-LS grad<sub>opp</sub>** CEST-linescan sequence with alternating  $G_{sat}$  sign

**Cr** creatine

**CNS** Central Nervous System

$d_{read}$  distance of the CEST-LS ROI center to the isocenter on the read direction

**CT** Computerized Tomography

**diaCEST** CEST with diamagnetic compound

**DGE** Dynamic Glucose Enhancement

**DS** Direct Saturation

**EPI** Echo Planar Imaging

**FDA** Food and Drug Administration

**FDG** [18F]-Fluoro-deoxy-glucose

**fMRI** functional Magnetic Resonance Imaging

**FOV** Field Of View

$G_{acq}$  CEST-LS acquisition gradient

- $G_{sat}$  CEST-LS saturation gradient
- GE** Gradient Echo
- gluCEST** glutamate-weighted CEST contrast
- glucoCEST** glucose-weighted CEST contrast
- GP** Gaussian Process
- HLSVD** Hankel Lanczos singular value decomposition
- hyperCEST** CEST using hyperpolarized gases
- $k$  exchange rate
- lipoCEST** CEST using liposome
- LASER** Localization by Adiabatic SElective Refocusing
- $M_{x,y,z}$  Components of the magnetization in the rotating frame
- $M_0$  Initial (longitudinal) magnetization
- MRF** Magnetic Resonance Finger Printing
- MRI** Magnetic Resonance Imaging
- MRS** Magnetic Resonance Spectroscopy
- MRSI** Magnetic Resonance Spectroscopy Imaging
- MT** Magnetization Transfer
- MTC** Magnetization Transfer Contrast
- MTR<sub>asym</sub>** asymmetrical Magnetization Transfer Ratio
- ND** Neurodegenerative Disease
- NOE** Nuclear Overhauser Enhancement
- $N_{pts}$  Number of points of a CEST-LS profile
- PET** Positron Emission Tomography
- PD** Parkinson's disease
- SPECT** Single Photon Positron Emission Computerized Tomography
- TE** Echo Time
- TR** Repetition Time
- T1** longitudinal (spin-lattice) relaxation time
- T2** transverse (spin-spin) relaxation time

$t_{sat}$  saturation time

**T2\*** transverse relaxation time including the decay due to magnetic field inhomogeneities

**ppm** parts per million

**paraCEST** CEST with paramagnetic compound

**PBS** Phosphate-Buffered Saline

**PTE** Proton Transfer Enhancement

**PTR** Proton Transfer Ratio

$r$  CEST-LS ratio

**R-spectrum** Spectrum obtained with the CEST-LS  $\text{grad}_{\text{opp}}$

**R1** longitudinal relaxation rate

**R2** transverse relaxation rate

**RARE** Rapid Acquisition with Relaxation Enhancement

**RF** Radio Frequency

**ROI** Region Of Interest

**RG** Receiver Gain

**SAR** Specific Absorption Rate

**SE** Spin Echo

**SNR** Signal-to-Noise Ratio

**SPM** Statistical Parametric Mapping

**ss** steady-state

**UHF** Ultra-high Field

**VOI** volume-of-interest

**Z-spectrum** Spectrum obtained with a traditional CEST-PRESS or classic CEST-LS sequences

**2DG** 2-deoxy-D-glucose

**3OMG** 3-O-Methyl-D-glucose

$^1H$  Proton

$\alpha$  Saturation efficiency

$\delta$  Saturation offset

$\Delta$  Chemical shift with respect to the  $\omega_0$ , the reference frequency

$\gamma$   $^1H$  nuclear gyromagnetic ratio ( $\gamma = 42.576 \cdot 10^6 \text{ MHz} \cdot \text{T}^{-1}$ )



# Chapter 1

## Introduction to metabolic imaging using CEST MR

This chapter starts with a brief introduction to metabolic imaging. Next, a history of CEST is presented followed by the description of its principles and the theoretical aspects underlying CEST imaging. In the last section, we give an overview of the main endogenous CEST contrasts and their recent developments and applications to image *in vivo* metabolism, neurotransmission and other physiological states. This opening chapter is notably inspired by the reviews of Zhou et al. ([J. Zhou and Zijl 2006; J. Zhou, Wilson, et al. 2004]) and El Mamoune et al. ([El Mamoune et al. 2021]).

### Contents

---

<b>1.1 Introduction to metabolic imaging</b>	<b>3</b>
<b>1.2 Chemical Exchange Saturation Transfer : Origin and theory</b>	<b>4</b>
1.2.1 The emergence of CEST	4
1.2.1.1 The early stages of Saturation Transfer Experiments	4
1.2.1.2 General principle	5
1.2.1.3 Bloch-McConnell equations	6
1.2.2 Slow-to-intermediate exchange condition	7
1.2.3 Saturation Transfer	10
1.2.3.1 Approximation of a complete saturation	10
1.2.3.2 Steady-state solutions under the weak saturation pulse approximation	11
1.2.3.3 Time-dependent solutions under the weak saturation pulse approximation	12
1.2.4 Sensitivity enhancement mechanism	13
1.2.5 Saturation transfer signal Characterization	14
<b>1.3 Applications</b>	<b>15</b>
1.3.1 Overview of all the applications	15
1.3.2 Different CEST contrasts	16
1.3.2.1 Amide Proton Transfer (APT)	16
1.3.2.2 GluCEST	18

1.3.2.3 CrCEST and LATEST . . . . .	18
1.3.2.4 GlucoCEST . . . . .	19
1.3.2.5 Other contrasts . . . . .	21
1.3.3 Conclusion . . . . .	21

---

## 1.1 Introduction to metabolic imaging

Medical imaging aims at accessing the inner workings, organization, defects of an organ so as to orient a diagnosis or establish the aetiology of a disease. The history of medical imaging starts in 1895 with the discovery by Wilhelm Roentgen (inaugural Nobel prize of physics in 1901) of the X-rays and the invention of Radiography.

Today there is a multitude of medical imaging techniques: Computerized Tomography (CT), ultrasonography (US), Positron Emission Tomography (PET), Single Photon Emission Computerized Tomography (SPECT) and of course Magnetic Resonance Imaging (MRI). Those medical imaging techniques are classically used to access anatomical or structural information about the solid (CT) or soft (MRI, US) tissues but they can also be used to probe functional, mechanical, vascular or even molecular events and properties of our bodies.

Molecular Imaging is a vibrant branch of Medical imaging whose goal is to detect, quantify and image biologic processes (such as gene expression or enzymatic reaction) and biomarkers of pathology (proteins, receptors) *in vivo*. Often, Molecular imaging is performed with the help of contrast agents or radiotracers like in PET and SPECT that target specifically a biological process of interest. [18F]-Fluoro-deoxy-glucose (FDG) PET is probably the most common Molecular imaging examination, performed to track tumors and metastases. Derived from the autoradiographic 2-deoxy-glucose (2DG) method developed by Sokoloff in [Sokoloff 1977], FDG-PET allows the cartography of the regional metabolic rate of glucose consumption and has been used successfully in Neurosciences to investigate brain activity and organization via patterns of enhanced glucose utilization ([Posner et al. 1988]).

One could then define "Metabolic Imaging" as the sub-field of molecular imaging techniques giving access to metabolic information via the detection, quantification and mapping of metabolites or ions concentrations (Glu, Na<sup>+</sup>, ...), metabolic pathways (CMRGlc, CMRO<sub>2</sub>, TCA cycle rate...) or physiologic states (pH, pO<sub>2</sub>,...) *in vivo*.

MR-based Metabolic Imaging is probably the most versatile, non-invasive and non-radioactive tool. Indeed, there is a plethora of NMR signals from metabolites (or ions) relevant for the study of cellular physiology or metabolism using <sup>1</sup>H or X-nuclei NMR. The canonical approach for MR-based metabolic imaging is *in vivo* NMR spectroscopy (MRS) and spectroscopic imaging (MRSI).

*In vivo* NMR Spectroscopy is not the focus of this PhD thesis and therefore we will not introduce the principles and methods of MRS and MRSI. It is enough to understand that MRS/MRSI share the same basis as MRI, the main difference is that MRS exploits the fact that the effective magnetic field experienced by a nucleus is influenced by the electrons surrounding it: it is the shielding effect. As the electronic clouds around nuclei are different for different molecules, this shielding effect manifests by different set of Larmor frequencies for these nuclei in any given molecules. We can then recognize a molecule by its NMR spectrum. While NMR spectroscopy remains a very powerful tool to investigate metabolism through the many (more than 20 at 17T) metabolites that can be detected and quantified in the brain or in other organs, it is limited by the necessity to preserve the spectral information while encoding k-space (lengthening the acquisition) and by the low concentrations of these metabolites.

Compared to conventional MRS or MRSI, Chemical Exchange Saturation Transfer (CEST) MR presents a number of advantages that will be explained in this chapter.

## 1.2 Chemical Exchange Saturation Transfer : Origin and theory

### 1.2.1 The emergence of CEST

#### 1.2.1.1 The early stages of Saturation Transfer Experiments

Knowledge about biochemical processes is a prerequisite for a better understanding of mechanisms underlying brain activity and other metabolic pathways, both in healthy and pathological subjects. Chemical exchanges occurring at the molecular or atomic level are at the heart of these biochemical reactions. This is why the study of these chemical exchanges and their dynamics has been of great interest very early on and continues to be intensively investigated using NMR.

The phenomenon of intermolecular saturation transfer through proton exchange was known as early as 1960s when the very first effects of chemical exchange on the NMR spectrum were reported in 1951 by Liddel and Ramsey ([Liddel and Ramsey 1951]) and Arnold and Packard ([Arnold and Packard 1951]). Seven years later, Harden McConnell derived Bloch's equations to formalize the equations that govern the evolution of magnetization and incorporate the effects of proton exchange between two species ([McConnell 1958]). Based on McConnell's newly established equations, Forsén and Hoffman developed a nuclear magnetic double-resonance method for the determination of chemical exchange rates ([Forsén and Hoffman 1963]). Since then, NMR exchange applications have grown considerably by exploiting the significant gain in sensitivity conferred by saturation transfer experiments.

This approach was applied to *in vivo* MRI for the first time by Wolff and Balaban [Wolff and Balaban 1989]. In this seminal work, they generated contrast related to proton exchange between free water and semi-mobile macromolecules in rabbit kidney and skeletal muscle, defining magnetization transfer (MT) MRI as a new modality for soft tissue characterization in clinical research. Using small molecules (ammonia [Guivel-Scharen et al. 1998], urea [Dagher et al. 2000]), Balaban et al. were the first to demonstrate that chemical exchange between free water and labile protons of low-concentration solutes can be harnessed, via the application of a frequency-selective radiofrequency (RF) saturation, to generate a bulk water signal change and suggested using it as a new MRI modality ([Ward, Aletras, and Balaban 2000; Wolff and Balaban 1990]). They named this approach "Chemical Exchange Saturation Transfer" or "CEST" MRI ([Ward, Aletras, and Balaban 2000]).

Van Zijl and colleagues later extended this findings on small solutes to polymers with a large number of exchanging sites of similar chemical shift for which they reached record enhancements ( $10^6$  to  $10^7$ ) ([Goffeney et al. 2001; Snoussi et al. 2003]). To date, CEST MRI has been exploited to detect a broad spectrum of compounds, both exogenously and endogenously. It has been applied to several paramagnetic CEST agents ("PARACEST") ([Shanrong Zhang, Winter, et al. 2001; Shanrong Zhang and Sherry 2003; Aime, Barge, et al. 2002; Don-

ald E Woessner et al. 2005]) which contributed to extending the range of detectable chemical shifts with this technique. As opposed to paraCEST, other diamagnetic compounds are called diaCEST and were investigated for the first time in 2003 by Zhou et al. ([J. Zhou, Payen, et al. 2003; J. Zhou, Lal, et al. 2003]) that showed that endogenous mobile proteins and peptides could also be detected using CEST. An overview of the detection of those endogenous molecules in biological tissue is presented with more details in section 1.3.

CEST approaches exist for other nuclei than  $^1\text{H}$ , notably for  $^{31}\text{P}$  ([Zhu, M. Lu, and W. Chen 2018] for review) and  $^{13}\text{C}$  MRS ([Rothman, De Feyter, et al. 2011] for review). In those studies, saturation transfer is used to investigate enzymatic reaction rates such as the creatine kinase ( $\text{PCr} + \text{ADP} + \text{H}^+ \rightarrow \text{Cr} + \text{ATP}$ ) or the lactate dehydrogenase (lactate to pyruvate conversion).

### 1.2.1.2 General principle

As suggested by its acronym, the principles of CEST imaging rely on the observation of a transfer of saturation between two or more pools of protons between which protons are exchanged. To better describe the effect, let's consider a two-pool exchange with pool A being the water protons and pool B the labile protons of the solute present at a much smaller concentration. Those pools are characterized by many parameters presented below Equation 1.1 and particularly by  $k_{AB}$  and  $k_{BA}$ , the exchange rates rates govern the dynamics of the exchange from pool A to pool B and vice versa.

As presented in Figure 1.1, a standard saturation transfer sequence is composed of two distinct steps: a first module that disturbs the spin system and a second readout module which measures the response of the spin system to the perturbation.

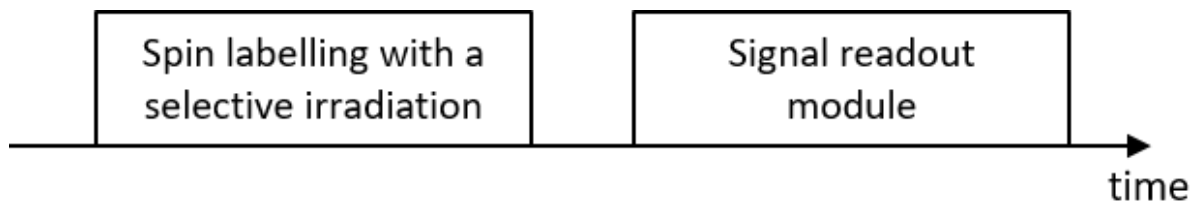


Figure 1.1: Schematic representation of a standard saturation transfer sequence.

As schematically represented in Figure 1.2A, before saturation is applied, a small solute proton peak can generally be detected in the NMR spectrum, unless exchange is very fast on the NMR time scale. Considering the two-pool system described just above, the disruption of the signal consists in applying a RF pulse at the resonance frequency of the solute protons B. The saturation pulse progressively dephases the spins of pool B, which results in spoiling their longitudinal net magnetization (Figure 1.2B). With the constant chemical exchange, this saturation is subsequently transferred to the bulk water protons (pool A), leading to a decrease of their longitudinal magnetization. The detected water signal measured in the second step is therefore attenuated (Figure 1.2C). This explains how the protons of the pool B can indirectly be detected through the signal of water.

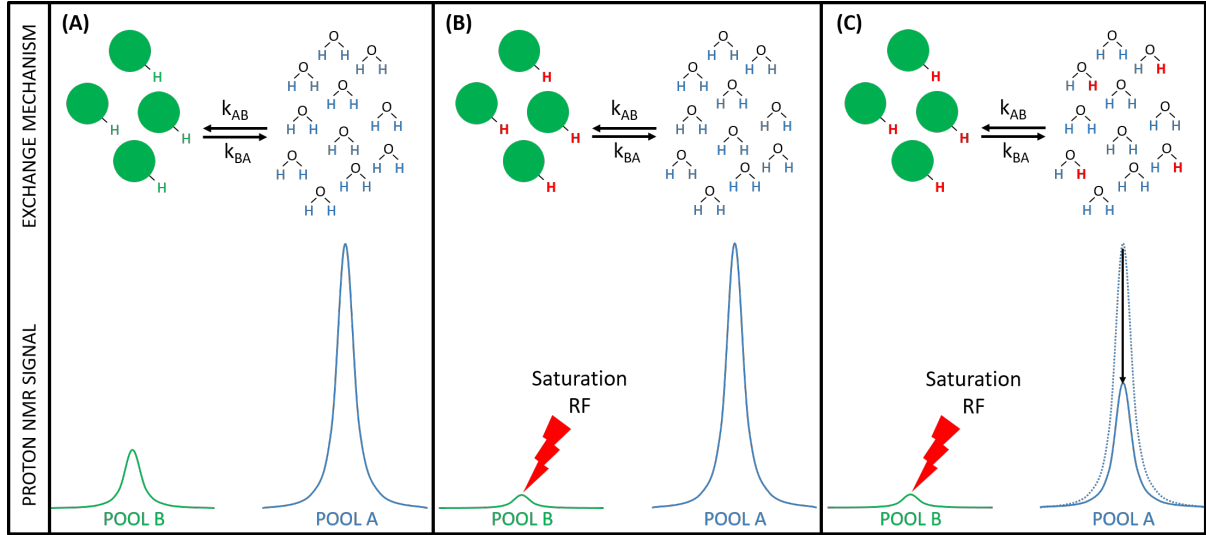


Figure 1.2: Schematic representation of the CEST effect between a bulk water protons pool (pool A) and solute protons pool (pool B). (A) Situation before the RF saturation. The NMR signal show a small peak for the low concentration solute pool and a bigger peak for the bulk water protons (not at scale) (B) Solute exchangeable protons are labeled (in red) by saturating their exchangeable protons with selective RF irradiation (applied at their resonance frequency). The NMR signal shows a decrease of the solute proton peak. (C) The saturated protons are transferred from pool B to pool A and the RF pulse keeps saturating the solute protons. The water NMR signal is partially saturated and therefore reduced.

In order to give a more accurate description of the theoretical evolution of the magnetizations of pool A and B, we use the Bloch-McConnell equations.

### 1.2.1.3 Bloch-McConnell equations

In 1946, Felix Bloch proposed in [Bloch 1946] a set of equations to describe the time dependence of the net magnetization during the course of the NMR experiment. Those equations were later extended to a system also accounting for the magnetization exchange via the forward and reverse chemical reactions called the Bloch-McConnell equations ([McConnell 1958; D. Woessner 1961]). Considering the application of a RF pulse along the  $x$  axis in the rotating frame, the magnetization evolution of the two pool spin systems previously introduced can be described by the equation system 1.1:

$$\frac{d}{dt} \begin{pmatrix} M_x^A \\ M_y^A \\ M_z^A \\ M_x^B \\ M_y^B \\ M_z^B \end{pmatrix} = \begin{pmatrix} -\rho_{2A} & -\Delta_A & 0 & k_{BA} & 0 & 0 \\ \Delta_A & -\rho_{2A} & \omega_1 & 0 & k_{BA} & 0 \\ 0 & -\omega_1 & -\rho_{1A} & 0 & 0 & k_{BA} \\ k_{AB} & 0 & 0 & -\rho_{2B} & -\Delta_B & 0 \\ 0 & k_{AB} & 0 & \Delta_B & -\rho_{2B} & \omega_1 \\ 0 & 0 & k_{AB} & 0 & -\omega_1 & -\rho_{1B} \end{pmatrix} \cdot \begin{pmatrix} M_x^A \\ M_y^A \\ M_z^A \\ M_x^B \\ M_y^B \\ M_z^B \end{pmatrix} + \begin{pmatrix} 0 \\ 0 \\ R_{1A}M_0^A \\ 0 \\ 0 \\ R_{1B}M_0^B \end{pmatrix} \quad (1.1)$$

with :

- $M_{x,y,z}^A$  and  $M_{x,y,z}^B$  the components in the rotating frame of the magnetization.

- $M_0^A$  and  $M_0^B$ , the initial magnetization. The magnetization vectors are initially aligned with the z-axis (collinear with  $\vec{B}_0$ ).
- $k_{AB}$  and  $k_{BA}$  are the exchange rate of protons from pool A to pool B and vice versa.
- $\omega_1 = \gamma B_{1,sat}$  where  $\gamma$  is the  $^1\text{H}$  nuclear gyromagnetic ratio and  $B_{1,sat}$  is the RF pulse field strength.
- $\Delta_{A,B} = \omega_{A,B} - \omega_0$  the frequency shifts with respect to  $\omega_0$ , the reference frequency of the rotating frame with  $\omega_0 = \gamma B_0$  and  $B_0$  is the main magnetic field strength.
- $R_{1A} = \frac{1}{T_{1A}}$  and  $R_{1B} = \frac{1}{T_{1B}}$  are the longitudinal relaxation rate.
- $R_{2A} = \frac{1}{T_{2A}}$  and  $R_{2B} = \frac{1}{T_{2B}}$  are the transverse relaxation rate.
- $\rho_{1A} = R_{1A} + k_{AB}$   
 $\rho_{2A} = R_{2A} + k_{AB}$   
 $\rho_{1B} = R_{1B} + k_{BA}$   
 $\rho_{2B} = R_{2B} + k_{BA}$

The system under steady-state obeys the relationship:

$$k_{AB}M_0^A = k_{BA}M_0^B \quad (1.2)$$

## 1.2.2 Slow-to-intermediate exchange condition

In this section, we consider that the system is disturbed by a non-selective RF 90 °C pulse. At  $t = 0$ , the magnetizations of the A and B pool are tilted in the transverse plane, giving us the following initial conditions :

$$\begin{pmatrix} M_x^A \\ M_y^A \\ M_z^A \\ M_x^B \\ M_y^B \\ M_z^B \end{pmatrix} (t=0) = \begin{pmatrix} 0 \\ M_0^A \\ 0 \\ 0 \\ M_0^B \\ 0 \end{pmatrix} \quad (1.3)$$

The magnetization evolution in the transverse plane is given by :

$$\frac{d}{dt} \begin{pmatrix} M_x^A \\ M_y^A \\ M_x^B \\ M_y^B \end{pmatrix} = \begin{pmatrix} -\rho_{2A} & -\Delta_A & k_{BA} & 0 \\ \Delta_A & -\rho_{2A} & 0 & k_{BA} \\ k_{AB} & 0 & -\rho_{2B} & -\Delta_B \\ 0 & k_{AB} & \Delta_B & -\rho_{2B} \end{pmatrix} \cdot \begin{pmatrix} M_x^A \\ M_y^A \\ M_x^B \\ M_y^B \end{pmatrix} \quad (1.4)$$

Using the expression of the complex transverse magnetization (1.5), the system 1.4 can be rewritten as 1.6.

$$M_T^A = M_y^A - iM_x^A \quad ; \quad M_T^B = M_y^B - iM_x^B \quad (1.5)$$

$$\frac{d}{dt} \begin{pmatrix} M_T^A \\ M_T^B \end{pmatrix} = \begin{pmatrix} i\Delta_A - \rho_{2A} & k_{BA} \\ k_{AB} & i\Delta_B - \rho_{2B} \end{pmatrix} \cdot \begin{pmatrix} M_T^A \\ M_T^B \end{pmatrix} \quad (1.6)$$

The analytical solution of the system 1.6 give us the temporal evolution of the transverse magnetizations in the presence of chemical exchange and the solutions can be written as :

$$M_T^A(t) = c_1^A \exp(\lambda_1 t) + c_2^A \exp(\lambda_2 t) \quad (1.7)$$

$$M_T^B(t) = c_1^B \exp(\lambda_1 t) + c_2^B \exp(\lambda_2 t) \quad (1.8)$$

with  $\lambda_1$  and  $\lambda_2$ , the eigenvalues of the matrix.

In order to simplify the expression of the solution, let's consider the particular case when the transverse relaxation is neglected and the initial magnetizations of pool A and B are equal,  $M_0^A = M_0^B = M_0$ , with  $M_0$  the common value of the initial magnetization. With the steady-state relationship 1.2, this implies that  $k_{AB} = k_{BA} = k$ , with  $k$  the common value of the exchange rate. In this case, the eigenvalues can be rewritten as:

$$\lambda_{1,2} = i \frac{(\Delta_A + \Delta_B)}{2} - k \pm W \quad (1.9)$$

with  $W = \sqrt{k^2 - \frac{i}{4}(\Delta_A - \Delta_B)^2}$ .

The  $c_1^A, c_2^A, c_1^B, c_2^B$  coefficients can be determined using the initial conditions 1.3

$$c_1^A = \frac{M_0}{2W} \left( i \left( \frac{\Delta_A - \Delta_B}{2} \right) + k + W \right) \quad (1.10)$$

$$c_2^A = \frac{M_0}{2W} \left( -i \left( \frac{\Delta_A - \Delta_B}{2} \right) + k + W \right) \quad (1.11)$$

$$c_1^B = \frac{M_0}{2W} \left( i \left( \frac{\Delta_A - \Delta_B}{2} \right) + k + W \right) \quad (1.12)$$

$$c_2^B = \frac{M_0}{2W} \left( -i \left( \frac{\Delta_A - \Delta_B}{2} \right) + k + W \right) \quad (1.13)$$

The detected signal  $S(t)$  in the readout module is proportional to the sum of the transverse magnetizations of the pool A and B.

$$S(t) \propto M_T^A(t) + M_T^B(t) \quad (1.14)$$

From this point, two scenarios can be considered : the slow exchange and the fast exchange.

### Slow exchange

With the slow exchange condition formulated as  $k \ll |\Delta_A - \Delta_B|$ , the analytical solutions can be rewritten with:

$$W \approx \frac{i}{2}(\Delta_A - \Delta_B) \quad (1.15)$$

$$\lambda_1 \approx i\Delta_A - k \quad ; \quad \lambda_2 \approx i\Delta_B - k \quad (1.16)$$

$$c_1^A \approx c_1^B \approx M_0 \quad ; \quad c_2^A \approx c_2^B \approx 0 \quad (1.17)$$

Using those simplified expressions, the temporal evolution of the signal can be written as:

$$S(t) \propto M_0 [\exp((i\Delta_A - k)t) + \exp((i\Delta_B - k)t)] \quad (1.18)$$

The Fourier transform of this signal corresponds to a spectrum with two peaks of  $M_0$  intensity centered on  $\Delta_A$  and  $\Delta_B$ , both having a full width at half maximum of  $2k$  (bottom of Figure 1.3).

### Fast exchange

With the fast exchange condition formulated as  $k \gg |\Delta_A - \Delta_B|$ , the analytical solutions can be rewritten with:

$$W \approx k \left( 1 - \frac{(\Delta_A - \Delta_B)^2}{8k^2} \right) \quad (1.19)$$

$$\lambda_{1,2} \approx i \frac{(\Delta_A + \Delta_B)}{2} - k \pm k \left( 1 - \frac{(\Delta_A - \Delta_B)^2}{8k^2} \right) \quad (1.20)$$

$$c_1^A \approx c_1^B \approx M_0 \quad ; \quad c_2^A \approx c_2^B \approx 0 \quad (1.21)$$

Using those simplified expressions, the temporal evolution of the signal can be written as:

$$S(t) \propto M_0 \left[ \exp \left( \left( i \frac{(\Delta_A + \Delta_B)}{2} - \frac{(\Delta_A - \Delta_B)^2}{8k} \right) t \right) + \exp \left( \left( i \frac{(\Delta_A + \Delta_B)}{2} + \frac{(\Delta_A - \Delta_B)^2}{8k} \right) t \right) \right] \quad (1.22)$$

The Fourier transform of this signal corresponds to a spectrum with a unique  $M_0$  intensity peak centered on  $\frac{\Delta_A + \Delta_B}{2}$ , with a full width at half maximum of  $\frac{(\Delta_A - \Delta_B)^2}{4k}$  (top of Figure 1.3).

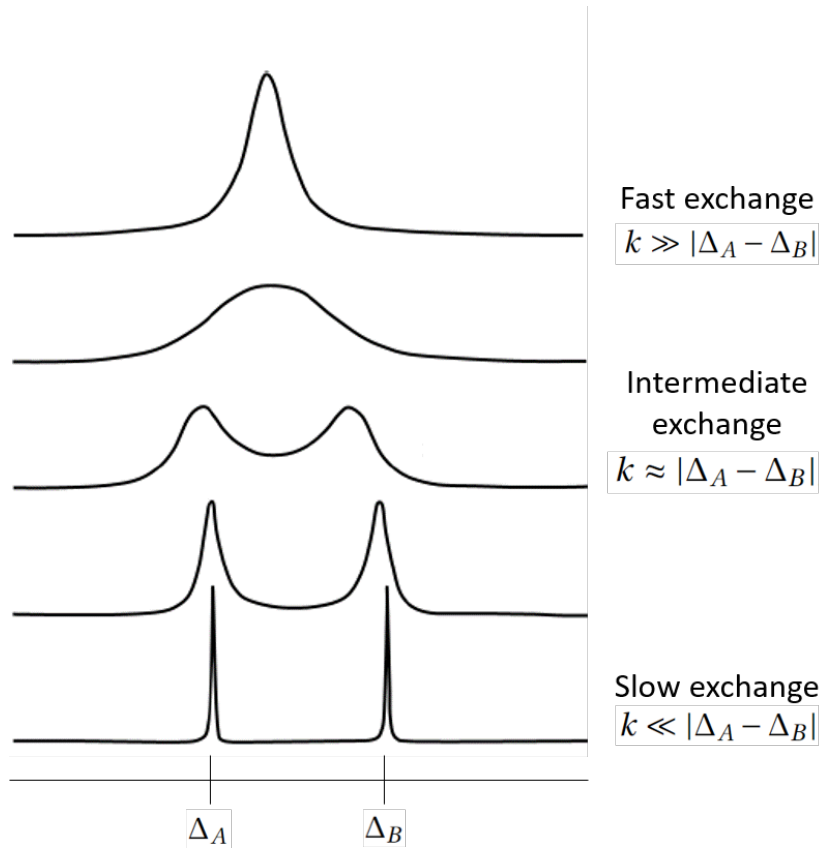


Figure 1.3: Spectra representing the spin systems of pool A and B under several exchange regimes (slow, intermediate and fast)

In the fast exchange scenario, the two protons pools are not spectrally distinct, demonstrating that the magnetization transfer is not possible in such conditions. In order to observe a CEST contrast, the resolutions of the Bloch-McConnell equations have shown that the slow-to-intermediate exchange condition must be fulfilled :

$$k \ll |\Delta_A - \Delta_B| \quad (1.23)$$

We can already notice that this condition is easier to meet at higher magnetic fields since they provide a more important chemical shift dispersion. The set of CEST-observable protons at high field is larger than the one at low fields.

### 1.2.3 Saturation Transfer

The previous section has shown that the distinct resonances identity of each proton pool is the prerequisite for successful application of CEST experiments. In this section, we consider it to be the case and present the description of the evolution of pool A and B magnetization when they undergo a magnetization transfer. The exact analytical solutions of the system equation 1.1 are difficult to obtain but using reasonable assumptions allow to simplify the equations and obtain representative solutions.

#### 1.2.3.1 Approximation of a complete saturation

If we now assume that the RF pulse is applied to solute pool (pool B) only, leaving the water pool (pool A) unperturbed. We therefore have  $M_z^B(t) = 0$ . From the Bloch-McConnell

equations (1.1), we obtain the temporal evolution of the longitudinal magnetization of pool A:

$$\frac{M_z^A(t_{sat})}{M_0^A} = \frac{R_{1A}}{\rho_{1A}} + \frac{k}{\rho_{1A}} \exp(-\rho_{1A} t_{sat}) \quad (1.24)$$

with  $t_{sat}$  the saturation time. The efficiency of the saturation of the pool A spin system can be evaluated through the Proton Transfer Ratio (PTR). When  $t \rightarrow +\infty$ , it can be written as:

$$PTR = 1 - \frac{M_z^A(t \rightarrow +\infty)}{M_0^A} = \frac{k_{AB}}{R_{1A} + k_{AB}} \quad (1.25)$$

Equation 1.25 shows that the maximum saturation rate of the spins from the pool A increases with the exchange rate from pool A to pool B but remains limited by the competition with the effect of longitudinal relaxation of the spins A.

### 1.2.3.2 Steady-state solutions under the weak saturation pulse approximation

The hypothesis of the complete saturation of pool B used in the previous section remains an approximation since it can only be obtained under a very strong RF pulse, which is not true in practice. We now consider the application of a weak RF pulse to the solute pool (pool B), causing a partial saturation of the spins B. For simplicity, we introduce the following case-sensitive definitions :

$$m_z^A = M_z^A - M_0^A \quad ; \quad m_z^B = M_z^B - M_0^B \quad (1.26)$$

The assumption that the RF pulse is applied to pool B (solute protons) with pool A (water protons) unperturbed theoretically corresponds to  $\Delta_A = 0$  and  $\Delta_B \rightarrow \infty$  (thus neglected effects  $\Delta_A, \Delta_B, \omega_1$  of terms on the water pool (A)). Consequently, the time processes of the system can be described by:

$$\frac{d}{dt} \begin{pmatrix} M_y^A \\ m_z^A \\ M_y^B \\ m_z^B \end{pmatrix} = \begin{pmatrix} -\rho_{2A} & 0 & k_{BA} & 0 \\ 0 & -\rho_{1A} & 0 & k_{BA} \\ k_{AB} & 0 & -\rho_{2B} & \omega_1 \\ 0 & k_{AB} & -\omega_1 & -\rho_{1B} \end{pmatrix} \cdot \begin{pmatrix} M_y^A \\ m_z^A \\ M_y^B \\ m_z^B \end{pmatrix} + \begin{pmatrix} 0 \\ 0 \\ \omega_1 M_0^B \\ 0 \end{pmatrix} \quad (1.27)$$

The steady-state (ss) solutions of this system can be obtained considering that the left term is equal to null vector and the results are presented in Equations 1.28,1.29,1.30,1.31.

$$M_y^A(ss) = -\frac{k_{BA}}{\rho_{2A}} \frac{\omega_1 q M_0^B}{(\omega_1^2 + pq)} = -\frac{k_{AB}}{\rho_{2A}} \frac{\omega_1^2 q M_0^A}{(\omega_1^2 + pq)} \quad (1.28)$$

$$m_z^A(ss) = -\frac{k_{BA}}{\rho_{1A}} \frac{\omega_1^2 M_0^B}{(\omega_1^2 + pq)} = -\frac{k_{AB}}{\rho_{1A}} \frac{\omega_1^2 M_0^A}{(\omega_1^2 + pq)} \quad (1.29)$$

$$M_y^B(ss) = -\frac{\omega_1 q M_0^B}{\omega_1^2 + pq} \quad (1.30)$$

$$m_z^B(ss) = -\frac{\omega_1^2 M_0^B}{\omega_1^2 + pq} \quad \text{or} \quad M_z^B(ss) = \frac{pq M_0^B}{\omega_1^2 + pq} \quad (1.31)$$

with,

$$p = \rho_{2B} - \frac{k_{AB}k_{BA}}{\rho_{2A}} \quad \text{and} \quad q = \rho_{1B} - \frac{k_{AB}k_{BA}}{\rho_{1A}} \quad (1.32)$$

From those equations, we can express  $\alpha$ , the saturation efficiency of the solute protons (pool B) with:

$$\alpha = \frac{M_0^B - M_z^B(ss)}{M_0^B} = \frac{-m_z^B}{M_0^B} = \frac{\omega_1^2}{\omega_1^2 + pq} \quad (1.33)$$

Equation 1.33 confirms what was mentioned at the beginning of the section: only with an infinite RF saturation power does the solute protons (pool B) approach the maximum saturation state with  $\alpha = 1$ .

### 1.2.3.3 Time-dependent solutions under the weak saturation pulse approximation

We finally consider the saturation transfer evolution with respect to the saturation time  $t_{sat}$ . In order to obtain an analytical solution to the system, two approximations are necessary: (1) the pool B magnetization almost instantaneously reaches the steady-state, thus leading to Equation 1.30 and 1.31; (2) The pool A magnetization remains unperturbed during this short time ( $M_z^A(t=0) = M_0^A$ ). With those two assumptions, the dynamics for pool A (water protons) can be described by:

$$\frac{dm_z^A}{dt} = -\rho_{1A}m_z^A + k_{BA}m_z^B(ss) \quad (1.34)$$

Using the weak pulse approximation ( $M_z^A(t=0) = M_0^A$  (ie.)  $m_z^A(t=0) = 0$ ) for the initial conditions, we obtain the following temporal solution:

$$m_z^A(t) = \frac{k_{BA}m_z^B(ss)}{\rho_{1A}} [1 - \exp(-\rho_{1A}t)] \quad (1.35)$$

With Equation 1.31, the PTR in the water pool can therefore be derived to be:

$$PTR(t_{sat}) = -\frac{m_z^A(t_{sat})}{M_0^A} = \frac{k_{BA}M_0^B\omega_1}{M_0^A\rho_{1A}(\omega_1^2 + pq)} [1 - \exp(-\rho_{1A}t_{sat})] \quad (1.36)$$

Using  $\alpha$  the saturation efficiency of pool B (Eq. 1.33) and knowing that in the steady state, the exchanging protons groups satisfy the condition expressed in Equation 1.2, the equation 1.36 can be reformulated as :

$$PTR(t_{sat}) = \frac{k_{AB}\alpha}{R_{1A} + k_{AB}} [1 - \exp(-\rho_{1A}t_{sat})] \quad (1.37)$$

Equations 1.36 and 1.37 reflect that the PTR, and thus the associated CEST effect, depends on the saturation time ( $t_{sat}$ ), the solute concentration ( $M_0^B$ ), the chemical exchange rate of solute protons with bulk water ( $k_{BA}$ ), the longitudinal relaxation time of water protons ( $R_{1A} = \frac{1}{T_{1A}}$ ), as well as on the saturation efficiency of the solute pool ( $\alpha$ ), which itself depends on the saturation power ( $\omega_1 = \gamma B_{1,sat}$ ).

In particular, the PTR increases with the the saturation time but we can consider that the steady-state is reached when  $t_{sat} > 5\rho_{1A}$ , which corresponds to  $t_{sat}$  of a few seconds. The PTR also increases with the number of exchangeable protons, which is related to the solute

concentration and the number of exchangeable protons for each molecule in solution. The PTR necessarily increases with the exchange rate  $k_{AB}$  but this is limited to exchange rates remaining in the slow exchange regime determined by the slow exchange condition (1.23).

Higher PTR are favored by longer  $T_1$ s. This is one of the advantage of performing CEST experiments at high magnetic field since longitudinal relaxation times for  $^1\text{H}$  metabolites and  $^1\text{H}_2\text{O}$  in tissues are longer ([Lopez-Kolkovsky, Sebastien Mériaux, and Boumezbeur 2016]). We also notice that longer  $T_1$ s (and thus the shorter  $R_1$ s) increase the influence of the back exchange term ( $k_{AB}$ ) on the PTR. The PTR is directly proportional to  $\alpha$ , the saturation efficiency of pool B. However, if  $\alpha$  increases with  $\omega_1$  and therefore with the saturation power  $B_{1,sat}$ , the application of an intense saturation also leads to an increase in the Direct Saturation (DS) of the pool A (or spill-over effect). Therefore, there is an optimal intensity for which the trade-off between saturation transfer and direct saturation of free protons leads to a PTR maximum. This intensity can be obtained by canceling the first derivative with respect to  $\omega_1$  of equation 1.25. A numerical resolution reported by Woessner and co-workers indicates that the optimal value of the  $\omega_{1,opt}$  saturation intensity varies linearly with  $k_{BA}$ , the exchange rate between A and B spins ([Sun, Van Zijl, and J. Zhou 2005; Donald E Woessner et al. 2005]). The optimal saturation intensity  $B_{1,sat,opt}$  verifies the following equation:

$$B_{1,sat,opt} = \frac{\omega_{1,opt}}{\gamma} = \frac{k_{BA}}{\gamma} \quad (1.38)$$

#### 1.2.4 Sensitivity enhancement mechanism

In view of the low concentration of solute ( $\mu\text{M}$  to  $\text{mM}$  range), a single transfer of saturation would be insufficient to show any discernable effect on water protons, the concentration of which is 110 M in pure water solution or about 80 M in most tissues, which is  $10^4$  and  $10^6$  times more concentrated. However, CEST NMR sequences allow to detect and image the water-exchangeable protons of solutes by indirectly measuring the decrease of the bulk water signal. Depending on the experimental conditions and saturation parameters, the CEST contrast can lead to a relative signal change of 50% its initial magnetization  $M_0^A$ . This illustrates the capability of CEST methods to enhance significantly the detection of those solutes by several order of magnitudes.

During the application of the frequency-selective RF pulse, saturation exchanges (forward and backward) between the solute and the water protons take place. Because the water pool is much larger than the solute proton pool, saturated solute protons are replaced repeatedly by non-saturated water protons, which are then again saturated, and accumulation of saturated protons in the water pool acts as a "saturation amplifier". Saturation transfer therefore leads to a substantial enhancement in sensitivity allowing the detection of low-concentration solute. The effect of this amplification can be expressed with the Proton Transfer Enhancement (PTE) ([Goffeney et al. 2001; Snoussi et al. 2003]):

$$PTE(t_{sat}) = \frac{M_z^A - M_0^A}{M_0^B} = \frac{M_0^A PTR}{M_0^B} = \frac{M_0^A k_{AB} \alpha}{M_0^B (R_{1A} + k_{AB})} [1 - \exp(-\rho_{1A} t_{sat})] \quad (1.39)$$

The greatest enhancements are achieved when the solute concentration is much smaller than the solvent concentration because this ensures a high probability that saturated solute

protons are replaced by unsaturated protons from the much larger water pool. For example, if we consider the magnetization transfer occurring in a 10 mM aqueous solution of glutamate (pH = 7.0 and T = 37 °C) at high field when a RF pulse is applied at the frequency of the two glutamate exchangeable protons, the following set of parameters can be used:

$$k_{BA} = 5000 \text{ Hz}, M_0^A = 110 \text{ M}, M_0^B = 10 \text{ mM}, k_{BA} = 0.9 \text{ Hz}, T_{1A} = 2.5 \text{ s}, \alpha = 0.5, t_{sat} \gg \frac{1}{\rho_{1A}}$$

With the computation of the PTR for pool A (1.25), this magnetization transfer results in a 35% water signal decrease, corresponding to an enhancement factor of 1910 (1.39).

This sensitivity enhancement scheme in which continuous saturation of the small solute pool causes cumulative saturation of the large water pool is the reason why saturation transfer imaging is a very promising approach to increase the detection sensitivity of MR-based molecular imaging.

### 1.2.5 Saturation transfer signal Characterization

In general, the equations describing the magnetization temporal evolution occurring during a magnetization/saturation transfer experiment are very rarely derived from an analytical resolution of the Bloch-McConnell equations because of the complexity of the biological systems, especially *in vivo*. In practice, it is more common to consider the numerical calculation or the experimental measurement of Z-spectra ([Grad et al. 1991]). This quantity corresponds to the measure of the net longitudinal magnetization of the water pool ( $M_z^A$ ) normalized by its initial value ( $M_0^A$ ) with respect to the saturation offset. Figure 1.4A represents a simulated Z-spectrum simulated considering a two pool system between the water pool and an arbitrary CEST agent.

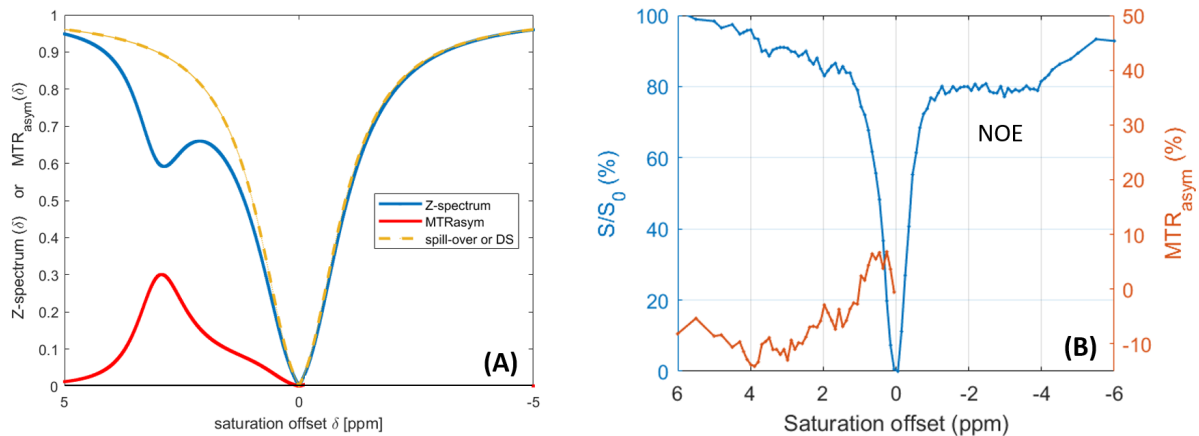


Figure 1.4: *In vitro* and *in vivo* Z-spectrum and  $MTR_{asym}$ . (A) Simulated Z-spectrum (blue curve) considering a two-pool system. The corresponding  $MTR_{asym}$  value is plotted in red and the spill-over effect is represented with a yellow dashed line. (B) *In vivo* Experimental Z-spectrum and corresponding  $MTR_{asym}$  obtained in a rat brain at 17.2 T with  $B_{1,sat} = 0.5 \mu T$

According to Figure 1.4, the saturation effect is most visible at the resonance frequency of the proton pools (water and CEST agent). The fact that a saturation effect is still observed outside of these frequencies is due to the saturation exchange taking place "off-resonance", the most visible one being the "spill-over effect" ([Baguet and Roby 1997]) due to the direct saturation (DS) of bulk water. As a first approach, one can consider that this DS effect is

symmetric. It is therefore possible to get rid of it by using the value of the water signal at the opposite saturation offset. This measure is known as the  $MTR_{asym}$  profile for asymmetrical Magnetization Transfer Ratio and is defined by:

$$MTR_{asym}(\delta) = Z\text{-spectrum}(-\delta) - Z\text{-spectrum}(\delta) = \frac{S(-\delta) - S(\delta)}{S_0} \quad (1.40)$$

where  $S(\pm\delta)$  indicates the water signals measured at the saturation offsets  $\pm\delta$  (corresponding to the previous  $M_z^A(\pm\delta)$ ) and  $S_0$  is the reference water signal measured without any RF saturation (corresponding to the previous  $M_0^A$ ).

The estimation of the  $MTR_{asym}$  is a very reliable and relatively easy-to-interpret metric for *in vitro* studies as no other effects than the one due to the CEST agent is expected. However, *in vivo* CEST studies are contaminated with two main (most of the time) confounding contrasts: the Magnetization Transfer Contrast (MTC) and the Nuclear Overhauser Enhancement (NOE) effect. These two contributions are based on additional mechanism that can cause polarization transfer even if protons are not exchanged. The MTC refers to magnetization transfer with the proton pools of semi-solid tissue components (like membranes or myelin sheets) that have very short T2s and exhibit large dipolar couplings while NOE is a transfer of polarization from one pool of spins to another via cross-relaxation due to the existence of a dipolar coupling between the two pools [Solomon 1955]. The NOE effect generates a broad contribution that is located in the upfield part of the Z-spectrum. It is for example very visible on Figure 1.4 which shows the experimental Z-spectrum acquired in a rat brain at 17.2 T. In cases when the upfield NOE contributions are larger than the downfield CEST contributions, the  $MTR_{asym}$  reaches negative values and its interpretation is hampered.

## 1.3 Applications

In the previous section, we have provided a brief theoretical framework to understand the principle of CEST experiments. The potential of CEST imaging has encouraged the development of a wide range of biomedical imaging applications and remains a rapidly growing field in the MR community. Compared to MRS, CEST offers excellent spatial resolution and therefore allows the study of specific regions, particularly by obtaining metabolic maps. With this enhancement mechanism described in section 1.2.4, CEST approaches are, under some conditions and for specific molecules, more sensitive than direct approaches such as MRS/MRSI sequences. Furthermore, the use of a selective saturation pulse frequency to saturate the solute protons allows the contrast to be switched on and off. By combining good spatial resolution, spectral specificity, great sensitivity and the ability to be turned on and off (with sequence parameters), the CEST imaging (CEST MRI) concept has led to many applications.

### 1.3.1 Overview of all the applications

CEST MRI has the potential to provide comprehensive view of molecular aspects of neuronal tissue environment such as metabolite concentration, tissue pH and metabolism. Endogenous CEST relies on exchanging groups and molecules already present in the tissue. These "agents" do not require any injection or other form of administration and no additional approval from regulatory entities (Food and Drugs Administration, European Community,

ANSM...). Still many exogenous CEST agents have been proposed and developed for MR-based Molecular imaging: paraCEST, lipoCEST which are encapsulated CEST agents using liposomes [Aime, Delli Castelli, and Terreno 2005; Flament et al. 2013; Chahid et al. 2014], and other nanoparticulate constructs such as in [Castelli et al. 2008].

To stay within the scope of this manuscript, this section focuses on endogenous molecules and aims at presenting the imaging applications of endogenous CEST contrasts. This domain of the CEST MRI is called diaCEST but encompassed several contrast to which a specific name was given. We will adhere to the conventional names and use them in this section. The chemical shift of these compounds ranges from  $-5$  to  $5$  ppm and their exchangeable proton are found in hydroxyl (-OH), amine (-NH<sub>2</sub>) or amide (-NH) groups.

## 1.3.2 Different CEST contrasts

### 1.3.2.1 Amide Proton Transfer (APT)

Probably the most developed technique to-date, APT imaging was introduced by Zhou and co-workers ([J. Zhou, Lal, et al. 2003]) and examines the detection of exchangeable amide protons of endogenous mobile proteins and peptides. Those protons have a relatively narrow range of resonance frequency centered at  $\sim 3.5$  ppm downfield from water. The CEST detection of amide protons is made possible thanks to their high concentrations (5 - 8 mM in most tissues ([J. Zhou, Payen, et al. 2003; Yan et al. 2015])) and their low exchange rates ( $\sim 30$  Hz), making the slow-to-intermediate condition easier to satisfy at 1.5 or 3T, the usual magnetic fields in clinic.

APT imaging has achieved many notable successes such as identifying ischemic regions of brain tissues in patients who have suffered a cerebrovascular stroke. Reduced cerebral blood flow during a stroke indeed causes intracellular pH to decrease ([Sun, Cheung, et al. 2011]). The APT effect varies strongly with pH since the exchange rate of those amide protons dramatically decreases with decreasing pH, therefore reducing the APT contrast in oxygen deprived areas. The ischemic core show a significant decrease in APT compared to the regions surrounding the infarct, also called penumbra ([Harston et al. 2015; Tietze et al. 2014; Sun, J. Zhou, et al. 2007]). Thanks to this approach, APT imaging allow a non-invasive monitoring of pH changes and is therefore sometimes referred to as "pH-weighted MRI". More specific studies were carried out in order to distinguish the origin of strokes between cerebral ischemia and intracerebral hemorrhages ([Jeong et al. 2017; Ma et al. 2017]).

APT imaging has also been used empirically to examine solid tumors. In this case, the APT contrast changes are linked to the proliferating tumors and their larger amount of mobile proteins ([Warburg, Wind, and Negelein 1927]) than the surrounding tissue. The feasibility of this technique was first demonstrated on a rat brain tumor [J. Zhou, Lal, et al. 2003]. Numerous clinical studies have shown promising results using APT imaging to assess tumors in the breast ([Schmitt et al. 2011]), the prostate ([Jia et al. 2011]) or the brain ([C. K. Jones, Schlosser, et al. 2006; J. Zhou, J. O. Blakeley, et al. 2008; Y. Yang et al. 2020; Togao et al. 2014; Jiang et al. 2016; Zhao, Wen, F. Huang, et al. 2011]). In addition to detecting the tumor, the APT contrast allows to estimate the tumor grade ([Togao et al. 2014; Zhao, Wen, G. Zhang, et al. 2013; Wen et al. 2010]). The studies presented in References [J. Zhou, Tryggestad, et al. 2011; Park et al. 2016] indicate that APT imaging may provide differentiation between active glioma and radiation necrosis, and could serve to evaluate tumor response to therapy.

Figure 1.5 is adapted from Reference [Zhao, Wen, F Huang, et al. 2011] and shows hypo-intense  $MTR_{asym}$  values (Figure 1.5B) correlating with the oxygen-deprived areas (Figure 1.5A) as well as hyper-intense  $MTR_{asym}$  values ((Figure 1.5D) in a malignant tumor (Figure 1.5C).

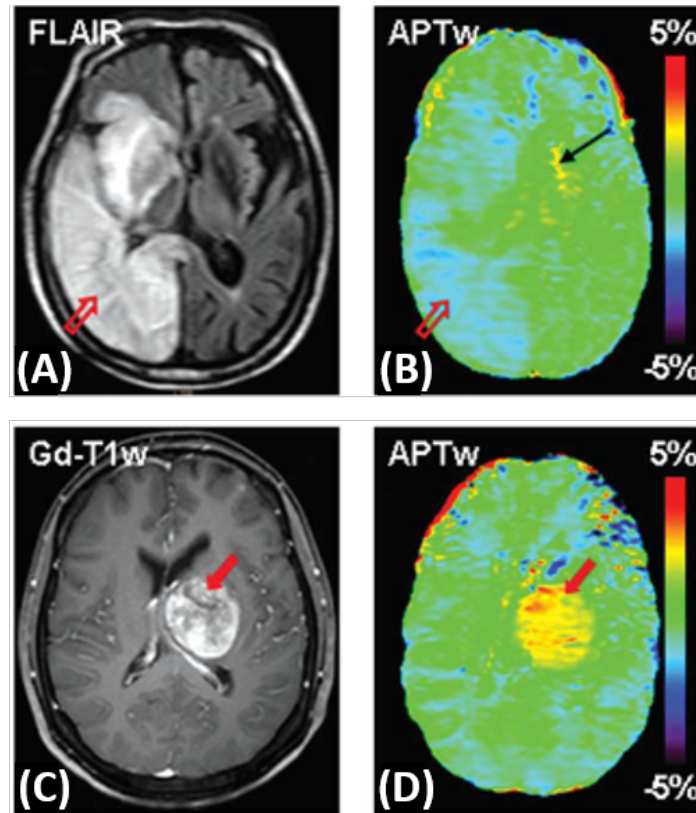


Figure 1.5: Conventional (A) and APT (B) images of a patient with stroke at 5 days postonset. Conventional (C) and APT (D) images of a patient with lung cancer metastasis. The tumor (solid red arrow) is hyperintense, while the stroke (open red arrow) is hypointense on the APT images. The hyperintense signal in the basal ganglia region (black arrow) contralateral to ischemia on the APT image (h) is an artifact. Figure adapted from [Zhao, Wen, F Huang, et al. 2011].

Although less frequently used for this application, APT imaging has recently proven its interest in the study of neurodegenerative diseases like Alzheimer's (AD) or Parkinson's (PD) diseases. AD is an age-related neurodegenerative disorder characterized by an accumulation of abnormal  $\beta$ -Amyloid and phosphorylated Tau proteins. Wang and co-workers ([R. Wang et al. 2015]) successfully tested the feasibility of APT imaging to detect affected brain regions in AD patients via hyperintense APT contrasts, changes which could be used to discriminate between more or less severely affected AD patients. PD is also a neurodegenerative disease characterized by a decreased dopamine level, especially in the substantia nigra. Li et al. ([C. Li, M. Chen, et al. 2017; C. Li, R. Wang, et al. 2015]) used APT imaging in PD patients and detected significantly reduced APT contrast in brain regions affected by PD. These preliminary results suggest that APT imaging may be valuable to detect early stages of AD and PD and to monitor their progression non-invasively.

### 1.3.2.2 GluCEST

As the major excitatory neurotransmitter in the brain, glutamate is involved in most of the Central Nervous System (CNS). Its (high) concentration not only evolves in normal conditions during neuronal activation but also in pathological conditions such as during neurodegenerative processes or in various neurological and psychiatric pathologies. Glutamate is a reliable biomarker of the neuronal density and viability. As a consequence, gluCEST should be a particularly relevant tool for Neurosciences and biomedical research. The CEST signal of glutamate is located at approximately 3 ppm downfield from water. It is, like most of the CEST contrasts, pH-dependent.

As for APT, one of the first application of gluCEST was to exploit this pH-dependence of the gluCEST signal to study ischemic tissues in rat brains ([Cai, Mohammad Haris, et al. 2012]). However, the more popular application of gluCEST is to study neurodegenerative diseases, in particular in animal models of Alzheimer's disease [Mohammad Haris, Nath, et al. 2013], of Huntington's disease [Pépin et al. 2016], or Tau pathology [Crescenzi et al. 2014]. This approach was also applied in clinical research studies in the context of AD ([Cai, Singh, et al. 2015]) and other neurological pathologies such as temporal lobe epilepsy ([K. A. Davis et al. 2015]) and multiple sclerosis ([O'Grady et al. 2019]).

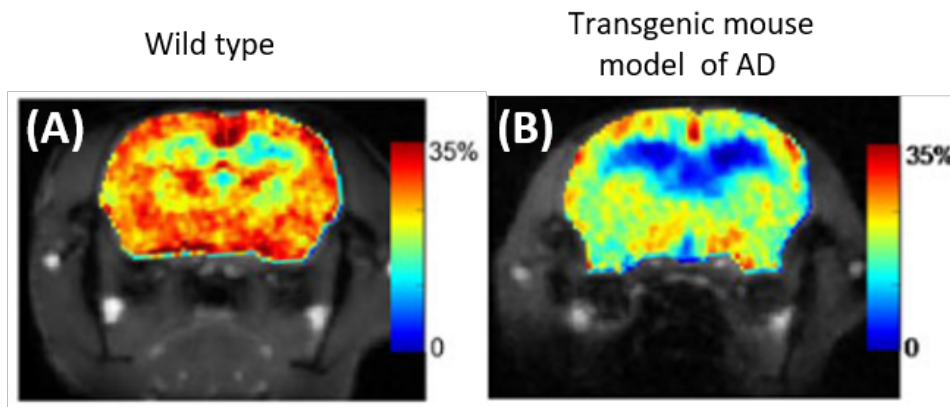


Figure 1.6: gluCEST maps showing the regional distribution of glutamate in the brain of a wild-type mouse and a transgenic mouse model of AD. Figure adapted from [Mohammad Haris, Nath, et al. 2013]

For example, Figure 1.6 shows the great correlation of the gluCEST hypointensities in transgenic mouse model of AD with the expected decrease in glutamate concentration in the early stages of the AD-like neurodegenerative process.

GluCEST is a very promising method that provides a noninvasive biomarker for the diagnosis of several neurological and psychiatric diseases at different stages and could be harnessed to accelerate the development of innovative therapies.

### 1.3.2.3 CrCEST and LATEST

Creatine has two exchangeable protons originating from two amine functions (referred to as the guanidinium group) both resonating at 1.8 ppm from water and is highly concentrated

in the muscle fibers (30-40 mmol/L) and to a lesser extent in the brain (3-4 mmol/L). CrCEST was first applied to the detection of creatine concentration changes in the skeletal muscle during exercise ([Kogan, Mohammad Haris, Debrosse, et al. 2014; Kogan, Mohammad Haris, Singh, et al. 2014; Rerich et al. 2015]). It was also used in neuroimaging to help detecting brain tumors with CrCEST maps [Cai, Singh, et al. 2015] and was recently applied to the study of epileptic seizures ([D.-H. Lee et al. 2019]).

Phosphocreatine also possess a CEST contrast with labile protons resonating at 2.1 ppm. While the concentration of phosphocreatine is close to the one of creatine, its exchange rate is much lower leading to its CEST effect being overwhelm by the CrCEST contrast in most cases.

We note that, similarly to CrCEST, lactate CEST (LATEST) was also used in muscle metabolism imaging ([DeBrosse et al. 2016]). The results of similar experiments are shown in figure 1.7

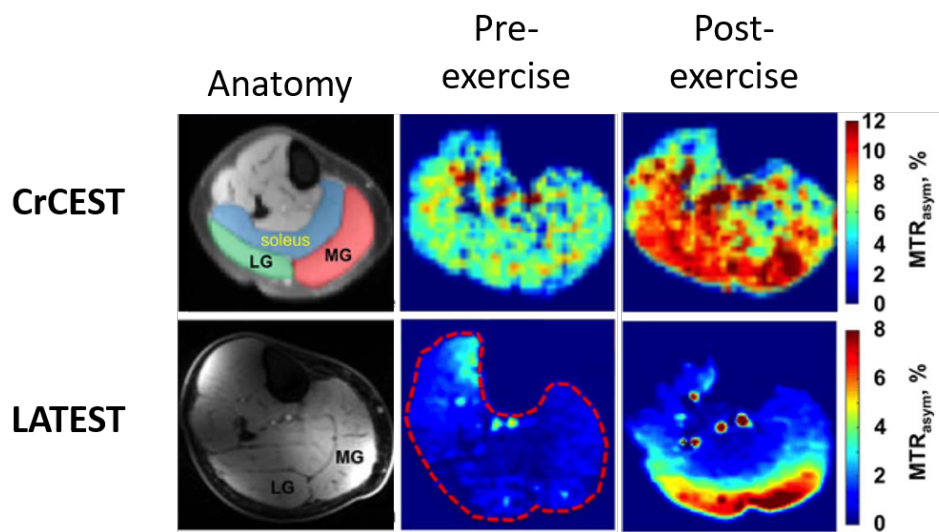


Figure 1.7: CrCEST and LATEST MRI of human calf metabolism before and after exercise. Figure adapted from [Kogan, Mohammad Haris, Singh, et al. 2014; Kogan, Mohammad Haris, Debrosse, et al. 2014; DeBrosse et al. 2016] and inspired from [K. M. Jones, A. C. Pollard, and Pagel 2018]

#### 1.3.2.4 GlucoCEST

Being the most important source of energy, glucose has been for many years at the heart of many metabolic imaging modalities. GlucoCEST imaging has been proposed as an alternative to FDG-PET and promises to image brain glucose signal changes to better understand brain energy metabolism in normal and pathological conditions where energy metabolism is perturbed. In particular, cancer cells are characterized by altered glucose metabolism known as the Warburg effect in which glucose is taken up more than needed. This is due to anaerobic glycolysis being up-regulated in tumors where the supply of oxygen is a limiting factor for proliferation. D-glucose generates a broad CEST effect included in the 0.8 - 2.2 ppm range originating from its five hydroxyl protons. In practice, glucoCEST is focused on its maximum  $MTR_{asym}$  effect at 1.2 ppm.

The feasibility of tumor detection using glucoCEST was demonstrated for the first time in a preclinical study by Chan and colleagues in which they showed that breast tumor exhibit significant glucoCEST signal enhancement during systemic sugar infusion ([Chan et

al. 2012]). Most of the glucoCEST studies rely on the injection of non-metabolized glucose analogs (2-deoxy-D-glucose (2DG) or 3-O-Methyl-D-glucose (3OMG)). Following the levels of 2DG or 3OMG can then provide information on cerebral metabolism and tumor metabolism. This approach was used both in preclinical research ([Walker-Samuel et al. 2013; Sehgal et al. 2019]) in which they used glucoCEST signal to detect the glucose accumulation in the tumor region (Figure 1.8A,B) and in clinical research ([X. Xu, Sehgal, et al. 2020; X. Xu, Chan, et al. 2015]) studies in which they used DGE (Dynamic Glucose Enhancement) to monitor the glucose analog uptake in tumor. This method was also used to study brain activity through the monitoring of glucose consumption in [Nasrallah et al. 2013] in which the authors demonstrated that the CEST signal changed with 2DG concentration, and was reduced by suppressing cerebral metabolism with increased general anesthesia (Figure 1.8C).

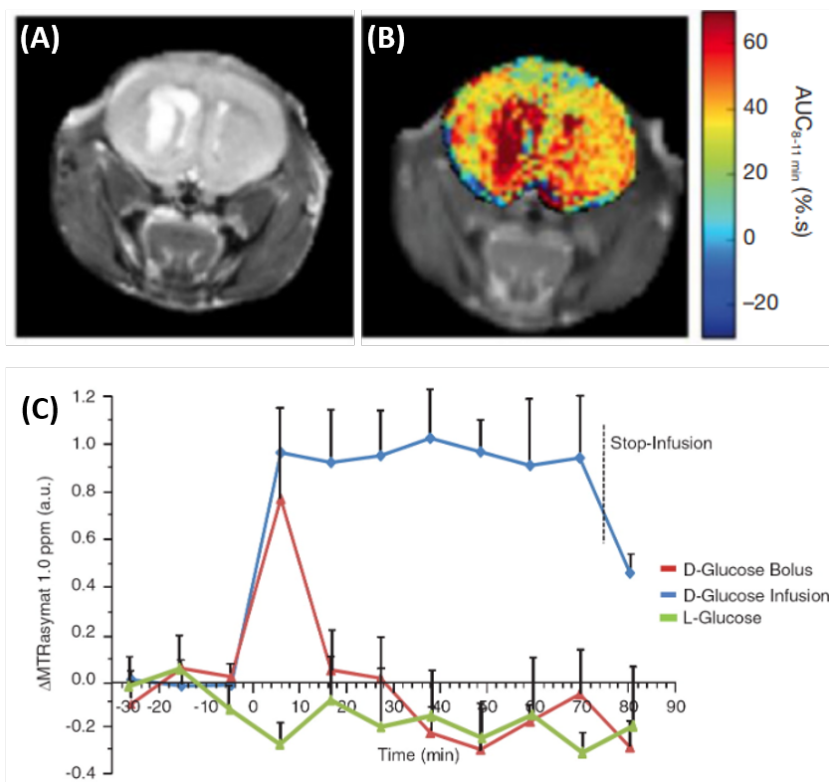


Figure 1.8: Applications of glucoCEST in preclinical (A,B) and clinical (C) studies (A) Anatomical image of the mouse (B) Area under the curve image calculated for the last three minutes of the scan, a period of 8-11 min postinjection of 3-OMG. Figures from [Sehgal et al. 2019] (C) Time courses of glucoCEST signal under constant infusion of D-glucose, after a D-glucose bolus injection, and after an L-glucose bolus injection. Figure from [Nasrallah et al. 2013]

These approaches present the advantage that they use biodegradable CEST agents and could therefore potentially avoid using excessive ionization of patients by substituting PET with DGE imaging in some cases. Because of the information it provides about brain metabolism, glucoCEST may prove to be a suitable biomarker for the study of neurological disorders.

### 1.3.2.5 Other contrasts

Many other CEST contrasts have proven their usefulness in different domains such as MICEST, gagCEST. MICEST was also considered as a potential tool for non-invasive detection of molecular changes in AD ([Mohammad Haris, Singh, et al. 2013]) through the acquisition of MICEST maps reflecting the regional distribution of myo-inositol, a mainly glial metabolite for which increased concentrations were reported in AD patients due to glial activation. GagCEST has shown promise for diagnosing osteoarthritis in the knee ([Krishnamoorthy et al. 2017]) or for analyzing the glycosaminoglycans composition of intervertebral disks ([Wada et al. 2017]). Also targeting exchanging hydroxyl protons groups, glycoCEST aims at detecting glycogen, a glucose polymer invisible using direct  $^1\text{H}$  MRS, found in relatively high concentrations in the liver and muscles. The first glycoCEST application was demonstrated in a perfused liver *ex vivo* by van Zijl and colleagues in [Van Zijl et al. 2007].

### 1.3.3 Conclusion

CEST MRI provides new opportunities for preclinical and clinical molecular imaging. It has already led to introduction of innovative detection methods and to new investigations on how to employ embedded exchange in tissues. Compared to other MRI contrast agents (using gadolinium for example), CEST is an on/off switch contrast that can be activated at will. CEST contrasts are numerous. CEST techniques explore a broad research field and show promising practical utility for evaluating cerebrovascular stroke, tumors, muscle physiology, metabolism and neurological disorders. The topic is in constant evolution and is ever the source of new emergent applications. In this manuscript, we also attempt to push the limits of CEST detection by seeking to detect *in vivo* molecules generating tenuous CEST effects and by developing innovative sequences sensitive to small metabolic variations over time.



# Chapter 2

## Material and Methods

This chapter presents all the hardware equipment used to perform the experiments. The subject of the experiments are also described: a list of every phantom and every animal used in this manuscript is given. The animal experimentation steps prior to imaging protocols are described. Finally, the adjustment protocol common to every experiment are presented in details. This is a chapter to which one can refer in order to have information about the phantom description or the equipment and the first adjustments made to obtain the results presented in chapter 3, 4 and 5.

### Contents

---

<b>2.1 Imaging systems</b>	<b>24</b>
2.1.1 Magnets and gradients	24
2.1.2 Radio-Frequency (RF) coils	25
2.1.3 Adjustments	27
<b>2.2 Phantoms</b>	<b>28</b>
<b>2.3 Animal experimentation</b>	<b>30</b>
2.3.1 Animals	30
2.3.2 Experimentation protocols	31
2.3.2.1 Positioning	31
2.3.2.2 Breathing and temperature control	32
2.3.2.3 Medical gas and anesthesia	33
2.3.2.4 Functional stimulation system	34

---

## 2.1 Imaging systems

### 2.1.1 Magnets and gradients

Four preclinical MRI scanners from Bruker Biospin (Ettlingen, Germany) were used to carry out all the experiments. The scanner that was used to perform most of the experiments was a 17.2 T scanner. Three other scanners were used to run preliminary comparison studies, their magnetic field strengths are the following: 7, 9.4 and 11.7 T. Pictures of all four MRI scanners are shown in Figure 2.1 and their main features are detailed in Table 2.1.



Figure 2.1: Pictures of the four pre-clinical scanners : 7, 9.4, 11.7 and 17.2 T (from left to right).

Field (T)	1H Larmor Frequency (MHz)	Gradient strength (mT/m)	Magnet bore (cm)	Gradient bore (cm)	Location
7	300	740	25	8.5	NS
9.4	400	1000	20	6	WWU
11.7	500	760	16	9	NS
17.2	730.2	1000	16	9	NS

Table 2.1: Characteristics of the four MRI scanners. NeuroSpin (NS) and Westfälische Wilhelms-Universität (WWU) are respectively located in Gif-sur-Yvette, France and Münster, Germany.

The inner diameter of the gradient bore defines the cylindrical space available to house the whole experimental set-up including the rf coil, the animal cradle and the animal itself. Considering such modest dimensions (from 6 to 9 cm), those MRI scanners are suitable for scanning small animals such as mice or rats. Except for the 17.2 T scanner, the other magnets are actively shielded to contain the static fringe field.

The four scanners are actively shielded to limit the extent of  $B_0$  outside the magnet except for the 17.2 T which is passively shielded with a Faraday cage (Figure 2.2). The scanners are also equipped with passive radiofrequency shielding, that is crucial to prevent interferences from external electromagnetic signals.

**Zoom on the 17.2T scanner:** Apart from the comparative study for CEST signal at different magnetic fields (chapter 3), every results presented in this manuscript is obtained

with the 17.2 T scanner. It is currently the strongest horizontal magnet in the world and is equipped with very strong gradients (1000 mT/s) that can switch from 5% to 95% of their maximum within only 100  $\mu$ s. It is also equipped with five second order shim coils.



Figure 2.2: The Faraday cage surrounding the 17.2 T pre-clinical scanner

### 2.1.2 Radio-Frequency (RF) coils

RF coils functions are to excite the spin system (transmitter) and to detect the oscillating net transverse magnetization that induces an electromotive force inside the coil (receiver). Different RF coils are to be used depending on the subject or organ-of interest and scientific questions studied. This is due to the fact that RF coil size, design and other electronic characteristics have an impact on the overall quality (SNR, homogeneity, contrast, coverage...) of the obtained MR images. The coils used during this PhD thesis are referenced in Table 2.2 and a picture of every coil is shown in Figure 2.3 and 2.4.

n°	Nucleus	Op Freq (MHz)	Design	RF Pola	Inner Ø (cm)	Chapters
1	$^1\text{H}$	300	Volume (TX/RX)	Quadrature	3.8	4
2	$^1\text{H}$	400	Volume (TX/RX)	Quadrature	3.5	4
3	$^1\text{H}$	500	Surface (TX/RX)	Quadrature	2.0	4
4	$^1\text{H}$	730.2	Volume (TX/RX)	Quadrature	2.5	4,5
5	$^1\text{H}$	730.2	Volume(TX)/Surface(RX)	Linear	-	4,5,6
6	$^1\text{H}$	730.2	Surface (TX/RX)	Linear	-	6
7	$^1\text{H}$	730.2	Surface (TX/RX)	Linear	2	6

Table 2.2: Characteristics of the different RF coils. "Op Freq" means Operating Frequency. TX means transmitter and RX receiver.

For volume coils, the inner diameter corresponds to the diameter of the available cylindrical space. For surface coils, it refers to the radius of curvature of the coil. Coils n°1,2,3 and 4 are only used to image phantoms in different magnetic field strength whereas other coils

n°5,6 and 7 are employed for *in vivo* studies at 17.2T. Coils n°1,3 and 6 have been purchased from Bruker BioSpin (Ettlingen, Germany) while coils n°2,4,5 and 7 have been designed by Rapid Biomedical GmbH (Rimpar, Germany). Due the uniqueness of the 17.2T magnetic field, manufacturers have to design custom coils specifically adapted to this unusual frequency.

Coil n°5 is actually a combination of two coils. A volume coil that can be used in a Transmit-Receive mode but is only used as a transmitter in our experiments in chapter 4. It is used in combination with a surface coil which plays the role of a receiver (Figure 2.5). By using a volume coil as our transmitter coil, we benefit from its  $B_1$  homogeneity which is of great importance when realizing CEST MRI experiments. Additionally, using a surface coil very close to the area of interest to receive the signal allows to acquire the useful signal without detecting too much noise from the other parts of the brain and therefore maximizes the SNR in that region.

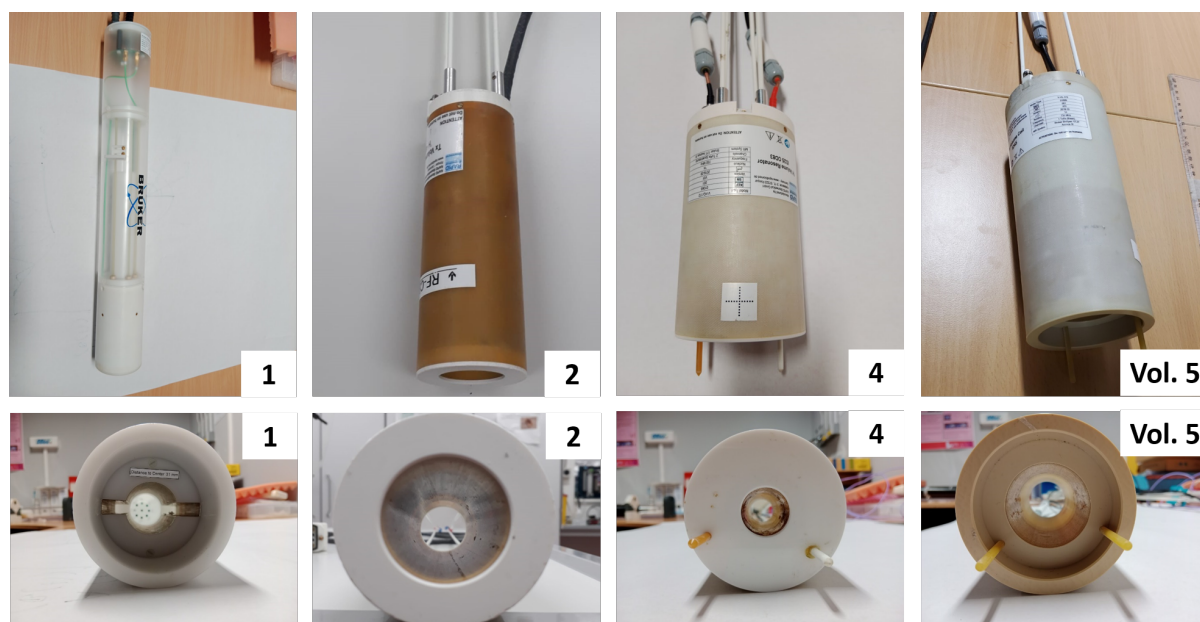


Figure 2.3: View from above (top) and axial view (bottom) of the volume coils : coil n°1, coil n°2, coil n°4 and volume coil from combination n°5

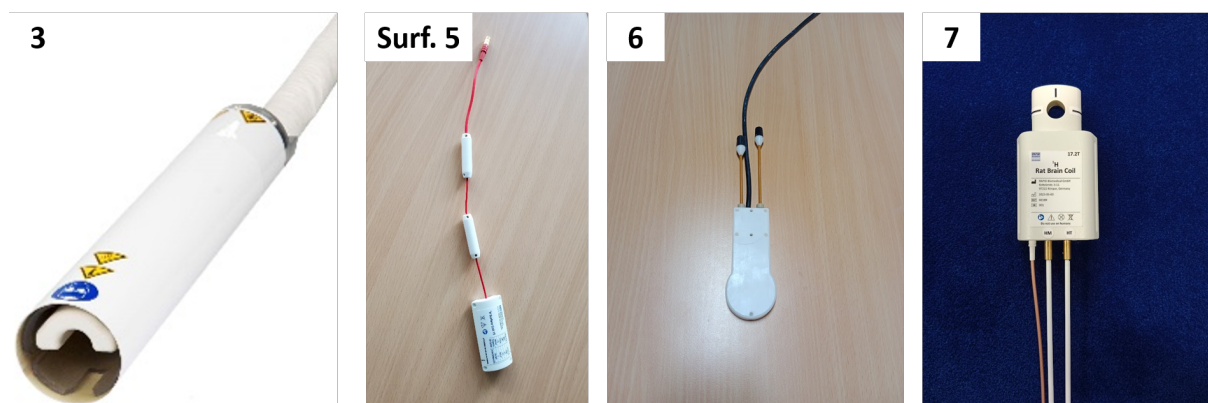


Figure 2.4: Surface coils : coil n°3, surface coil from combination n°5, coil n°6, coil n°7

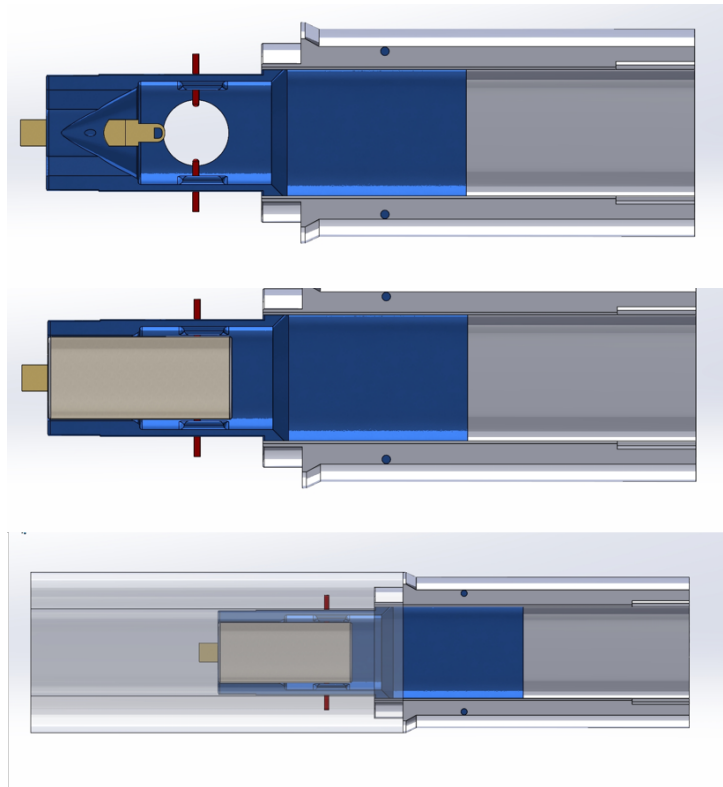


Figure 2.5: Schematic representation of coil combination n°5. Top: mask without any coil. Middle: mask with surface coil as a receiver. Bottom: Final setup with mask with surface coil as a receiver and volume coil as a transmitter. Drawings made on Solidworks by Jérémy Bernard.

### 2.1.3 Adjustments

At the beginning of every MRI procedures, a series of adjustments are made to maximize the signal obtained from the sample and start the experiments in the best conditions possible. In the following paragraph, the word "sample" refers either to an *in vitro* preparation or to the tissue of a living animal (brain or muscle).

Once the center of the RF coil is positioned precisely atop the sample, the sample in its cradle are set at the center of the magnet bore. The coil is then tuned and matched so that its impedance is adjusted at 50 Ohms at the Larmor frequency, maximizing the energy transfer between the coil and the spin system. In the particular case of coil n° 6, this adjustment had to be performed before pushing the sample inside the magnet bore. A first localizer scan is performed to check whether the sample is correctly positioned with respect to the coil (maximum of signal in the ROI) and with respect to the center of the magnet (ROI as close as possible to the isocenter). If necessary, the coil, sample or bed can be re-positioned to achieve an optimal experimental setting.

Prior to all other scans, the reference power of the transmitter coil is calibrated in order to derive the intensities of the RF pulses necessary to achieve the target flip angles in all sequences. For volume coils, this calibration is performed over a large volume to provide a homogeneous RF excitation across the whole sample. For surface coils, the calibration of the reference power is performed for a slice parallel to the coil encompassing our eventual

ROI.

To compensate for  $B_0$  inhomogeneities, a global FID-shim procedure is performed on the entire sample. A  $B_0$  field map is then acquired and local  $B_0$  field homogenization is performed in the ROI (slice or voxel) using an automatic shimming routine. This adjustment is repeated everytime the ROI changes.

Additionally to shimming procedures, the water frequency is regularly adjusted so that the scanner operates at the proper frequency.

The last calibration step performed before a scan is the adjustment of the receiver gain (RG). The latter is adjusted with respect to the maximum MR signal occurring during the imaging sequence and optimized to prevent data clipping (if RG is too high) and limit the image noise (if RG is too low). This adjustment is repeated everytime any sequence parameter is modified or if the ROI is changed.

## 2.2 Phantoms

A list of the different phantoms used for every *in vitro* studies is given below 2.3.

Number	Composition	pH	container
n° 1	40 mM L-(+)-Lactic Acid (lactate)	7	0.5 mL
n° 2	20 mM D-Glucose (glucose)	7	0.5 mL
n° 3	20 mM L-Glutamic Acid (glutamate)	7	0.5 mL
n° 4	40 mM lactate, 20 mM glucose, 20 mM glutamate	7	0.5 mL
n° 5	2 % Agarose gel	-	50 mL
n° 6	1 mM L-Carnosine (carnosine)	7.2	15 mL
n° 7	2.5 mM carnosine	7.2	15 mL
n° 8	5 mM carnosine	7.2	15 mL
n° 9	10 mM carnosine	7.2	15 mL
n° 10	20 mM carnosine	7.2	15 mL
n° 11	10 mM carnosine, 10 mM anserine, 20 mM homocarnosine	7.2	2.5 mL
n° 12	1 mM Hydrogen Peroxide	6.5	15 mL
n° 13	20 mM glutamate	7	15 mL
n° 14	10 mM carnosine	7.2	2.5 mL
n° 15	10 mM anserine	7.2	2.5 mL
n° 16	10 mM homocarnosine	7.2	2.5 mL

Table 2.3: List of phantoms and brief description. The chemical nomenclature of carnosine, anserine and homocarnosine are  $\beta$ -alanyl-L-histidine,  $\beta$ -alanyl-3-methylhistidine and  $\gamma$ -amino-buteryl-histidine, respectively.

All chemical compounds were purchased from Sigma-Aldrich (Saint-Louis, Missouri) except for homocarnosine which was purchased from Cayman Chemical (Ann Arbor, MI, USA). The chemical solutions were prepared by dissolving the chemical compound (powder or liquid) in a solution of PBS (phosphate-buffered saline) at concentration 0.01 M. The pH was then adjusted to the target pH value by adding high-concentrated base (NaOH) or acide (HCl) and controlling its changes with a pH-meter (Mettler-Toledo, Viroflay, France) that is

calibrated weekly. Sodium azide was also added to inhibit bacterial proliferation. Samples n°1,2,3 and 4 were combined into one 4-compartment phantom.

Four different types of container were used to prepare those phantoms (Figure 2.6) : 0.5 mL syringe, 2.5 mL syringe, 15 mL tube, 50 mL tube. Most of the phantoms were prepared in 15 mL Falcon tubes that were filled with the solutions and closed so that no air bubbles would be trapped in the sample. If needed, a plastic joint from the plunger of a syringe can be used to seal the sample and make sure no air would enter. For the most expensive compounds, 2.5 mL syringes (Dutscher, Bernolsheim, France) were used. Heated wax was used to seal the tip of the plastic syringe and additional Parafilm (Sigma-Aldrich, Saint-Louis, Missouri) was added to prevent any potential leaks. For the specific 4-compartment phantom (composed of samples n°1,2,3 and 4), four 0.5 mL syringes were filled with the different solutions, the metallic needle was removed and the syringes were sealed with heated wax. The four samples were then inserted inside a 15 mL Falcon tube filled with Fluorinert FC-40, an immiscible fluorocarbon oil to make sure no signal could be detected outside of the four syringes. Finally, the biggest container was a 50 mL Falcon tube (Dutscher, Bernolsheim, France) which was used for SNR comparison purpose only.

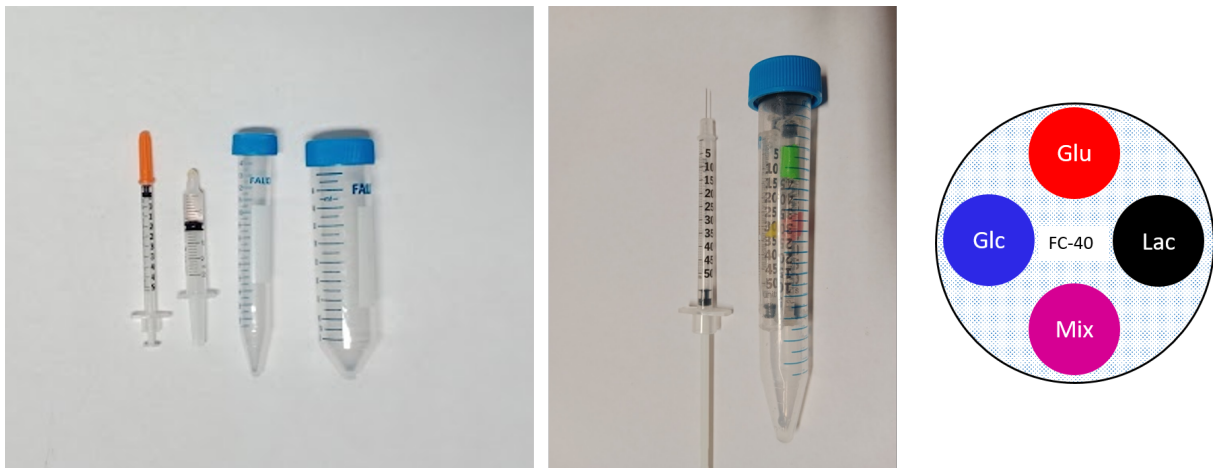


Figure 2.6: Phantom containers. Left: 0.5 mL syringe, 2.5 mL plastic syringe, 15 mL Falcon tube, 50 mL Falcon tubes. Middle: Example of a 0.5 mL syringe next to the 15 mL Falcon tube enclosing the four 0.5 mL syringes. Right: Schematic representation of the 4-compartment phantom, the four syringes are surrounded by FC-40.

For phantom studies under physiological conditions, the temperature had to be stabilized around  $37 \pm 1$  °C. The temperature was measured with a temperature probe inserted in the sample through a hole that was drilled in the plastic blue cap (Figure 2.7). At first, the temperature is controlled with the water heating system presented in Figure 2.11. This concerns sample n° 1,2,3 and 4. Later in the research project, a feedback controlled air heating system is installed. This system is more efficient and provides a more homogeneous heating of the sample, and was therefore preferentially used for all other samples.



Figure 2.7: Temperature probe inserted in a phantom

## 2.3 Animal experimentation

### 2.3.1 Animals

Rats and mice are the preferred species to serve as animal models for biomedical research due to their anatomical, physiological, and genetic similarity to humans. Even though their brains are smaller and less complex than the human brain, it was shown that the two are remarkably similar in structure and function ([Beauchamp et al. 2022; Luhmann and Fukuda 2020; Ellenbroek and Youn 2016]). Those models are frequently studied, cheap and easy to get and to handle. With adapted devices (beds, masks and RF coils), murine rodents can easily fit in the tunnel of a preclinical MRI scanner. Specifically in this work, rats were chosen over mice because they are approximately ten times larger (in volume) and therefore provide bigger volumes of homogeneous tissues. There are abundant genetic resources for mice but no specific genetic model is required in the case of a methodological work such as the one presented in this manuscript.

The rats used for our experiments belong to the species *Rattus Norvegicus*. More specifically, the rats selected for the experiments in chapter 3 and 4 are Dark Agouti because the rats of this strain are known to present higher amounts of carnosine and carnosine derivated metabolites, our molecules-of-interest. In chapter 5, the experiments were realized with Sprague-Dawley rats, solely for practical reasons. All animals used for experimentation are summarized in Table 2.4. Only animals leading to results shown in this manuscript are referenced, more animals were actually needed to calibrate the experiments.

chapters	strain	sex	N
3	Dark Agouti	male	1
4	Dark Agouti	male	8
5	Sprague Dawley	female	16

Table 2.4: List of animals used for the experiments and their characteristics

All animal were purchased from Janvier Labs (Saint-Berthevin, France) at a young adult age which approximately correspond to 40 days for male and 50 days for female, their weight being about 200g at these ages. The animals were then housed by pair under a 12-h night/12-h daylight cycle with water and food available ad libitum.

### 2.3.2 Experimentation protocols

All animal procedures were approved by the Comité d’Ethique en Expérimentation Animale, Commissariat à l’Energie Atomique et aux Énergies Alternatives, and by the Ministère de l’Education Nationale, de l’Enseignement Supérieur et de la Recherche (France) under reference A15-40 and were conducted in strict accordance with the recommendations and guidelines of the European Union (Directive 2010/63/EU) and the French National Committee (Décret 2013–118).

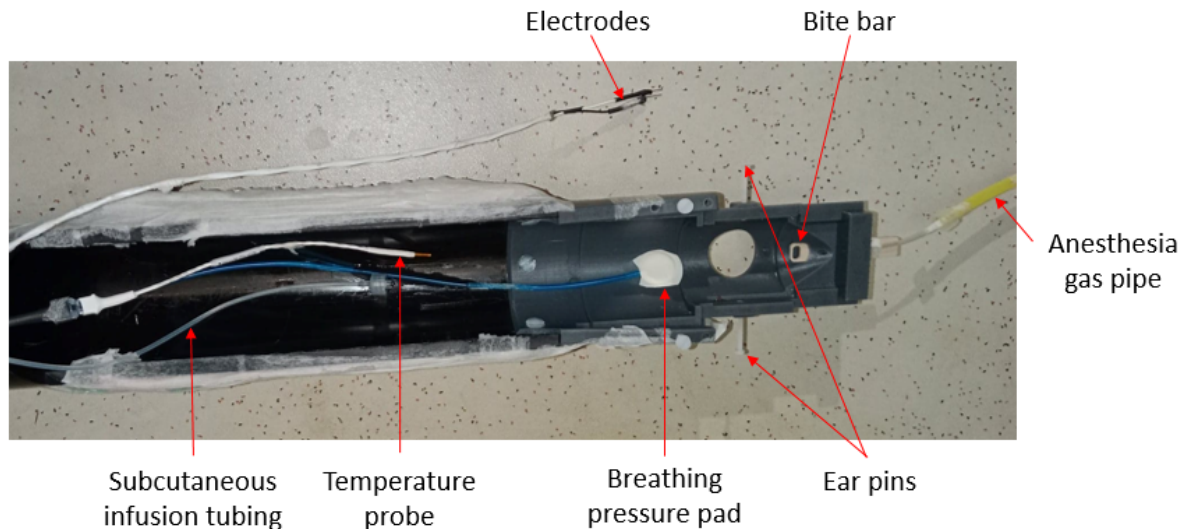


Figure 2.8: Experimental setup for animal scanning showing the subcutaneous infusion tubing, the temperature probe, the breathing pressure pas, the two ear pins, the anesthesia gas pipe, the bite bar and the electrodes.

#### 2.3.2.1 Positioning

As depicted in picture 2.8, we can see the experimental setup used for our rat examinations. The rat head is positioned in the mask such as his teeth are inserted in the bite bar and the ear pins in his ear canals (Figure 2.9). This prevents head movement and therefore limits motion artifacts during the MRI examination. In the particular case of the leg imaging (chapter 4), the rat is positioned back to front with the leg on the mask and elevated with tulle pads.

Another mobile mask is used to deliver the anaesthetic gas in Air/O<sub>2</sub> mixture to the rat. The mask were specifically designed to fit with the shape of the coil. They are drawn on Solidworks, and then 3D-printed in the prototyping laboratory with the help of J r my Bernard.

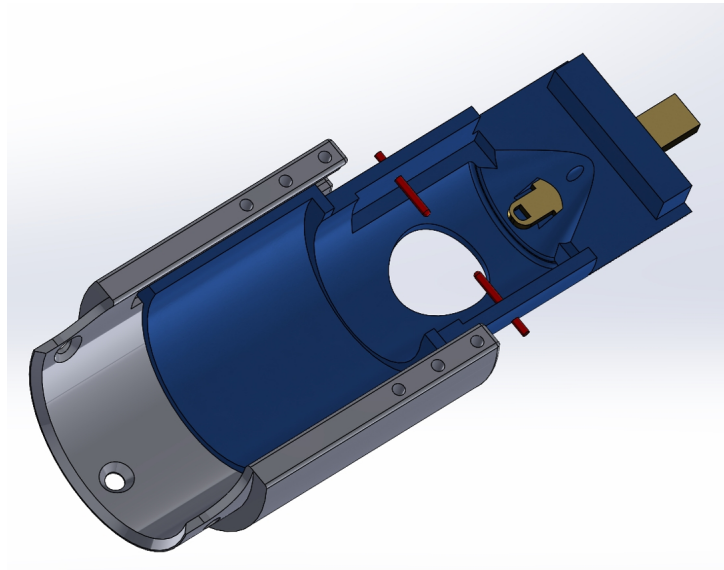


Figure 2.9: Example of a mask (blue piece) used for in vivo experiments. The mask can slide in a rail machined in the bed (gray piece). The bite bar is represented in beige and the ear pins in red. The small hole just above the bar bite corresponds to the arrival of medical air and gas anesthesia. Drawings made on Solidworks by J r my Bernard.

### 2.3.2.2 Breathing and temperature control

During all MRI exams, the respiration rate and the body temperature are monitored using a small animal monitoring system (SA Instruments Inc) shown in Figure 2.10 connected to a breathing pressure pad and a rectal temperature probe as shown on Figure 2.8.

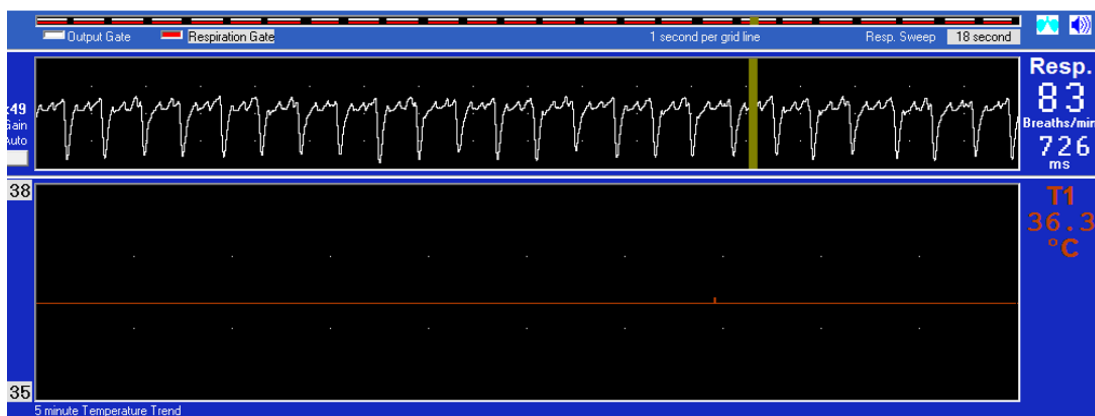


Figure 2.10: Example of temperature (36.3  C) and breathing rate (98 breaths / mn) monitoring

The body temperature is kept between 36 and 38  C by manually adjusting the temperature of the water bath (Grant TC120, Grant Instruments, Shepreth, UK) and thus of the water circulating in the blanket covering the animal (Figure 2.11). The breathing rate depends on the anesthesia and is discussed in detail for each experiment in the next paragraph.



Figure 2.11: Heating system : water bath with an adjustable temperature (left) connected to a blanket (right) wrapped around the animal (or the sample)

### 2.3.2.3 Medical gas and anesthesia

During all MRI exams, an air-oxygen mixture (2:1) (Figure 2.12 A) is continuously delivered to the animals through the nose cone mask for spontaneous respiration 2.9. For induction, the animal is placed in an induction chamber (Figure 2.12 B) and a halogenated anesthetic gas called isoflurane is administered at 3% during three minutes.

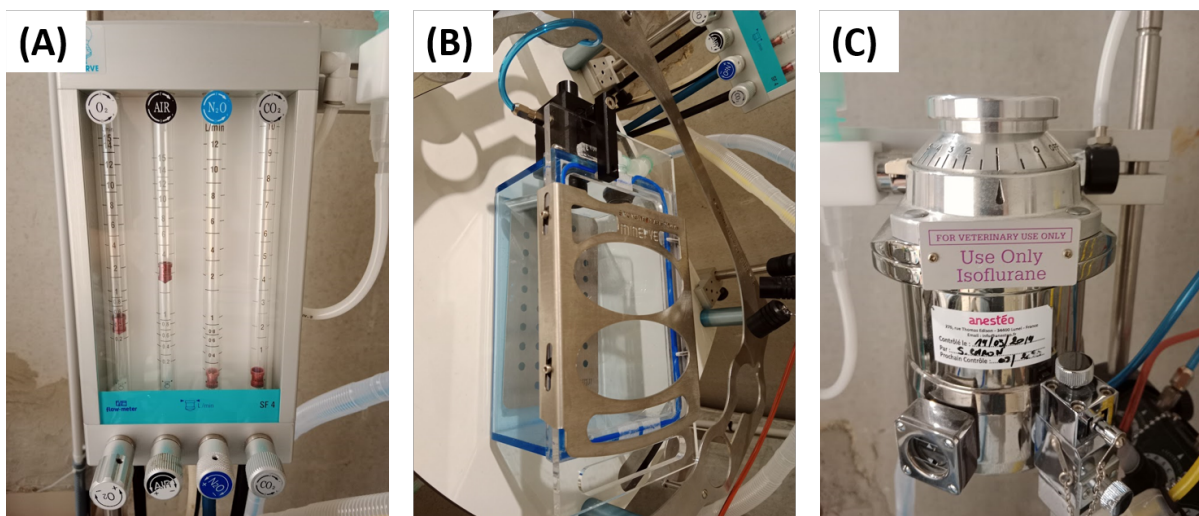


Figure 2.12: Air and gas anesthesia delivery system. (A) Medical air mixer, (B) induction chamber, (C) isoflurane regulator

The anesthesia and the breathing rate are then monitored differently for the following three types of acquisitions:

- For classic imaging acquisitions that did not involve any neuronal activation or hypercapnia (chapter 2 and 4), the isoflurane is then lowered to 1.5-2% and controlled throughout the experiment to maintain the respiration rate around 60 breaths/min. The isoflurane level can be adjusted with a regulator (Figure 2.12 C).
- For acquisitions performed during hypercapnia experiments (first section of chapter 5). Three first scans (3 scans last approximately 10 minutes) are acquired under pure  $O_2$  and 1.5% isoflurane, the  $CO_2$  level is then raised to 30% and the isoflurane is lowered to 1%. After 5 minutes, three scans are acquired in the established presence of  $CO_2$ . After restoring the initial situation and another 5 minutes break, three last CEST-LS acquisitions are performed. The breathing rate is approximately around 70 breaths/min, and usually increased during  $CO_2$  administration.
- For acquisitions with sensory stimulation (second section of chapter 5), a bolus of 50  $\mu\text{g}/\text{kg}$  medetomidine (Domitor, Orion Pharma, Espoo, Finland) is injected subcutaneously while the isoflurane is gradually reduced and cut approximately 15 minutes after the bolus injection. A continuous subcutaneous infusion of 100  $\mu\text{g}/\text{kg}$  medetomidine is started immediately after the bolus injection using an infusion pump (HARVARD PHD2000, Harvard Apparatus, Holliston, MA, USA) pictured in Figure 2.13. Under such anesthesia, the breathing rate of the animal usually stays between 70 and 90 breaths/min.



Figure 2.13: Infusion pump

#### 2.3.2.4 Functional stimulation system

To generate an activation in the brain, an electrical forepaw stimulation is implemented. A pair of 26 gauge-needle electrodes (Figure 2.14) are inserted under the skin of one of the two forepaws (between digits 2 and 3 and digits 4 and 5). The electrical pulses are generated by an isolated pulse stimulator (Model 2100; A-M Systems, WA, USA) (Figure 2.14), triggered by a logic gate pulse from the Bruker imaging system. With such a system, the user could select the ON and OFF time periods, the pulse shape and duration, the current amplitude and frequency. These parameters are presented in chapter 5.

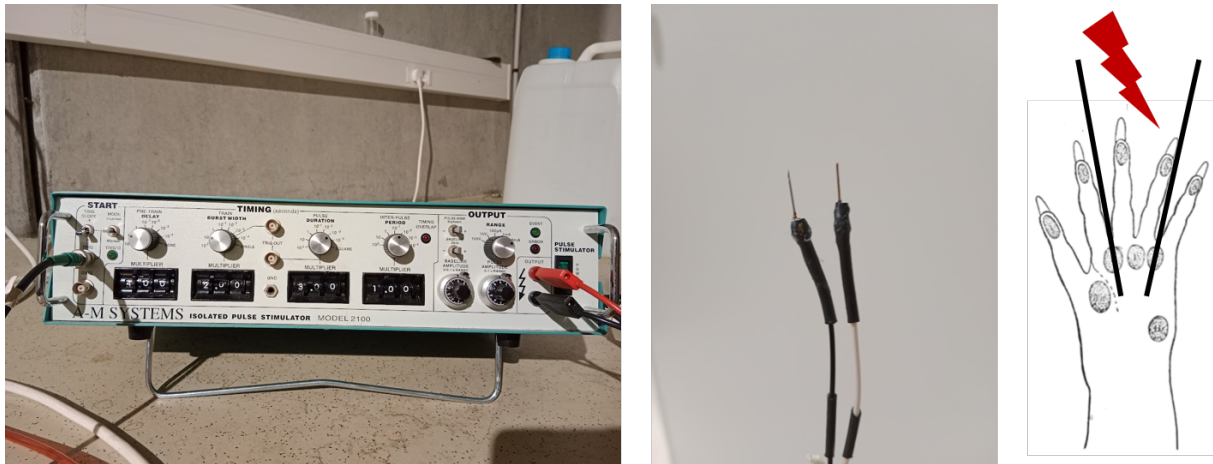


Figure 2.14: The electro-stimulation system used for sensory stimulation. Left: Electrical pulses generator. Middle: Electrodes inserted in the paw of the rat. Right: Position of the electrodes (between digits 2 and 3 and digits 4 and 5)



# Chapter 3

## Development of a new CEST MR methodology

This chapter presents our developments in CEST MR, the work performed *in vitro* and our subsequent results. In the first section, a general exploration of typical metabolite CEST contrast is presented. We analyze the CEST responses of these metabolites under different experimental conditions. The advantage of high field and the CEST signal selectivity are discussed and illustrated through few experiments. The following section describes the principle of a new ultrafast CEST MR acquisition method. Finally, we introduce and present a software tool designed for the analysis of CEST contributions. Those two CEST-related tools were developed and optimized for the experiments presented in preparation of the following chapters.

### Contents

---

<b>3.1 Exploration of CEST contrasts in phantoms at 17.2 T</b> . . . . .	<b>39</b>
3.1.1 Z-spectra of lactate, glucose and glutamate at high fields . . . . .	39
3.1.2 Optimization of the $B_{1,sat}$ saturation power, influence of the $B_0$ static field and of the temperature . . . . .	41
3.1.3 Influence of the pH . . . . .	44
3.1.4 Selectivity towards a specific metabolite . . . . .	45
3.1.4.1 Mixture of lactate, glucose and glutamate : the advantage of very high magnetic field . . . . .	46
3.1.4.2 Metabolic imaging of a Cherry tomato : selecting a specific CEST contrast . . . . .	47
3.1.5 Conclusion . . . . .	48
<b>3.2 Ultra-fast CEST MR acquisition sequence</b> . . . . .	<b>49</b>
3.2.1 On the importance of a fast CEST MR sequence . . . . .	49
3.2.2 Principle and sequence pulse diagram . . . . .	49
3.2.3 Data analysis . . . . .	51
3.2.4 Conclusion . . . . .	53
<b>3.3 Development of a Z-spectrum analysis tool</b> . . . . .	<b>54</b>
3.3.1 Principle of the PEAKIT software tool . . . . .	55
3.3.1.1 Peak detection . . . . .	55

3.3.1.2	Baseline estimation . . . . .	57
3.3.1.3	Peak significance computation . . . . .	58
3.3.2	Demonstration . . . . .	59
3.3.2.1	Phantoms . . . . .	59
3.3.2.2	<i>In vivo</i> . . . . .	60
3.3.3	Conclusion, discussion and perspective . . . . .	62

---



composed of samples n°1 (lactate), 2 (glucose), 3 (glutamate) and 4 (a mixture of lactate, glucose and glutamate). Combining those four samples into one phantom allows to have the same imaging conditions for every metabolite studied and limits the introduction of experimental bias that are bound to happen from one experiment to another. The same phantom was scanned with three scanners at three different magnetic fields: 9.4, 11.7 and 17.2 T. The acquisitions were performed at room temperature (21°C) and body temperature (37°C).

CEST PRESS experiments were performed sequentially by carefully changing the voxel position from one syringe to another. An example of the voxel position is given in Figure 3.2. The CEST module was parameterized as follows : 35 rectangular, 50 ms long pulses separated by an interpulse delay of 0.01 ms, resulting in a saturation time of 1.75 s. The saturation offsets ranged from -10 to 10 ppm starting with those specific offsets  $\pm[10, 7.5, 6, 5.5, 5, 4.8, 4.5]$  followed by regularly distributed offsets between  $\pm 4.3$  and 0. Every offset was acquired consecutively with its opposite offset. The readout module had the following parameters : TE/TR = 15/2500 ms, voxel size =  $2 \times 2 \times 4$  mm<sup>3</sup> and total acquisition time = 4 m 10 s. The  $B_{1,sat}$  power varied between different experiments and are reported in each section.

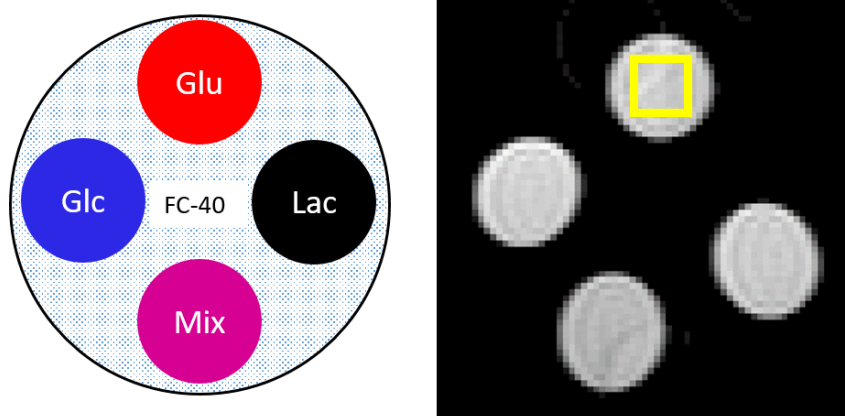


Figure 3.2: Schematic representation (left) and anatomical image (right) of the quadruple phantom. The yellow squares shows the position of the CEST PRESS voxel.

Figure 3.3 shows the Z-spectra and the corresponding  $MTR_{asym}$  profiles of lactate, glucose and glutamate obtained with  $B_{1,sat}$  set at 2.6  $\mu$ T, 5.0  $\mu$ T and 7.0  $\mu$ T, respectively. The chemical shifts (and corresponding saturation frequency offsets) associated with each metabolite were determined by the position of their respective maximum  $MTR_{asym}$  contrast. The chemical shifts and exchange rates of the three metabolites have been summarized in Table 3.1.

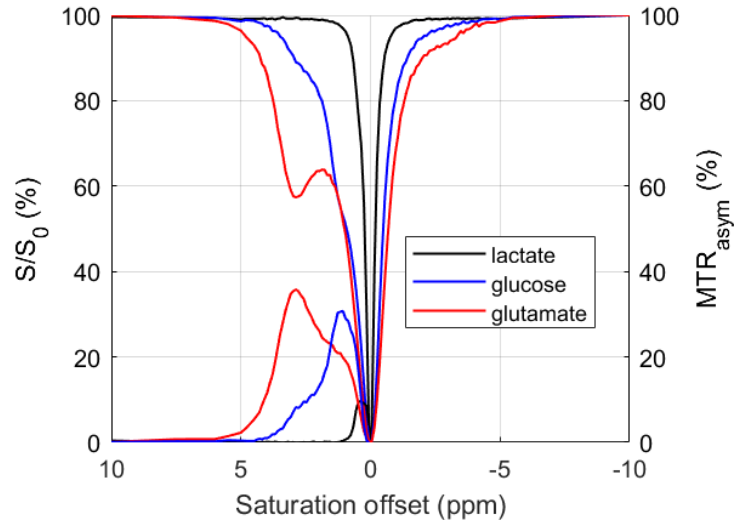


Figure 3.3: Z-spectrum of lactate, glucose and glutamate with their corresponding  $MTR_{asym}$  obtained with  $B_{1,sat}$  2.6  $\mu T$ , 5.0  $\mu T$  and 7.0  $\mu T$  respectively.

	CEST functional group	$\Delta\delta$ (ppm)	$k$ ( $s^{-1}$ )
lactate	hydroxyl	0.4	360 +- 50
glucose	hydroxyl	1.2	3940 +- 260
glutamate	amine	2.8	7490 +- 90

Table 3.1: Chemical shifts and exchange rates at 37 °C for lactate, glucose and glutamate. The exchange rates were reported in [DeBrosse et al. 2016] for lactate and in [Khlebnikov, Kemp, et al. 2019] for glucose and glutamate

### 3.1.2 Optimization of the $B_{1,sat}$ saturation power, influence of the $B_0$ static field and of the temperature

Estimating the optimal  $B_{1,sat}$  from *in vitro* acquisitions is not straightforward because there is no predefined criteria for it. Thus, we selected these  $B_{1,sat}$  saturation powers based on a compromise between a high CEST contrast ( $=MTR_{asym}$ ) and an acceptable line broadening. An example of  $B_{1,sat}$  optimization is given in Figure 3.4.

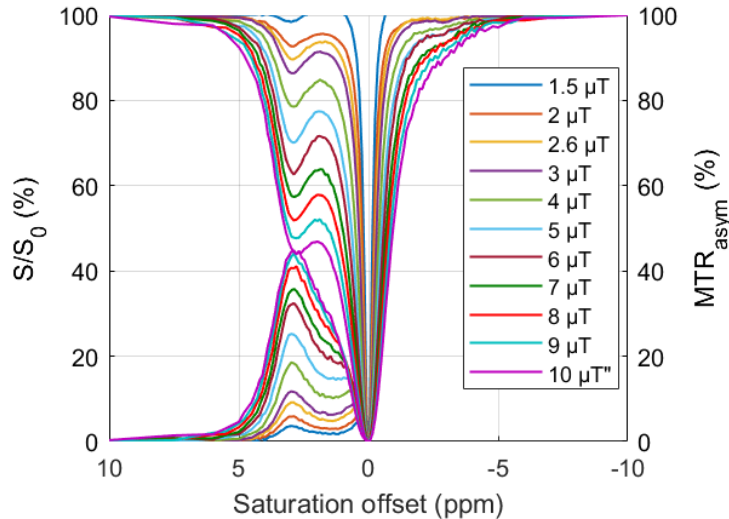


Figure 3.4: Example of  $B_{1,sat}$  optimization experiment for a 20 mM glutamate solution ( $T^{\circ}=21^{\circ}\text{C}$ ,  $\text{pH}=7.0$ ).

Table 3.2 summarizes the results of this optimization performed for all three metabolites, at 3 different magnetic fields (7 T, 11.7 T and 17.2 T) and at two temperatures (21 °C and 37 °C). Overall, the optimal  $B_{1,sat}$  saturation power for each metabolite was found to be globally independent of the  $B_0$  field intensity and the temperature of the sample for the range of  $B_0$  and  $T^{\circ}$  explored in this work.

Metabolites	Optimal $B_{1,sat}$ [ $\mu\text{T}$ ]					
	9.4T		11.7T		17.2T	
	RT	37°C	RT	37°C	RT	37°C
lactate (0.4ppm)	2.5	2.5	2.0	-	2.5	2.5
glucose (1.2ppm)	5.0	5.0	5.0	-	6.0	5.0
glutamate (2.8ppm)	7.0	8.0	7.0	-	8.0	8.0

Table 3.2: Optimized  $B_{1,sat}$  saturation power at 3 static fields (9.4 T, 11.7 T, 17.2 T) at two temperatures (21 °C and 37 °C) for lactate, glucose and glutamate

In Table 3.3, we report the CEST contrasts obtained for the optimal  $B_{1,sat}$  values. For all metabolites and for the considered temperature, an increase in  $B_0$  leads to an increase in the CEST contrast. There are two main reasons for this increased sensitivity of CEST at higher magnetic fields: (i) the longer T1 relaxation times that participate to a more efficient saturation and (ii) the fact that the CEST condition (Table 3.4) is better satisfied due to the improved spectral resolution at higher magnetic fields, especially for metabolites with slow to intermediate exchange rates. The  $B_0$ -dependency of the  $MTR_{asym}$  profile of glucose is presented as an example in Figure 3.5.

Metabolite	Maximum CEST contrast [%] at optimal $B_{1,sat}$					
	9.4T		11.7T		17.2T	
	RT	37°C	RT	37°C	RT	37°C
lactate (0.4ppm)	8.6	9.5	9.5		10.0	12.0
glucose (1.2ppm)	21.5	14.2	27.2		33.7	30.6
glutamate (2.8ppm)	30.0	13.5	33.6		42.1	29.8

Table 3.3: CEST contrast (%) obtained with optimal  $B_{1,sat}$  saturation power at three static field (9.4 T, 11.7 T, 17.2 T) at two temperatures (21 °C and 37 °C) for lactate, glucose and glutamate

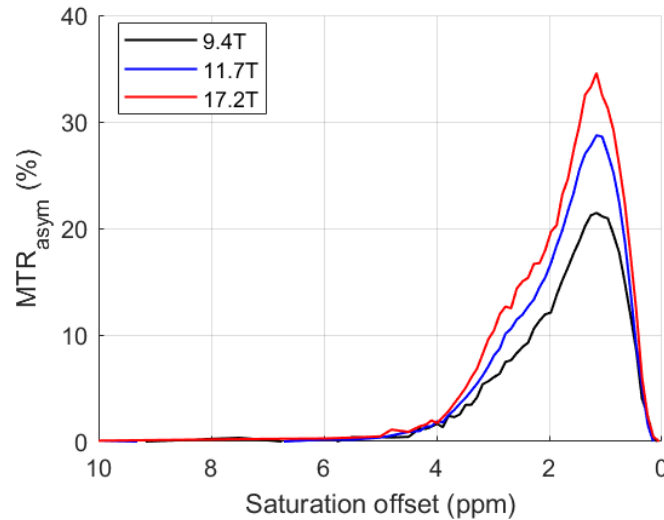


Figure 3.5: Glucose at room temperature (21 °C) with optimized  $B_{1,sat}$  saturation power at three static fields (9.4 T, 11.7 T and 17.2 T)

	$\Delta\delta$ (ppm)	k (s-1)	$\frac{k}{\Delta\omega}$ @9.4T	$\frac{k}{\Delta\omega}$ @11.7T	$\frac{k}{\Delta\omega}$ @17.2T
lactate	0.4	360 +- 50	2.2	1.8	1.2
glucose	1.2	3940 +- 260	8.2	6.5	4.5
glutamate	2.8	7490 +- 90	6.7	5.4	3.6

Table 3.4: Evolution of the "exchange rate (at 37 °C) to chemical shift" ratio across our three static magnetic field strength (9.4 T, 11.7 T, 17.2 T) for lactate, glucose and glutamate

The temperature increase from "room" (21 °C) to a physiological temperature (37°C) leads to increased exchange rates. Depending on the regime, this will be favorable (slow to intermediate) or unfavorable (intermediate to fast) to the CEST contrast. For example, this temperature increase is most favorable for lactate because its exchange rate is slow on the MR scale at the  $B_0$  fields considered but decreased CEST contrasts are observed for glucose and glutamate which are moving towards the fast regime. For instance, the CEST contrast for glutamate decreases from 30% to 13.5% at 9.4 T and 42.1% to 29.8% at 17.2 T while it only decreases by a 7 % at 9.4 T and a mere 3 at 17.2 T% for glucose ( Figure 3.6). This temperature dependency of the CEST contrast could constitute a challenge for *in vivo* acquisitions as a possible confounding factor, especially for gluCEST acquisitions. Yet one can notice that this sensitivity to temperature is somewhat mitigated at higher  $B_0$ . Also this changes with temperature could be harnessed for gluCEST acquisitions at "low temperature" (at 15-22°C) in

zebra fish as suggested by Wermter et al. ([Wermter, Bock, and Dreher 2015]).

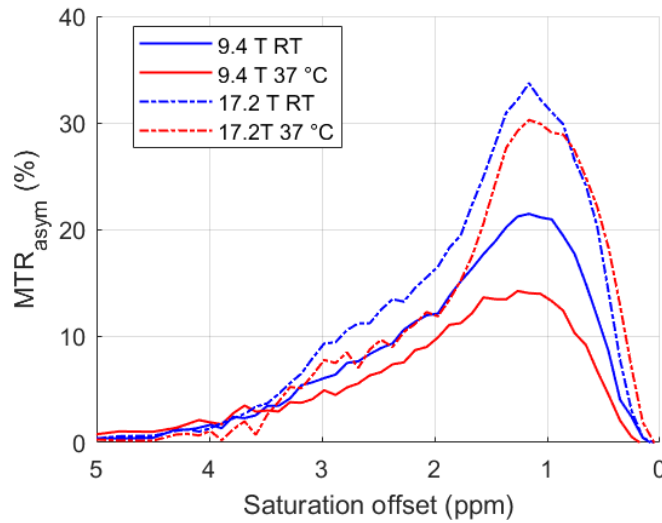


Figure 3.6:  $MTR_{asym}$  spectra of glucose at RT and 37 °C for two static fields (9.4 T, 17.2 T) with optimized  $B_{1,sat}$  power

### 3.1.3 Influence of the pH

Among our three metabolites-of-interest, glutamate (or glutamic acid), as an amino acid, is the most sensitive to "physiological" pH variations. This sensitivity to pH of the CEST contrast from amine and amide protons has been proposed as a way to investigate pH changes using CEST MRI ([R. J. Harris et al. 2015; J. Zhou, Payen, et al. 2003]).

Z-spectra and corresponding  $MTR_{asym}$  profiles of glutamate at two different physiological pH values (7.0 and 7.2) are shown in Figure 3.7. Notably, this modest increase of 0.2 in pH leads to a significant shift of  $\approx 1$  ppm towards water of the maximum of  $MTR_{asym}$ , and a corresponding decreases of  $MTR_{asym}$  of about 8%. As for the influence of temperature, this pH increase leads to an accelerated proton exchange and pushes glutamate further towards the fast regime. This manifests in broader NMR resonances for the labile protons which is typical of the intermediate-to-fast regime and to a subsequent 8% drop in the maximum  $MTR_{asym}$  value.

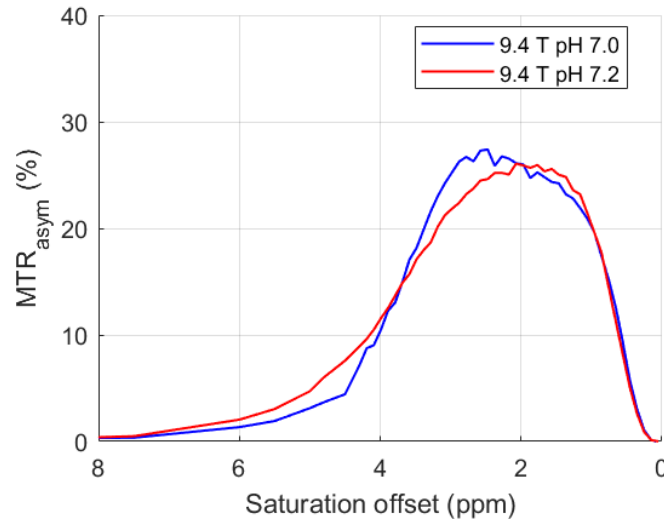


Figure 3.7: Z-spectrum and corresponding  $MTR_{asym}$  of glutamate at pH 7.0 and pH 7.2 at 37 °C, with optimized  $B_{1,sat}$  ( $7 \mu T$ )

Larger pH variations can have even more drastic impact on the Z-spectrum (and  $MTR_{asym}$  profile). This is notably the case for glucose (Figure 3.8) in acidic conditions (pH = 6.0). Indeed, acidifying the glucose solution slows down the exchange rates revealing additional CEST resonances between 2.1 and 2.9 ppm (from the bulk) corresponding to  $-OH$  groups that were not fulfilling the CEST condition due to their (too) fast exchange rates at pH 7.0.

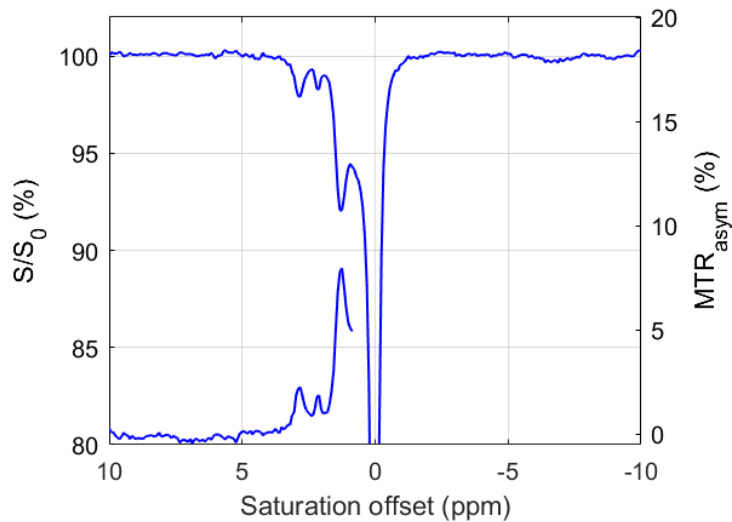


Figure 3.8: Z-spectrum and corresponding  $MTR_{asym}$  of glucose at pH 6.0

This example illustrates the need to estimate the CEST characteristics of a metabolite at physiological pH values.

### 3.1.4 Selectivity towards a specific metabolite

While the sensitivity of CEST can be seen as its strength compared to conventional MRS techniques, one can argue that its chemical specificity or selectivity towards a specific metabolite-

of-interest is its Achilles' heel. The goal is thus to find a way to obtain the maximum signal/contrast from this metabolite-of-interest while limiting the contamination from other metabolites whose labile protons resonate close by.

### 3.1.4.1 Mixture of lactate, glucose and glutamate : the advantage of very high magnetic field

Knowing the chemical shift of a metabolite and optimizing the  $B_{1,sat}$  power for it definitely helps weighting the CEST signal towards the contribution of this metabolite. However, it is impossible to isolate its signal as it is always be in competition with other CEST effects *in vivo*.

In this subsection, we are investigating the possibility to disentangle CEST contributions from a solution composed of 40 mM lactate, 20 mM glucose and 20 mM glutamate (sample #4). Z-spectra and corresponding  $MTR_{asym}$  spectra of lactate, glucose, glutamate and their mixture are shown in Figure 3.9.

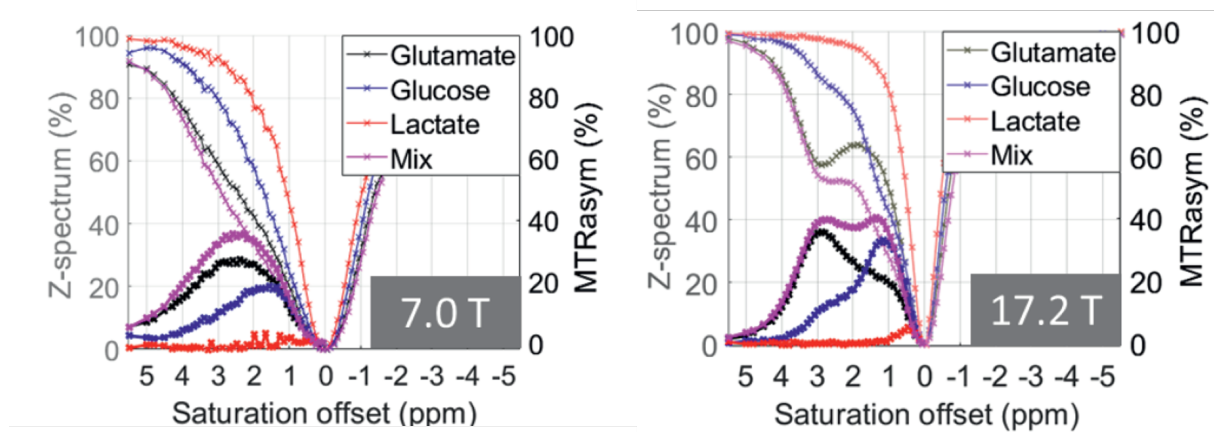


Figure 3.9: Z-spectrum and  $MTR_{asym}$  of lactate, glucose, glutamate and a mixture of all three at 7.0 T and 17.2 T acquired with  $B_{1,sat} = 7.0 \mu T$ .

At 7.0 T, the  $MTR_{asym}$  profile of the mixture shows one broad CEST contribution with its maximum centered close to the expected chemical shift of glutamate. Even though the glucose CEST effect contributes to the increase in MTR, there is no local maximum that we can associate to glucose. The lactate CEST signal is barely detectable.

At 17.2 T, the equivalent  $MTR_{asym}$  profile exhibits two clearly identifiable maxima positioned close to the chemical shifts of glucose and glutamate. The contributions of these two metabolites can be easily deduced from the mixture. However, lactate contribution is still indistinguishable from the  $MTR_{asym}$  of the mixture, even at such a large concentration.

This experiment shows that using ultra-high field like the 17.2 T improves the disentanglement of metabolite contributions. However, it does not lead to a complete separation of the different CEST contributions. In the next section, we present how the choice of  $B_{1,sat}$  is a final possible lever to drive the CEST contrast weighting towards a metabolite more than another.

### 3.1.4.2 Metabolic imaging of a Cherry tomato : selecting a specific CEST contrast

As explained previously, high and ultra-high magnetic fields can contribute significantly to the improvement of the chemical specificity of CEST MR. It is fortunate then, that in the context of this PhD thesis, our focus is on the exploration of CEST effects at 17.2 T.

In collaboration with Julia R. Krug who did a 6-month internship in our team during her PhD thesis, we evaluated the feasibility of LATEST, glucoCEST and gluCEST on a vegetal model: the cherry tomato.

Using a CEST-PRESS sequence in a voxel located in the pericarp of the tomato, two experimental Z-spectra were acquired from -10 to 10 ppm starting with those specific offsets  $\pm [10, 7.5, 6, 5.5, 5, 4.8, 4.5]$  followed by regularly distributed offsets between  $\pm 4.3$  and 0. Every offset was acquired consecutively with its opposite offset. The CEST saturation module consisted in 35 rectangular, 50 ms long pulses separated by an interpulse delay of 0.01 ms, resulting in a saturation time of 1.75 s. The readout module had the following parameters : TE/TR = 15/2500 ms, voxel size =  $2 \times 2 \times 4$  mm<sup>3</sup> and total acquisition time = 4 m 10 s. The acquisitions were performed for  $B_{1,sat}$  set at 1.5  $\mu$ T and 7  $\mu$ T and the results are shown in Figure 3.10A.

Additionally, CEST-RARE images of a cherry tomato were acquired with  $B_{1,sat} = 1.5$   $\mu$ T (Figure 3.10 B) and  $B_{1,sat} = 7$   $\mu$ T (Figure 3.10C) using the same CEST saturation module than for the CEST-PRESS experiment and with TE/TR = 5/3000 ms, matrix size =  $128 \times 128$  and FOV=  $10 \times 10$  mm<sup>2</sup>.

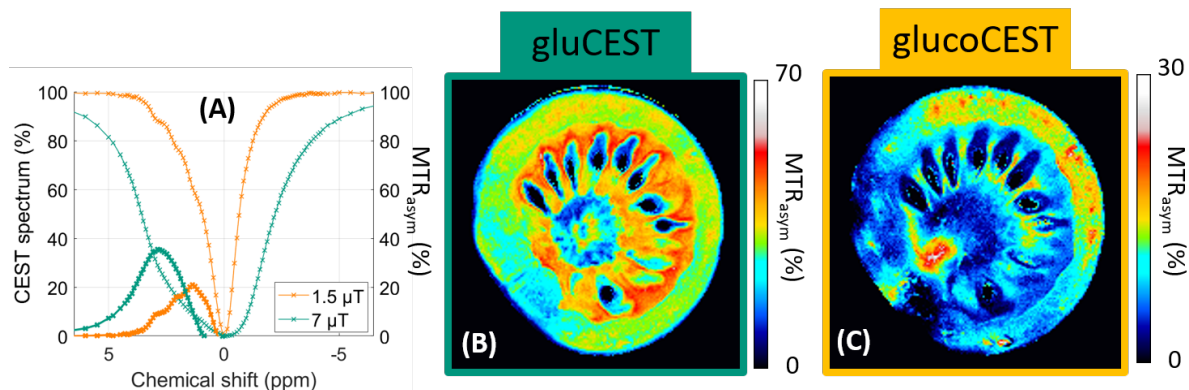


Figure 3.10: CEST contrast selection on a cherry tomato. (A) Z-spectrum (thin line) and corresponding  $MTR_{asym}$  ratio (bold line) obtained in a  $3 \times 3 \times 3$  mm<sup>3</sup> voxel located in the pericarp tissue for two different  $B_{1,sat}$  values (B) CEST-RARE image of a tomato oriented towards the gluCEST contrast (parameters  $B_{1,sat} = 7$   $\mu$ T, saturation offset 3 ppm) (C) CEST-RARE image of a tomato oriented towards the glucoCEST contrast (parameters  $B_{1,sat} = 1.5$   $\mu$ T, saturation offset 1.2 ppm)

By applying one or the other  $B_{1,sat}$  saturation power (1.5  $\mu$ T or 7  $\mu$ T), one can obtain very different  $MTR_{asym}$  profiles. Indeed, at the stronger  $B_{1,sat}$  value, the saturation is most effective for metabolite whose labile <sup>1</sup>H are in relatively fast exchange with water. Concomitantly, the direct water saturation (spill-over effect) at such saturation power limit drastically the visibility of the metabolite whose labile <sup>1</sup>H resonates close to water. These conditions are

logically favorable for the visualization of the gluCEST effect. This is confirmed by the maximum  $MTR_{asym}$  at about 2.8 ppm.

At the more moderate  $B_{1,sat}$  of 1.5  $\mu$ T, the saturation is efficient for metabolites whose exchange rates are lower and the spill-over effect is sufficiently mild that more CEST contributions can be observed. From the allure of the  $MTR_{asym}$  whose maximum at about 1.2 ppm matches with the one of glucose, one can conclude that glucose is the main contributor to the CEST contrast in those conditions.

As in the sample mix, the lactate CEST signal is barely detectable. For those two saturation powers and for their saturation offsets set at 1.2 and 2.8 ppm, the CEST images are mostly weighted by glucose (Figure 3.10C) and glutamate (Figure 3.10B) respectively. The glucoCEST and gluCEST images suggest that there is more glucose and other sugars with hydroxyl functions in the pericarp region than in the locule and that the glutamate is predominantly located in the locular tissue. Due to the incomplete disentanglement of CEST contributions, the observed glucoCEST and gluCEST signals can not entirely be attributed to glucose or glutamate and further investigations would be necessary to confirm these chemical composition and distribution ([Davies and Kempton 1975; Sorrequieta et al. 2010]). Interestingly, those glucoCEST and gluCEST acquisitions could motivate further developments to use CEST MR as a way to investigate non-invasively the "rough" composition and distribution of sugars and amino-acids in different fruit varieties and maturation stages.

This experiment has demonstrated the viability of glucoCEST and gluCEST experiments on the cherry tomato at 17.2 T. We have demonstrated the possibility to select a CEST-contrast that is more representative of a metabolite than another by carefully choosing the  $B_{1,sat}$ . However, this experiment also showed that despite a careful weighting of the CEST contrast in favor of a metabolite, CEST MR cannot reflect the sole contribution of that metabolite in biological media.

### 3.1.5 Conclusion

In the first section of this chapter, we experienced and evaluated the clear benefits of realizing CEST acquisitions at high magnetic fields. Based on the classical estimation of the CEST contrast ( $MTR_{asym}$ ), we proposed viable sets of acquisition parameters for *in vivo* CEST MR experiments for three major metabolites (lactate, glucose and glutamate). We demonstrated that for a given solute, and equivalent saturation conditions, the increase in  $B_0$  always leads to an increase in the CEST contrast. Moreover, by working at ultra-high magnetic field like at 17.2 T Tesla, we have access to a larger frequency dispersion and it is therefore easier to meet the slow-to-intermediate condition previously established. Most importantly, a larger frequency dispersion gives access to better resolved Z-spectrum, leading to a better chemical specificity for CEST (as long as the  $B_0$  inhomogeneities are properly corrected). For these reasons, the highest magnetic field (17.2 T) magnet was used for every experiment presented thereafter. Finally, it was shown in a vegetal model: the cherry tomato that it is indeed possible to select a CEST contrast that is mostly weighted toward glucose or glutamate by adjusting the  $B_{1,sat}$  values and saturation offsets. While the *in vitro* characterization of the CEST contrast of a metabolite-of-interest in physiological conditions ( $37 \pm 1$  °C and pH  $7 \pm 0.1$ ) is a necessary step to narrow down the optimal saturation parameters in preparation for its detection *in vivo*, further adjustments have to be made during those *in vivo* CEST MR stud-

ies to account for the complexity of biological media and their many CEST, MT and NOE contributions.

## 3.2 Ultra-fast CEST MR acquisition sequence

### 3.2.1 On the importance of a fast CEST MR sequence

Conventional CEST acquisitions consist in the acquisition of the water signal (without and following the application of a presaturation module consisting in a train of RF pulses applied at varying saturation frequency offsets: the so-called "Z-spectrum". Such acquisitions are time-consuming and therefore prone to various artifacts : spurious movements of the animal, frequency drifts and temperature fluctuations, resulting in poor signal stability over time, and compromised detection sensitivity. For this reason, we have developed a fast acquisition approach which we call CEST-linescan (CEST-LS), that enables the acquisition of an entire Z-spectrum in only two scans. The CEST-LS pulse sequence was developed according to the ultrafast Z-spectrum (UFZ) methodology introduced by Xu et al. ([X. Xu, J.-S. Lee, and Jerschow 2013; Boutin et al. 2013]) and it is based on the application of magnetic field gradients during the saturation module resulting in the spatial encoding of the saturation frequency. Because it allows a dramatic reduction in acquisition time, CEST-LS results in increased signal stability while maintaining a contrast-to-noise ratio similar to that of standard CEST sequences, which is particularly useful for *in vivo* applications.

### 3.2.2 Principle and sequence pulse diagram

A CEST-linescan (CEST-LS) sequence was developed for Paravision 6.0.1 starting from a standard gradient echo pulse sequence in which the phase encoding gradient is deactivated and the CEST saturation module was added. Compared to the simplest implementation of the UFZ technique ([X. Xu, J.-S. Lee, and Jerschow 2013]), the CEST-LS sequence used here includes a slice selection gradient and outer-volume saturation (OVS) bands (Figure 3.11), in order to limit the CEST acquisition to a given region-of-interest (ROI). The saturation module consists in saturation pulses applied on-resonance in the presence of a 1D spatial encoding gradient. As a result, spins that are located along the direction of the gradient at a distance  $d$  from the isocenter will experience an irradiation at saturation offsets given by  $\gamma \times G_{sat} \times d$ , where  $\gamma$  is the gyromagnetic ratio of  $^1\text{H}$  and  $G_{sat}$  is the amplitude of the gradient. During the acquisition, a gradient  $G_{acq}$  is applied along the same direction as the saturation gradient. The saturation range,  $BW_{sat}$ , is dictated by the acquisition bandwidth,  $BW_{acq}$  are related to the ratio  $r$  between the saturation gradient  $G_{sat}$  and the acquisition gradient  $G_{acq}$ , according to the following equation:

$$r = \frac{G_{sat}}{G_{acq}} = \frac{BW_{sat}}{BW_{acq}} \quad (3.1)$$

It follows that, for an acquisition of  $N$  points, the effective spectral resolution of the CEST-LS acquisition, equivalent to the saturation frequency increment in conventional Z-spectra is equal to  $(r \times BW_{acq})/N$ .

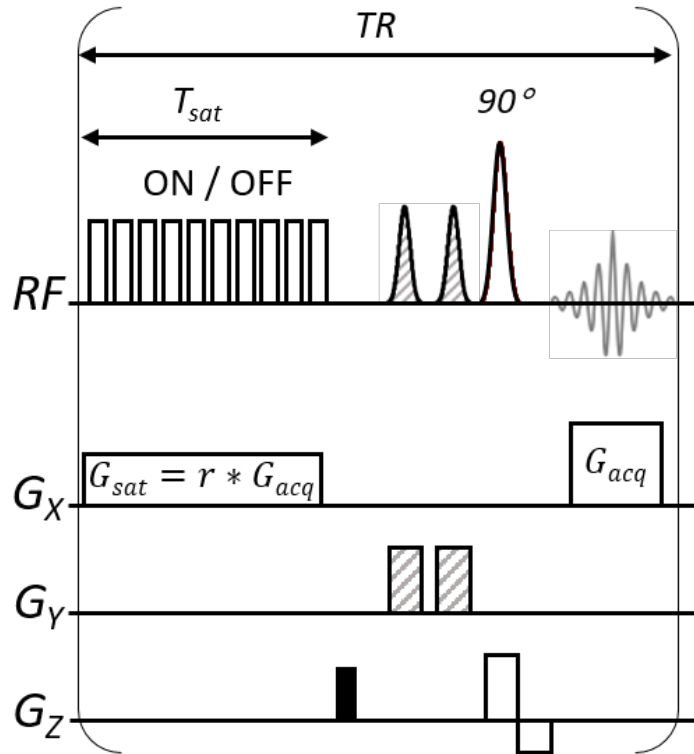


Figure 3.11: CEST-LS pulse sequence. The CEST saturation module was placed in front of a standard gradient echo sequence in which the phase encoding gradient was removed. Gradient spoilers were applied on the z direction (solid black rectangle). FOV saturation bands were added to eliminate the signal outside the desired ROI (hatch pattern). The CEST saturation pulses are switched ON and OFF (amplitude at zero) to generate saturated or reference profiles, respectively. The X-axis is also called the read direction.

Figure 3.11 shows the course of a single repetition but the complete sequence consists in several repetitions. Saturated profiles are consecutively acquired eight times. To compensate for the irregular 1D profile along the read direction, eight reference profiles are then acquired, with the saturation pulse turned off (corresponding to the proton density distribution along the line). The loop (8 saturated profiles followed by 8 reference profiles) can then be repeated over time, at the user's convenience.

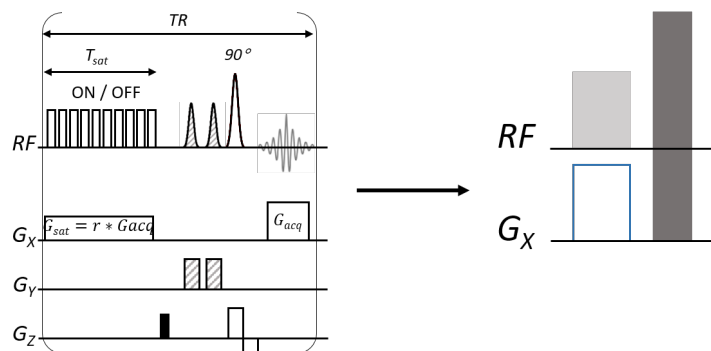


Figure 3.12: Simplified representation of one repetition of the CEST-LS pulse sequence. The saturation pulses are grouped in a light gray rectangle, under which the saturation gradient is shown by a blue line. The entire readout module is represented by a large dark gray rectangle.

For a clearer representation of the different repetitions, the single repetition pulse sequence was schematically simplified as shown in Figure 3.12. Only the time courses of the RF pulses and the gradient on the  $G_X$  direction (read direction) were represented and the readout module was simplified to a single block. Using this simplified representation, the long time course of a whole sequence is represented in Figure 3.13.

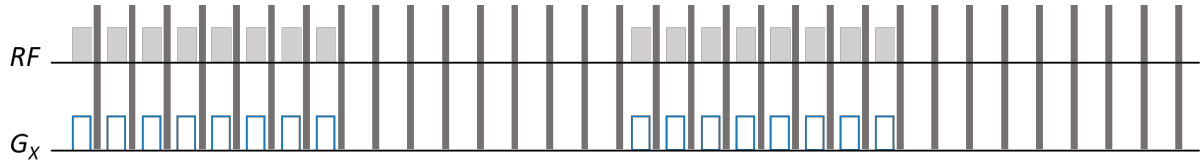


Figure 3.13: Simplified pulse designs of the CEST-LS sequence. In this example, the loop of 8 saturated profiles followed by 8 reference profiles is repeated twice and 32 profiles (16 saturated, 16 reference) are acquired in total.

With that sequence, it is possible to select the width of the chemical shift range by tuning the ratio  $r$ . If the voxel is not positioned at zero on the read direction, the read offset  $d_{read}$  associated with the voxel position needs to be compensated by applying the same additional saturation frequency offset ( $\text{Offset}_{\text{geom}}$ ) to every saturation frequency.

$$\text{Offset}_{\text{geom}} = \gamma \times G_{acq} \times r \times d_{read} \quad (3.2)$$

The center of the chemical shift range can also be customized by applying another additional desired saturation frequency offset ( $\text{Offset}_{\text{center}}$ ). The offset the user must enter is the sum of these two offsets.

$$\text{Offset}_{\text{user}} = \text{Offset}_{\text{geom}} + \text{Offset}_{\text{center}} = \gamma \times G_{acq} \times r \times d_{read} + \text{Offset}_{\text{center}} \quad (3.3)$$

where  $\gamma$  is the gyromagnetic ratio of  $^1H$ ,  $r$  the ratio as defined in 3.1,  $G_{acq}$  is the acquisition gradient.

For example, if the voxel is 2 mm away from the center (on the read direction) and the user wants to center the saturation range on 3 ppm, and if the parameters are  $G_{sat} = 0.0827 \text{ T.m}^{-1}$ ;  $r = -0.15$ ; the user should therefore enter :

$$\text{Offset}_{\text{user}} = 42.576 \times 10^6 \times 0.0827 \times 0.15 \times 2 \times 10^3 + 3 \times 730.2 = 3247\text{Hz} \quad (3.4)$$

### 3.2.3 Data analysis

All CEST-LS data were analyzed using in-house written MATLAB scripts (Mathworks, version 9.7, R2019b). An example of data analysis is shown in Figure 3.14. Those data were obtained in a 20 mM glutamate phantom (phantom #13) that presents a CEST effect centered on 2.8 ppm. To obtain a Z-spectrum from a simple loop (8 saturated profiles followed by 8 reference profiles) acquired in the red voxel depicted in Figure 3.14A, CEST data are processed as follows: after a zero-filling which doubled the number of FID data points, every FID signal acquired through time is Fourier transformed and has  $N_{pts}$  points. The eight saturated profiles are averaged together as  $S$  represented in orange in Figure 3.14B. In this example, the water peak is recognizable. The eight reference profiles are averaged together as  $S_0$  represented in blue in Figure 3.14B. The blue and orange curves are almost superimposed where

the CEST effect is minimal (for saturation above 4 ppm or under  $-4$  ppm). The ratio between  $S$  and  $S_0$  is plotted against the saturation frequency offsets (Figure 3.14C).

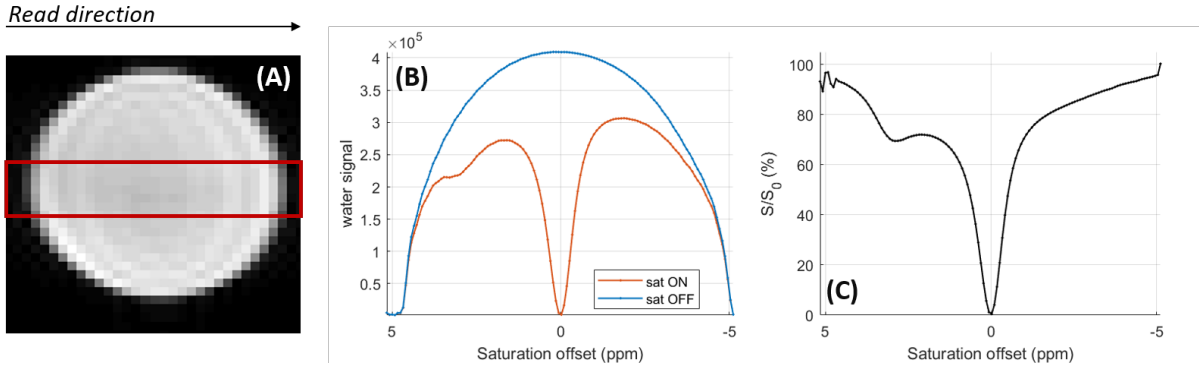


Figure 3.14: CEST-LS analysis for data acquired in a 20 mM glutamate sample shown in (A). The red box shows the voxel in which the data were acquired. (B) Averaged saturated and averaged reference water profiles. (C) Ratio between the saturated and the reference profile.

The saturation offset  $\delta$ -axis of the Z-spectrum is computed according to the saturation bandwidth  $BW_{sat}$ , the geometric offset  $Offset_{geom}$  associated with the read offset  $d_{read}$  of the voxel (using Equation 3.2) and the offset chosen by the user  $Offset_{user}$ , the formula is the following:

$$\delta = \text{sign}(r) \times \text{linspace}\left(\frac{-BW_{sat}}{2} - Offset_{geom} + Offset_{user}, \frac{BW_{sat}}{2} - Offset_{geom} + Offset_{user}, N_{pts}\right) \quad (3.5)$$

with *linspace* a Matlab function generating a row vector of  $N_{pts}$  evenly spaced points between  $-BW_{sat}/2$  and  $BW_{sat}/2$ . This axis can be switched to ppm values by dividing all the saturation offsets by a factor of 730.2 (1ppm@17.2 T = 730.2 Hz). In the situation when the user has correctly calculated the compensation of the geometric offset, equation 3.5 becomes:

$$\delta = \text{sign}(r) \times \text{linspace}\left(\frac{-BW_{sat}}{2} + Offset_{center}, \frac{BW_{sat}}{2} + Offset_{center}, N_{pts}\right) \quad (3.6)$$

Otherwise, if the user's calculation does not compensate correctly for the geometric offset, it appears on the graph that the saturation range covered with the acquisition is not centered on the desired offset.

Once the offset is properly calculated, it is possible to correct the  $\delta$ -axis of the profile even more precisely (below the profile resolution) with a post-acquisition step. By interpolating the data using a cubic spline interpolation and slightly shifting the  $\delta$ -axis in order to center the interpolated water peak at 0 ppm (or any other available peaks with a well-established chemical shift), the  $\delta$ -axis is more accurately positioned with respect to the CEST contributions. This subtle offset is called  $Offset_{post-acq}$ . In the end, the entire  $\delta$ -axis formula is:

$$\delta = \text{sign}(r) \times \text{linspace}\left(\frac{-BW_{sat}}{2} + Offset_{center} + Offset_{post-acq}, \frac{BW_{sat}}{2} + Offset_{center} + Offset_{post-acq}, N_{pts}\right) \quad (3.7)$$

Figure 3.15 shows another example of CEST-LS acquisition on phantom n° 12 of 1 mM hydrogen peroxide obtained with a saturation module of 10 successive 400 ms pulses and a saturation power of 6  $\mu$ T and a TR of 8 s. Both the Z-spectrum and the  $MTR_{asym}$  spectrum show a CEST peak at 6.2 ppm, this is in agreement with the results presented in [Ryoo et al. 2017].

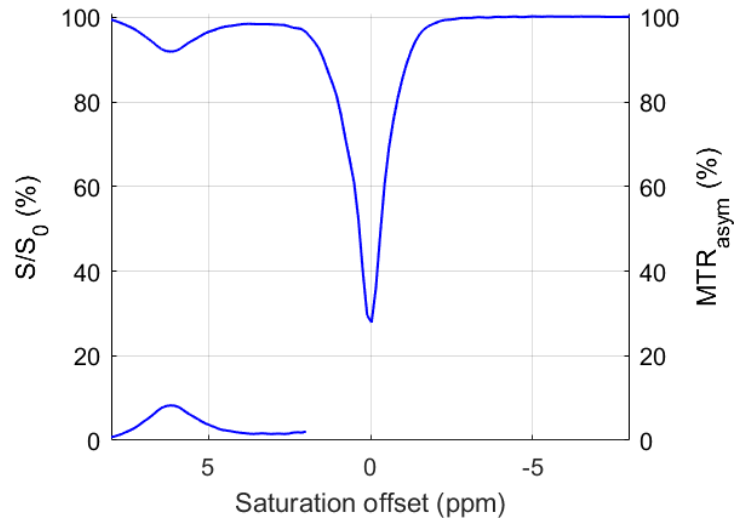


Figure 3.15: CEST-LS Z-spectrum and  $MTR_{asym}$  of hydrogen peroxide

### 3.2.4 Conclusion

This section presents the development and implementation of the CEST-LS sequence based on the same principle that traditional CEST sequences to which a pair of gradient were added. Examples of *in vitro* CEST-LS acquisitions and data processing are also presented. With this new concept, the acquisition of a Z-spectrum only requires two TR. This very fast method opens the door for enhanced time resolution, which can be useful in two types of experiment. In case of a static experiment (measurement of a Z-spectrum), it gives access to a better signal stability because it makes the CEST detection less sensitive to physiological drifts over time. In case of dynamic experiment (with expected metabolic changes), being able to acquire a Z-spectrum in such a short time enables the detection of transient metabolic changes using CEST. Those two advantages are exploited in the studies presented in the next two chapters.

### 3.3 Development of a Z-spectrum analysis tool

Regardless of the acquisition method, analyzing Z-spectra has always been a challenge in the CEST community. The actual acquisition merges the CEST (and NOE) contributions from many different metabolites (and lipids/macromolecules), as well as the direct water saturation (DS or "spill-over" effect) and the magnetization transfer (MT) mediated by protons bound to macromolecules and bulk water molecules.

Many (semi)-quantification techniques have been proposed in order to best evaluate the different CEST contributions to a Z-spectrum. The most common evaluation method consists in computing the  $MTR_{asym}$  described in and is based on the assumption that the DS and MT effect have the same chemical shift and are symmetric, an assumption which still raises controversy within the CEST community ([Hua et al. 2007; Pekar et al. 1996; Swanson and Pang 2003]). Additionally, because the  $MTR_{asym}$  analysis method computes the difference between the signals obtained at two saturation frequencies symmetric with respect to water, it reflects a quantity combining up-field and downfield effects. The Nuclear Overhauser Effect (NOE) ([C. K. Jones, A. Huang, et al. 2013]) spanning from  $-5$  to  $-1$  ppm prevents the  $MTR_{asym}$  computed between 1 and 5 ppm from strictly reflecting the upfield CEST contribution.

Alternative evaluation methods perform Lorentzian fitting analysis of Z-spectra to independently estimate the DS, MT, NOE and CEST contributions ([Zaiß, Benjamin Schmitt, and Bachert 2011]). Those methods allow to efficiently separate different CEST peaks but are generally limited by the need of a priori knowledge about the number of pools of labile protons, their chemical shift and the shape of their contributions. Methods for finding the exchange rate and the labile proton ratio by fitting numerical or approximate analytical solutions of the Bloch-McConnell equations have also been proposed ([McMahon et al. 2006; Zaiss, Angelovski, et al. 2018]). They typically require long acquisition times, can be computationally demanding, and may introduce errors due to the approximations made in using analytical solutions. Recently, the use of magnetic resonance finger-printing (MRF) for CEST quantification has been reported both on phantoms and *in vivo* ([S. Huang et al. 2017; Perlman et al. 2020]). The accuracy of the results obtained with MRF depends on the size of the dictionaries used for matching the experimental CEST data. Deep neural networks can help improve this accuracy ([Kim et al. 2020]).

For all these reasons, we decided to develop a new approach adapted to the automatic detection of CEST peaks without having to make any assumptions about the frequency offset or the underlying line shape. This work was made in collaboration with Michele Lecis, who did his master thesis in our team at NeuroSpin. Michele was in charge of developing the algorithm and helped with the acquisitions and the interpretation of the results. PEAKIT is the name of the python-based algorithm developed along with a more user-friendly software tool. This analysis tool allows to detect statistically-significant CEST peaks and computes their peak height, area and significance. To limit the impact of DS and NOE effects, the baseline used for the peak characterization is estimated using a Gaussian Process (GP) regression model. The principle and main steps of the peak detection using PEAKIT are described in the next section. Then, applications of this analysis tool are presented for *in vitro* and *in vivo* data.

PEAKIT is open-source, and freely available for download from github at: <https://github.com/SKMikee/PeakIt>.

This work was published in Journal of Magnetic Resonance under the following reference: [Lecis et al. 2022].

### 3.3.1 Principle of the PEAKIT software tool

PEAKIT was developed with Python 3.8 and provided with a user interface through the *tkinter* package. The tool takes as input a Z-spectrum consisting of saturation offsets on the  $x$  axis and the normalized signal intensities on the  $y$  axis, and it outputs the location (chemical shift offset) of each detected peak along with the peak's height, area and statistical significance (p-value). There are three steps to the PEAKIT algorithm, corresponding to the peak detection, the baseline estimation, and the p-value computation, respectively. A detailed description of each of these three steps is given in the following sections.

#### 3.3.1.1 Peak detection

The peak detection process (Figure 3.16) is based on an iterative approach exploiting the local properties of the spectrum ([Chekanov and M. Erickson 2013]). Specifically, for each point  $i$  of coordinates  $(x_i, y_i)$ , a slope  $\alpha_i$  is computed as follows:

$$\alpha_i = \frac{y_{i+1} - y_i}{x_{i+1} - x_i} \quad (3.8)$$

Furthermore, at any point  $i$  we compute the moving average of the  $r$  preceding slopes as follows:

$$\bar{\alpha}_i = \frac{1}{r} \sum_{j=i-r+1}^{i-1} \alpha_j \quad (3.9)$$

where  $r$  is the number of consecutive points preceding point  $i$ . The appropriate choice of  $r$  depends on the noise level as well as on the shape of the spectrum: a dataset with numerous small peaks requires small values of  $r$  as the slope varies rapidly. PEAKIT algorithm detects the apparition of a peak at point  $i_b$  (henceforth referred to as the beginning of the peak) if the following two conditions are met simultaneously:

$$\alpha_{i_b} - \bar{\alpha}_{i_b} > \Delta \quad (3.10)$$

$$\alpha_{i_{b+1}} - \bar{\alpha}_{i_b} > \Delta \quad (3.11)$$

where the threshold  $\Delta$  is a free positive parameter which can be defined by the user. Specifically, in the PEAKIT tool,  $\Delta$  is expressed as a percentage of the maximum  $\alpha_i$  present in the spectrum; the user may input any  $\Delta$  value between 0 and 100 (see Figure 3.16). We make the following observations related to the choice of this parameter :

- Setting  $\Delta = 0$  implies that a peak is detected when the slopes at two consecutive points  $i_b$  and  $i_{b+1}$  exceed the moving average at point  $i_b$ .

- In case of noisy shapes, two random fluctuations occurring consecutively may trigger the detection of a peak when none is in fact present. In these cases, setting a higher threshold  $\Delta$  helps to reduce the rate of false positives and thus to improve the precision of peak detection.
- Finally, setting  $\Delta = 100$  guarantees that neither of the conditions (3.10) and (3.11) will be met, and, as a result, no peak will be found.

As soon as the detection of a peak is triggered, the PEAKIT algorithm scans through the points  $i_b + 1, i_b + 2, \dots$  until the peak maximum is reached at point  $i_m$ :

$$\alpha_{i_m} - \bar{\alpha}_{i_b} < \Delta^* \quad (3.12)$$

Thus, the maximum is detected when the slope is found to be smaller than the moving average recorded at the beginning of the peak ( $\bar{\alpha}_{i_b}$ ), net of a threshold parameter  $\Delta^*$ . The default value of  $\Delta^*$  is set to 0, as in the most common cases it is sufficient that  $\alpha_{i_{m+1}} - \bar{\alpha}_{i_b}$  is negative. In the case of adjacent and partially overlapping peaks it may be necessary to increase the  $\Delta^*$  value (between 0 and 100) to prevent detecting multiple peaks as a single one. (Note: For positive peaks, the inequalities (3.10), (3.11) and (3.12) reverse signs.)

By default, the PEAKIT algorithm assumes the peak to be symmetric and adds an equal number of points to the right side of the peak maximum to complete peak detection. Thus, the end of the peak will occur at point  $i_e = 2i_m - i_b$ . In conclusion, the output of the peak detection process consists of a set of three points for each detected peak:  $i_b, i_m$ , and  $i_e$  corresponding to the beginning, the maximum, and the end of the peak, respectively. In cases in which the result of the automated peak detection algorithm is judged to be inaccurate, the selection of the peak can also be made manually, by entering the beginning and the end values of the peak in the "point\_min" and "point\_max" fields, respectively. Regardless of how the peak is selected (automatically or manually), there is no impact on the subsequent steps of the analysis which include the baseline estimation and the peak significance computation, described in the two next sessions.

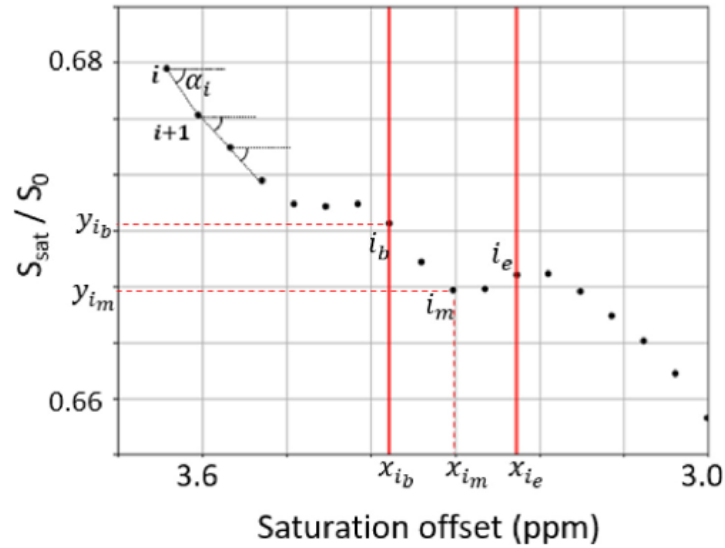


Figure 3.16: Schematic representation of the peak detection process. The algorithm computes the slopes successively, checking at every step whether the peak conditions (3.10), (3.11) are satisfied. For each identified peak, the algorithm outputs a set of three points: the beginning ( $i_b$ ), the maximum ( $i_m$ ), and the end ( $i_e$ ) of the peak. The slopes  $\alpha_i$  are defined in the text.

### 3.3.1.2 Baseline estimation

In this section, we describe the baseline estimation for each detected peak. In essence, the baseline level estimates the shape of the spectrum if the detected peak were absent. Under this hypothesis, the baseline profile  $\{b_i\}$  should match the spectrum  $y_i$  located just outside the peak. To ensure this matching, our technique uses a set of  $2r$  “training points” formed by the  $r$  points in the spectrum immediately preceding the peak, and the same number  $r$  of points immediately succeeding the peak.

The baseline estimation process relies on a Gaussian Process (GP) regression implemented via the GPy Python package available on [[github.com/SheffieldML](https://github.com/SheffieldML) 2018]. An excellent introduction to Gaussian Processes can be found in Reference [Rasmussen 2006], this reference notably includes a chapter dedicated to GP regression which contains the full mathematical details of the method employed in PEAKIT. Without delving into these details, we mention that the GP technique produces, for all points  $\{x_i\}$  within the peak region  $i_b \leq i \leq i_e$ , the predicted baseline levels  $\{b_i\}$  along with their standard deviations  $\{\sigma_i\}$  (Figure 3.17). The values  $\{\sigma_i\}$  form the uncertainty band around the predicted baseline shape. We note that the uncertainty band narrows as  $r$  increases. We also note that, for a given value of  $r$ , a noisier dataset  $\{y_{i_b-r}, \dots, y_{i_b-1}, y_{i_e+1}, \dots, y_{i_e+r}\}$  will produce a wider uncertainty band.

Once the baseline level is established, it is possible to quantify how much of the height and area of the peak can be attributed to signal. These contributions are inferred from the observed data by subtracting the baseline estimation. In addition, we re-compute the peak center location by identifying the point  $i$  in the peak region of the spectrum for which the difference ( $y_i - b_i$ ) is maximum.

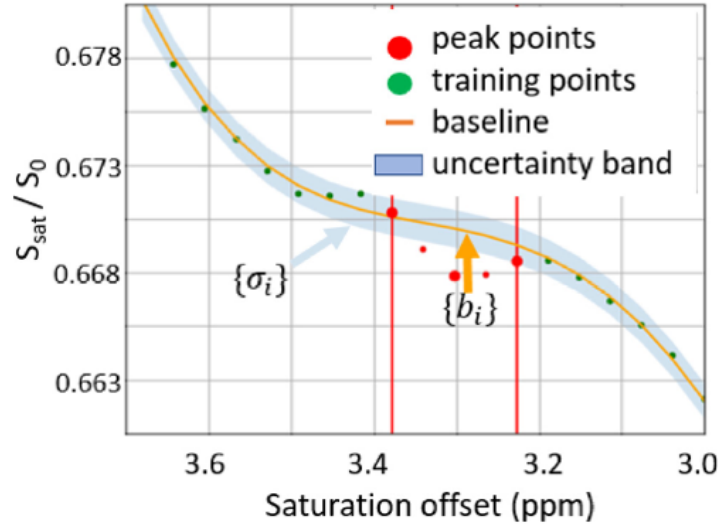


Figure 3.17: Based on the training points (green markers), the GP regression produces, for all points in the peak region, a baseline shape  $\{b_i\}$  (orange line) along with their standard deviations  $\{\sigma_i\}$  (shaded band).

### 3.3.1.3 Peak significance computation

The third and final goal of the PEAKIT tool is to compute a p-value for each detected peak. If the p-value is smaller than a certain threshold (for example,  $p < 0.005$ ), then the detection of the given peak is confirmed. If, on the other hand, the p-value exceeds the threshold ( $p > 0.005$ ) then the peak is not statistically significant, and is consequently discarded.

The significance assessment is based on the null hypothesis, which assumes the detected peak is not due to the CEST signal but is instead generated by random fluctuations of the noise around the baseline. In order to test the null hypothesis, noise fluctuations are randomly generated in a Monte Carlo simulation.

Specifically, at every point  $i$  in the peak region  $i_b \leq i \leq i_e$ , we generate a random number  $B_i$  from the Gaussian distribution whose mean and standard deviation are the predicted  $b_i$  and  $\sigma_i$ , respectively. The ensemble of values  $\{B_i\}$  forms a pseudo-experiment, which is simply a spectrum randomly generated from the baseline shape according to its uncertainty band.

Next, we compute a measure of how consistent this pseudo-experiment is with the baseline data using a  $\chi^2$  approach :

$$\chi_{pseudo}^2 = \sum_{i=i_b}^{i_e} \frac{(B_i - b_i)^2}{b_i} \quad (3.13)$$

The process is repeated  $N$  times to generate a large number of pseudo-experiments (for example,  $N = 100,000$ ), and for each pseudo-experiment we record its corresponding  $\chi^2$  value calculated using the above equation. The larger its  $\chi^2$  value, the more the pseudo-experiment will have deviated from the baseline shape.

To estimate the p-value, we compute the fraction of pseudo-experiments which deviate from the baseline as much as the data or more, or in mathematical terms the fraction of pseudo-experiments having  $\chi_{pseudo}^2 \geq \chi_{data}^2$ , where  $\chi_{data}^2$  given by:

$$\chi_{data}^2 = \sum_{i=i_b}^{i_e} \frac{(y_i - b_i)^2}{b_i} \quad (3.14)$$

where  $y_i$  are the experimental points and  $b_i$  are, as in the previous formulae, the baseline points predicted by the GP regression. If the detected peak is generated by signal (as opposed to noise), then the experimental points will deviate significantly from the predicted baseline shape, resulting in a large value of  $\chi^2$  data. As consequence, very few pseudo-experiments, if any, will fluctuate to the level of the experimental data or more ( $\chi_{pseudo}^2 \geq \chi_{data}^2$ ) and the p-value will consequently be very small. This allows to reject the null hypothesis and confirm peak detection. Finally, if none of the pseudo-experiments have  $\chi_{pseudo}^2 \geq \chi_{data}^2$ , this implies that the number of pseudo-experiments N is insufficient for extracting a precise p-value, and an upper bound can be set:  $p < 1/N$ . For example, if  $N = 100,000$  and we register no pseudo-experiments with  $\chi_{pseudo}^2 \geq \chi_{data}^2$  then we conclude that the p-value satisfies  $p < 0.001\%$ . As a general rule, choosing an appropriate number N of pseudo-experiments is a trade-off between ensuring a high statistical precision (larger N is better) and maintaining a short computation time (smaller N is better).

### 3.3.2 Demonstration

To test the performance of the PEAKIT analysis tool, Z-spectra are acquired both *in vitro* (carnosine phantoms) and *in vivo* (rat leg muscle) and are then analysed using PEAKIT.

For both *in vitro* and *in vivo* studies, the experimental parameters are the following: the Z-spectra are acquired using the CEST-LS sequence previously described with a nominal spectral resolution of 0.054 ppm (zero-filled to 0.027) using a saturation power  $B1 = 1 \mu\text{T}$ . Each Z-spectrum is the average of 80 transients, for an acquisition time of 21 min.

#### 3.3.2.1 Phantoms

To evaluate the performance of the PEAKIT analysis tool, we acquired Z-spectra on five phantom samples with a different concentration of carnosine (phantoms n°6 to n°10), that are heated to 37 °C. Indeed, carnosine is known to present a CEST peak ([Bodet et al. 2015]).

The analysis process of the PEAKIT detection are presented for the samples with the highest and the lowest concentration (Figure 3.19 A and Figure 3.19 B). For all concentrations, PEAKIT detected a peak centered at 3.3 ppm, as expected. Carnosine being the only molecule generating a CEST effect in the sample, a large number of training points around the carnosine peak are exploitable to generate the baseline. We used thirty training points ( $r=15$ ) which allowed to minimize the uncertainty around the baseline. Therefore, very few fluctuations of the pseudo-experiments went beyond the data points, resulting in p-values  $p < 5 \cdot 10^{-7}$  for all concentrations studied.

Additionally to peak detection and significance estimation, PEAKIT computed the height and area of each peak. The plots from Figure 3.19 C and 3.19 D show that the height and

area of the peaks are linearly correlated with the carnosine concentration. This linearity can be used to get a first estimation of the carnosine concentration in similar samples. However, this does not allow to unambiguously quantify the carnosine concentration in samples having other CEST contributions like tissue samples. The estimation of the baseline, and therefore the estimated area and height of each peak, are dependent on the local shape of the Z-spectrum, which in turn depends on the sample (presence of MT or multiple peaks, for example) and the experimental parameters. Thus, PEAKIT is suited to conducting semi-quantitative analyses and comparisons between spectra generated by very similar samples, and acquired under the same experimental conditions.

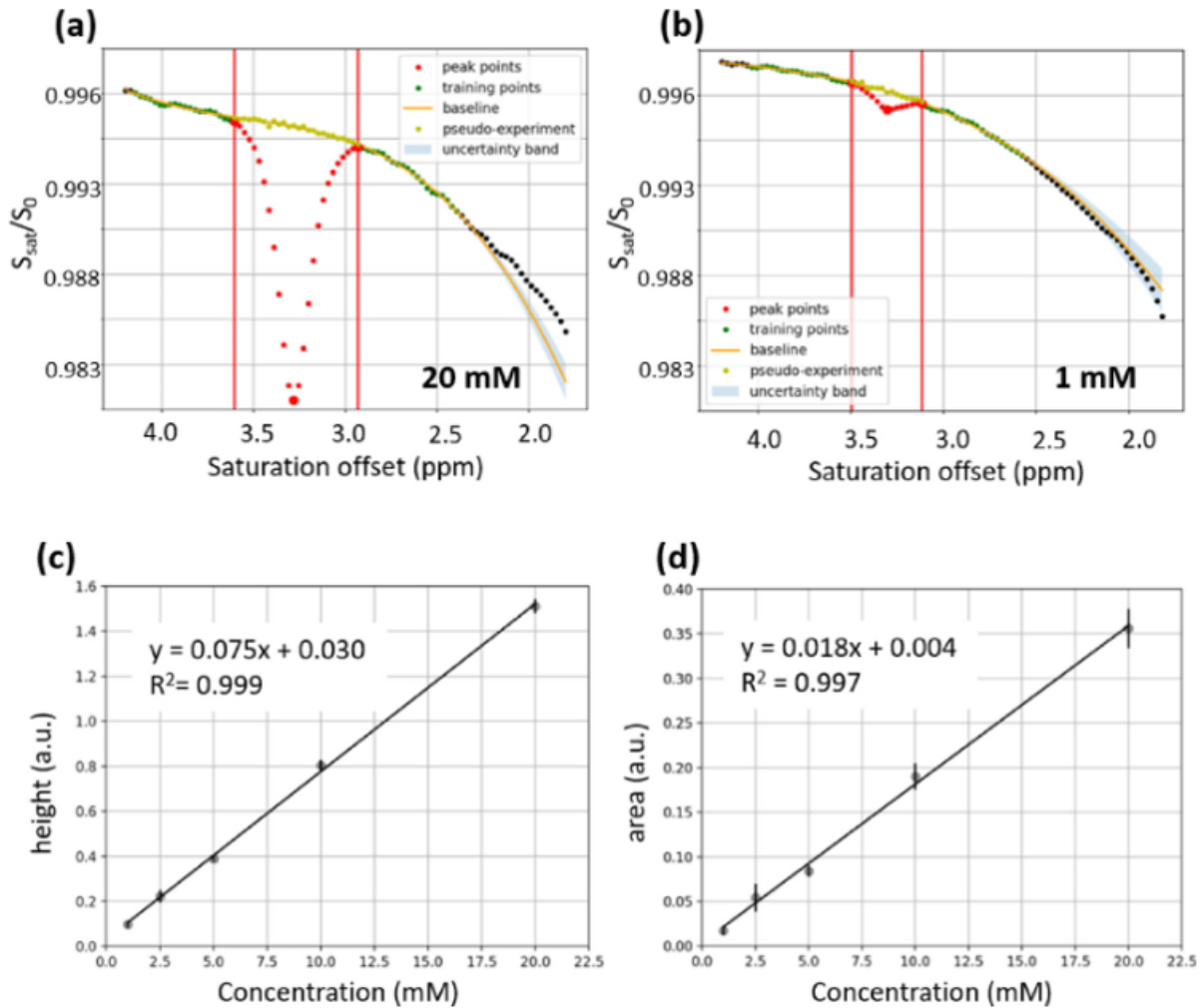


Figure 3.18: Examples of PEAKIT analysis of Z-spectra acquired on carnosine phantoms in PBS at different concentrations: 20 mM (a) and 1 mM (b). The Z-spectra show a significant peak centered at 3.3 ppm. The peak height (c) and the peak area (d) increase linearly with the metabolite concentration.

### 3.3.2.2 *In vivo*

The final assessment of PEAKIT performance is made *in vivo* data, acquired on the skeletal leg muscle of a Dark Agouti rat. The Z-spectrum acquired is partially represented in Figure 4.4 A where four peaks can be identified. The peaks at 1.9 and 2.6 ppm respectively correspond to creatine (Cr) and phosphocreatine (PCr) ([Pavuluri et al. 2020]). Due to the

asymmetric shape of the peaks, the automatic detection is manually adjusted to the range 2.32 - 1.64 ppm for Cr (Figure 3.18 B) and 2.85 - 2.32 ppm for PCr (Figure 3.18 C). For those two peaks, ten training points ( $r=5$ ) are used for the baseline estimation and the significance evaluation returned p-value  $p < 5 \cdot 10^{-7}$ . The small peak detected at 3.3 ppm is attributable to carnosine and is also detected with a p-value  $p < 5 \cdot 10^{-7}$ . The amide proton transfer (APT) located at 3.5 ppm is also found significant with a p-value  $p = 3.7 \cdot 10^{-7}$ . The results of the PEAKIT analysis of the four peaks are summarized in Table 3.5.

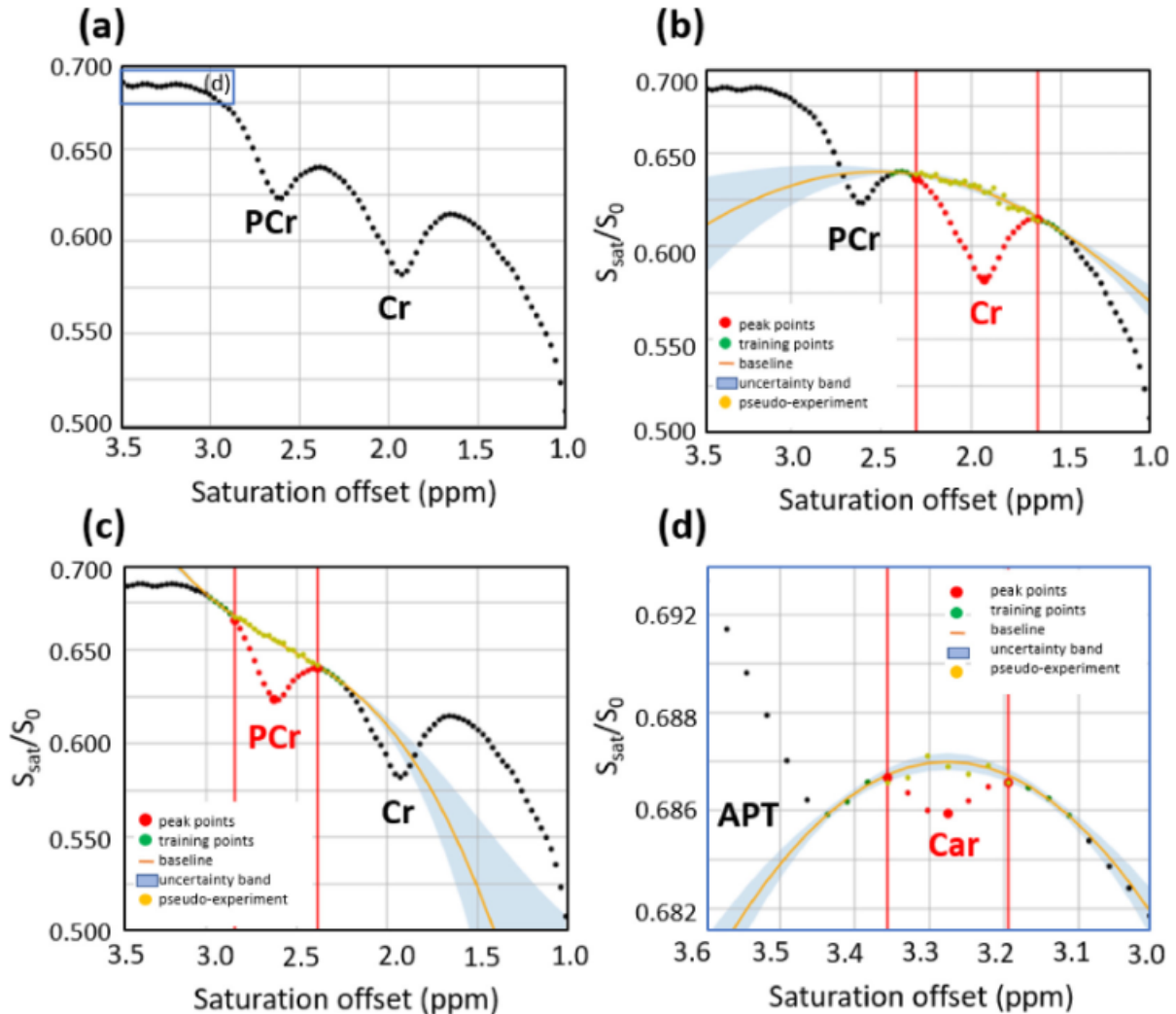


Figure 3.19: PEAKIT analysis of a Z-spectrum acquired *in vivo* on a rat leg muscle. (a) Down-field region of the spectrum in which are apparent four significant CEST peaks corresponding to creatine, phosphocreatine, carnosine and APT. The analyses of the creatine and phosphocreatine CEST peaks are shown in (b) and (c), respectively. (d) Zoom on the 3.0–3.6 ppm range showing the PEAKIT analysis of the carnosine CEST peak.

Metabolite	Peak freq. offset (ppm)	Height (a. u.)	Area (a. u.)	p-value
Creatine	1.93	$4.8 \pm 0.4$	$1.55 \pm 0.2$	$< 5 \cdot 10^{-7}$
Phosphocreatine	2.63	$3.6 \pm 0.1$	$(9.3 \pm 0.5) \times 10^{-1}$	$< 5 \cdot 10^{-7}$
Carnosine	3.28	$(4.1 \pm 0.4) \times 10^{-1}$	$(4.2 \pm 0.6) \times 10^{-2}$	$< 5 \cdot 10^{-7}$
APT	3.46	$(3.8 \pm 1.54) \times 10^{-1}$	$(4.2 \pm 2.4) \times 10^{-2}$	$3.7 \cdot 10^{-3}$

Table 3.5: PEAKIT output obtained on the Z-spectrum of a rat leg muscle from Figure 3.18

### 3.3.3 Conclusion, discussion and perspective

In this section, the development and testing of PEAKIT - a software tool for the detection and characterization of CEST peaks is presented. The performance of the tool was evaluated through the analysis of *in vitro* and *in vivo* CEST data acquired using the CEST-LS sequence presented in Section 5.1.0.2. The software is easy to use and of reduced computational cost. Compared to other existing tools used for the detection and characterization of CEST peaks, PEAKIT has the advantage that it does not require assumptions regarding the position and the shape of the peaks. The tool is not intended for the detection of highly overlapping peaks for which other analysis approaches should be employed ([Zaiß, Benjamin Schmitt, and Bachert 2011; Zaiss, Angelovski, et al. 2018]). However, PEAKIT tends to perform better in portions of the Z-spectrum where the baseline is more steady and therefore easier to estimate. For this reason, we believe that the tool is more adapted to the characterization of CEST contributions located far away from the water peak.

For each detected peak, PEAKIT returns its height, area, and statistical significance. While these are quantitative measures characterizing the signal, care must be exerted when interpreting the analysis results. Specifically, these variables as well as other similar CEST metrics ([Heo, D.-H. Lee, et al. 2017]) depend on the RF saturation power levels, the  $B_0$  field strength, the exchange rates, and the local shape of the Z-spectrum. As a result, one cannot directly compare results obtained from samples having very different molecular composition (e.g. metabolites in solutions vs tissue samples). Absolute quantification is possible, however, if an a priori calibration is available, under the same experimental conditions. We note that PEAKIT can be a helpful tool in the characterization of new CEST agents.

# Chapter 4

## Applications to the detection of low concentrated metabolites

This chapter presents the application of the ultrafast CEST-LS sequence combined with the PEAKIT analysis tool to the detection *in vivo* of a metabolite that was never detected before using CEST : carnosine and its derivatives anserine and homocarnosine. First their CEST responses are characterized *in vitro*. The detection of these metabolites is then demonstrated *in vivo*, in the skeletal muscle and in the brain. For comparison purposes, corresponding localized MR spectra as well as liquid chromatography–electrospray ionization–tandem mass spectrometer experiments are presented.

This work was published in Magnetic Resonance in Medicine under the following reference: [Bardin et al. 2022].

### Contents

---

<b>4.1 Carnosine and its derivatives: roles and bio-distribution</b>	<b>65</b>
<b>4.2 <i>In vitro</i> study</b>	<b>66</b>
4.2.1 Experimental protocol	66
4.2.2 Results	66
<b>4.3 <i>In vivo</i> study</b>	<b>68</b>
4.3.1 Experimental protocol	68
4.3.1.1 <i>In vivo</i> experiments: CEST-LS and MRS	68
4.3.1.2 Ex-vivo experiments: LC-ESI-MS/MS	69
4.3.2 Data analysis	69
4.3.2.1 CEST-LS	69
4.3.2.2 MRS	70
4.3.3 Results	70
4.3.3.1 Lower-leg skeletal muscle	70
4.3.3.2 Olfactory bulb	71
4.3.3.3 Neocortex	72
4.3.3.4 <i>In vivo</i> <sup>1</sup> H-NMR spectroscopy results	72
4.3.3.5 LC-ESI-MS/MS	73
<b>4.4 Conclusion, discussion and perspectives</b>	<b>74</b>



## 4.1 Carnosine and its derivatives: roles and bio-distribution

In the last ten years, CEST techniques have been widely applied to detect and map important metabolites such as glucose, glutamate and creatine. Yet, it remains challenging to investigate weaker CEST effects from less concentrated metabolites or metabolites with slow exchange rates. In this study, we focused our attention on carnosine, for which the CEST detection has only been reported *in vitro*. Bodet et al. ([Bodet et al. 2015]) have studied the CEST effect of carnosine in aqueous solutions (at a concentration of 50 mmol/L) and demonstrated that at 7 T, under physiological conditions (T=37°C, pH=7.1), carnosine can induce a CEST effect of about 1% ( $MTR_{asym}$ ) at approximately 3.1 ppm away from water.

Carnosine ( $\beta$ -alanyl-L-histidine) is a small endogenous dipeptide present in relatively high concentrations in several excitable tissues in mammals ([Alexander A Boldyrev, Aldini, and Derave 2013]). In particular, carnosine can be found in skeletal muscles (from 5 to 7 mmol/L in humans ([Krššák et al. 2021]) and 3 to 5 mmol/L in rats ([Aldini, Facino, et al. 2005])). In rodents, carnosine is present in the muscles together with a methylated derivative called anserine ( $\beta$ -alanyl-3-methylhistidine) whose concentration can reach even higher values ([Aldini, Facino, et al. 2005]). Relatively large amounts of carnosine have also been reported in the olfactory bulb ([Bonfanti et al. 1999]). In the rest of the brain, the concentration of carnosine decreases below 0.2 mmol/L but another carnosine derivative is also present, homocarnosine ( $\gamma$ -amino-butyryl-histidine) at slightly higher concentrations ( $\approx$  0.5 mmol/L in the rat brain ([O'Dowd et al. 1990]) and  $\approx$  0.3-0.4 mmol/L in the human brain ([Landheer et al. 2020])).

The chemical structures of all three derivatives are represented in Figure 4.1 As carnosine, both anserine and homocarnosine have a labile proton capable of generating CEST effect (the amide proton of the peptide bond). Compared to other metabolites, such as glutamate or glucose, the exchange rate of carnosine is one order of magnitude lower ([Bodet et al. 2015]), which limits the attainable signal amplification through CEST and makes its indirect detection *in vivo* more challenging.

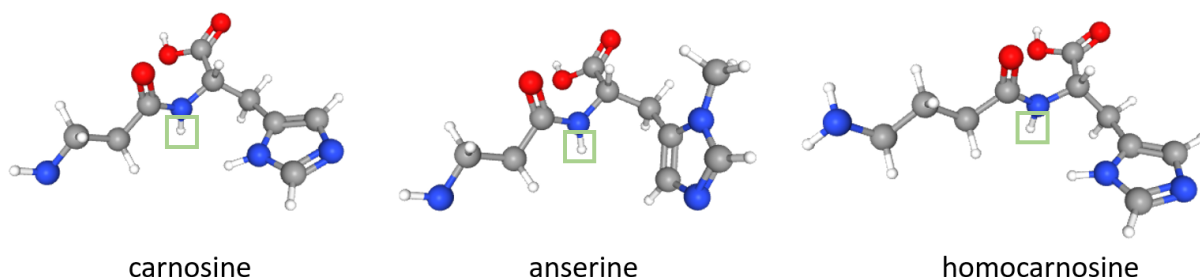


Figure 4.1: 3D representation of the chemical structure of carnosine, anserine and homocarnosine. The gray, blue, red and white spheres represented the carbon, nitrogen, oxygen and hydrogen atoms. The green squares show which protons are the labile protons detectable with CEST experiment.

Using the CEST-LS approach described in 3 in combination with an ultra-high magnetic

field (17.2 T), we demonstrate the detection of carnosine and its derivatives *in vivo*, in the brain and the skeletal muscle of healthy adult rats.

## 4.2 *In vitro* study

### 4.2.1 Experimental protocol

The phantom studied here is sample n° 11. During MR acquisitions, the syringe is maintained at 37 °C using a feedback controlled air heating system. For all CEST acquisitions, the saturation module consisted in 10 rectangular pulses of 400 ms duration, separated by a 0.01 ms delay. Z-spectra are acquired in a  $8 \times 9 \times 5 \text{ mm}^3$  ROI using saturation  $B_{1,sat}$  powers ranging between 0.15 and 1  $\mu\text{T}$ . Two different spectral resolutions are used: 0.03 ppm and 0.005 ppm, corresponding to ratios  $r$  of 0.05 and 0.01, respectively.

Single-voxel  $^1\text{H}$ -NMR spectra were additionally acquired from three distinct samples of 10 mM carnosine (sample n° 14), 10 mM anserine (sample n° 15) and 10 mM homocarnosine (sample n° 16) using LASER ([Garwood and DelaBarre 2001]) (TE/TR = 25/3000 ms, 128 averages, 8k spectral bandwidth, 4096 points) from  $2.5 \times 2.5 \times 2.5 \text{ mm}^3$  voxel.

### 4.2.2 Results

Figure 4.2 shows representative Z-spectra acquired on the mixture sample with  $B_{1,sat}$  of 0.15  $\mu\text{T}$  and spectral resolution 0.005 ppm (Figure 4.2A) and  $B_{1,sat}$  of 1  $\mu\text{T}$  and spectral resolution 0.03 ppm (Figure 4.2B). The very low  $B_{1,sat}$  of 0.15  $\mu\text{T}$  coupled with a very high spectral resolution (0.005 ppm) allows to accurately separate and detect the CEST effects of homocarnosine (hcar), carnosine (car) and anserine (ans) at  $3.20 \pm 0.01 \text{ ppm}$ ,  $3.31 \pm 0.01 \text{ ppm}$  and  $3.43 \pm 0.01 \text{ ppm}$ , respectively. These parameters do not, however, give satisfactory results *in vivo* due to the low contrast-to-noise ratio. Moreover, we aim at covering a range of frequencies sufficiently large to encompass reference peaks such as creatine or phosphocreatine, which sets a higher bound for the resolution at 0.03 ppm (see next section). Therefore, We used a  $B_{1,sat}$  value of 1  $\mu\text{T}$  and a spectral resolution equal or lower than 0.03 ppm for all *in vivo* acquisitions. Figure 4.2B shows the CEST-LS Z-spectrum obtained on the mixture sample with  $B_{1,sat}$  of 1  $\mu\text{T}$  and spectral resolution of 0.03 ppm. The lower spectral resolution and more intense saturation do not allow the separation of the CEST contrasts from the three peptides. Thus, we conclude that the contributions of carnosine, anserine and homocarnosine can not be separated *in vivo* at 17.2 T (and at lower magnetic fields).

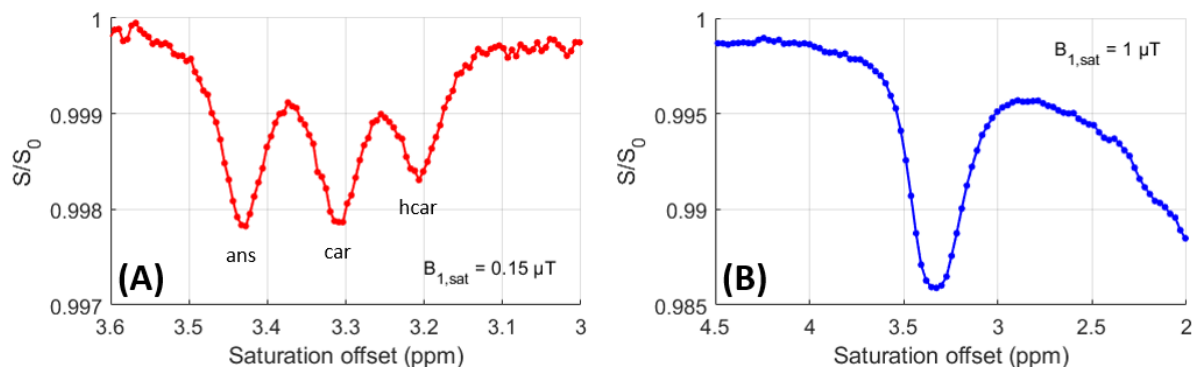


Figure 4.2: CEST-LS results on sample n° 11 containing anserine, carnosine and homocarnosine. (A) CEST-LS Z-spectrum obtained with  $B_{1,sat} = 0.15 \mu T$  and a resolution of 0.005 ppm. Homocarnosine, carnosine and anserine peaks are clearly visible and distinct. (B) CEST-LS Z-spectrum obtained with  $B_{1,sat} = 1 \mu T$  and a resolution of 0.03 ppm. The Z-spectra in A and B were averaged over 10 and 18 repetitions, respectively. We note that in [Bodet et al. 2015], the CEST effect of carnosine was reported at 3.1 ppm which is slightly different from our results. This is most likely due to slight differences in pH.

The model  $^1H$ -NMR spectra (Figure ??) of homocarnosine, carnosine and anserine were simulated by considering the histidine and alanine resonances for carnosine and anserine and by considering the histidine and GABA resonances for homocarnosine. The model  $^1H$ -NMR spectra were obtained after adapting the parameters (chemical shift and J-coupling constants) of histidine, alanine and GABA so that the spectra would fit the *in vitro* data. The initial parameters were taken from [Govindaraju, Young, and Maudsley 2000; Govind, Young, and Maudsley 2015]. These data were then used to establish the basis for the *in vivo* data.

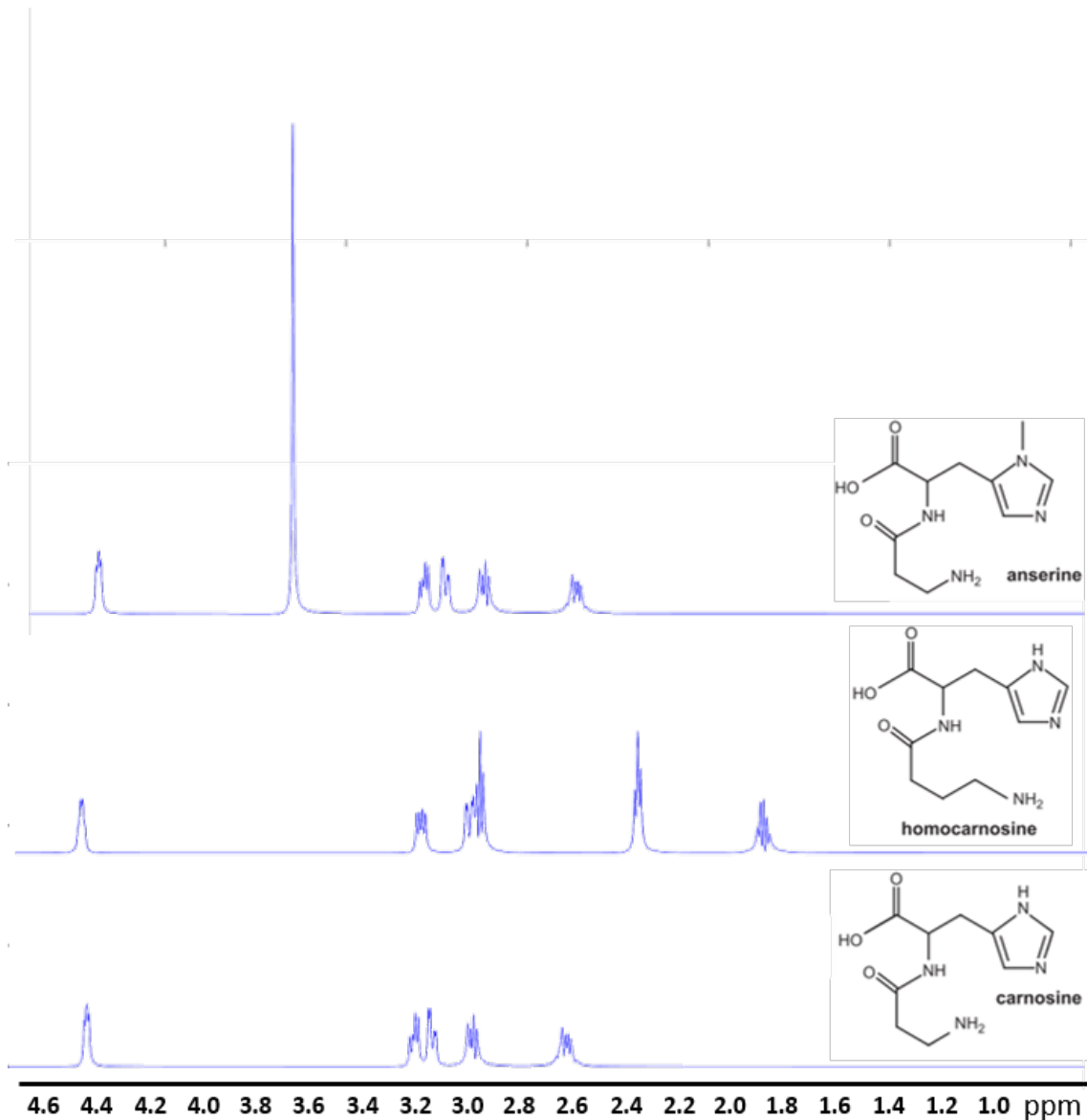


Figure 4.3: Model  $^1\text{H}$ -NMR spectra of homocarnosine, carnosine and anserine

## 4.3 *In vivo* study

### 4.3.1 Experimental protocol

Eight male adult Dark Agouti rats were used in this study. This strain has been selected because Agouti rats are known to present higher amounts of carnosine and anserine ([Alexander A Boldyrev, Aldini, and Derave 2013]).

#### 4.3.1.1 *In vivo* experiments: CEST-LS and MRS

At the start of each exam, an anatomical T2-weighted reference image was acquired to guide the positioning of the CEST-LS ROI (Figures 4.4A, 4.5A and 4.6A). Local  $B_0$  shimming was performed prior to the CEST-LS acquisitions using an automatic shimming routine. All CEST-LS data were acquired with the following parameters: TE/TR= 3/8000 ms (with negligible T1- or

T2\* -weightings) and a saturation power of 1  $\mu$ T, with a saturation module of 10 rectangular pulses of 400 ms duration, separated by a 0.01 ms delay. Other parameters varied depending on the investigated region and are detailed in Table 4.1. Eighty repetitions (pairs of CEST-LS datasets with and without saturation) were acquired to increase the SNR for a total acquisition time of 21m20 s.

	muscle		olfactory bulb		neocortex	
CEST-LS ROI dimension (mm <sup>3</sup> )	9 × 4 × 2		4 × 1.8 × 2.5		7 × 3 × 2	
Z-spectrum	full	zoom	full	zoom	full	zoom
ratio $r$	0.15	0.05	0.15	0.07	0.15	0.07
saturation range (ppm)	10.3	3.4	10.3	4.8	10.3	4.8
spectral resolution after zero-filling (ppm)	0.08	0.03	0.08	0.04	0.08	0.04

Table 4.1: Parameters used for *in vivo* Z-spectra generated with CEST-LS.  $r$  is the ratio between the saturation gradient  $G_{sat}$  and the acquisition gradient  $G_{acq}$ . Please note that the spectral resolution is given after zero-filling with a factor of 2. In the manuscript, only zero-filled data are shown, and zero-filled spectral resolutions are given.

Additionally, single-voxel <sup>1</sup>H-NMR spectra were acquired using LASER ([Garwood and DelaBarre 2001]) (TE/TR = 25/3000 ms, 128 to 512 averages, 8 kHz acquisition bandwidth, 4096 points) from 8 to 16  $\mu$ L voxel placed at the center of the CEST-LS ROI (Figure 4.4A). Water suppression was achieved using VAPOR ([Tkáč et al. 1999]).

#### 4.3.1.2 Ex-vivo experiments: LC-ESI-MS/MS

After all MRI experiments, the animals were sacrificed and tissue samples were extracted, frozen and subsequently sent to our collaborators Giancarlo Aldini and his team (Department of Pharmaceutical Sciences, University of Milan) who performed LC-ESI-MS (Liquid Chromatography - ElectroSpray Ionization - Mass Spectrometry). More details about the methods and the analysis can be found in Reference [Bardin et al. 2022].

### 4.3.2 Data analysis

#### 4.3.2.1 CEST-LS

The CEST-LS data were analyzed according to 3.2.3. As 64 FID data points are acquired, the zero-filling step doubles this number to 128 points. For high resolution Z-spectra, not covering the water peak, the chemical shift correction was performed using other known, major peaks: phosphocreatine at 2.6 ppm in the muscle and creatine at 2 ppm in the olfactory bulb and neocortex.

The *in vivo* Z-spectra were further analyzed using the analysis tool PEAKIT described in 3 which is able to detect, calculate heights and areas and evaluate the statistical significance of CEST peaks. For the skeletal muscle, only the significance of the "carnosine + anserine" peak was assessed while for the olfactory bulb and cortex, the areas of the "carnosine + homocarnosine" and APT peaks were determined. The area of the APT peak was calculated over

a range of 2.8 ppm and centered on the peak maximum, as found by PEAKIT. For the "carnosine + homocarnosine" peak, the range for area calculation was automatically selected by PEAKIT.

#### 4.3.2.2 MRS

Following removal of the residual water signal using the Hankel Lanczos singular value decomposition (HLSVD) algorithm, *in vivo*  $^1\text{H}$ -NMR spectra were processed over the [0.5 - 9] ppm range using LCMoDel 6.2 ([Provencher 1993]). Metabolic profiles from the rat brain were decomposed along a basis set of 21+2 metabolites (the addition corresponding to carnosine and homocarnosine) to which was added 4 groups of macromolecular resonances as detailed in Lopez et al. ([Lopez-Kolkovsky, Sebastien Mériaux, and Boumezbeur 2016]). For the skeletal muscle, the basis set was composed of 11 model spectra (Cr, PCr, Taurine, Glycerol, Alanine, Lactate, Glucose, Carnitine, Acetyl-Carnitine, Carnosine and Anserine) to which was added few Gaussian functions to fit the intra- (IML) and extra-myocellular lipids (EML) ([Krššák et al. 2021]). The basis set of model spectra were simulated using a spin simulation software implemented in Matlab (SpinWizard developed by R.A de Graaf) and based on the density matrix formalism. The chemical shifts and coupling constants were extracted or adapted from those proposed by Govindaraju et al. in [Govindaraju, Young, and Maudsley 2000]. The histidine peaks were estimated separately from the alanine and GABA peaks since they are arguably common to anserine, carnosine and homocarnosine. A constraint was added to the LCMoDel parameters (in the control file) to match the sum of the areas/concentrations of the alanine and GABA resonances to those of the histidine resonances. The decision to separate the fit of the histidine resonances was motivated by their large sensitivity to pH ([Bodet et al. 2015]). Thus, it was easier for LCMoDel to detect and estimate those resonances in a predetermined range of chemical shifts values.

### 4.3.3 Results

#### 4.3.3.1 Lower-leg skeletal muscle

The position of the CEST-LS acquisition is depicted by the orange ROI shown on the anatomical image of a rat lower-leg in Figure 4.4A. Figure 4.4B shows an example of a Z-spectrum (spectral resolution 0.08 ppm) acquired in the orange rectangle in Figure 4.4A, in which we can recognize the creatine (Cr) and phosphocreatine (PCr) CEST peaks on the left, as well as a broad peak corresponding to the NOE effect from aliphatic protons (Nuclear Overhauser Enhancement) on the right. Figure 4.4C shows a higher spectral resolution Z-spectrum (0.03 ppm resolution) which was acquired using a weaker CEST saturation gradient ( $r=0.05$  vs 0.15). The Cr and PCr peaks are more evident at higher spectral resolution. Moreover, two additional peaks corresponding to the combination of carnosine and anserine at  $3.32 \pm 0.06$  ppm and APT at  $3.5 \pm 0.06$  ppm are also visible.

Similar results were obtained on four different animals. The analyses performed with PEAKIT confirmed the significance of all "carnosine + anserine" peaks ( $p < 0.05$ ).

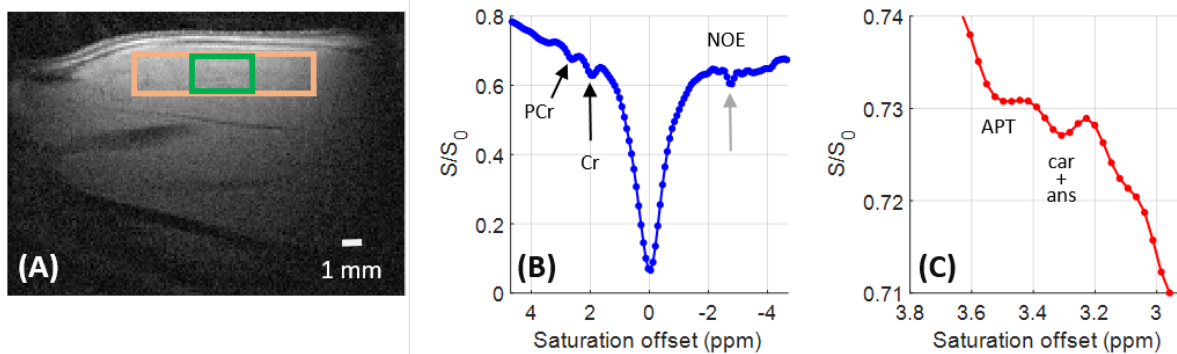


Figure 4.4: CEST-LS results on a rat leg skeletal muscle (A) Anatomical image of a rat lower-leg muscle showing the ROI used for CEST-LS in orange and the voxel for  $^1\text{H}$ -NMR spectroscopy in green. (B) Low resolution Z-spectrum showing the Creatine (Cr) and PhosphoCreatine (PCr). The sharp peak indicated by a gray arrow at -2.7 ppm corresponds to fat ([Triplett et al. 2014]) (C) Zoom showing combined car + ans and APT peaks. All Z-spectra were acquired with  $B_{1,sat}=1 \mu\text{T}$ .

#### 4.3.3.2 Olfactory bulb

As the olfactory bulb is a relatively small region, the ROIs chosen for the CEST-LS acquisitions were smaller than those selected in the leg (Figure 4.5A and Table 1). The Z-spectrum in Figure 4.5B shows clearly a peak at 2 ppm, as well as a shoulder at 2.6 ppm corresponding to Cr and PCr, respectively. By increasing the spectral resolution to 0.04 ppm (Figure 4.5C), we put in evidence the APT peak at 3.5 ppm. Close to it, the "carnosine + homocarnosine" peak is recognizable. Note that the spectral resolution for the Z-spectrum in Figure 4.5C was slightly lower than for the leg muscle to compensate for the lower signal-to-noise ratio due to the smaller ROI size. Similar results were obtained in four animals with the significance for the "carnosine + homocarnosine" peak confirmed by PEAKIT ( $p < 0.05$ ). The average ratio of the carnosine to the APT peak areas was estimated at  $0.51 \pm 0.31$ .

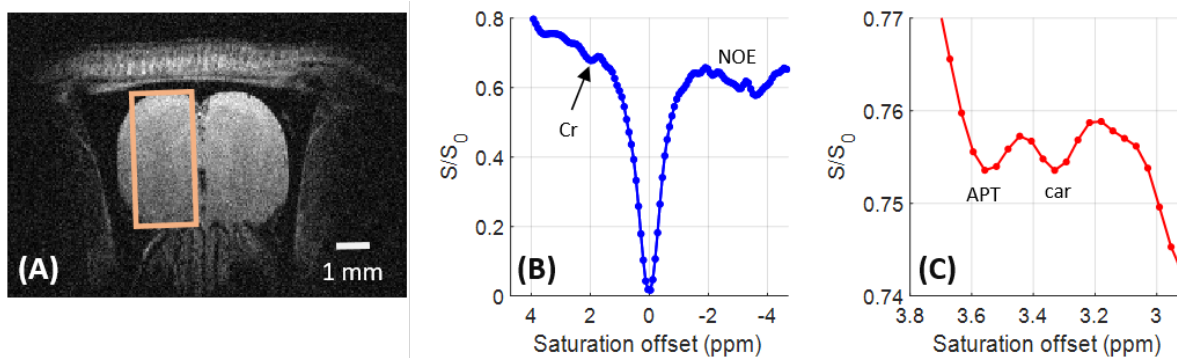


Figure 4.5: CEST-LS results on a rat olfactory bulb. (A) Anatomical image of a rat olfactory bulb showing the ROI used for the CEST-LS acquisitions (B) Low resolution Z-spectrum showing the Cr peak (C) High resolution Z-spectrum showing car and APT peaks. All Z-spectra were acquired with  $B_{1,sat}=1 \mu\text{T}$ .

### 4.3.3.3 Neocortex

Finally, the last set of experiments was performed in the neocortex. Despite an expectedly lower content in histidine dipeptides ([Aldini, Facino, et al. 2005]), the larger size of this brain structure and the better  $B_0$  homogeneity compared to the olfactory bulb are beneficial to the SNR of these experiments. From the low resolution Z-spectrum (Figure 4.6B) acquired in the orange ROI (Figure 4.6A), we can recognize the 2 ppm Cr peak ([Cai, Singh, et al. 2015]). The zoom on the high resolution Z-spectrum (4.6B) shows a broad APT peak as well as a local decrease around 3.2 ppm which corresponds to the CEST contribution of homocarnosine. The homocarnosine peaks are detected with a p-value below 0.05 using PEAKIT for all four animals scanned. The average ratio of the homocarnosine to the APT peak areas is found to be  $0.21 \pm 0.06$ , which is 2.4 times lower than the carnosine/APT ratio found in the olfactory bulb.

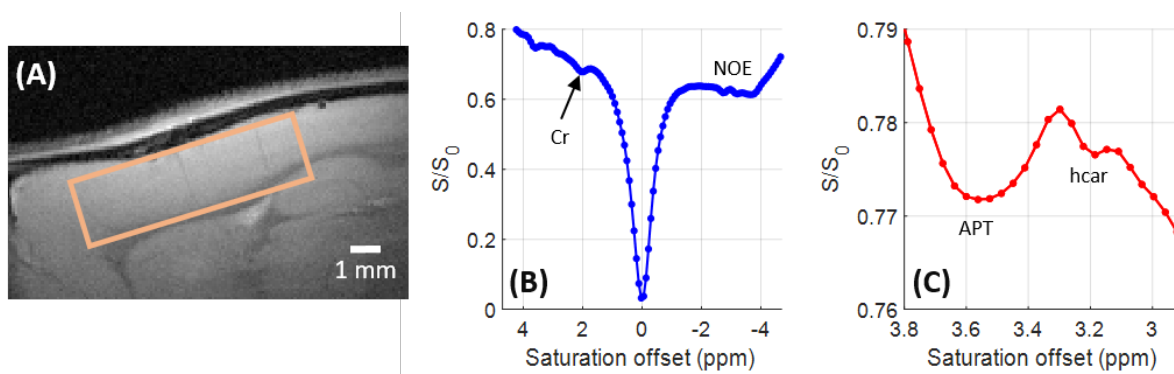


Figure 4.6: CEST-LS results on a rat neocortex (A) Anatomical image of a rat neocortex showing the ROI used for the CEST-LS acquisitions. (B) Low resolution Z-spectrum showing the Cr peak. (C) High resolution Z-spectrum showing the hcar and APT peaks. All Z-spectra were acquired with  $B_{1,sat} = 1 \mu T$ .

### 4.3.3.4 *In vivo* $^1H$ -NMR spectroscopy results

The  $^1H$ -NMR spectra of carnosine and carnosine derivatives samples show two distinct resonances downfield from water at about 7.08 and 8.08 ppm, corresponding to the C4 and C2 histidine-imidazole protons, respectively. These two resonances are easily identifiable on the spectrum in Figure 4.7, which was obtained in the green voxel showed in Figure 4.4A, confirming the presence of carnosine and anserine (whose methyl resonance can be appreciated at 3.74 ppm) in the leg skeletal muscle. From the decomposition of the  $^1H$ -NMR spectra using the LCMoDel ([Provencher 1993]), we estimate an average (N=4 animals) of total carnosine concentration of  $(8.4 \pm 0.5)$  mmol/L considering a Cr+PCr concentration of 38 mmol/L.

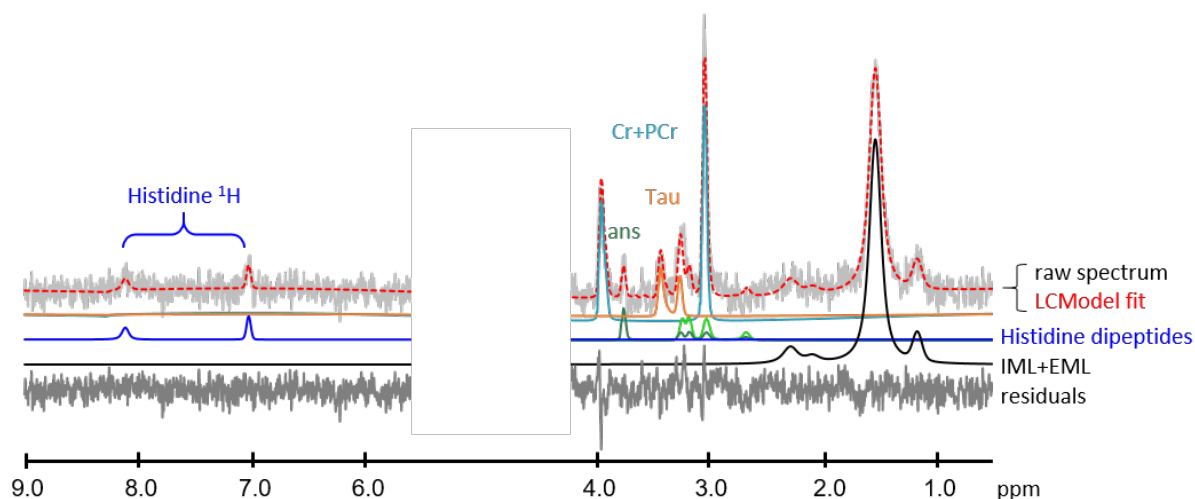


Figure 4.7: *In vivo* NMR spectrum acquired on a  $3 \times 1.8 \times 1.5 \text{ mm}^3$  voxel in the leg skeletal muscle (green box in Figure 4.4A). Peaks at approximately 7.08 and 8.08 ppm are the signature of both carnosine and anserine (labelled Histidine dipeptides and represented in blue) while the peak at 3.7 ppm is proper to anserine (dark green). The light green line on the right represents carnosine.

For the olfactory bulb and the neocortex,  $^1\text{H}$ -MRS did not allow the reliable (Cramer-Rao lower bounds above 30%) detection of neither carnosine nor homocarnosine. The heterogeneity and the small size of the olfactory bulb as well as the low concentration expected in the neocortex may explain why we were below the limit of detection in both cases.

#### 4.3.3.5 LC-ESI-MS/MS

Table 4.2 reports the mean  $\pm$  SD of carnosine, anserine and homocarnosine in the rat tissues. Anserine is the most abundant histidine dipeptide in skeletal muscle, with a concentration of almost 36% higher than carnosine while homocarnosine is not detected. The olfactory bulb contains only carnosine while anserine and homocarnosine are both undetectable. Homocarnosine was the most abundant histidine dipeptide in the brain with a content about three time higher than that of carnosine while anserine was not detected. Table 4.2 also reports the total amount of histidine dipeptides calculated as the sum of "carnosine + anserine + homocarnosine". The skeletal muscle is the tissue characterized by the highest amount of histidine dipeptides with a content almost 13 and 25 folds higher than that of the bulb and brain, respectively.

	concentration (nmoles/g of wet tissue)			
	carnosine	anserine	homocarnosine	histidine dipeptides
Muscle	$2262.2 \pm 1254.7$	$3518.5 \pm 774.6$	N.D.	5780
Olfactory bulb	$447.5 \pm 116.0$	N.D.	N.D.	447.5
Brain	$55.7 \pm 18.4$	N.D.	$168.9 \pm 39.9$	224.6

Table 4.2: Carnosine, anserine, homocarnosine and total histidine dipeptides concentrations found in the muscle, olfactory bulb and brain. The values are averaged over four rats and reported as nmoles of dipeptide per gram of wet tissue  $\pm$  SD. N.D. = not detected

## 4.4 Conclusion, discussion and perspectives

In this study, we demonstrated the *in vivo* detection of carnosine and its derivatives in rats using chemical exchange saturation transfer. This was accomplished by using the CEST-LS sequence in combination with an ultra-high magnetic field (17.2 T) imaging system. The characterization of the CEST effect was performed using the PEAKIT software, which makes a local estimation of the baseline and therefore reduces the contamination from other broad CEST signals (e.g. taurine, glutamine, glutamate in the brain ([Khlebnikov, Kemp, et al. 2019])) improving the detection selectivity of the technique. We cannot however, completely exclude any signal contamination from other metabolites or peptides if present. The presence of carnosine and derivatives was validated in the leg with *in vivo*  $^1\text{H}$ -NMR spectroscopy but it was not possible to be conclusive for the olfactory bulb and the neocortex experiments. This confirms that, under our experimental conditions, CEST is a more sensitive approach than localized MRS.

Moreover, by optimizing the CEST-LS acquisition parameters we were able to disentangle the contributions of carnosine, anserine and homocarnosine in a phantom sample. This was, however, not possible *in vivo* due to the low CEST effects that would have been achieved if such a low saturation power (0.15  $\mu\text{T}$ ) had been used and the presence of other CEST contributions.

The LC-ESI-MS/MS quantification of carnosine, anserine and homocarnosine reports a content of histidine dipetides of more than 13 and 25 times higher in the skeletal muscle than in the olfactory bulb and brain, respectively. These data explain well the  $^1\text{H}$ -MRS results and in particular the fact that it was not able to detect reliably these peptides in the olfactory bulb and neocortex. According to the LC-ESI-MS/MS analysis the concentration of carnosine in the olfactory bulb is approximately 2.6 times higher than the homocarnosine concentration found in the rest of the brain. These results are in agreement with CEST-LS data, which, taking into account the area ratio carnosine/APT for the olfactory bulb and homocarnosine/APT for the neocortex as an index of the relative histidine dipeptide content indicate a 2.4 times higher concentration in the olfactory bulb.

Even though some of its physiological functions are still being investigated, it has been clearly established that carnosine presents direct and indirect antioxidant activity through its ability to scavenge free radicals ([Kohen 1988; A. Boldyrev et al. 1988]), inhibit protein carbonylation and glycoxidation ([Hipkiss 2011; Aldini, Courten, et al. 2020]), and chelate metallic ions ([Brown, Schroeder, and Ferris 1979]). Carnosine was suggested to be involved in various biochemical processes, including pH-buffering in the muscle ([R. C. Harris et al. 2006]) and  $\text{Ca}^{2+}$  regulation ([Dutka et al. 2012]). Tiedje and colleagues ([Tiedje et al. 2010]) have also presented carnosine as an important neurotransmitter in the olfactory bulb. Homocarnosine is seen in long range projecting GABAergic neurons ([Kish, Perry, and Hansen 1979]) and appears to possess anticonvulsant properties as well as to play a role in modulating cortical excitability ([Petroff and Anne Williamson 2009; A. Williamson, Petroff, and Spencer 2007]).

Despite this, there are very few human study reporting homocarnosine/carnosine detection using *in vivo* MRS ([Vermathen, Capizzano, and Maudsley 2000; Solis et al. 2015; Landheer et al. 2020; Rothman, Behar, et al. 1997]) and, to our knowledge, none using CEST. This

is nevertheless due to the low concentrations at which these metabolites are present in the brain.

While the CEST-linescan strategy presented here offers the great advantage of being minimally affected by temporal variations in frequency, temperature or physiological parameters, it has as main limitation the local nature of the detection. It should be noted, however, that the technique does not require a homogeneous sample along the gradient direction for accurate local measurements, as the signal is normalized by the reference signal at each position acquired in the absence of saturation. This normalization procedure also makes the CEST-LS technique less susceptible to  $B_0$  inhomogeneities compared to standard CEST approaches. In the current study, we used the water peak or other known CEST peaks to find the chemical shift offset of the peaks under study. The precision of such referencing can be affected by large  $B_0$  fluctuations, which can however be corrected by acquiring a  $B_0$  map in the CEST-LS ROI. The implementation of such correction step is underway.

We note that a similar approach, ultrafast localized CEST-spectroscopy with PRESS (UCEPR) ([Z. Liu et al. 2016]), has been previously used for performing CEST acquisitions in the human brain at 3 T. Compared to UCEPR, our CEST-LS approach offers more flexibility in the choice of the acquisition parameters, allowing for shorter echo times.

In conclusion, the CEST-LS sequence was found to be a reliable option to acquire Z-spectra without being impacted by temperature variations and opens the door to the robust CEST detection of other low-concentrated metabolites with slow exchange rates.



# Chapter 5

## Applications to the detection of transient metabolic changes during neuronal activation

This chapter presents the development of a CEST-based functional MRI strategy and protocol aimed at assessing transient metabolic changes related to neuronal activation. After a short introduction, a preliminary evaluation is performed in the rat brain of the metabolic changes induced by a pH decrease caused by hypercapnia. Next, acquisition and processing strategies for detecting metabolic changes induced by neuronal activity using CEST MR are considered. An experimental protocol involving a CEST sequence called CEST-LS grad<sub>opp</sub> that was directly modified and adapted from the CEST-LS sequence previously presented is proposed and implemented. Finally, the results of this experiment are presented and discussed.

### Contents

---

<b>5.1 State-of-the-art</b>	<b>79</b>
5.1.0.1 CEST changes induced by hypercapnia	79
5.1.0.2 CEST changes induced by neuronal activation	79
<b>5.2 Assessment of CEST changes due to a controlled pH decrease</b>	<b>80</b>
5.2.1 Experimental protocol	80
5.2.1.1 Sequence update and parameters	80
5.2.1.2 Hypercapnia	81
5.2.1.3 Processing	81
5.2.2 Results	81
5.2.2.1 Global water signal changes	81
5.2.2.2 Evolution of the amine and amide CEST contributions	83
<b>5.3 Modification of the CEST-LS sequence and acquisition strategy to minimize BOLD confound</b>	<b>84</b>
5.3.1 Challenge of CEST detection in the context of neuronal activity	84
5.3.1.1 Reducing BOLD signal using a SE readout module	85
5.3.1.2 Eliminating the remaining BOLD signal with a different acquisition strategy	86

*CHAPTER 5. APPLICATIONS TO THE DETECTION OF TRANSIENT METABOLIC  
CHANGES DURING NEURONAL ACTIVATION*

---

5.3.2	Presentation of the principle of the $\text{grad}_{\text{opp}}$ CEST-LS sequence . . . . .	86
5.3.3	Summary . . . . .	89
5.3.4	Convention and graphical codes . . . . .	89
<b>5.4</b>	<b>Experimental protocols . . . . .</b>	<b>89</b>
5.4.1	Neuronal activation induced by forepaw electrical stimulation . . . . .	90
5.4.1.1	Methods . . . . .	90
5.4.1.2	Activation example . . . . .	90
5.4.2	CEST-LS $\text{grad}_{\text{opp}}$ implementation . . . . .	91
5.4.2.1	Positioning . . . . .	91
5.4.2.2	CEST-LS $\text{grad}_{\text{opp}}$ adjustment scans . . . . .	91
5.4.2.3	CEST-LS $\text{grad}_{\text{opp}}$ and activation . . . . .	94
5.4.2.4	CEST-LS $\text{grad}_{\text{opp}}$ stimulation protocols . . . . .	96
5.4.3	Processing . . . . .	99
<b>5.5</b>	<b>Results . . . . .</b>	<b>99</b>
5.5.1	Results for experiment 1.1 and 1.2 . . . . .	100
5.5.2	Experiment 2 . . . . .	105
5.5.3	Conclusion . . . . .	107

---

## 5.1 State-of-the-art

### 5.1.0.1 CEST changes induced by hypercapnia

Hypercapnia is known to cause a reduction of the cerebral intracellular pH ([Martoft et al. 2003]). Some studies have already shown the possibility to detect pH variations caused by hypercapnia using CrCEST ([L. Chen et al. 2021]). According to the results of [Nishimura et al. 1989], a hypercapnia experiment can cause a decrease of 0.1 pH unit, which would approximately result in the exchange rate being multiplied by a factor of 0.8, according to:

$$k(pH_{ref} - 0.1) = k(pH_{ref}) \times 10^{-0.1} \quad (5.1)$$

### 5.1.0.2 CEST changes induced by neuronal activation

Blood Oxygen Level Dependent (BOLD) fMRI is the most widely used method for studying human brain activity, it detects cerebral brain activity based on the neuro-vascular coupling by measuring the changes in the blood flow oxygenation level ([Ogawa, Tank, et al. 1992; Ogawa, Tank, et al. 1992; Logothetis 2008; K. L. Davis et al. 2002]). In addition to blood flow changes, other modalities such as fMRS and diffusion-weighted fMRI have also shown that activated neurons induce few transient metabolic ([Mangia, Giove, et al. 2009]) and structural changes ([H. Lu and Zijl 2012; Le Bihan 2003]).

In particular, fMRS studies have reported decreased glucose levels with neuronal activation that could be linked to increased local glucose consumption rate ([W. Chen et al. 1993; Hyder et al. 1997]). Changes in Glutamate, Aspartate ([Mangia, Tkáč, et al. 2007]) and PCr to Cr ratio ([Just and Faber 2019]) during neuronal activation have also been reported. Just et al. demonstrated using fMRS that upon electrical forepaw stimulation the glutamate levels significantly increased by 9.9% in the rat brain. Moreover, a significant decrease of 30 in the PCr to Cr ratio (which is linked to the ATP to Pi ratio via the creatine kinase reaction) was also observed during activation.

Previously, Mangia et al. had observed at 7T in the human visual cortex a 3% increase in glutamate, a 23 – 30% increase in lactate levels, accompanied by concomitant –15 – 16% decreases in Aspartate and Glucose levels ([Mangia, Tkáč, et al. 2007; Bednarik et al. 2015]). These fMRS observations are all consistent with a mostly aerobic increase in energy metabolism (as evidenced by the Glu and Asp changes probably mediated by the mitochondrial aspartate transaminase reaction coupled to the tricarboxylic or Krebs cycle). Depending on the intensity and length of the neuronal stimulation, Lactate accumulates due to the transient anaerobic glycolysis taking place between neurons and astrocytes as hypothesized by Magistretti and Pellerin with the Astrocyte-neuron lactate shuttle (ANLS) ([Pellerin and Magistretti 1994]).

Interestingly, the concentration changes observed by Mangia et al. were all estimated to correspond to approximately 0.2 – 0.3 mmol/L ([Mangia, Tkáč, et al. 2007; Bednarik et al. 2015]). Detecting such minute changes in concentration requires ideal conditions starting with high or ultra high magnetic fields, optimal and very stable stimulation and acquisition protocols, as well as precise spectral analysis and quantification (accounting properly for the BOLD effect).

In this challenging context, it would be of great interest to dispose of an intrinsically more stable, more sensitive approach to investigate metabolic modulations related to focused neuronal activity. This could enable the study of more local, less intense stimuli compared to those previous fMRS studies.

Therefore, this chapter explores the possibility to use CEST based sequences to detect eventual metabolic changes induced by neuronal activation in rat brains at 17.2 T. The use of CEST to detect brain functional metabolic changes has been proposed in [Roussel et al. 2019; Khlebnikov, Siero, et al. 2018], but its practicality remains to be demonstrated. Acquiring CEST images typically requires long repetition times in order to accommodate adequate saturation times. Moreover, monitoring multiple metabolites simultaneously implies saturating at several different frequencies increasing even further the acquisition time. Beyond these considerations, it is not straightforward to detect functional CEST metabolic changes as they are overpowered by the much stronger BOLD signal. The authors of [Khlebnikov, Siero, et al. 2018] acquired 3D APT-CEST volumes to detect brain pH changes in response to visual stimulation but were limited by the confounding BOLD effect. By performing numerical simulations, Roussel et al. ([Roussel et al. 2019]) have designed the optimal acquisition and processing pipeline to minimize/eliminate BOLD from the GlucoCEST signal and have successfully observed decreased in glucose CEST contrast during electrical forepaw stimulation in rats.

Compared to this initial effort using GlucoCEST, the CEST-LS sequence described in section offers the possibility to acquire metabolic information over a large saturation offset range within only two TRs, which gives the possibility to monitor simultaneously several CEST contributions.

## 5.2 Assessment of CEST changes due to a controlled pH decrease

In this section, the CEST-LS sequence was used to evaluate *in vivo* the metabolic changes detectable using CEST MR over a wide spectral range (Z-spectrum spanning from -5 to 5ppm) following a pH decrease induced by controlled hypercapnia. Several CEST contributions, including amine (2.7-2.8 ppm) and Amide Proton Transfer (APT, 3.5 ppm), were analyzed. In this manuscript, this approach was considered as a first step towards the development of a strategy for detecting neuronal activity induced metabolic changes devoid as much as possible from confounding BOLD effects.

### 5.2.1 Experimental protocol

#### 5.2.1.1 Sequence update and parameters

Anatomical T2-weighted reference images of the rat brain were acquired using a 2D-RARE sequence (in-plane resolution  $80 \times 80 \mu\text{m}^2$ , slice thickness 1 mm). CEST-LS acquisitions (TE/TR=5/2500 ms) were performed on a voxel ( $6 \times 3 \times 2 \text{ mm}^3$ ) positioned in the cortex close to the surface coil. The saturation module consisted of  $10 \times 100$  ms Gaussian pulses with peak amplitude  $B_{1,sat} = 0.8 \mu\text{T}$ , 64 offsets from -5 to 5 ppm corresponding to  $r = 0.15$ , and

80 repetitions (40 pairs of saturated /reference profiles). The CEST-LS sequence used for this experiment was the same than the one presented in section 3.2.3 except for the pulse shape that was changed to Gaussian pulses instead of rectangular pulses. Thanks to their narrower spectral bandwidth, these pulses allow a more selective saturation and therefore minimize line-broadening along the Z-spectrum. Moreover, instead of having a cycle of 8 repetitions with the saturation module turned on and then off, the saturation module was alternatively turned on and off every repetition as shown in Figure 5.1. This was made in order to improve the time resolution of the Z-spectrum acquisition.

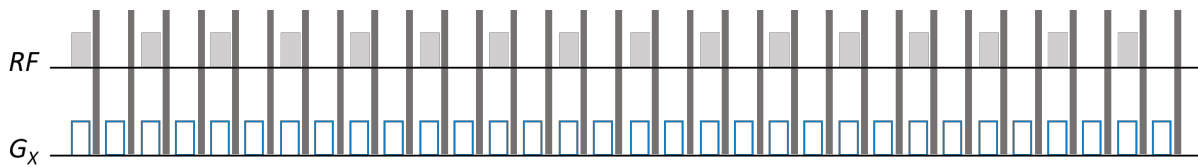


Figure 5.1: CEST-LS sequence with the saturation module alternatively turned on and off. This representation of the CEST-LS sequence is based on the simplified pulse sequence shown in Figure 3.12. In this example, 32 profiles (16 positive and 16 negative) are acquired in total.

### 5.2.1.2 Hypercapnia

As summarized in Table 5.1, three first CEST-LS scans were acquired under pure O<sub>2</sub> and 1.5% isoflurane, the CO<sub>2</sub> level was then raised to 30% and the isoflurane was lowered to 1%. After 5 minutes, three CEST-LS scans were acquired in the established presence of CO<sub>2</sub>. After restoring the initial situation and another 5 minutes break, three last CEST-LS acquisitions were performed. The experiment was performed on three animals.

Nscans	O <sub>2</sub> (%)	CO <sub>2</sub> (%)	isoflurane (%)
3	98.5	-	1.5
3	69	30	1
3	98.5	-	1.5

Table 5.1: Hypercapnia protocol

### 5.2.1.3 Processing

The data were processed as explained in the section 3.2.3 except that the ratio was computed between a saturated and its consecutive reference profile. The data were then averaged over the different time periods (before, during and after CO<sub>2</sub> administration). The Offset<sub>center</sub> introduced in Equation 3.3 was equal to zero since the Z-spectrum had to be centered on the water peak. Only the geometrical offset (Eq. 3.2) had to be compensated for (Offset<sub>user</sub> = Offset<sub>center</sub>).

## 5.2.2 Results

### 5.2.2.1 Global water signal changes

Figure 5.2B presents the *in vivo* Z-spectra obtained in the rat cortex using a CEST-LS sequence (voxel position depicted in Figure 5.2A). In Figure 5.2B, the APT, amine, creatine

([Cai, Singh, et al. 2015]) CEST contributions as well as the NOE (Nuclear Overhauser Enhancement) contrast (on the right) can be recognized.

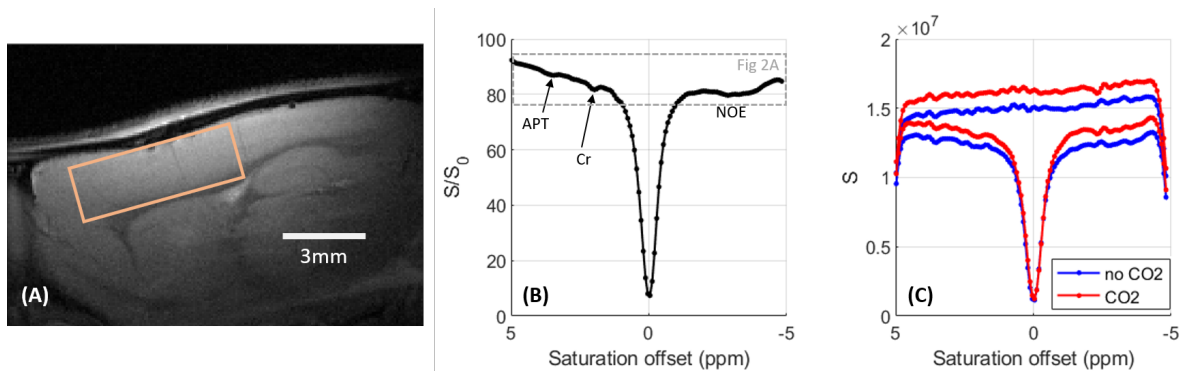


Figure 5.2: Influence of the  $\text{CO}_2$  administration on the profiles baseline (A) Anatomical image of a rat brain and position of the voxel used for CEST-LS acquisitions (B) Z-spectrum obtained with CEST-LS showing the APT, creatine and NOE (C) Saturated and reference profiles with (red) and without  $\text{CO}_2$  (blue)

Before analyzing individual CEST contributions, the reference and saturated profiles with and without administration of  $\text{CO}_2$  were compared. As presented in Figure 5.2C, both profiles show a higher signal under  $\text{CO}_2$  administration due to increased cerebral perfusion. The signal is even higher for the reference profile than for the saturated one in the downfield region (0-5ppm), explaining why the baseline is globally lower during  $\text{CO}_2$  administration in this region. The opposite effect is observed upfield where the baseline of the Z-spectrum is slightly higher with  $\text{CO}_2$ . Therefore simply comparing the Z-spectra under different conditions (Figure 5.3A) can not reflect strictly metabolic changes as they would be overpowered by global signal modifications. To a lesser extent, such a situation could be encountered when performing task-based fMRI studies due to local increase in the MR signal. Alternative processing strategies must therefore be employed.

### 5.2.2.2 Evolution of the amine and amide CEST contributions

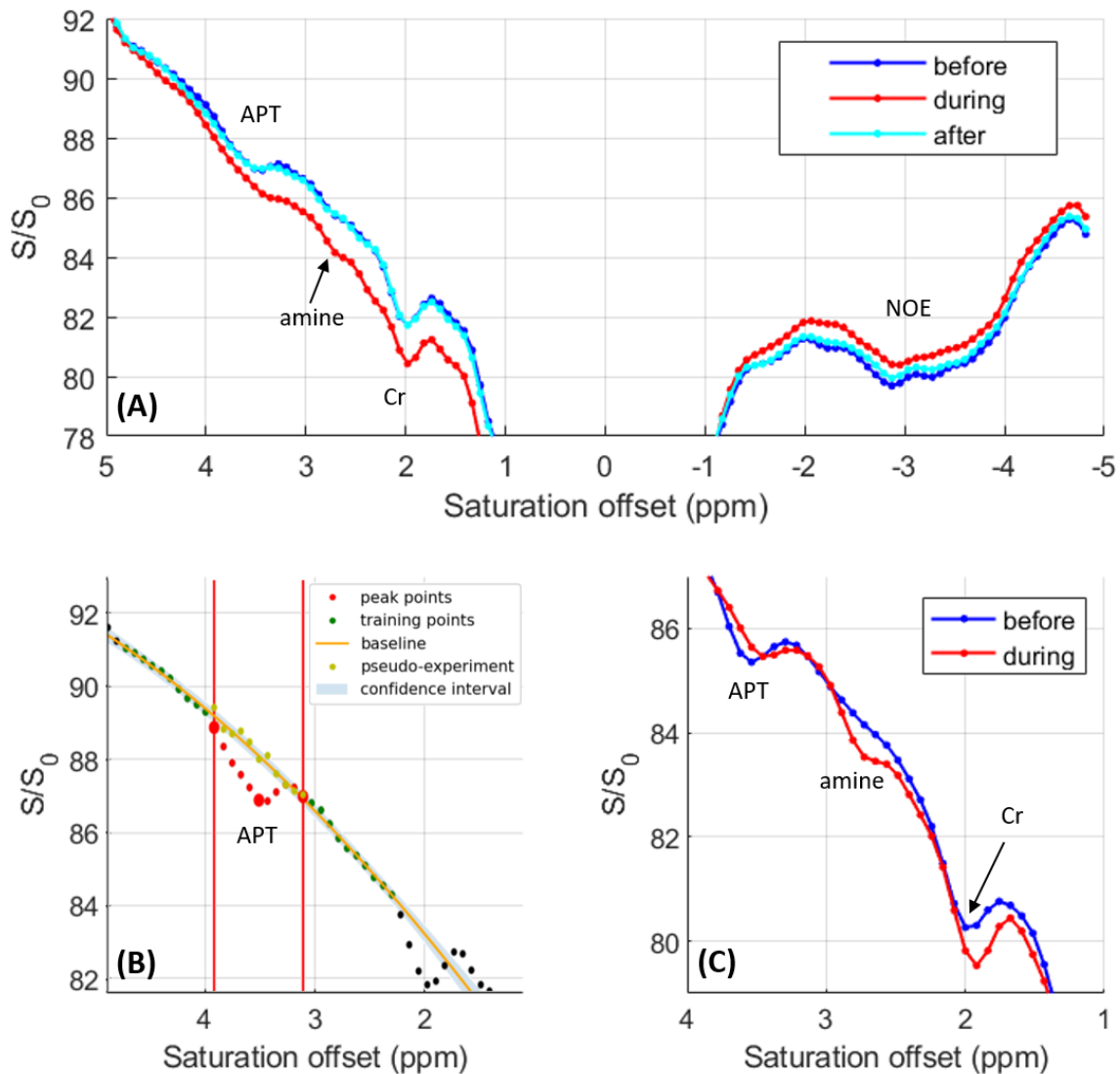


Figure 5.3: Z-spectrum evolution with  $CO_2$  administration and CEST contribution estimation. (A) Zoomed Z-spectrum for the three time periods in rat 1 (before (dark blue), during (red) and after (light blue) the administration of  $CO_2$ ). We recognize the APT, amine, creatine and NOE. Baseline changes due to increased cerebral perfusion are visible (B) Example of PEAKIT analysis of the APT peak of one Z-spectrum before  $CO_2$  administration (C) Evolution of the amide and amine CEST signal for rat 2 before and after  $CO_2$  administration

To evaluate the effect of the  $CO_2$  administration on the CEST signal, the PEAKIT software previously presented in 3.3 was used. An example of the PEAKIT analysis on the acquired Z-spectrum is given in Figure 5.3B showing the local baseline estimation. The APT-CEST results obtained are presented in Table 5.2. As expected, the pH decrease induced by hypercapnia lead to a decrease in the APT-CEST contrast ([C. K. Jones, Schlosser, et al. 2006]). Both the height and area of the APT peak were divided by a factor of minimum two in presence of  $CO_2$ . Once the  $CO_2$  was discontinued, the APT-CEST contrast was recovered (Figure 5.3A). No significant difference was detected in the amplitude/area of the creatine CEST signal when  $CO_2$  was added. Using PEAKIT, a difference was also detected in the amine CEST

region (2.7-2.8 ppm) where the amplitude and area of the CEST peak increased by a factor of two with CO<sub>2</sub> administration. The CEST contrast in this region is largely determined by exchangeable amine protons of relatively highly concentrated amino acids (alanine, GABA, aspartate, taurine) ([Wermter, Bock, and Dreher 2015]) for which the exchange rates should decrease with pH, bringing them closer to the intermediate regime favorable to CEST (Figure 5.3C). As PEAKIT is not adapted to analyze the broader NOE contrasts, changes in those signals with hypercapnia remain to be performed, eventually using alternative tool/approach.

		RAT 1		RAT 2		RAT 3	
		height	area	height	area	height	area
amide (APT)	before CO <sub>2</sub>	0.99	0.51	1.29	0.7	1.23	0.55
	during CO <sub>2</sub>	0.53	0.3	NS	NS	0.94	0.44
	after CO <sub>2</sub>	0.8	0.4	1.02	0.39	1.01	0.53
amine	before CO <sub>2</sub>	NS	NS	NS	NS	0.47	0.16
	during CO <sub>2</sub>	0.63	0.17	0.63	0.14	0.93	0.35
	after CO <sub>2</sub>	0.31	0.06	0.42	0.08	0.43	0.14

Table 5.2: PEAKIT analysis of amide (3.5-3.6 ppm) and amine (2.7-2.8 ppm) CEST signals. For each time period (before, during and after the administration of CO<sub>2</sub>), the data were averaged over three scans. The decrease in pH induces a decrease in the APT-CEST contrast and an increase in the amine CEST signal. The height values are given in %, as referred on a Z-spectrum and the area are given in arbitrary units. In the Table, « NS » corresponds to cases for which PEAKIT did not detect significant CEST peaks ( $p>0.05$ ).

These results demonstrate that accelerated acquisitions with the CEST-linescan sequence coupled with the estimation of the local baseline for the analysis of the Z-spectra allowed to track simultaneously dynamic changes at multiple saturation frequency offsets induced by a controlled pH decrease. In the next section, the focus shifts on detecting metabolic changes due to neuronal activation using a dedicated version of the CEST-LS sequence.

### 5.3 Modification of the CEST-LS sequence and acquisition strategy to minimize BOLD confound

Besides the high temporal resolution and good signal stability necessary to detect small metabolic changes, appropriate adjustments of the sequence and acquisition protocol are necessary to eliminate confounding factors (BOLD, increase in cerebral blood flow (CBF)). The peak analysis approach presented in the previous section can be employed when discrete peaks can be detected. Other strategies should be considered for broader CEST contributions.

In this section, CEST-LS grad<sub>opp</sub>, a sequence derived from the CEST-LS and adapted to functional experiments is introduced.

#### 5.3.1 Challenge of CEST detection in the context of neuronal activity

Choosing and optimizing the stimulation protocol maximizes the opportunity to trigger neuronal activation and metabolic changes. However, acquiring CEST data in such conditions

is delicate because of the presence of the BOLD effect itself.

### 5.3.1.1 Reducing BOLD signal using a SE readout module

The currently accepted model of BOLD contrast has a linear relation between the echo time and the fractional signal intensity change  $\frac{\Delta S}{S}$  observed upon neuronal activation with T2\* - weighted data ([Ravi S Menon et al. 1993]):

$$\frac{\Delta S}{S} = -TE \cdot \Delta \left( \frac{1}{T2^*} \right) \quad (5.2)$$

The same expression can be used for T2-weighted data as well, with the relaxation rate  $\Delta \left( \frac{1}{T2^*} \right)$  replaced by  $\Delta \left( \frac{1}{T2} \right)$ . One condition of the BOLD model is that the change in relaxation rate,  $\Delta \left( \frac{1}{T2} \right)$  should be at least a factor of 3 smaller than  $\Delta \left( \frac{1}{T2^*} \right)$ . As a result, the intensity changes observed with gradient echo techniques are expected to be at least 3 times greater than those observed with spin-echo techniques [Bandettini et al. 1994; Ogawa, R. Menon, et al. 1993].

In [Stroman et al. 2001], Stroman and co-workers have experimentally illustrated this result showing that the BOLD signal changes in the visual cortex measured with spin-echo and gradient-echo EPI followed a linear function of the echo time. Figure 5.4 shows the result of their experience at 3 T. The empirically-determined slope of the linear function measured with spin-echo EPI was indeed between 3 and 4 times smaller than the one measured with gradient-echo.

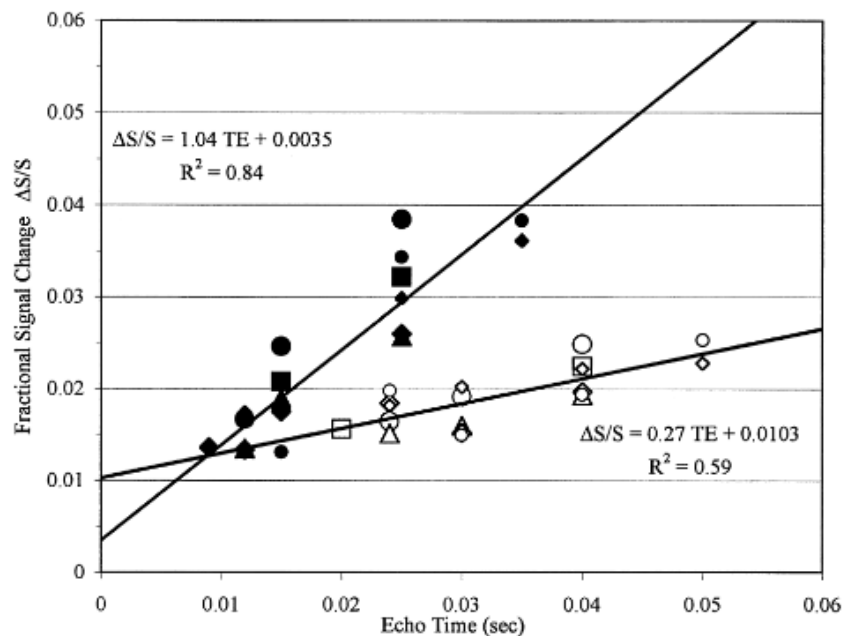


Figure 5.4: BOLD signal enhancement dependence on echo time with gradient-echo (filled symbols) and spin-echo (open symbols) EPI at 3 T. Data obtained from 3 different subjects, each subject is represented with a different symbol. Figure extracted from [Stroman et al. 2001]

These elements clearly establish that choosing a SE readout sequence over a GE is a relevant choice in order to reduce the BOLD signal. Also, the shorter the TE, the weaker the

BOLD contrast.

### 5.3.1.2 Eliminating the remaining BOLD signal with a different acquisition strategy

Using functional CEST simulations, the authors of [Roussel et al. 2019] have evaluated the impact of a the BOLD signal for the following different CEST-fMRI acquisitions and reconstruction strategies :

$$S(+\delta), \frac{S(+\delta)}{S(\delta_{ref})}, S(-\delta) - S(+\delta), S(+\delta) - S(\delta_{ref}), \frac{S(+\delta)}{S(-\delta)}, MTR_{asym}(\delta) \quad (5.3)$$

$\delta$  being the chemical shift offset and  $S(\delta)$  the water signal measured at the chemical shift  $\delta$ .  $\delta_{ref} = 100$  ppm. The  $MTR_{asym}$  is defined as in Equation 1.40

They concluded that studying the ratio between the water signal obtained at a certain saturation offset divided by the water signal obtained at the opposite saturation offset instead of every other quantities was the most efficient way to eliminate the BOLD signal from the output data and still reflect the changes in the CEST contributions (Figure 5.5).

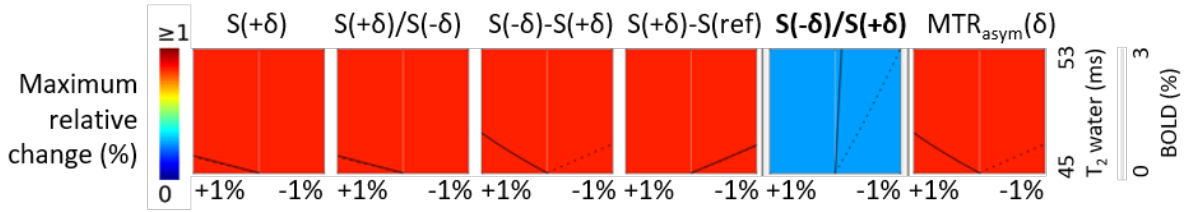


Figure 5.5: Functional CEST simulations results. Figure adapted from [Roussel et al. 2019]. CEST-fMRI contrasts calculated and correlated against water  $T_2^*$  / BOLD effect for different CEST-fMRI acquisition and reconstruction strategies. The y-axes are expressed in percent (%) of relative changes and range between  $-1$  and  $+1\%$ . The plot color is scaled according to the maximum relative change observed.

Based on this strategy, we decided to implement the acquisition of this ratio. Instead of acquiring an image with a saturation offset followed by the image at the opposite offset as proposed by [Roussel et al. 2019], we extend the concept to the acquisition of this ratio for every saturation offsets within a chosen range simultaneously. Such acquisitions can be made by adapting the CEST-LS sequence previously introduced in 3.

### 5.3.2 Presentation of the principle of the $grad_{opp}$ CEST-LS sequence

Figure 5.6 details the principle of the CEST-LS  $grad_{opp}$  compared to classic CEST-LS sequence and shows the application of both sequences to a 20 mM glutamate phantom (phantom #13). As shown in the chronogram of the classic CEST-LS sequence (5.6A), the saturation pulses are alternatively turned ON and OFF from one repetition to another and the saturation gradient  $G_{sat}$  is kept constant. On the other hand, in the CEST-LS  $grad_{opp}$  (5.6B), the saturation pulses are always turned ON and the sign of the saturation gradient  $G_{sat}$  alternates every TR. However, its absolute amplitude remains the same for every repetition. The readout module uses a GE sequence in classic CEST-LS and a SE readout module in CEST-LS  $grad_{opp}$ . The sign and

amplitude of the acquisition gradient  $G_{acq}$  are kept constant in both sequences.

Figure 5.6C show the two saturated and reference profiles obtained with the classic CEST-LS. The two types of profiles obtained with two consecutive repetitions of CEST-LS  $grad_{opp}$  are presented in Figure 5.6D. The saturation offsets were chosen so that both profiles have the water peak (0 ppm) at the center of their offsets range (more practical explanations about this adjustment are given in the next section). The two profiles are therefore symmetric with respect to the water resonance (0 ppm). The glutamate contribution is visible close to 3 ppm both on the positive and the negative profile. The ratio of the two profiles (orange by blue) give a familiar Z-spectrum (Figure 5.6E) with classic CEST-LS - where we can clearly recognize the glutamate CEST peak at 3 ppm - and a  $R$ -spectrum ( $R$  for ratio) (Figure 5.6F) with CEST-LS  $grad_{opp}$ . The  $R$ -spectrum is an even function of the saturation offset. The glutamate peak is visible twice, downwards at 3 ppm and upwards at  $-3$  ppm.

With only 2 TR, the CEST-LS  $grad_{opp}$  allows to estimate this ratio for every offset in the chosen saturation offset range (between 0 and  $\pm 5$  ppm in our example). Centering the profiles on the water peak allows to have the information twice which offers the possibility to run the similar experiment on the two halves of the line simultaneously.

The CEST-LS  $grad_{opp}$  sequence offers multiple choice to the user. The position and dimensions of the acquisition voxel can be selected as desired. The saturation module is still customizable ( $B_{1,sat}$  saturation power, pulse shape and duration, interpulse delay). The extent of the saturation offset range can be chosen by tuning the parameter  $r$  and the center of this range can be selected by carefully choosing the frequency offset of the saturation pulse applied during the acquisition of the positive or negative profile. Those offsets are respectively called Offset+ and Offset-.

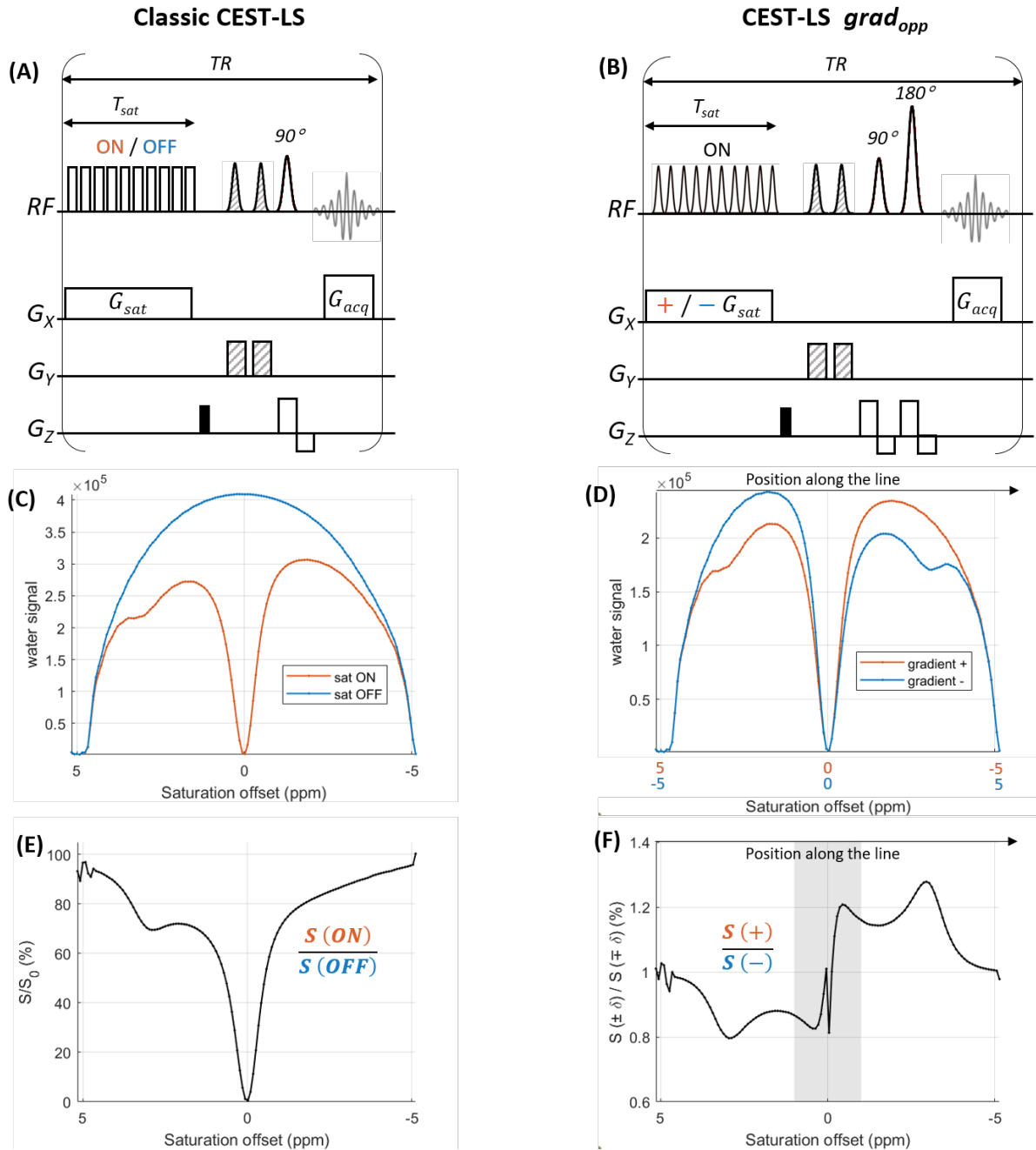


Figure 5.6: From classic CEST-LS to CEST-LS  $grad_{opp}$ . Chronogram of the "classic" CEST-LS (A) and CEST-LS  $grad_{opp}$  sequences (B). Gradient spoilers are applied on the z direction (solid black rectangle). FOV saturation bands are added to eliminate the signal outside the desired ROI (hatch pattern). In (A), the saturation pulses are alternatively switched ON and OFF and the saturation gradient  $G_{sat}$  is kept constant. In (B), the saturation module is always turned ON and the sign of the saturation gradient  $G_{sat}$  alternates every TR. The signal is read using a GE in (A) and a SE in (B). Two types of profiles obtained with two consecutive repetitions of classic CEST-LS (C) and CEST-LS  $grad_{opp}$  (D). (C) shows a profile obtained with the saturation module turned ON (orange) and a reference profile obtained with the saturation module turned OFF (blue). (D) shows a profile obtained with a positive saturation gradient  $G_{sat}$  (orange) and a profile obtained with the opposite saturation gradient  $G_{sat}$  (blue). (E) shows the Z-spectrum given by the ratio between the two profiles generated by the classic CEST-LS. (F) shows the R-spectrum given by the ratio between the profiles with positive  $G_{sat}$  and negative  $G_{sat}$ . In this example, the data were obtained from a 20 mM glutamate sample at pH 7.0

### 5.3.3 Summary

The following list summarizes the three different modifications implemented to develop a sequence devoid of BOLD confound, as much as possible.

- The readout module was changed from gradient echo to spin echo to reduce the BOLD signal. The use of spin-echo is made possible by the long TR employed in CEST detection and confers a better SNR than gradient echo sequences. The TE was reduced to 5 ms, also contributing to minimizing the BOLD signal contrast.
- The saturation module and acquisition strategy was changed to the computation of the ratio between the water signal obtained at a certain saturation offset divided by the water signal obtained at the opposite saturation offset.

### 5.3.4 Convention and graphical codes

To make the representation of this data the clearest possible, the following conventions were taken.

- First of all, the profiles are always represented with respect to their common spatial position. Data points coming from the same position in space will always have the same x-coordinate in a graph. The spatial axis like the arrow "Position along the line" from Figure 5.6D will not always be explicitly represented but remains valid.
- This x-axis also corresponds to the offsets distribution of the profiles. Since the gradients are opposite, the offsets distribution are spatially opposed. Profiles with 5 to 0 ppm on the left half of the line and 0 to -5 ppm on the right half are the "positive gradient" profiles, they are represented in orange and are referred to as "positive profile". Profiles with -5 to 0 ppm on the left half and 0 to 5 ppm on the right half are the "negative gradient" profiles, they are represented in blue and are referred to as "negative profile". When only one axis could be displayed, the choice was made to only represent the offsets distribution of the positive profile (orange).
- To obtain a  $R$ -spectrum, the positive profile is always divided by the negative gradient profile. Based on the previous point, the left half of the graph therefore shows the ratio between positive offsets and negative ones while the right part shows the ratio between negative offsets and positive ones. The left part is therefore "Z-spectrum-like" meaning that a downward peak in a regular Z-spectrum will also look downward in a  $R$ -spectrum. On the other hand, the right part is reversed and a downward peak in a regular Z-spectrum will appear upwards. The x-axis chosen to represent a  $R$ -spectrum is the offsets distribution of the positive profile. In other word, a x-coordinate  $x$  corresponds to a saturation offset  $\delta$  for which the  $R$ -spectrum is defined as :

$$R\text{-spectrum}(x) = R\text{-spectrum}(\delta) = \frac{S(\delta)}{S(-\delta)} = \frac{S_{grad+}(\delta)}{S_{grad-}(\delta)} \quad (5.4)$$

## 5.4 Experimental protocols

This section presents the functional experiment and the protocol involving the CEST-LS  $grad_{opp}$ .

## 5.4.1 Neuronal activation induced by forepaw electrical stimulation

To study the metabolic changes accompanying a neuronal activation, the electrical forepaw stimulation was chosen because it is known to produce robust activation and because the cortical area activated is located close to the surface RF coil. This leads to favorable conditions in term of SNR to detect the expected CEST signal changes.

### 5.4.1.1 Methods

Based on an anatomical T2-weighted reference image, the slices of interest were identified and a standard BOLD fMRI was performed using multi-slice GE-EPI (5 slices) in order to determine the BOLD activation area. Before this, a 3D  $B_0$  map was acquired and good field homogeneity was ensured using standard automatic shimming routine on a large volume-of-interest encompassing most of the rat brain. The acquisition parameters for GE-EPI acquisitions were  $1.8 \times 1.8 \text{ cm}^2$  FOV,  $90 \times 90$  matrix size, 1 mm slice thickness, TE/TR=10/1000 ms.

Three different activation paradigm listed in Table 5.3 (located in page 96) were tested. Except for the ON and OFF time periods that varied, the stimulation paradigm consists of consecutive OFF periods followed by ON periods during which rectangular pulses with 3 ms duration, 1.5 mA current amplitude, and 10 Hz frequency are applied. Details about the positioning of the electrodes and the electro-stimulation system are given in 3.

### 5.4.1.2 Activation example

Figure 5.7 shows an example of activation obtained during a 5 min long paradigm consisting of consecutive 30s-rest period followed by 20s-ON stimulation period. Using the SPM12 (Statistical Parametric Mapping) software (Wellcome Trust Centre for Neuroimaging, London, UK), an axial (Figure 5.7A) a sagittal (Figure 5.7B) and a coronal view (Figure 5.7C) of the T-score maps were obtained. They show an activation volume located in the primary somatosensory cortex of the right hemisphere (for a left paw stimulation). In case any BOLD signal was detected in the thalamus, the experiment was interrupted not to cause pain to the animal ([K. D. Davis et al. 1998; Bingel et al. 2003]). The temporal BOLD signal shown in Figure 5.7D exhibits a 12% increase in the BOLD signal. Such a nice activation was not obtained for every animals. Because of their different response to anesthesia, only one animal out of eight would present a very stable, clear and intense activation like the one presented in Figure 5.7. Each animal was only scanned twice (right paw and left paw) with a minimum one week break between the two experiments.

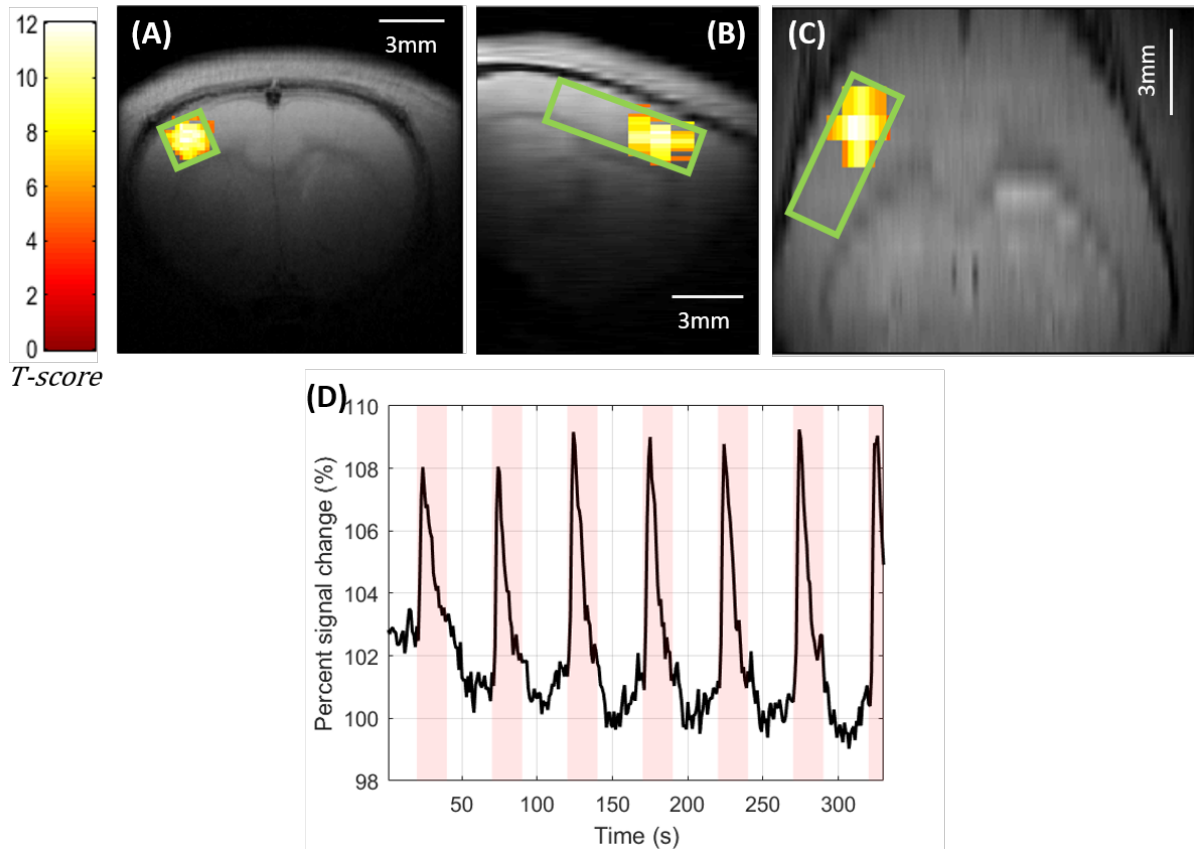


Figure 5.7: BOLD signal obtained with a (left) forepaw electrical stimulation shown. T-scores activation maps co-registered on a anatomical axial view (A), sagittal view (B) and coronal view (C). The green voxel represents the position of the line in which the CEST data are acquired. (D) Temporal evolution of the BOLD signal collected in a region included in the activation area (obtained for a stimulation pattern of 20 s ON, 30 s OFF).

## 5.4.2 CEST-LS $\text{grad}_{\text{opp}}$ implementation

### 5.4.2.1 Positioning

The CEST-LS voxel was positioned so that half of the line covered the maximum activation and the other half would not cover activation at all. More precisely, the slice with the strongest BOLD effect was positioned at the first quarter of the line. The rest of the line was oriented towards the back of the brain (Figure 5.7A, 5.7B and 5.7C). Based on the best cases, the activation was detected from a volume of approximately  $15 \mu\text{L}$  ( $2.5 \times 2.5 \times 2.5 \text{ mm}^3$ ) (Figure 5.7A, 5.7B and 5.7C). For weaker activation, the short dimensions of the CEST-LS line (in our case : dimension along the phase and slice thickness) were both set at 2 mm in order to form a  $2 \text{ mm}^2$  square, improving the amount of signal available. The long dimension of the line (along the read direction) was fixed at 6.4 mm so that the activation would occupy exactly one half of the line.

### 5.4.2.2 CEST-LS $\text{grad}_{\text{opp}}$ adjustment scans

With the position fixed, a  $2^{\text{nd}}$  order shimming procedure was performed using MAPSHIM on the volume of the CEST-LS line with an extra 0.1 mm on every dimension. Two adjustment

CEST-LS  $\text{grad}_{\text{opp}}$  scans with a very low repetition number ( $N_{\text{rep}} = 8$ ) and no activation were run. FOV saturation bands were added on the phase dimension. The CEST-LS acquisitions were performed with  $\text{TE} = 5$  ms and a saturation power of  $1.5 \mu\text{T}$ , with a saturation module of 10 rectangular pulses of 100 ms duration, separated by a 0.01 ms delay. The  $r$  ratio was fixed at 0.15 resulting in a saturation bandwidth of 10.3 ppm according to

$$BW_{\text{sat}} = r \times BW_{\text{acq}} \quad (5.5)$$

with  $BW_{\text{acq}} = 50\text{kHZ} = 68.5\text{ppm}$ . The number of points  $N_{\text{points}}$  along the read direction is 64. The TR varied with the different experiment and are reported in Table 5.3.

The goal is to center the saturation bandwidth on the water peak for both profiles (0 ppm). The computation of Offset+ and Offset- takes into account the coordinate on the read direction  $d_{\text{read}}$  of the line so that the central saturation offset of both profile is 0 ppm using the Offset<sub>geom</sub> previously introduced in equation 3.2. In the first place, we use :

$$\text{Offset}\pm = \text{Offset}_{\text{geom}} = \gamma \times G_{\text{sat}} \times d_{\text{read}} \quad (5.6)$$

It should be noted that the result obtained with this equation depends on the gradient sign. and due to the opposite sign of  $G_{\text{sat}}$  between positive and negative profiles, we have Offset- = -Offset+.

The first CEST-LS  $\text{grad}_{\text{opp}}$  adjustment scan was run in those conditions and gave profiles such as the one presented in Figure 5.8A. Indeed, both profiles cover a saturation bandwidth of 10.3 ppm and appear at first glance to be centered at 0 ppm. By zooming in close to 0 ppm (see bottom right of Figure 5.8A), a small shift compared to the theoretical saturation offset axis is observed for both profiles. This slight frequency shift originates from the local difference between the operating frequency and the local Larmor frequency despite our  $B_0$  shimming steps. This small frequency shift affects our experiment in two ways:

(1) the saturation pulse is no longer applied at the exact central frequency of the saturation bandwidth for each profile,

(2) the readout gradient no longer collects the acquisition bandwidth corresponding to the exact same position.

(1) causes the actual saturation offset distribution to move away on both sides of the 0 theoretical offset while (2) results in a shift of both profiles in one direction because acquisition bandwidth now corresponds to a slight change in position for both profiles.

Because the readout gradient  $G_{\text{acq}}$  is 7 times stronger than the saturation gradient  $G_{\text{sat}}$ , the second effect is usually negligible compared to the first one. To correct for this main issue, the chemical shifts  $\delta+$  and  $\delta-$  are measured on the results of the first CEST-LS  $\text{grad}_{\text{opp}}$  adjustment scan (Figure 5.8A). Offset+ and Offset- are then corrected by adding or subtracting  $\delta+$  and  $\delta-$ , respectively.

This calculation of Offset+ and Offset- is the only way to guarantee that the signal obtained for a given positive offset and its corresponding negative offset originates from the same spatial position, thus limiting the introduction of any bias. The second CEST-LS  $\text{grad}_{\text{opp}}$

adjustment scan was run with these new two frequency offsets. The result of this correction is shown in Figure 5.8B where the profiles coincide perfectly at 0 ppm.

The  $R$ -spectrum obtained from the two profiles once matched at 0 ppm is presented in Figure 5.8C on which we can recognize remarkable CEST contributions such as the creatine at 2 ppm and the APT at 3.5 ppm. Because of the proximity and the low values reached by the two profiles in the  $[-1 : 1]$  ppm portion, the corresponding ratio in that region was always noisy (gray rectangle in Figure 5.8C) and was thus excluded from any further interpretation.

Starting from this adjustments, the  $B_0$  shimming and CEST-LS  $\text{grad}_{\text{opp}}$  were left untouched for the rest of the experiment.

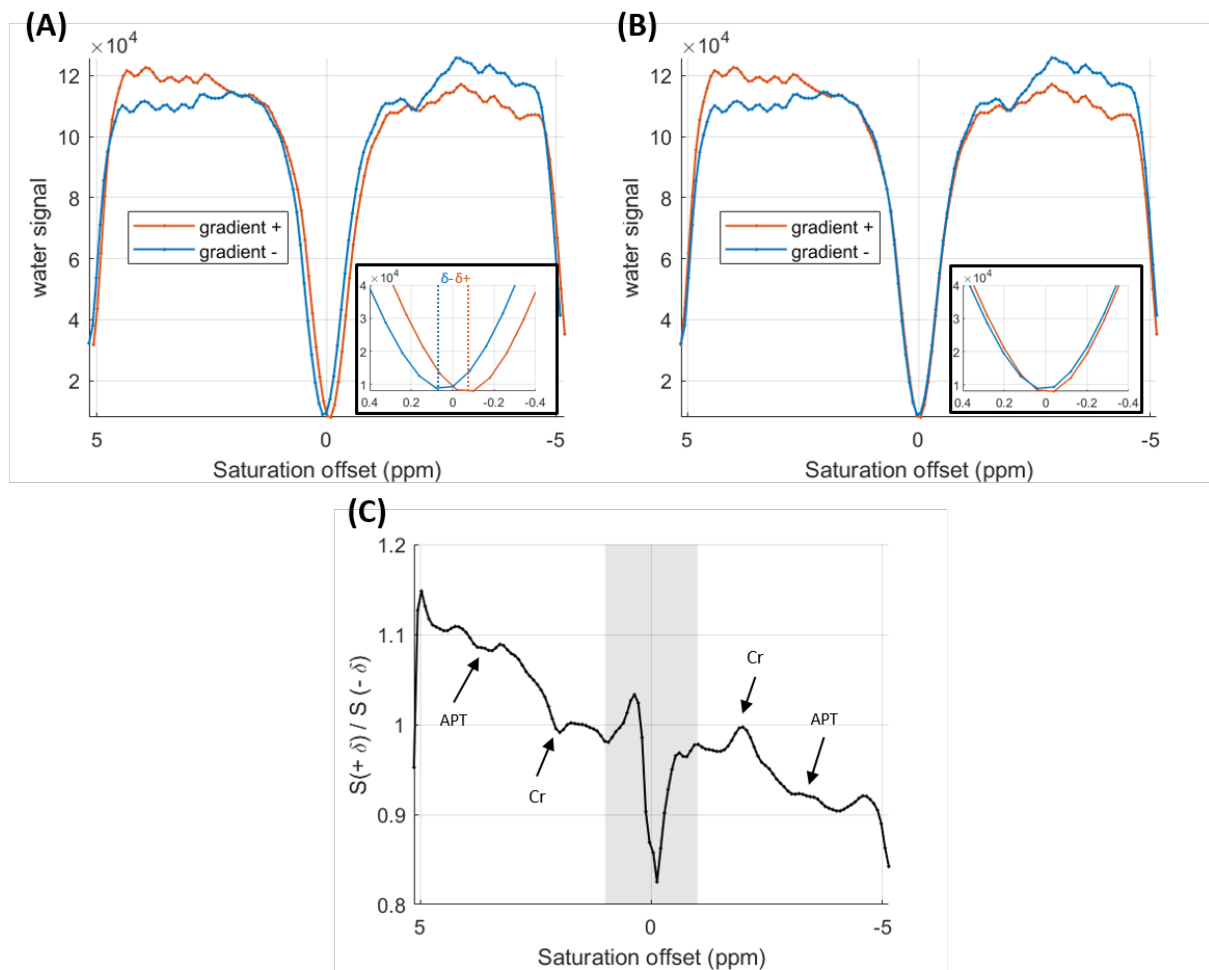


Figure 5.8: CEST-LS  $\text{grad}_{\text{opp}}$  profiles and  $R$ -spectrum acquired in the cortex. (A) CEST-LS  $\text{grad}_{\text{opp}}$  positive and negative profiles before correction of the  $B_0$  inhomogeneities and zoom on the  $[-0.4, 0.4]$  ppm range. (B) CEST-LS  $\text{grad}_{\text{opp}}$  positive and negative profiles after correction for the  $B_0$  inhomogeneities and zoom on the  $[-0.4, 0.4]$  ppm range. (C)  $R$ -spectrum obtained with the two profiles shown in (B) showing the creatine and APT peaks. Because of the low value of the profiles around the water peak at 0 ppm, the calculation of the ratio in the  $[-1 : 1]$  ppm region results in unexploitable values, indicated by a light gray rectangle. Eight profiles were alternatively acquired with gradient positive and negative. The profiles obtained in (A) and (B) are the result of the average over the four repetitions for each profile. For (C), the ratio were computed every two consecutive profiles acquired and then averaged together.

### 5.4.2.3 CEST-LS $\text{grad}_{\text{opp}}$ and activation

The line being correctly positioned and the parameters precisely set, CEST-LS  $\text{grad}_{\text{opp}}$  repetitions were run together with stimulation. As shown in Figure 5.7A, 5.9B and 5.7C, the line was positioned such as half of it would cover the activation area and half of it would not. This was done in order to acquire the  $R$ -spectrum over the [0 : 5] offset range in an activated region while simultaneously acquiring the same information in a non-activated region.

Changing to a SE readout module and shortening the TE contributed to reduce the BOLD effect visible on the water signal. The remaining BOLD effect (before doing the ratio) served as a control for the activation in the CEST data. After separating the profiles obtained during the ON-stimulation from the ones obtained during the rest period, each group was averaged. The results are shown in Figure 5.9B for positive profiles and in 5.9C for gradient negative profiles. No difference is observed in the control area for any profile. However the ON profiles appears slightly over in the activated region for both profiles. The difference is clearly visible in Figure 5.9D and Figure 5.9E showing the zoom in the activated area for positive profiles (D) and for gradient negative profiles (E). This remaining water signal difference is approximately of 1% and is clearly visible in the activated area for both profile.

#### **Convention**

Similarly to the data presented in Figure 5.9, the activated half part of the line is always located on the right half of the graph on profiles as well as on  $R$ -spectra.

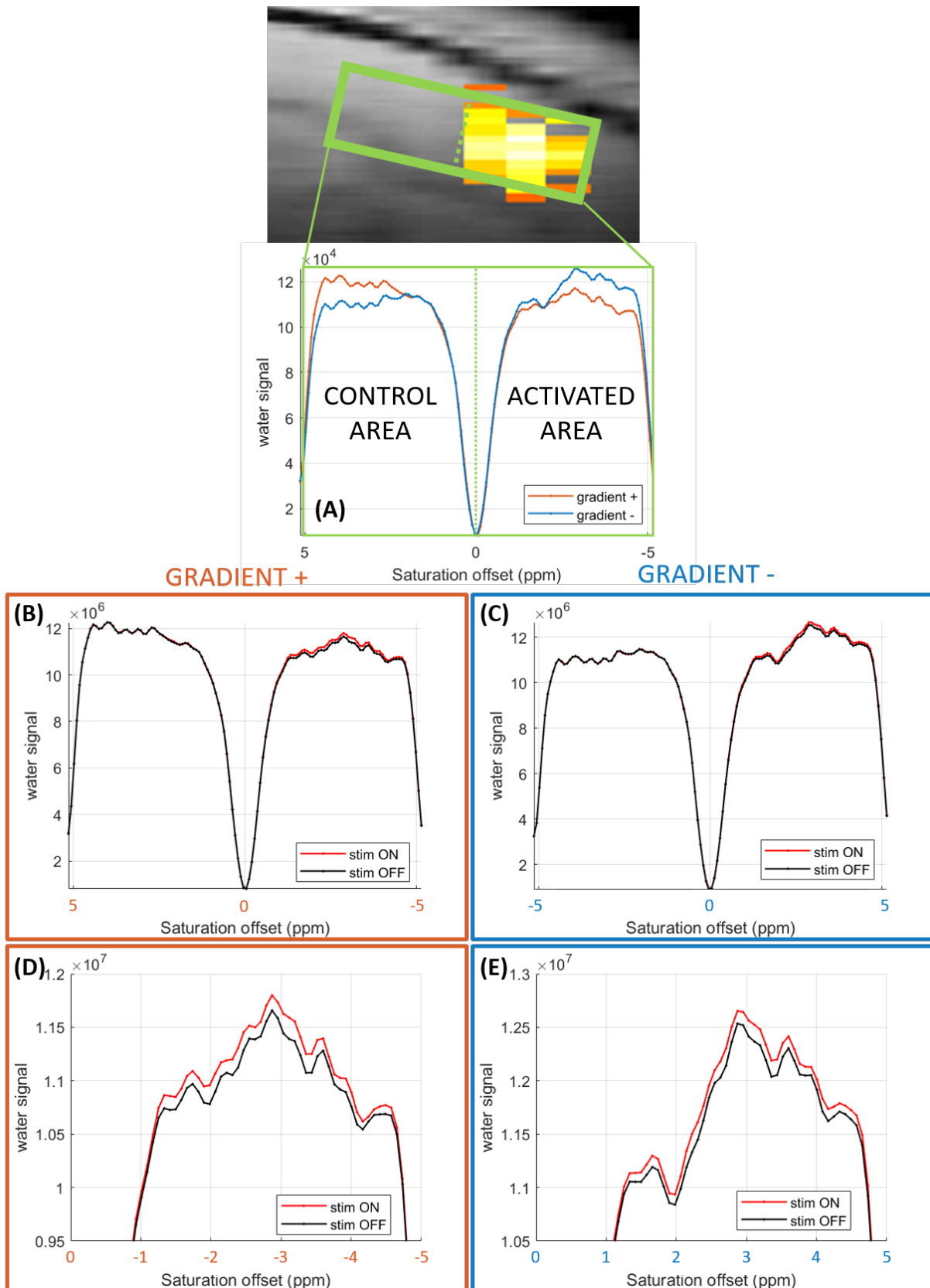


Figure 5.9: CEST-LS  $grad_{opp}$  positive and negative profiles temporal analysis through activation. (A) Positive and negative profiles and spatial correspondence with the activated and control area shown on the activation map. The green voxel represent the CEST-LS  $grad_{opp}$  acquisition line. Positive (B) and negative (C) profiles averaged over the ON-stimulation period (red) and rest period (black). Zoom on the activated area for the positive (D) and negative (E) profiles averaged over the ON-stimulation period (red) and rest period (black).

#### 5.4.2.4 CEST-LS $\text{grad}_{\text{opp}}$ stimulation protocols

Once the parameters were correctly set, and the activation was effectively detected on the profiles, the CEST-LS  $\text{grad}_{\text{opp}}$  scans with activation were repeated 6 times in a row with a five minute break planned between every scan to avoid animals getting accustomed to the stimulation. Several different paradigms (for activation and CEST-LS  $\text{grad}_{\text{opp}}$  versions) were tested, the parameters of each of them are listed in Table 5.3. To generate similar activation conditions, the stimulation block was always chosen the closest possible to 20s ON stimulation and 30s OFF rest period. However, other time constraints had to be respected to ensure CEST-LS  $\text{grad}_{\text{opp}}$  acquisition periods could properly match with the stimulation paradigm. For every paradigm, we made sure that the duration of a the ON and OFF-stimulation periods were chosen so that an even number of profiles (TR) could be acquired.

Experiment n°	OFF period (s)	ON period (s)	$N_{\text{bloc}}$	$\text{grad}_{\text{opp}}$	TR (s)	N rats
1.1	30	20	6	with switch	2.5	7
1.2	30	21	5	with switch	1.5	2
2	27	21	8	with block	1.5	4

*Table 5.3: Experimental parameters for the three different experiments]*

As presented on Figure 5.10A, CEST-LS  $\text{grad}_{\text{opp}}$  consists of acquiring alternatively positive and negative profiles. However, because a stimulation block allows the acquisition of an even number of profiles, such an alternation would cause the stimulation block to always begin with the same gradient sign. To avoid introducing this bias, an additional "switch" was implemented in the gradient sign alternation scheme. This allows to interrupt the monotony of the gradient sign alternation and reverse the alternation every eight repetitions, as shown on Figure 5.10B. This version of CEST-LS  $\text{grad}_{\text{opp}}$  is called "with switch". Experiment 1.1 and 1.2 are based on this principle. The principle of the experiment number 2 will be detailed in the results section.

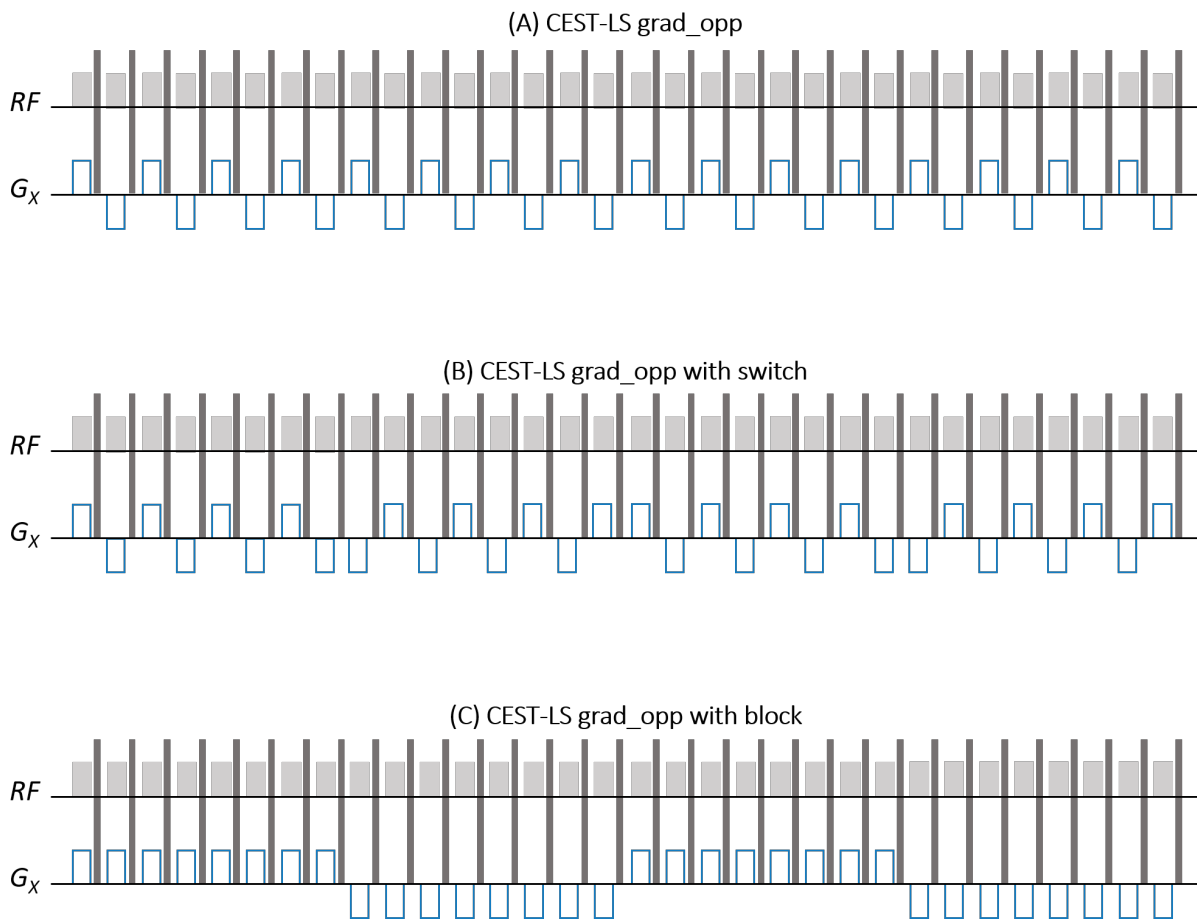


Figure 5.10: Simplified sequence pulse designs of different version of the CEST-LS  $grad_{opp}$  sequence. (A) Simple CEST-LS  $grad_{opp}$  sequence. (B) CEST-LS  $grad_{opp}$  sequence with switch every 8 repetitions. (C) CEST-LS  $grad_{opp}$  sequence with sign blocks of 8 repetitions. In practice, the number of repetitions for each block was 32. This representation of the CEST-LS sequence is based on the simplified pulse sequence shown in Figure 3.12. In this example, 32 profiles (16 positive and 16 negative) are acquired in total.

Figure 5.11 presents for each experiment a table with a list through time of every profile, their corresponding sign, and every  $R$ -spectrum associated to a pair of  $+/-$  profile. A color-coded information about the stimulation (red for ON and gray for OFF) was added. One column corresponds to the acquisition of one profile. The profiles are numbered according to their order of acquisition. Time points are regularly spaced every TR. The gradient sign of each profile is specified. The  $R$ -spectrum number that a profile is contributing to is given in the line "Ratio nb". Two profiles (with opposite gradient sign) are necessary to form a  $R$ -spectrum. The  $R$ -spectrum number is only given with the last profile that completes a pair. For every first profile of a pair, no number is specified in the "Ratio" field. For experiment 1.1 and 1.2, every consecutive profile forms a pair of positive and negative profiles. The specificity of experiment 2 on this point is detailed in the Results section (5.5).

CHAPTER 5. APPLICATIONS TO THE DETECTION OF TRANSIENT METABOLIC CHANGES DURING NEURONAL ACTIVATION

EXPERIMENT 1.1

time (s)	0.0	0.0	0.0	0.0	2.5	5.0	7.5	10.0	12.5	15.0	17.5	20.0	22.5	25.0	27.5	30.0	32.5	35.0	37.5	40.0	42.5	45.0	47.5	50.0	52.5	55.0	57.5	60.0	62.5	65.0	67.5	70.0	72.5	75.0	
grad sign	(+)	(-)	(+)	(-)	+	-	+	-	+	-	+	-	+	-	+	-	+	-	+	-	+	-	+	-	+	-	+	-	+	-	+	-	+	-	+
Profile nb	0.0	0.0	0.0	0.0	1.0	2.0	3.0	4.0	5.0	6.0	7.0	8.0	9.0	10.0	11.0	12.0	13.0	14.0	15.0	16.0	17.0	18.0	19.0	20.0	21.0	22.0	23.0	24.0	25.0	26.0	27.0	28.0	29.0	30.0	
Ratio nb	0.0	0.0	0.0	0.0	1.0	2.0	3.0	4.0	5.0	6.0	7.0	8.0	9.0	10.0	11.0	12.0	13.0	14.0	15.0	16.0	17.0	18.0	19.0	20.0	21.0	22.0	23.0	24.0	25.0	26.0	27.0	28.0	29.0	30.0	

time (s)	77.5	80.0	82.5	85.0	87.5	90.0	92.5	95.0	97.5	100.0	102.5	105.0	107.5	110.0	112.5	115.0	117.5	120.0	122.5	125.0	127.5	130.0	132.5	135.0	137.5	140.0	142.5	145.0	147.5	150.0	152.5	155.0	157.5	160.0	
grad sign	-	+	+	-	+	-	+	-	+	-	+	-	+	-	+	-	+	-	+	-	+	-	+	-	+	-	+	-	+	-	+	-	+	-	+
Profile nb	31.0	32.0	33.0	34.0	35.0	36.0	37.0	38.0	39.0	40.0	41.0	42.0	43.0	44.0	45.0	46.0	47.0	48.0	49.0	50.0	51.0	52.0	53.0	54.0	55.0	56.0	57.0	58.0	59.0	60.0	61.0	62.0	63.0	64.0	
Ratio nb	16.0	17.0	17.0	18.0	18.0	19.0	19.0	20.0	20.0	21.0	21.0	22.0	22.0	23.0	23.0	24.0	24.0	25.0	25.0	26.0	26.0	27.0	27.0	28.0	28.0	29.0	29.0	30.0	30.0	31.0	31.0	32.0	32.0		

time (s)	162.5	165.0	167.5	170.0	172.5	175.0	180.0	182.5	185.0	187.5	190.0	192.5	195.0	197.5	200.0	202.5	205.0	207.5	210.0	212.5	215.0	217.5	220.0	222.5	225.0	227.5	230.0	232.5	235.0	237.5	240.0	242.5	245.0	
grad sign	+	+	+	+	+	+	+	+	+	+	+	+	+	+	+	+	+	+	+	+	+	+	+	+	+	+	+	+	+	+	+	+	+	+
Profile nb	65.0	66.0	67.0	68.0	69.0	70.0	71.0	72.0	73.0	74.0	75.0	76.0	77.0	78.0	79.0	80.0	81.0	82.0	83.0	84.0	85.0	86.0	87.0	88.0	89.0	90.0	91.0	92.0	93.0	94.0	95.0	96.0	97.0	98.0
Ratio nb	33.0	34.0	34.0	35.0	35.0	36.0	36.0	37.0	37.0	38.0	38.0	39.0	39.0	40.0	40.0	41.0	41.0	42.0	42.0	43.0	43.0	44.0	44.0	45.0	45.0	46.0	46.0	47.0	47.0	48.0	48.0	49.0	49.0	

time (s)	247.5	250.0	252.5	255.0	260.0	262.5	265.0	267.5	270.0	272.5	275.0	280.0	282.5	285.0	287.5	290.0	292.5	295.0	297.5	300.0		
grad sign	+	-	+	-	+	-	+	-	+	-	+	-	+	-	+	-	+	-	+	-		
Profile nb	99.0	100.0	101.0	102.0	103.0	104.0	105.0	106.0	107.0	108.0	109.0	110.0	111.0	112.0	113.0	114.0	115.0	116.0	117.0	118.0	119.0	120.0
Ratio nb	50.0	51.0	52.0	53.0	54.0	55.0	56.0	57.0	58.0	59.0	60.0											

EXPERIMENT 1.2

time (s)	0.0	0.0	0.0	0.0	1.5	3.0	4.5	6.0	7.5	9.0	10.5	12.0	13.5	15.0	16.5	18.0	19.5	21.0	22.5	24.0	25.5	27.0	28.5	30.0	31.5	33.0	34.5	36.0	37.5	39.0	40.5	42.0	43.5	45.0	
grad sign	(+)	(-)	(+)	(-)	+	-	+	-	+	-	+	-	+	-	+	-	+	-	+	-	+	-	+	-	+	-	+	-	+	-	+	-	+	-	+
Profile nb	0.0	0.0	0.0	0.0	1.0	2.0	3.0	4.0	5.0	6.0	7.0	8.0	9.0	10.0	11.0	12.0	13.0	14.0	15.0	16.0	17.0	18.0	19.0	20.0	21.0	22.0	23.0	24.0	25.0	26.0	27.0	28.0	29.0	30.0	
Ratio nb	0.0	0.0	0.0	0.0	1.0	2.0	3.0	4.0	5.0	6.0	7.0	8.0	9.0	10.0	11.0	12.0	13.0	14.0	15.0	16.0	17.0	18.0	19.0	20.0	21.0	22.0	23.0	24.0	25.0	26.0	27.0	28.0	29.0	30.0	

time (s)	46.5	48.0	49.5	51.0	52.5	54.0	55.5	57.0	58.5	60.0	61.5	63.0	64.5	66.0	67.5	69.0	70.5	72.0	73.5	75.0	76.5	78.0	79.5	81.0	82.5	84.0	85.5	87.0	88.5	90.0	91.5	93.0	94.5	96.0	
grad sign	-	+	+	-	+	-	+	-	+	-	+	-	+	-	+	-	+	-	+	-	+	-	+	-	+	-	+	-	+	-	+	-	+	-	+
Profile nb	31.0	32.0	33.0	34.0	35.0	36.0	37.0	38.0	39.0	40.0	41.0	42.0	43.0	44.0	45.0	46.0	47.0	48.0	49.0	50.0	51.0	52.0	53.0	54.0	55.0	56.0	57.0	58.0	59.0	60.0	61.0	62.0	63.0	64.0	
Ratio nb	16.0	17.0	17.0	18.0	18.0	19.0	19.0	20.0	20.0	21.0	21.0	22.0	22.0	23.0	23.0	24.0	24.0	25.0	25.0	26.0	26.0	27.0	27.0	28.0	28.0	29.0	29.0	30.0	30.0	31.0	31.0	32.0	32.0		

time (s)	97.5	99.0	100.5	102.0	103.5	105.0	106.5	108.0	109.5	111.0	112.5	114.0	115.5	117.0	118.5	120.0	121.5	123.0	124.5	126.0	127.5	129.0	130.5	132.0	133.5	135.0	136.5	138.0	139.5	141.0	142.5	144.0	145.5	147.0	
grad sign	+	-	+	-	+	-	+	-	+	-	+	-	+	-	+	-	+	-	+	-	+	-	+	-	+	-	+	-	+	-	+	-	+	-	+
Profile nb	65.0	66.0	67.0	68.0	69.0	70.0	71.0	72.0	73.0	74.0	75.0	76.0	77.0	78.0	79.0	80.0	81.0	82.0	83.0	84.0	85.0	86.0	87.0	88.0	89.0	90.0	91.0	92.0	93.0	94.0	95.0	96.0	97.0	98.0	
Ratio nb	33.0	34.0	34.0	35.0	35.0	36.0	36.0	37.0	37.0	38.0	38.0	39.0	39.0	40.0	40.0	41.0	41.0	42.0	42.0	43.0	43.0	44.0	44.0	45.0	45.0	46.0	46.0	47.0	47.0	48.0	48.0	49.0	49.0		

time (s)	148.5	150.0	151.5	153.0	154.5	156.0	157.5	159.0	160.5	162.0	163.5	165.0	166.5	168.0	169.5	171.0	172.5	174.0	175.5	177.0	178.5	180.0	181.5	183.0	184.5	186.0	187.5	189.0	190.5	192.0	193.5	195.0	196.5	198.0	
grad sign	+	-	+	-	+	-	+	-	+	-	+	-	+	-	+	-	+	-	+	-	+	-	+	-	+	-	+	-	+	-	+	-	+	-	+
Profile nb	99.0	100.0	101.0	102.0	103.0	104.0	105.0	106.0	107.0	108.0	109.0	110.0	111.0	112.0	113.0	114.0	115.0	116.0	117.0	118.0	119.0	120.0	121.0	122.0	123.0	124.0	125.0	126.0	127.0	128.0	129.0	130.0	131.0	132.0	
Ratio nb	50.0	51.0	52.0	53.0	54.0	55.0	56.0	57.0	58.0	59.0	60.0	61.0	62.0	63.0	64.0	65.0	66.0																		

time (s)	199.5	201.0	202.5	204.0	205.5	207.0	208.5	210.0	211.5	213.0	214.5	216.0	217.5	219.0	220.5	222.0	223.5	225.0	226.5	228.0	229.5	231.0	232.5	234.0	235.5	237.0	238.5	240.0	241.5	243.0	244.5	246.0	247.5	249.0	
grad sign	+	-	+	-	+	-	+	-	+	-	+	-	+	-	+	-	+	-	+	-	+	-	+	-	+	-	+	-	+	-	+	-	+	-	+
Profile nb	133.0	134.0	135.0	136.0	137.0	138.0	139.0	140.0	141.0	142.0	143.0	144.0	145.0	146.0	147.0	148.0	149.0	150.0	151.0	152.0	153.0	154.0	155.0	156.0	157.0	158.0	159.0	160.0	161.0	162.0	163.0	164.0	165.0	166.0	
Ratio nb	67.0	68.0	68.0	69.0	69.0	70.0	70.0	71.0	71.0	72.0	72.0	73.0	73.0	74.0	74.0	75.0	75.0	76.0	76.0	77.0	77.0	78.0	78.0	79.0	79.0	80.0	80.0	81.0	81.0	82.0	82.0	83.0	83.0		

time (s)	250.5	252.0	253.5	255.0	256.5	258.0	259.5	261.0	262.5	264.0
grad sign	+	-	+	-	+	-	+	-	+	-
Profile nb	167.0	168.0	169.0	170.0	171.0	172.0	173.0	174.0	175.0	176.0
Ratio nb	84.0	85.0	86.0	87.0	88.0					

EXPERIMENT 2

time (s)	0.0	0.0	0.0	0.0	1.5	3.0	4.5	6.0	7.5	9.0	10.5	12.0	13.5	15.0	16.5	18.0	19.5	21.0	22.5	24.0	25.5	27.0	28.5	30.0	31.5	33.0	34.5	36.0	37.5	39.0	40.5	42.0	43.5	45.0
grad sign	(+)	(+)	(+)	(+)	+	+	+	+	+	+	+	+	+	+	+	+	+	+	+	+	+	+	+	+	+	+	+	+	+	+	+	+	+	+
Profile nb	0.0	0.0	0.0	0.0	1.0	2.0	3.0	4.0	5.0	6.0	7.0	8.0	9.0	10.0	11.0	12.0	13.0	14.0	15.0	16.0	17.0	18.0	19.0	20.0	21.0	22.0	23.0	24.0	25.0	26.0	27.0	28.0	29.0	30.0
Ratio nb	0.0	0.0	0.0	0.0	1.0	2.0	3.0	4.0	5.0	6.0	7.0	8.0	9.0	10.0	11.0	12.0	13.0	14.0	15.0	16.0	17.0	18.0	19.0	20.0	21.0	22.0	23.0	24.0	25.0	26.0	27.0	28.0	29.0	30.0

time (s)	46.5	48.0	49.5	51.0	52.5	54.0	55.5	57.0	58.5	60.0	61.5	63.0	64.5	66.0	67.5	69.0	70.5	72.0	73.5	75.0	76.5	78.0	79.5	81.0	82.5	84.0	85.5	87.0	88.5	90.0	91.5	93.0	94.5	96.0	
grad sign	+	+	+	-	+	-	+	-	+	-	+	-	+	-	+	-	+	-	+	-	+	-	+	-	+	-	+	-	+	-	+	-	+	-	+
Profile nb	31.0	32.0	33.0	34.0	35.0	36.0	37.0	38.0	39.0	40.0	41.0	42.0	43.0	44.0	45.0	46.0	47.0	48.0	49.0	50.0	51.0	52.0	53.0	54.0	55.0	56.									

### 5.4.3 Processing

The data were processed as described in section 3.2.3 except that the ratio was not computed between a saturated profile and its corresponding unsaturated one but between a positive profile and its corresponding negative one. After the Fourier transform of each unit FID, profiles were then paired together. For experiments 1.1 and 1.2, two consecutive profiles always formed a pair of positive and negative profiles. Profiles pairing for experiment 2 is detailed in the result section. No matter the order with which they were acquired, the  $R$ -spectrum was always computed with the positive gradient as the numerator and negative gradient as the denominator. For one scan, a set of  $R$ -spectra acquired through time was obtained. This whole set was averaged over the series of six scans.

## 5.5 Results

This section presents the results obtained with the protocols previously described.

The typical results obtained with experiment 1.1 on one animal are shown in Figure 5.12. Similar data were obtained for experiment 1.2 and 2. Figure 5.12A shows the average 3D-representation of  $R$ -spectra plotted against time and saturation offsets (the  $[-1 : 1]$  ppm range being removed to improve the readability of the graph). The part of the line included in the activation area and the control area are reminded. At any time point included in the protocol, a  $R$ -spectrum was acquired. For example, Figure 5.12C shows the  $R$ -spectrum obtained at  $T = 30\text{s}$  (more precisely, it shows the average over the 6 repetitions). The temporal evolution of a given saturation offset (yellow arrow) can also be followed as shown in Figure 5.12B in which the evolution of the  $R$ -spectrum at point  $\delta = 2.5$  ppm is represented (once again, it shows the average over the 6 repetitions). The TR used in this experiment 1.1 was 2.5 s, which led to a 5 s temporal resolution for each  $R$ -spectrum.

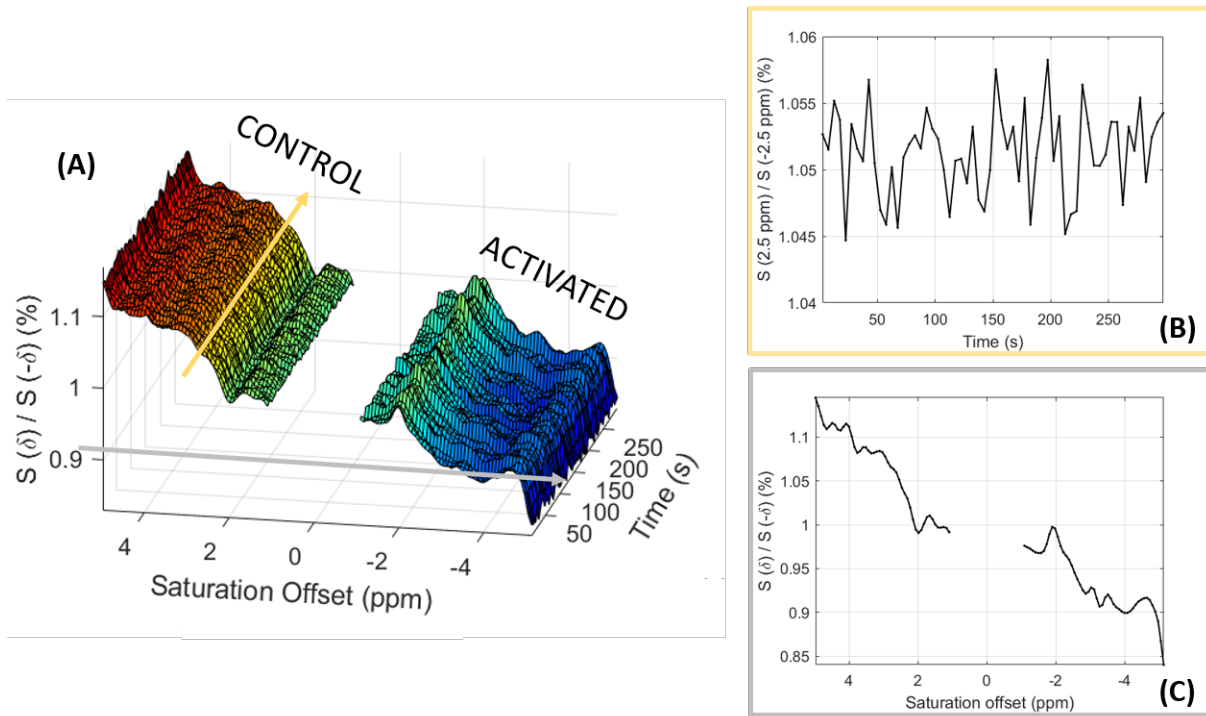


Figure 5.12: Typical data obtained with experiment 1.1. (A)  $R$ -spectra value at each saturation offset and for every time point. (B) Temporal evolution of the  $R$ -spectrum at  $\delta = 2.5$  ppm. (C)  $R$ -spectrum over every saturation offsets at  $T = 30$  s

### 5.5.1 Results for experiment 1.1 and 1.2

Using a color scale, the 3D data previously shown can also be represented in a 2D view as in Figure 5.13A. The  $[-1 : 1]$  ppm gap was filled with pale pink rectangles representing the ON-stimulation periods.

In this 2D-view, a regular pattern is visible in the activated region and is somehow correlated with the stimulation paradigm. To represent this pattern more clearly, the difference between the  $R$ -spectrum and its average over time was plotted against time and saturation offsets in Figure 5.13B. With this new representation, the pattern appears more clearly. For every saturation offset in the activated area, the beginning of each stimulation block generated an increase or a decrease in the  $R$ -spectrum. The fact that this pattern has very similar values for every saturation offset shows that this effect is unfortunately not due to metabolic changes. The fact that this pattern only appears in the activated region and has a temporal evolution correlated to the stimulation paradigm shows that the effect most likely comes from neuronal activation.

This pattern can also be represented plotting the temporal evolution of a given saturation offset. For clarity, we selected only three offsets that were located at the center of the activated region. The plots are represented in Figure 5.13C and show that the effect follows the sequence : increase, increase, decrease, decrease, increase, increase. This sequence was observed on each animal for which the activation was sufficiently important.

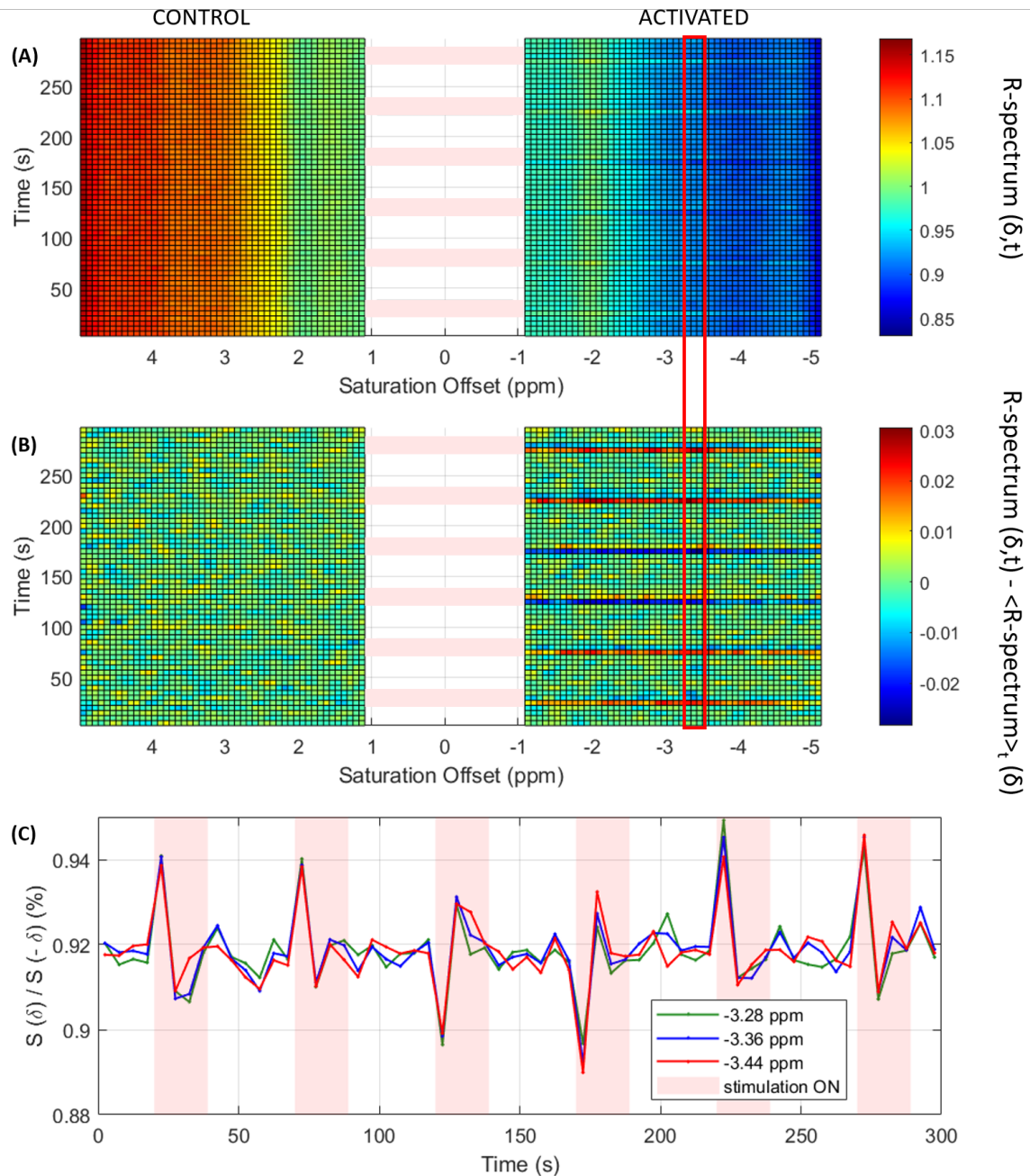


Figure 5.13: CEST-LS  $grad_{opp}$  results obtained with experiment 1.1. (A) 2D-view of the set of R-spectra plotted against time and saturation offset. (B) Difference between the R-spectrum volume and its temporal average plotted against time and saturation offset. In (A), (B) and (C) the pale pink rectangles represent the ON-stimulation period. The bright red rectangle encircling three saturation offset represents the data presented in (C). (C) Temporal evolution of the R-spectrum for three saturation offsets.

Our hypothesis is that this pattern actually comes from a bias introduced by the timing of our activation paradigm and switch of our readout gradient polarity (Figures 5.11 and 5.14). Because profiles were acquired successively, they were not necessarily obtained in similar conditions during the hemodynamic response function (HRF) in response to activation. Without claiming that BOLD directly represents neuronal activity, we consider that it is sufficiently correlated with the latter to consider that the BOLD signal gives a good first

approach of the evolution of neuronal activity. Figure 5.14A schematically represents the typical BOLD response to the stimulation used in the experiment. In the first five seconds of stimulation, the BOLD signal changed from the value at rest to its maximum value and decreased in the following fifteen seconds. Figure 5.14B and 5.14C shows for the first 10 seconds of activation, the moments when each positive (marked with an orange "+") and each negative (marked with a blue "-") profile were acquired.

It is clear that the two first profiles are acquired at two very different stages of the BOLD response, and therefore at two different levels of neuronal activity. Because of this effect, the ratio calculated for a pair of profiles is artificially high or low depending on the order of profile acquisition (+ first and - second or vice versa). This also applies to the following pairs of profiles. However, since the first pair of profiles is the one with the largest difference in BOLD signal, it is also the pair for which the ratio value is the most different from the other ratio values.

In a way, the signal changes in our  $R$ -spectra reflects the derivative function of the HRF with a temporal resolution of 5s. The sign of this derivative is flipped when the polarity of the CEST-LS readout gradient is switched as described in Figure 5.11.

To get into more details, we can differentiate two cases: (1) the gradient sign distribution is such that the first profile acquired during the activation period is a positive profile; (2) the gradient sign distribution is such that the first profile acquired during the activation period is a negative profile.

Figure 5.14B shows the gradient sign distribution for case (1). In such a case, the positive profile has less BOLD effect than the following negative profile. Because the  $R$ -spectrum always represents the ratio between the positive and the negative profile, this should theoretically cause an artificial decrease in the  $R$ -spectrum at the beginning of the activation block. With the same reasoning, with the gradient sign distribution described for case (2) and represented in Figure 5.14C, the  $R$ -spectrum should artificially increase at the beginning of the activation block. In order to relate these theoretical results to our experiment timelines, we can refer to Figure 5.11 that shows that the gradient signs at the beginning of the six activation blocks of experiment 1.1 are: -, -, +, +, -, -, corresponding to gradient sign distribution in the following order (2),(2),(1),(1),(2),(2). This observation indeed coincides with the sequence observed in Figure 5.13: increase, increase, decrease, decrease, increase, increase.

This finding demonstrates that the time resolution of the sequence used in this experiment is not high enough for two consecutive profiles to be acquired with equivalent activation conditions. Experiment 1.1 did not allow the detection of transient metabolic changes during neuronal activation because we still have BOLD contamination due to the too large delay between two acquisition time points. In order to reduce the influence of the differential BOLD contrasts during the time-course of our  $R$ -spectra, a possible solution would be to reduce the TR of our CEST-LS  $\text{grad}_{\text{opp}}$  acquisitions.

That's the reason why experiment 1.2 was tested, experiment 1.2 was identical to experiment 1.1 but with a one second shorter TR (TR = 1.5 s). For practical reasons, small activation paradigm adjustments had to be made (see Table 5.3) in order to adapt the paradigm to this new TR with as little change as possible in the activation and rest periods. The TR used in

experiment 1.2 was 1.5 s, which lead to the acquisition of a  $R$ -spectrum every 3 s.

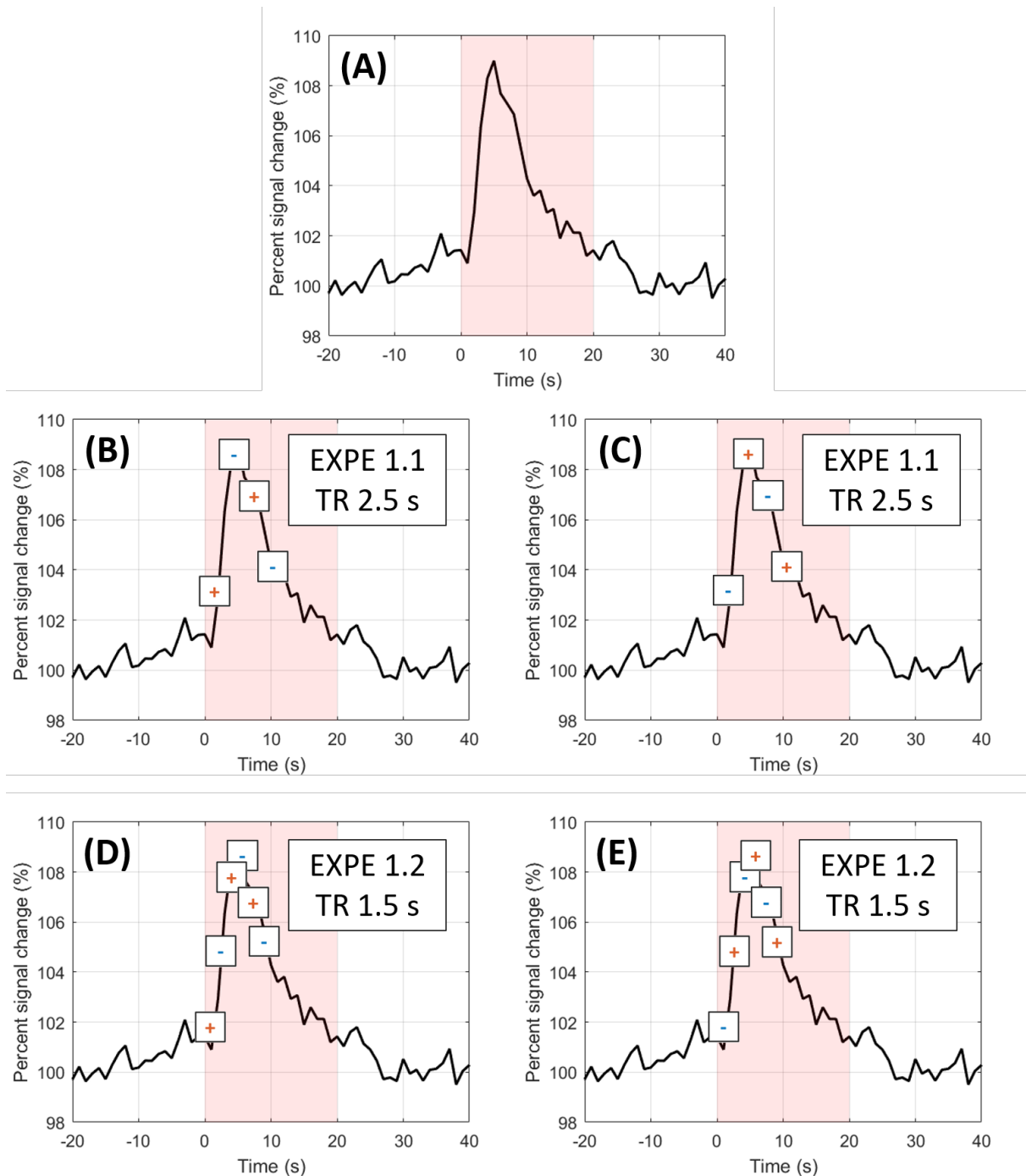


Figure 5.14: Illustration of the problem faced in experiment 1.1 and 1.2. (A) Typical BOLD response to a 20 s stimulation block. The stimulation starts at  $t = 0$  s. (B) Time positioning of the profile acquisitions for experiment 1.1 starting with a positive profile. (C) Time positioning of the profile acquisitions for experiment 1.1 starting with a negative profile. (D) Time positioning of the profile acquisitions for experiment 1.2 starting with a positive profile. (E) Time positioning of the profile acquisitions for experiment 1.2 starting with a negative profile. The pale pink rectangles represent the ON-stimulation period.

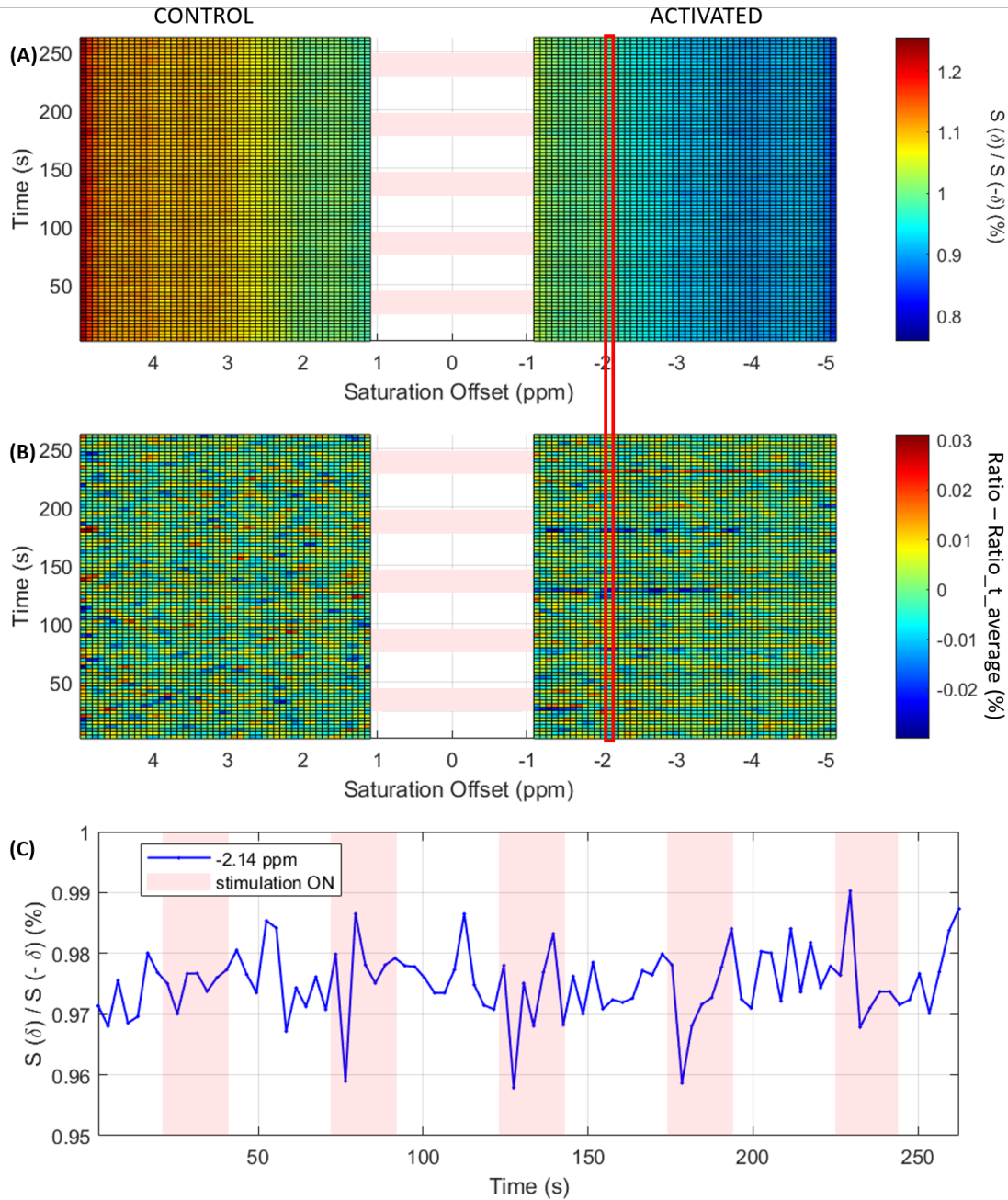


Figure 5.15: CEST-LS  $grad_{opp}$  results obtained with experiment 1.2. (A) 2D-view of the set of  $R$ -spectra plotted against time and saturation offset. (B) Difference between the  $R$ -spectrum volume and its temporal average plotted against time and saturation offset. In (A), (B) and (C), the pale pink rectangles represent the ON-stimulation time period. The bright red rectangle encircling the data for one saturation offset represents the data presented in (C). (C) Temporal evolution of the  $R$ -spectrum for two saturation offsets.

Figure 5.14C and 5.14D shows the gradient sign distribution for cases (1) and (2), respectively. The resulting  $R$ -spectra are shown in Figure 5.16. As in experiment 1.1, a periodic pattern appeared in the activated area (Figure 5.16B). The sequence (decrease, decrease, decrease, decrease, increase) was once again coherent with the gradient sign at the beginning of the activation blocs (+,+,+,+,-), corresponding to the cases (1),(1),(1),(1),(2). The periodic pattern was certainly weaker but still present. Indeed the shorter TR allowed to limit the

BOLD signal gap, and therefore the difference in the activation levels but the effect remained visible.

For this reason, another version of the CEST-LS  $\text{grad}_{\text{opp}}$  sequence was tested in experiment 2.

### 5.5.2 Experiment 2

As Table 5.3 suggests, experiment 2 differs from experiment 1.1 and 1.2 because it was based on the version of CEST-LS  $\text{grad}_{\text{opp}}$  that uses the block sign design. This version of the sequence is schematically represented in Figure 5.10C. To avoid the problem faced with experiment 1.1 and 1.2, this new version of CEST-LS  $\text{grad}_{\text{opp}}$  was based on the acquisition of a whole stimulation block with only positive gradient followed by the acquisition of the following stimulation block with only negative gradient. The TR was kept at 1.5 s, and the number of repetitions within one sign block was 32, because this allowed to cover one complete stimulation bloc (27 s ON and 21 s OFF periods).

With this version of the sequence, during the first block, positive profiles are acquired at each TR and during the following block, negative profiles are acquired at equivalent time points. We use the term "equivalent time points" to designate two points that are separated by 32 repetitions. By construction of the sequence, two equivalent time points occur at the same moment of the activation paradigm. Assuming the neuronal activation response is the same for both block, two equivalent time points correspond to two identical activation condition.

As shown in Figure 5.16, the processing was made so that every positive profile of a block was paired with the negative profile acquired 32 repetitions later in the following block. Experiment 2 therefore aims at acquiring a positive profile and its corresponding negative one in the same activation conditions.

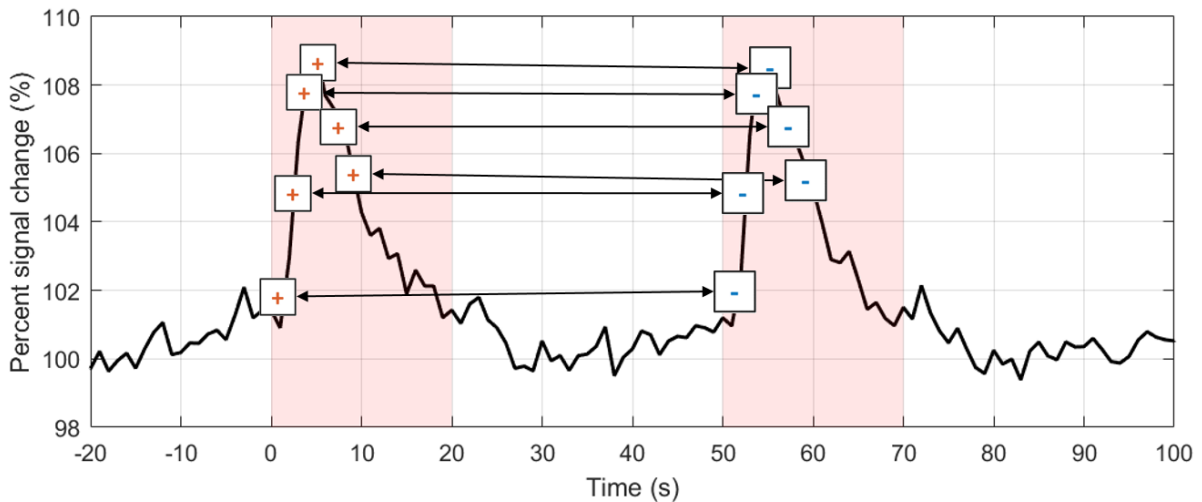


Figure 5.16: Schematic representation of the principle used in CEST-LS  $grad_{opp}$  with block in experiment 2. The "+" and "-" squares show the time positioning of the positive, resp. negative profile acquisition. The black arrow represents which profile are paired together to form a R-spectrum.

Four rats were scanned with the protocol of experiment 2. This time, no regular pattern common to every saturation offset was observed in the R-spectra covering the activated area. This shows that this new protocol allowed to reduce the bias observed with experiments 1.1 and 1.2.

Unfortunately, no conclusion could be made regarding metabolic changes due to neuronal activation because no correlation was detected between the activation paradigm and R-spectrum changes at any specific saturation offset. Our primary explanation is that the assumption of similarity/repeatability for two consecutive neuronal activation response is not satisfied. With limited time, only four rats could be scanned. Figure 5.17 shows the BOLD response obtained for the rat that had the most important and the most stable activation. It appears clearly that two consecutive stimulation block do not generate exactly the same temporal activation response. Figure 5.16 was first intended to describe the principle of experiment 2 but is actually presented on the experimental BOLD signal obtained for a rat scanned in the previous experiments. This BOLD time course is sufficiently stable for two paired profiles to actually be acquired in equivalent activation conditions. Indeed, the arrows pointing at two equivalent time points are almost all horizontal. If such a stable activation was obtained, we believe experiment 2 could bear fruit.

Over all experiments (1.1, 1.2 and 2), such a stability was obtained only for few animals. This might be influenced by the animal position (despite a good head positioning, very small head movements could still impact the activation and its detection using CEST MR), the animal response to anesthesia (a very well anesthetized animal is more likely to generate a regular response to the same stimulation block). To get a significant result, many more repetitions would be necessary in order to increase the statistical power. Another improvement axis would be to test other stimulation protocols and select the one that generates the most stable activations.

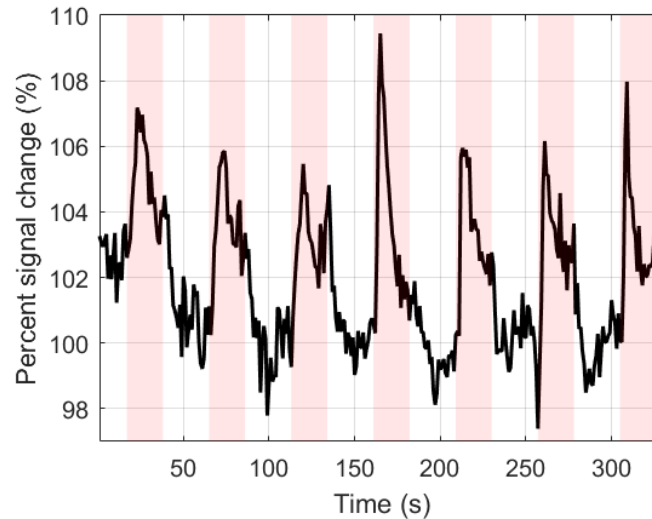


Figure 5.17: Temporal BOLD signal collected in the activated area during experiment 2 (with a stimulation pattern of 21 s ON, 27 s OFF) The pale pink rectangles represent the ON-stimulation period.

### 5.5.3 Conclusion

In this chapter, the objective was to apply the previously developed tools to the detection of transient metabolic changes during neuronal activation.

In a preliminary study, we showed that combining the ultrafast CEST-LS sequence together with the PEAKIT analysis tool allows to successfully detect metabolic changes due to a controlled pH decrease generated through an experiment of hypercapnia. Dynamic changes of the amide and amine CEST contributions were simultaneously tracked. The analysis with PEAKIT allowed to conclude that a pH decrease lead to a decrease in the APT-CEST contrast and an increase of the amine CEST contrast.

Based on this result, we further developed the approach in order to apply it to the detection of metabolic changes induced by a neuronal activation triggered with an electrical forepaw stimulation. Besides the high temporal resolution and good signal stability necessary to detect small metabolic changes, appropriate adjustments of the sequence and acquisition protocol were necessary to eliminate confounding factors (BOLD, increase in cerebral blood flow (CBF)). To do so, the CEST-LS  $\text{grad}_{opp}$  sequence was elaborated. This technique is directly derived from the previously introduced CEST-LS to which we have added the following modifications: (1) the saturation module was modified so that the saturation pulse was always turned on and the sign of the saturation gradient alternates every TR. The associated processing strategy was changed to the computation of the ratio between a profile obtained with a water profile acquired with a positive gradient divided by the following water profile acquired with a negative gradient; (2) The readout module was changed to a spin-echo approach; (3) the TE was reduced to 5 ms.

With these modifications designed to minimize the BOLD confound, experiments 1.1 and 1.2 (with slightly different TR) were performed. The analysis of the results revealed that the R-spectrum values obtained in the activated part followed a temporal pattern directly

related to the acquisition parameters and more precisely to the distribution order of the acquisition gradient sign. From this findings, we concluded that using the CEST-LS  $\text{grad}_{opp}$  with a reasonable TR for CEST could not allow the acquisition of two consecutive profiles (necessary to generate a R-spectrum) in the same neuronal activation conditions. In other words, experiments 1.1 and 1.2 were influenced by BOLD (and therefore neuronal activation) variations over time.

To meet this new challenge, the "with block" version of the CEST-LS  $\text{grad}_{opp}$  was developed. This modification consists in the acquisition of positive profiles only during a complete stimulation block followed the acquisition negative profiles only during the next stimulation block. Experiment 2 was implemented with this final version of the sequence. Although it didn't lead to the detection of significant changes for any CEST contribution, very promising progress were made regarding the BOLD signal elimination. We believe that employing different stimulation paradigms that generates more stable activation responses and increasing the number of animals could help detect metabolic changes induced by neuronal activity.

If such a result were achieved,  $^1\text{H}$ - $^{13}\text{C}$  NMR spectroscopy and optogenetic experiments could be performed to validate our observations in functional CEST imaging and to refine our metabolic models. These validation experiments could be carried out thanks to a collaboration between NeuroSpin and the University of Münster in Germany.

Overall, we propose a BOLD-free protocol and processing strategies that allow to monitor CEST contributions over a wide customizable range of saturation offsets. Additionally, this protocol allows the simultaneous acquisition of the metabolic information both in an activated and in a control area.

An example of functional CEST was demonstrated in [Cember et al. 2022] where they used gluCEST contrast to measure changes in glutamate concentration in response to Transcranial Magnetic Stimulation (TMS) in the motor cortex of healthy human subjects. The possibility and the advantages of transferring our experiment to human scanners are discussed in 6.2.

# Chapter 6

## Conclusion and perspectives

The final chapter summarizes the results obtained in the previous chapters and discusses some of the challenges inherent to the CEST techniques. The potential perspectives of CEST in general and of the approaches presented in this manuscript are discussed.

### Contents

---

<b>6.1 General conclusion</b> . . . . .	<b>110</b>
<b>6.2 Perspectives</b> . . . . .	<b>112</b>
6.2.1 CEST quantification . . . . .	112
6.2.2 Human scanners and clinical perspectives . . . . .	113
6.2.2.1 <i>In vivo</i> detection of carnosine and its derivatives . . . . .	115
6.2.2.2 Detection of metabolic changes induced by neuronal activation	116
6.2.3 Conclusion . . . . .	116

---

## 6.1 General conclusion

The objective of this work was to develop and implement new CEST techniques at ultra-high field in order to push the boundaries of already achieved CEST-based technical advances.

CEST has proven to be a very powerful techniques to detect or image endogenous and fundamental neurometabolites with enhanced sensitivity, temporal and spatial resolutions that can exceed, under some conditions, those of direct  $^1\text{H}$ -NMR direct spectroscopy detection. The developing field of CEST MRI has potential to provide molecular information for diagnosing pathological and the detection of molecular responses to treatment. Promising applications in different disciplines (e.g. oncology, musculoskeletal sciences, physiology or neurosciences) have already been demonstrated.

The development of CEST sequences for *in vivo* detection is however never straightforward because the CEST response of a single metabolite depends not only on many experimental parameters ( $B_{1,sat}$ ,  $t_{sat}$ ,  $\delta$  ... ) but also varies with the characteristics of the *in vivo* tissue analyzed ( $T_1, T_2$ ) and the physiological properties (T, pH) . On top of that, the CEST response of the molecule of interest is always entangled to other CEST contributions coming from molecules responsible for CEST effects (or more general CEST contribution including MT and NOE) occurring at the same saturation offset range. Although it is possible to select the sequence parameters that optimize the CEST response of a certain molecule with respect to other CEST effects for given physiological conditions, the selection of specific CEST contributions and their quantification remains the main challenge that CEST studies have to face. Many data analysis strategies have been proposed to address this challenge.

The very first step of this project consisted in demonstrating the advantage of ultra-high magnetic fields for CEST imaging through an *in vitro* investigation of the CEST contrast of three major neurometabolites: glucose, lactate and glutamate at different magnetic field strengths (9.4, 11.7 and 17.2 T). The saturation powers were optimized for every metabolite for all three static fields and two temperatures (21 °C and 37 °C). The comparison of the CEST contrast obtained with these optimized parameters led to the conclusion that, for a given solute, the increase in  $B_0$  always results in an increase in the CEST contrast. The other very precious technical advantage that comes with ultra high field is the higher chemical shift dispersion and therefore the better resolved Z-spectrum. The CEST experiment run on a mixture sample allowed to demonstrate that CEST-contrast specificity towards a certain metabolite increases with increasing  $B_0$  field strength. Finally, at higher magnetic fields, the longitudinal relaxation times  $T_1$  relaxation times of water and metabolites (in tissues) are generally longer. This allows to apply longer saturation efficiently and to increase the observable CEST contrast. For all the reasons given above, the highest magnetic field (17.2 T) magnet was used for every experiment presented in the rest of this manuscript. In this *in vitro* study, the influence of minor pH changes on the CEST contrast value and the position of the maximum CEST contrast was also investigated. Furthermore, it was also demonstrated that, for a given  $B_0$ , it is also possible to favor a specific CEST contrast (glucoCEST or gluCEST) by tuning the  $B_{1,sat}$ .

In the perspective of limiting signal instabilities over time due to frequency drifts and physiologically induced noise, a new sequence called CEST-LS based on a method proposed in [X. Xu, J.-S. Lee, and Jerschow 2013] was developed. To build the CEST-LS sequence, we

started from a traditional CEST sequence and we added a pair of gradient during the saturation module and the readout module, we eliminated the phase encode and we added saturation bands. Examples of *in vitro* CEST-LS acquisitions and data processing were presented. With this new concept, the acquisition of a Z-spectrum only requires two TRs. This very fast method opens the door for higher time resolution, which can be useful in both static and dynamic experiments. In case of a static experiments (measurement of a constant Z-spectrum), this higher temporal resolution allows better signal stability because it makes the CEST detection less sensitive to frequency variations and physiological drifts over time. In case of dynamic experiments (with expected metabolic changes), being able to acquire a Z-spectrum fast promises to detect CEST contrast changes in real time.

In parallel with the implementation of the CEST-LS sequence, the development and testing of an analysis tool called PEAKIT was realized. This work was made in collaboration with Michele Lecis, a master thesis student in our team. PEAKIT is a software tool designed for the detection and characterization of CEST peaks present in a Z-spectrum. Compared to other existing tools used for the detection and characterization of CEST peaks, PEAKIT has the advantage that it does not require assumptions regarding the frequency offset of peaks, their shape and the underlying value of the local baseline. After a baseline estimation based on Gaussian Process regression, PEAKIT outputs the chemical shift offsets, the areas, the heights and the statistical significance of the detected peaks. The performance of the tool was demonstrated and evaluated through the analysis of *in vitro* and *in vivo* CEST data acquired using the CEST-LS sequence.

With the help of those two acquisition and analysis tools specifically designed for the detection of tenuous CEST effects, we demonstrated, for the first time, the *in vivo* detection of carnosine and its derivatives. Carnosine is an endogenous dipeptide with important antioxidant functions known to be involved notably in the cellular response to high levels of inflammation. The CEST effects of carnosine, anserine and homocarnosine were first characterized in phantoms, demonstrating the possibility to separate individual contributions by employing high spectral resolution (0.005 ppm) and low CEST saturation power (0.15  $\mu$ T). The CEST signature of these peptides was then evidenced, *in vivo*, in the rat brain and skeletal muscle. The presence of carnosine and anserine in the muscle was corroborated by *in vivo* localized  $^1\text{H}$ -NMR spectroscopy. However, the sensitivity of MRS was insufficient for carnosine and homocarnosine detection in the brain. The absolute amounts of carnosine and derivatives in the investigated tissues were determined by liquid chromatography–electrospray ionization–tandem mass spectrometry using isotopic dilution standard methods and were in agreement with the CEST results. The robustness of the CEST-linescan approach and the favorable conditions for CEST at ultra-high magnetic field combined with the great characterization performances of the PEAKIT analysis tool allowed the *in vivo* CEST detection of carnosine and related peptides in the skeletal muscle and in the brain (olfactory bulb and neocortex).

In the last part of this project, we focused on adapting the ultrafast CEST-LS sequence for the investigation of dynamic metabolic changes in the rat brain. Through a preliminary study, we demonstrated the possibility to detect changes in the CEST contrast during the induction of a controlled pH decrease with a hypercapnia experiment. The analysis with PEAKIT allowed to conclude that a pH decrease lead to a decrease in the APT-CEST contrast and an increase of the amine CEST contrast. We then focused our work on monitoring

metabolic changes induced by neuronal activation triggered by an electrical forepaw stimulation in rats. We made several sequence modifications and implemented various acquisition strategies in order to minimize the BOLD contribution and improve the sensitivity and (biochemical) specificity of the CEST signal. Among other adjustments, an experimental protocol involving a new CEST module was proposed and implemented. The new version of the CEST-LS sequence was called CEST-LS  $\text{grad}_{\text{opp}}$  and is based on the computation of the ratio between the water signal obtained at a certain saturation offset divided by the water signal obtained at the opposite saturation offset. Even though the results obtained did not allow us to detect significant changes in specific CEST contributions during the functional task, we conclude that the imaging protocols developed are promising. By employing stimulation paradigms optimized for stable activation responses and increasing the number of animals for higher statistical power, we expect to be able to pinpoint transient metabolic changes driven by neuronal activity.

Overall, this project demonstrated that although CEST-based methods are challenging, ultra-high fields and methodological developments promise to allow its exploitation for advanced *in vivo* studies. Further development of advanced CEST MR sequences have great potential to improve the sensitivity and sensitivity of the detection and open new perspectives into studying brain metabolism.

## 6.2 Perspectives

In addition to the perspectives listed in each chapter, we focus here on two key aspects of CEST, which may determine the viability of the technique in the future.

### 6.2.1 CEST quantification

Although CEST is a powerful method providing information on the presence or absence of a given metabolite, extracting quantitative information from  $Z$ -spectra can be challenging due to the overlap of multiple contributions, the contamination from non-CEST signals and the limited knowledge about the characteristics of different exchanging pools. Accurate and complete assignment of all CEST contributions to a group of molecules is a task that remains to be solved. Quantification of signals is the crux of the matter for analysis of CEST data. Without this tool, applications of the CEST method will be limited to relative results and will always rely on the existence of a priori information or previously calibrated data. If a robust quantification method were established, the CEST method would take a step forward and could complement or replace other metabolic measurement modalities.

As presented in section 3.3, many promising analysis techniques have been developed but they all have one of the following drawbacks: need for a priori knowledge on the number of pools and their corresponding chemical shift, long acquisition times, introduction of errors due to the approximations made in using analytical solutions, accuracy limited by the size of the dictionaries (with MRF).

In this manuscript, PEAKIT is proposed as an alternative approach to quantifying CEST peaks, which requires no prior assumptions about the frequency offset or the underlying shape of the baseline. PEAKIT is able to identify relatively fine peaks that clearly stand out from the baseline but cannot analyze much broader CEST contributions like glutamate or

NOE. PEAKIT outputs the chemical shift offset of the detected CEST peak but the latter is affected to a given molecule thanks to a former *in vitro* study. PEAKIT also computes the area and the height of the detected peak but does not allow to infer the concentration of the detected molecule.

It is true that all the different analysis tools developed can answer specific questions and will increase the readability of the acquired CEST data, but the approaches remain semi-quantitative. Nowadays, methods based on deep learning are growing exponentially and multiplying their applications in all scientific fields. We could also consider using them to interpret CEST data by providing large databases acquired on phantoms and *in vivo* tissues necessary for the learning phase. Such approaches could potentially help design an universal and robust quantification tool. Developing a solid and reliable biomarker of brain metabolites would open up new possibilities in the CEST domain.

### 6.2.2 Human scanners and clinical perspectives

It is important to keep in mind that these technical insights are designed in order to be transposed to human scanners, and even to later be commonly used in the medical field. The knowledge gained at ultra-high fields allows to further develop the protocols and understand the CEST effects observable with clinical scanners. In this section, we present the advantages and challenges encountered when doing CEST experiments on human scanners and discuss the specific case of transposing the approaches presented in this manuscript to clinical use.

Because of the multiple technological challenges associated with building a whole body magnet, the human-sized MR scanners have lower magnetic field strength compared to state-of-the-art pre-clinical magnets. The most powerful human MR scanner is the 11.7 T ISEULT magnet installed at NeuroSpin and has recently unveiled its first images. In comparison, the most powerful horizontal preclinical magnetic resonance imaging system is the 17.2 T (NeuroSpin). While a few studies show that CEST effects are detectable at 3 or 4.7 T and can show hyperintensities in a brain region affected by tumor ([Heo, Y. Zhang, et al. 2016; W. Wei et al. 2014]), at these fields, CEST images suffer from low SNR and limited metabolic information. Indeed, such studies are very limited by the weak  $B_0$  which causes the following major drawbacks :

- The intrinsic SNR decreases linearly with decreasing  $B_0$  which is a disadvantage that can only be compensated by increasing the scan time or lowering the spatial resolution (increasing the voxel size).
- The chemical shift dispersion also decreases linearly with decreasing  $B_0$ . (1 ppm corresponds to 730 Hz at 17.2 T versus only 128 Hz at 3 T). The lower frequency separation makes the CEST peaks more difficult to differentiate and is also unfavorable to the detection of CEST resonances close to water like amine, guanidyl or hydroxyl groups.
- The relaxation time  $T_1$  decreases with decreasing  $B_0$ . A shorter  $T_1$  not only reduces the CEST effect but also limits the saturation duration and therefore reduces the efficiency of the saturation transfer from the saturated water pool to the solute pool.

These drawbacks are very limiting but alleviated in part by the increased availability of higher magnetic field human scanners. It has clearly become a consensus among the CEST

community that higher  $B_0$  (at least 7 T) allows to separate the CEST effects more clearly and allows the acquisition of better resolved CEST maps ([Zaiss, Windschuh, et al. 2015; Desmond, Moosvi, and Stanisz 2014; C. K. Jones, Polders, et al. 2012; C. K. Jones, A. Huang, et al. 2013; Zaiss, Ehses, and Scheffler 2018]). There are currently 98 high field MRI ( $B_0 \geq 7T$ ) human scanners installed worldwide, with most of them being 7 T scanners. The growing availability of 7T scanners in the research community suggests that these machines may be developed for clinical purposes in the near future, making CEST sequences potentially applicable for common use. However, performing CEST experiments with high-field human scanner requires facing the following two main challenges:

- The wavelength of the RF pulses (11 cm at 7 T) is smaller than the characteristic dimension of a human brain (20 cm) resulting in  $B_{1,sat}$  spatial inhomogeneities being more important than for a pre-clinical scanner. As a comparison, at 17.2 T, rat brains (2 cm characteristic dimension) only represent less than half of the RF pulse wavelength (5 cm). Without any correction, this problem can directly compromise the CEST effect because CEST effects strongly depend on the  $B_{1,sat}$  amplitude. Such an artifact can lead to misallocation of CEST signals and misinterpretation of CEST maps ([Windschuh et al. 2015]). This limitation is all the more problematic as the  $B_0$  increases.
- The Specific Absorption Rate (SAR) constraints are more restrictive for high field human scanner ([IEC 2010]). SAR refers to the amount of power deposited by a radiofrequency field in a certain mass of tissue. Though very complex to estimate in human subjects, simple models have provided considerable insight into the factors contributing to SAR and show that SAR increases with body size, and is proportional to the square of RF amplitude ( $B_1^2$ ) and to the square of the static magnetic field ( $B_0^2$ ). This explains why the allowed power range is often limited at high field. These restrictions are also more complex to deal with when the  $B_0$  field increases. The drawback mentioned above of shorter T1 at 7 T compared to ultra-high preclinical scanner is not as evident in practice since most of the time, the maximum  $t_{sat}$  is not reached because of SAR constraints.

Several solutions have been proposed to address the ongoing challenge of  $B_{1,sat}$  inhomogeneity. Post-processing strategies using roughly sampled calibration values ([Singh et al. 2013]) or acquisitions at different  $B_{1,sat}$  ([Windschuh et al. 2015]) have shown the possibility to correct for  $B_{1,sat}$  inhomogeneities. Although they provide a first solution, these strategies increase the total scan time and are not very accurate. Parallel transmission imaging ([Katscher and Börnert 2006; Padormo et al. 2016]) has emerged as a robust solution for mitigating  $B_{1,sat}$  inhomogeneities in CEST acquisitions at high field ([Silva et al. n.d.; Liebert et al. 2019]). Parallel transmission uses multiple RF transmit coils in order to create a more uniform transmit field. The technique is very promising but requires a careful optimization to improve the field homogeneity while staying below the SAR limits. Thaddée Delebarre, a PhD student in our team specifically works on the development of a CEST imaging sequences on a clinical 7 T Siemens scanner using parallel transmission.

Aside from the technical solutions, our team is also working to develop neural network algorithms capable of taking as input a Z-spectrum acquired at 7 T and outputting the equivalent Z-spectrum as if it had been acquired at 17 T. The project is still at a very early stage of development but may eventually take advantage of UHF acquisition conditions (like 17 T) by working with data initially acquired at lower field strength (including human data).

In summary, the high selectivity and signal-to-noise ratio provided by high-field human scanners, combined with promising techniques to overcome the technical hurdles raised by high fields, open up CEST applications to modern human scanners. Many studies have already showed potential clinical relevance and other provide deeper understanding of CEST effects.

At lower field strength, the experiments presented in this manuscript will encounter some of the obstacles mentioned but each situation is specific and comes with its own set of challenges and requirements.

### 6.2.2.1 *In vivo* detection of carnosine and its derivatives

Regarding the detection of carnosine, we believe that CEST approaches as the ones presented in this manuscript could potentially be extended to human studies.

The optimal  $B_{1,sat}$  power for *in vivo* carnosine detection is relatively low at  $1 \mu\text{T}$ , and therefore compatible with the specific absorption rate constraints imposed for human brain investigations. Carnosine presents a CEST contribution at 3.3 ppm away from water and therefore its detection is not dramatically affected by direct water saturation with the considered  $B_{1,sat}$  values. Numerical simulations performed at 11.7, 7 and 3 T show a carnosine CEST effect decrease by 8, 23 and 48 %, respectively, compared to that at 17.2 T.

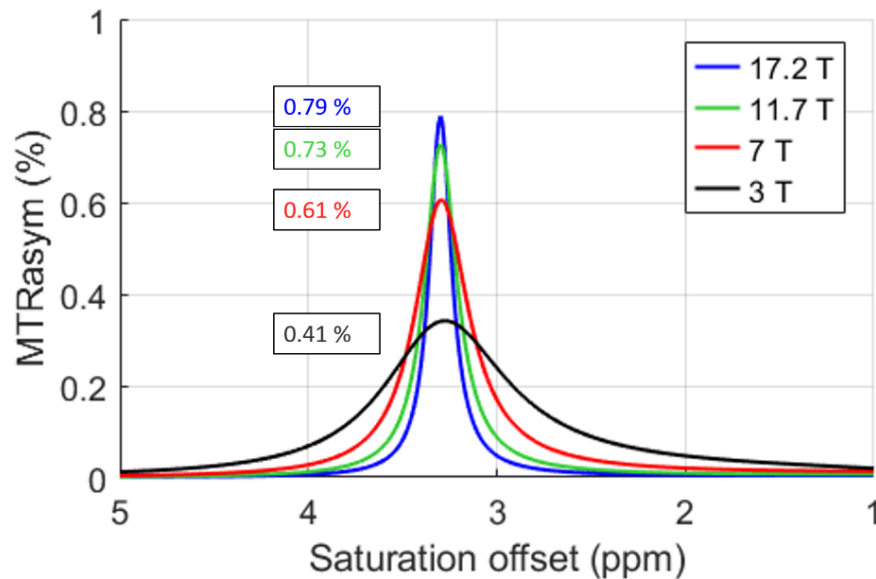


Figure 6.1: Simulated  $MTR_{asym}$  for a 10 mM carnosine solution at four different  $B_0$  magnetic fields: 3 T, 7 T, 11.7 T and 17.2 T. The Bloch-McConnell equations were solved using a two-pool exchange model and employing the Matlab tool “CEST sources” available at [www.cest-sources.org](http://www.cest-sources.org). For simulations, the relaxation parameters of gray matter water were taken to be  $T_1 = 1, 1.7, 2.1, 2.3$  s and  $T_2 = 0.08, 0.055, 0.035, 0.03$  s for  $B_0 = 3, 7, 11.7, 17.2$  T, respectively [Graaf et al. 2006; Yacoub et al. 2001; Lopez-Kolkovsky, Sebastien Mériaux, and Boumezbeur 2016; Wansapura et al. 1999]; the exchange rate of carnosine was set at 50 Hz and the saturation module consisted in 10 rectangular pulses of 400 ms duration with a duty cycle of 0.98.

This decrease will certainly make the *in vivo* detection of carnosine and derivatives at lower magnetic fields more challenging. However, we believe that the decrease is sufficiently

small ( $\leq 25\%$ ) for high magnetic field scanners (with  $B_0 \geq 7$  T) to allow the CEST detection of homocarnosine/carnosine in the human brain or anserine/carnosine in the skeletal muscle.

### 6.2.2.2 Detection of metabolic changes induced by neuronal activation

The authors of [Cember et al. 2022] have already demonstrated the possibility of using gluCEST as a way to measure changes in glutamate concentration in response to Transcranial Magnetic Stimulation in the motor cortex of healthy human subjects. This is a first step towards detecting metabolic changes induced by more natural stimulations such as visual or sensory stimulations. Compared to our preclinical study, many changes due to the translation to human scanners must be taken into account. Table 6.1 gives a non-exhaustive list of the advantages and disadvantages of using a human scanner for detecting metabolic changes induced by neuronal activation using CEST.

Advantages		Drawbacks	
less BOLD confound	+	lower intrinsic SNR	-
awake stimulation	+++	smaller chemical shift dispersion	--
reduced magnetic susceptibility artifacts	++	SAR constraints	---
		$B_{1,sat}$ inhomogeneities	-

Table 6.1: Advantages and drawbacks of human scanners for the CEST detection of metabolic changes induced by neuronal activation. The columns with "+" and "-" indicate the weight of each advantage and drawback.

The weaker BOLD sensitivity available at low field ([Ogawa, R. Menon, et al. 1993; Turner et al. 1993; Gati et al. 1997; Yacoub et al. 2001]) would surely become, in the case of our experiment, an additional lever to minimize BOLD confound. We do not consider this to be a major advantage since our acquisitions and processing strategies are meant to minimize BOLD confounds anyway. The biggest advantage of human studies is the possibility to study the stimulation performed on awake subjects. With no anesthesia, the neuronal activity and brain metabolism are no longer reduced. The metabolic changes induced by neuronal activation are both closer to natural processes and more important than with anesthesia, and therefore easier to detect. Working with no anesthesia also limits the neuronal response variability (within and between subjects) which confers an undeniable bonus to human experiment compared to rodents studies. These advantages combined with the generally reduced magnetic susceptibility artifacts can potentially outweigh the aforementioned drawbacks of CEST in clinical studies. By choosing the stimulation paradigm that elicits the most stable neuronal response over time and carefully tailoring the sequence parameters to the SAR constraints, the implementation of this experiment in clinical scanners could possibly allow the detection of metabolic changes induced by neuronal activation in humans.

### 6.2.3 Conclusion

Even though the high and ultra-high fields pre-clinical studies offer better chances to push the boundaries of CEST methods, they are always a first step towards their implementation in human protocols. With the significant advancements reported both in the acquisition strategies and processing pipelines and the increasing availability of high-field humans scanners, CEST MRI techniques are progressively making the leap from research to clinical

diagnostic use in the human brain.



# Chapter 7

## List of publications

The projects of this PhD thesis led to several publications and scientific communications.

### Peer-reviewed articles

- **S Bardin**, M Lecis, D Boido, G Baron, G Aldini, P Berthault, F Boumezbeur and L Ciobanu, *In vivo detection of carnosine and its derivatives using chemical exchange saturation transfer*, Magnetic Resonance in Medicine 2022
- M Lecis, **S Bardin**, CI Ciobanu, and L Ciobanu, *PEAKIT: A Gaussian Process regression analysis tool for chemical exchange saturation transfer spectra* Journal of Magnetic Resonance 2022, 334:107122.
- D Schache, **S Bardin**, L Ciobanu, C Faber and V Hoerr, *Ultrafast CEST line scanning as a method to quantify mutarotation kinetics*, Journal of Magnetic Resonance 2022, 342:107270.

### Conference communications

- **S Bardin**, F Boumezbeur and L Ciobanu, *Acquisition and data processing considerations in functional metabolic imaging using CEST*, ISMRM 2022, London - poster and power pitch
- I Uszynski, L Ciobanu, **S Bardin**, P Estienne, K Yamamoto and C Poupon, *Towards an ultra-high resolution structural connectivity atlas of the parrot brain using extreme high-field 17.2T diffusion MRI*, ISMRM 2022, London - oral
- **S Bardin**, M Lecis, D Boido, F Boumezbeur and L Ciobanu, *First in vivo detection of carnosine using CEST*, ISMRM 2021, Vancouver - e-oral ("Magna cum laude" award)
- D Schache, **S Bardin**, L Ciobanu, C Faber and V Hoerr, *Glucose mutarotation kinetics determined by ultrafast CEST line scanning*, ESMRMB 2021, online - poster
- **S Bardin**, H Lambers, D Schache, JR Krug, C Faber, F Boumezbeur and L Ciobanu, *CEST signal at different magnetic fields and temperature conditions for three main brain metabolites*, ESMRMB 2020, Barcelona - e-poster
- JR Krug, **S Bardin**, H Lambers, H Van Asa, AH Veldersa, C Faber, F Boumezbeur and L. Ciobanu - *Metabolic specificity analysis of CEST techniques at high and ultra-high magnetic fields* - ICMRM 2019, Paris - oral



# Chapter 8

## Bibliography

- Aime, Silvio, Alessandro Barge, et al. (2002). "Paramagnetic lanthanide (III) complexes as pH-sensitive chemical exchange saturation transfer (CEST) contrast agents for MRI applications". In: *Magnetic Resonance in Medicine: An Official Journal of the International Society for Magnetic Resonance in Medicine* 47.4, pp. 639–648.
- Aime, Silvio, Daniela Delli Castelli, and Enzo Terreno (2005). "Highly sensitive MRI chemical exchange saturation transfer agents using liposomes". In: *Angewandte Chemie International Edition* 44.34, pp. 5513–5515.
- Aldini, Giancarlo, Barbora de Courten, et al. (2020). "Understanding the antioxidant and carbonyl sequestering activity of carnosine: direct and indirect mechanisms". In: *Free Radical Research* 55, pp. 321–330.
- Aldini, Giancarlo, Roberto Maffei Facino, et al. (2005). "Carnosine and related dipeptides as quenchers of reactive carbonyl species: from structural studies to therapeutic perspectives". In: *Biofactors* 24.1-4, pp. 77–87.
- Arnold, JT and ME Packard (1951). "Variations in absolute chemical shift of nuclear induction signals of hydroxyl groups of methyl and ethyl alcohol". In: *The Journal of Chemical Physics* 19.12, pp. 1608–1609.
- Baguet, Evelyne and Claude Roby (1997). "Off-resonance irradiation effect in steady-state NMR saturation transfer". In: *Journal of Magnetic Resonance* 128.2, pp. 149–160.
- Bandettini, Peter A et al. (1994). "Spin-echo and gradient-echo EPI of human brain activation using BOLD contrast: a comparative study at 1.5 T". In: *NMR in Biomedicine* 7.1-2, pp. 12–20.
- Bardin, Solène et al. (2022). "In vivo detection of carnosine and its derivatives using chemical exchange saturation transfer". In: *Magnetic Resonance in Medicine*.
- Beauchamp, Antoine et al. (2022). "Whole-brain comparison of rodent and human brains using spatial transcriptomics". In: *bioRxiv*.
- Bednarik, Petr et al. (2015). "Neurochemical and BOLD responses during neuronal activation measured in the human visual cortex at 7 Tesla". In: *Journal of Cerebral Blood Flow & Metabolism* 35.4, pp. 601–610.

- Bingel, Ulrike et al. (2003). “Single trial fMRI reveals significant contralateral bias in responses to laser pain within thalamus and somatosensory cortices”. In: *Neuroimage* 18.3, pp. 740–748.
- Bloch, Felix (1946). “Nuclear induction”. In: *Physical review* 70.7-8, p. 460.
- Bodet, Olga et al. (2015). “Amide proton transfer of carnosine in aqueous solution studied in vitro by WEX and CEST experiments”. In: *NMR in Biomedicine* 28.9, pp. 1097–1103.
- Boldyrev, AA et al. (1988). “Antioxidative properties of histidine-containing dipeptides from skeletal muscles of vertebrates.” In: *Comparative Biochemistry and physiology. B, Comparative Biochemistry* 89.2, pp. 245–250.
- Boldyrev, Alexander A, Giancarlo Aldini, and Wim Derave (2013). “Physiology and pathophysiology of carnosine”. In: *Physiological reviews*.
- Bonfanti, Luca et al. (1999). “Carnosine-related dipeptides in the mammalian brain”. In: *Progress in neurobiology* 59.4, pp. 333–353.
- Boutin, Céline et al. (2013). “Ultrafast z-spectroscopy for  $^{129}\text{Xe}$  NMR-based sensors”. In: *The journal of physical chemistry letters* 4.23, pp. 4172–4176.
- Brown, Walter E, LeRoy W Schroeder, and James S Ferris (1979). “Interlayering of crystalline octacalcium phosphate and hydroxylapatite”. In: *Journal of Physical Chemistry* 83.11, pp. 1385–1388.
- Cai, Kejia, Mohammad Haris, et al. (2012). “Magnetic resonance imaging of glutamate”. In: *Nature medicine* 18.2, pp. 302–306.
- Cai, Kejia, Anup Singh, et al. (2015). “CEST signal at 2 ppm (CEST@ 2ppm) from Z-spectral fitting correlates with creatine distribution in brain tumor”. In: *NMR in biomedicine* 28.1, pp. 1–8.
- Castelli, Daniela Delli et al. (2008). “Metal containing nanosized systems for MR-molecular imaging applications”. In: *Coordination Chemistry Reviews* 252.21-22, pp. 2424–2443.
- Cember, Abigail TJ et al. (2022). “Glutamate-Weighted Magnetic Resonance Imaging (GluCEST) Detects Effects of Transcranial Magnetic Stimulation to the Motor Cortex”. In: *NeuroImage* 256, p. 119191.
- Chahid, Bochra et al. (2014). “Entrapment of a neutral Tm (III)-based complex with two inner-sphere coordinated water molecules into PEG-stabilized vesicles: towards an alternative strategy to develop high-performance LipoCEST contrast agents for MR imaging”. In: *Contrast Media & Molecular Imaging* 9.6, pp. 391–399.
- Chan, Kannie WY et al. (2012). “Natural D-glucose as a biodegradable MRI contrast agent for detecting cancer”. In: *Magnetic resonance in medicine* 68.6, pp. 1764–1773.
- Chekanov, SV and M Erickson (2013). “A nonparametric peak finder algorithm and its application in searches for new physics”. In: *Advances in High Energy Physics* 2013.
- Chen, Lin et al. (2021). “Early detection of Alzheimer’s disease using creatine chemical exchange saturation transfer magnetic resonance imaging”. In: *NeuroImage* 236, p. 118071.

- Chen, Wei et al. (1993). “Localized  $^1\text{H}$  NMR measurement of glucose consumption in the human brain during visual stimulation.” In: *Proceedings of the National Academy of Sciences* 90.21, pp. 9896–9900.
- Crescenzi, Rachele et al. (2014). “In vivo measurement of glutamate loss is associated with synapse loss in a mouse model of tauopathy”. In: *Neuroimage* 101, pp. 185–192.
- Dagher, Azar P et al. (2000). “Imaging of urea using chemical exchange-dependent saturation transfer at 1.5 T”. In: *Journal of Magnetic Resonance Imaging* 12.5, pp. 745–748.
- Davies, Jack N and Ronald J Kempton (1975). “Changes in the individual sugars of tomato fruit during ripening”. In: *Journal of the Science of Food and Agriculture* 26.8, pp. 1103–1110.
- Davis, Karen D et al. (1998). “Functional MRI study of thalamic and cortical activations evoked by cutaneous heat, cold, and tactile stimuli”. In: *Journal of Neurophysiology* 80.3, pp. 1533–1546.
- Davis, Kathryn Adamiak et al. (2015). “Glutamate imaging (GluCEST) lateralizes epileptic foci in nonlesional temporal lobe epilepsy”. In: *Science translational medicine* 7.309, 309ra161–309ra161.
- Davis, Kenneth L et al. (2002). *Neuropsychopharmacology: the fifth generation of progress: an official publication of the American College of Neuropsychopharmacology*. Lippincott Williams & Wilkins.
- DeBrosse, Catherine et al. (2016). “Lactate chemical exchange saturation transfer (LATEST) imaging in vivo: a biomarker for LDH activity”. In: *Scientific reports* 6.1, pp. 1–10.
- Desmond, Kimberly L, Firas Moosvi, and Greg J Stanisiz (2014). “Mapping of amide, amine, and aliphatic peaks in the CEST spectra of murine xenografts at 7 T”. In: *Magnetic resonance in medicine* 71.5, pp. 1841–1853.
- Dutka, T. L. et al. (2012). “Effects of carnosine on contractile apparatus  $\text{Ca}^{2+}$  sensitivity and sarcoplasmic reticulum  $\text{Ca}^{2+}$  release in human skeletal muscle fibers”. In: *Journal of Applied Physiology* 112, pp. 728–736.
- El Mamoune, Kahina et al. (2021). “Application of chemical exchange saturation transfer (CEST) in neuroimaging”. In: *Journal of Chemical Neuroanatomy* 114, p. 101944.
- Ellenbroek, Bart and Jiun Youn (2016). “Rodent models in neuroscience research: is it a rat race?” In: *Disease models & mechanisms* 9.10, pp. 1079–1087.
- Flament, Julien et al. (2013). “In vivo CEST MR imaging of U87 mice brain tumor angiogenesis using targeted LipoCEST contrast agent at 7 T”. In: *Magnetic Resonance in Medicine* 69.1, pp. 179–187.
- Forsén, Sture and Ragnar A Hoffman (1963). “Study of moderately rapid chemical exchange reactions by means of nuclear magnetic double resonance”. In: *The Journal of Chemical Physics* 39.11, pp. 2892–2901.

- Garwood, Michael and Lance DelaBarre (2001). “The return of the frequency sweep: designing adiabatic pulses for contemporary NMR”. In: *Journal of magnetic resonance* 153.2, pp. 155–177.
- Gati, Joseph S et al. (1997). “Experimental determination of the BOLD field strength dependence in vessels and tissue”. In: *Magnetic resonance in medicine* 38.2, pp. 296–302.
- github.com/SheffieldML (2018). “GPy: A Gaussian process framework in python, 2018for new physics”. In: <https://github.com/SheffieldML/GPy>.
- Goffeney, Nicholas et al. (2001). “Sensitive NMR detection of cationic-polymer-based gene delivery systems using saturation transfer via proton exchange”. In: *Journal of the American Chemical Society* 123.35, pp. 8628–8629.
- Govind, Varan, Karl Young, and Andrew A Maudsley (2015). “Corrigendum: proton NMR chemical shifts and coupling constants for brain metabolites. Govindaraju V, Young K, Maudsley AA, *NMR Biomed.* 2000; 13: 129–153”. In: *NMR in biomedicine* 28.7, pp. 923–924.
- Govindaraju, Varanavasi, Karl Young, and Andrew A Maudsley (2000). “Proton NMR chemical shifts and coupling constants for brain metabolites”. In: *NMR in Biomedicine: An International Journal Devoted to the Development and Application of Magnetic Resonance In Vivo* 13.3, pp. 129–153.
- Graaf, Robin A de et al. (2006). “High magnetic field water and metabolite proton T1 and T2 relaxation in rat brain in vivo”. In: *Magnetic resonance in medicine: An official journal of the international society for magnetic resonance in medicine* 56.2, pp. 386–394.
- Grad, Jonathan et al. (1991). “Applications of nuclear magnetic cross-relaxation spectroscopy to tissues”. In: *Magnetic resonance in medicine* 17.2, pp. 452–459.
- Guivel-Scharen, V et al. (1998). “Detection of proton chemical exchange between metabolites and water in biological tissues”. In: *Journal of Magnetic Resonance* 133.1, pp. 36–45.
- Haris, Mohammad, Kavindra Nath, et al. (2013). “Imaging of glutamate neurotransmitter alterations in Alzheimer’s disease”. In: *NMR in biomedicine* 26.4, pp. 386–391.
- Haris, Mohammad, Anup Singh, et al. (2013). “MICEST: a potential tool for non-invasive detection of molecular changes in Alzheimer’s disease”. In: *Journal of neuroscience methods* 212.1, pp. 87–93.
- Harris, Robert J et al. (2015). “pH-weighted molecular imaging of gliomas using amine chemical exchange saturation transfer MRI”. In: *Neuro-oncology* 17.11, pp. 1514–1524.
- Harris, Roger C et al. (2006). “The absorption of orally supplied  $\beta$ -alanine and its effect on muscle carnosine synthesis in human vastus lateralis”. In: *Amino acids* 30.3, pp. 279–289.
- Harston, George WJ et al. (2015). “Identifying the ischaemic penumbra using pH-weighted magnetic resonance imaging”. In: *Brain* 138.1, pp. 36–42.

- Heo, Hye-Young, Dong-Hoon Lee, et al. (2017). “Insight into the quantitative metrics of chemical exchange saturation transfer (CEST) imaging”. In: *Magnetic resonance in medicine* 77.5, pp. 1853–1865.
- Heo, Hye-Young, Yi Zhang, et al. (2016). “Quantitative assessment of amide proton transfer (APT) and nuclear overhauser enhancement (NOE) imaging with extrapolated semisolid magnetization transfer reference (EMR) signals: II. Comparison of three EMR models and application to human brain glioma at 3 Tesla”. In: *Magnetic resonance in medicine* 75.4, pp. 1630–1639.
- Hipkiss, Alan R (2011). “Energy metabolism, proteotoxic stress and age-related dysfunction—Protection by carnosine”. In: *Molecular Aspects of Medicine* 32.4-6, pp. 267–278.
- Hua, Jun et al. (2007). “Quantitative description of the asymmetry in magnetization transfer effects around the water resonance in the human brain”. In: *Magnetic Resonance in Medicine: An Official Journal of the International Society for Magnetic Resonance in Medicine* 58.4, pp. 786–793.
- Huang, Shuning et al. (2017). “Quantitative chemical exchange saturation transfer (CEST) imaging with magnetic resonance fingerprinting (MRF)”. In: *Proceedings of the 25th Annual Meeting of ISMRM, Honolulu, HI*, p. 196.
- Hyder, Fahmeed et al. (1997). “Oxidative glucose metabolism in rat brain during single forepaw stimulation: a spatially localized  $^1\text{H}$  [ $^{13}\text{C}$ ] nuclear magnetic resonance study”. In: *Journal of Cerebral Blood Flow & Metabolism* 17.10, pp. 1040–1047.
- IEC (2010). “International Electrotechnical Commission. International standard, medical electrical equipment. Part 2. Particular requirements for the safety of magnetic resonance equipment for medical diagnosis. At : Geneva: International Electrotechnical Commission”. In: 3rd ed.
- Jeong, Ha-Kyu et al. (2017). “Characterizing amide proton transfer imaging in haemorrhage brain lesions using 3T MRI”. In: *European radiology* 27.4, pp. 1577–1584.
- Jia, Guang et al. (2011). “Amide proton transfer MR imaging of prostate cancer: a preliminary study”. In: *Journal of Magnetic Resonance Imaging* 33.3, pp. 647–654.
- Jiang, Shanshan et al. (2016). “Molecular MRI differentiation between primary central nervous system lymphomas and high-grade gliomas using endogenous protein-based amide proton transfer MR imaging at 3 Tesla”. In: *European radiology* 26.1, pp. 64–71.
- Jones, Craig K, Alan Huang, et al. (2013). “Nuclear Overhauser enhancement (NOE) imaging in the human brain at 7 T”. In: *Neuroimage* 77, pp. 114–124.
- Jones, Craig K, Daniel Polders, et al. (2012). “In vivo three-dimensional whole-brain pulsed steady-state chemical exchange saturation transfer at 7 T”. In: *Magnetic resonance in medicine* 67.6, pp. 1579–1589.
- Jones, Craig K, Michael J Schlosser, et al. (2006). “Amide proton transfer imaging of human brain tumors at 3T”. In: *Magnetic Resonance in Medicine: An Official Journal of the International Society for Magnetic Resonance in Medicine* 56.3, pp. 585–592.

- Jones, Kyle M, Alyssa C Pollard, and Mark D Pagel (2018). “Clinical applications of chemical exchange saturation transfer (CEST) MRI”. In: *Journal of Magnetic Resonance Imaging* 47.1, pp. 11–27.
- Just, Nathalie and Cornelius Faber (2019). “Probing activation-induced neurochemical changes using optogenetics combined with functional magnetic resonance spectroscopy: a feasibility study in the rat primary somatosensory cortex”. In: *Journal of neurochemistry* 150.4, pp. 402–419.
- Katscher, Ulrich and Peter Börnert (2006). “Parallel RF transmission in MRI”. In: *NMR in Biomedicine: An International Journal Devoted to the Development and Application of Magnetic Resonance In vivo* 19.3, pp. 393–400.
- Khlebnikov, Vitaliy, Wybe JM van der Kemp, et al. (2019). “Analysis of chemical exchange saturation transfer contributions from brain metabolites to the Z-spectra at various field strengths and pH”. In: *Scientific reports* 9.1, pp. 1–11.
- Khlebnikov, Vitaliy, Jeroen CW Siero, et al. (2018). “Establishing upper limits on neuronal activity-evoked pH changes with APT-CEST MRI at 7 T”. In: *Magnetic resonance in medicine* 80.1, pp. 126–136.
- Kim, Byungjai et al. (2020). “A deep learning approach for magnetization transfer contrast MR fingerprinting and chemical exchange saturation transfer imaging”. In: *Neuroimage* 221, p. 117165.
- Kish, Stephen J, Thomas L Perry, and Shirley Hansen (1979). “Regional distribution of homocarnosine, homocarnosine-carnosine synthetase and homocarnosinase in human brain”. In: *Journal of neurochemistry* 32.6, pp. 1629–1636.
- Kogan, Feliks, Mohammad Haris, Catherine Debrosse, et al. (2014). “In vivo chemical exchange saturation transfer imaging of creatine (CrCEST) in skeletal muscle at 3T”. In: *Journal of Magnetic Resonance Imaging* 40.3, pp. 596–602.
- Kogan, Feliks, Mohammad Haris, Anup Singh, et al. (2014). “Method for high-resolution imaging of creatine in vivo using chemical exchange saturation transfer”. In: *Magnetic resonance in medicine* 71.1, pp. 164–172.
- Kohen, R (1988). “Yamamoto Y, Cundy KC, Ames BN”. In: *Antioxidant activity of carnosine, homocarnosine, and anserine present in muscle and brain. Proc Natl Acad Sci USA* 85, pp. 3175–3179.
- Krishnamoorthy, Guruprasad et al. (2017). “High quality three-dimensional gagCEST imaging of in vivo human knee cartilage at 7 Tesla”. In: *Magnetic resonance in medicine* 77.5, pp. 1866–1873.
- Krššák, Martin et al. (2021). “Proton magnetic resonance spectroscopy in skeletal muscle: Experts’ consensus recommendations”. In: *NMR in Biomedicine* 34.5, e4266.
- Landheer, Karl et al. (2020). “Elevated homocarnosine and GABA in subject on isoniazid as assessed through 1H MRS at 7T”. In: *Analytical biochemistry* 599, p. 113738.

- Le Bihan, Denis (2003). “Looking into the functional architecture of the brain with diffusion MRI”. In: *Nature reviews neuroscience* 4.6, pp. 469–480.
- Lecis, Michele et al. (2022). “PEAKIT: A Gaussian Process regression analysis tool for chemical exchange saturation transfer spectra”. In: *Journal of Magnetic Resonance* 334, p. 107122.
- Lee, Dong-Hoon et al. (2019). “In vivo mapping and quantification of creatine using chemical exchange saturation transfer imaging in rat models of epileptic seizure”. In: *Molecular Imaging and Biology* 21.2, pp. 232–239.
- Li, Chunmei, Min Chen, et al. (2017). “Chemical Exchange Saturation Transfer MRI Signal Loss of the Substantia Nigra as an Imaging Biomarker to Evaluate the Diagnosis and Severity of Parkinson’s Disease”. In: *Frontiers in Neuroscience* 11, p. 489.
- Li, Chunmei, Rui Wang, et al. (2015). “Chemical exchange saturation transfer MR imaging is superior to diffusion-tensor imaging in the diagnosis and severity evaluation of Parkinson’s disease: a study on substantia nigra and striatum”. In: *Frontiers in aging neuroscience* 7, p. 198.
- Liddel, Urner and Norman F Ramsey (1951). “Temperature dependent magnetic shielding in ethyl alcohol”. In: *The Journal of Chemical Physics* 19.12, pp. 1608–1608.
- Liebert, Andrzej et al. (2019). “Multiple interleaved mode saturation (MIMOSA) for B1+ inhomogeneity mitigation in chemical exchange saturation transfer”. In: *Magnetic Resonance in Medicine* 82.2, pp. 693–705.
- Liu, Zheng et al. (2016). “UCEPR: Ultrafast localized CEST-spectroscopy with PRESS in phantoms and in vivo”. In: *Magnetic resonance in medicine* 75.5, pp. 1875–1885.
- Logothetis, Nikos K (2008). “What we can do and what we cannot do with fMRI”. In: *Nature* 453.7197, pp. 869–878.
- Lopez-Kolkovsky, Alfredo L, Sebastien Mériaux, and Fawzi Boumezbeur (2016). “Metabolite and macromolecule T1 and T2 relaxation times in the rat brain in vivo at 17.2 T”. In: *Magnetic resonance in medicine* 75.2, pp. 503–514.
- Lu, Hanzhang and Peter CM van Zijl (2012). “A review of the development of Vascular-Space-Occupancy (VASO) fMRI”. In: *Neuroimage* 62.2, pp. 736–742.
- Luhmann, Heiko J and Atsuo Fukuda (2020). “Can we understand human brain development from experimental studies in rodents?” In: *Pediatrics International* 62.10, pp. 1139–1144.
- Ma, Xiaoyue et al. (2017). “Amide proton transfer magnetic resonance imaging in detecting intracranial hemorrhage at different stages: a comparative study with susceptibility weighted imaging”. In: *Scientific reports* 7.1, pp. 1–7.
- Mangia, Silvia, Federico Giove, et al. (2009). “Metabolic and hemodynamic events after changes in neuronal activity: current hypotheses, theoretical predictions and in vivo NMR experimental findings”. In: *Journal of Cerebral Blood Flow & Metabolism* 29.3, pp. 441–463.

- Mangia, Silvia, Ivan Tkáč, et al. (2007). “Sustained neuronal activation raises oxidative metabolism to a new steady-state level: evidence from  $^1\text{H}$  NMR spectroscopy in the human visual cortex”. In: *Journal of cerebral blood flow & metabolism* 27.5, pp. 1055–1063.
- Martoft, L et al. (2003). “CO<sub>2</sub> induced acute respiratory acidosis and brain tissue intracellular pH: a  $^{31}\text{P}$  NMR study in swine”. In: *Laboratory animals* 37.3, pp. 241–248.
- McConnell, Harden M (1958). “Reaction rates by nuclear magnetic resonance”. In: *The Journal of chemical physics* 28.3, pp. 430–431.
- McMahon, Michael T et al. (2006). “Quantifying exchange rates in chemical exchange saturation transfer agents using the saturation time and saturation power dependencies of the magnetization transfer effect on the magnetic resonance imaging signal (QUEST and QUESP): pH calibration for poly-L-lysine and a starburst dendrimer”. In: *Magnetic Resonance in Medicine: An Official Journal of the International Society for Magnetic Resonance in Medicine* 55.4, pp. 836–847.
- Menon, Ravi S et al. (1993). “4 Tesla gradient recalled echo characteristics of photic stimulation-induced signal changes in the human primary visual cortex”. In: *Magnetic Resonance in Medicine* 30.3, pp. 380–386.
- Nasrallah, Fatima A et al. (2013). “Imaging brain deoxyglucose uptake and metabolism by glucoCEST MRI”. In: *Journal of Cerebral Blood Flow & Metabolism* 33.8, pp. 1270–1278.
- Nishimura, MASAHARU et al. (1989). “Effects of hypercapnia on brain pH<sub>i</sub> and phosphate metabolite regulation by  $^{31}\text{P}$ -NMR”. In: *Journal of applied physiology* 66.5, pp. 2181–2188.
- O’Dowd, John J et al. (1990). “Analysis of carnosine, homocarnosine, and other histidyl derivatives in rat brain”. In: *Journal of neurochemistry* 55.2, pp. 446–452.
- O’Grady, Kristin P et al. (2019). “Glutamate-sensitive imaging and evaluation of cognitive impairment in multiple sclerosis”. In: *Multiple Sclerosis Journal* 25.12, pp. 1580–1592.
- Ogawa, Seiji, RS Menon, et al. (1993). “Functional brain mapping by blood oxygenation level-dependent contrast magnetic resonance imaging. A comparison of signal characteristics with a biophysical model”. In: *Biophysical journal* 64.3, pp. 803–812.
- Ogawa, Seiji, David W Tank, et al. (1992). “Intrinsic signal changes accompanying sensory stimulation: functional brain mapping with magnetic resonance imaging.” In: *Proceedings of the National Academy of Sciences* 89.13, pp. 5951–5955.
- Padormo, Francesco et al. (2016). “Parallel transmission for ultrahigh-field imaging”. In: *NMR in Biomedicine* 29.9, pp. 1145–1161.
- Park, Kye Jin et al. (2016). “Added value of amide proton transfer imaging to conventional and perfusion MR imaging for evaluating the treatment response of newly diagnosed glioblastoma”. In: *European radiology* 26.12, pp. 4390–4403.
- Pavuluri, KowsalyaDevi et al. (2020). “Amplified detection of phosphocreatine and creatine after supplementation using CEST MRI at high and ultrahigh magnetic fields”. In: *Journal of Magnetic Resonance* 313, p. 106703.

- Pekar, James et al. (1996). “Perfusion imaging with compensation for asymmetric magnetization transfer effects”. In: *Magnetic resonance in medicine* 35.1, pp. 70–79.
- Pellerin, Luc and Pierre J Magistretti (1994). “Glutamate uptake into astrocytes stimulates aerobic glycolysis: a mechanism coupling neuronal activity to glucose utilization.” In: *Proceedings of the National Academy of Sciences* 91.22, pp. 10625–10629.
- Pépin, Jérémy et al. (2016). “In vivo imaging of brain glutamate defects in a knock-in mouse model of Huntington’s disease”. In: *Neuroimage* 139, pp. 53–64.
- Perlman, Or et al. (2020). “CEST MR-Fingerprinting: Practical considerations and insights for acquisition schedule design and improved reconstruction”. In: *Magnetic resonance in medicine* 83.2, pp. 462–478.
- Petroff, O. and Anne Williamson (Jan. 2009). “Homocarnosine Enhances Inhibitory Tone in Rat Hippocampus”. In: S14–S14.
- Posner, Michael I et al. (1988). “Localization of cognitive operations in the human brain”. In: *Science* 240.4859, pp. 1627–1631.
- Provencher, Stephen W (1993). “Estimation of metabolite concentrations from localized in vivo proton NMR spectra”. In: *Magnetic resonance in medicine* 30.6, pp. 672–679.
- Rasmussen, CE (2006). *CKI Williams Gaussian processes for machine learning*.
- Reich, Eugenia et al. (2015). “Relaxation-compensated CEST-MRI at 7 T for mapping of creatine content and pH—preliminary application in human muscle tissue in vivo”. In: *NMR in Biomedicine* 28.11, pp. 1402–1412.
- Rothman, Douglas L, Kevin L Behar, et al. (1997). “Homocarnosine and the measurement of neuronal pH in patients with epilepsy”. In: *Magnetic resonance in medicine* 38.6, pp. 924–929.
- Rothman, Douglas L, Henk M De Feyter, et al. (2011). “<sup>13</sup>C MRS studies of neuroenergetics and neurotransmitter cycling in humans”. In: *NMR in biomedicine* 24.8, pp. 943–957.
- Roussel, Tangi et al. (2019). “Brain sugar consumption during neuronal activation detected by CEST functional MRI at ultra-high magnetic fields”. In: *Scientific reports* 9.1, pp. 1–11.
- Ryoo, David et al. (2017). “Detection and quantification of hydrogen peroxide in aqueous solutions using chemical exchange saturation transfer”. In: *Analytical chemistry* 89.14, pp. 7758–7764.
- Schmitt, B et al. (2011). “A new contrast in MR mammography by means of chemical exchange saturation transfer (CEST) imaging at 3 Tesla: preliminary results”. In: *RöFo-Fortschritte auf dem Gebiet der Röntgenstrahlen und der bildgebenden Verfahren*. Vol. 183. 11, pp. 1030–1036.
- Sehgal, Akansha Ashvani et al. (2019). “CEST MRI of 3-O-methyl-D-glucose uptake and accumulation in brain tumors”. In: *Magnetic resonance in medicine* 81.3, pp. 1993–2000.
- Silva, Nuno André da et al. (n.d.). “B1+ inhomogeneity mitigation in CEST using parallel transmission: pTxCEST”. In: ()

- Singh, Anup et al. (2013). “On B1 inhomogeneity correction of in vivo human brain glutamate chemical exchange saturation transfer contrast at 7T”. In: *Magnetic resonance in medicine* 69.3, pp. 818–824.
- Snoussi, Karim et al. (2003). “Sensitive CEST agents based on nucleic acid imino proton exchange: detection of poly (rU) and of a dendrimer-poly (rU) model for nucleic acid delivery and pharmacology”. In: *Magnetic Resonance in Medicine: An Official Journal of the International Society for Magnetic Resonance in Medicine* 49.6, pp. 998–1005.
- Sokoloff, L (1977). “Reivich M, Kennedy C, Des Rosiers MH, Patlak CS, Pettigrew KD, Sakurada O, Shinohara M”. In: *The [14C] deoxyglucose method for the measurement of local cerebral glucose utilization: theory, procedure, and normal values in the conscious and anesthetized albino rat. J Neurochem* 28, pp. 897–916.
- Solis, Marina Yazigi et al. (2015). “Effects of beta-alanine supplementation on brain homocarnosine/carnosine signal and cognitive function: an exploratory study”. In: *PloS one* 10.4, e0123857.
- Solomon, Ionel (1955). “Relaxation processes in a system of two spins”. In: *Physical Review* 99.2, p. 559.
- Sorrequieta, Augusto et al. (2010). “Free amino acid production during tomato fruit ripening: a focus on L-glutamate”. In: *Amino acids* 38.5, pp. 1523–1532.
- Stroman, PW et al. (2001). “Spin-echo versus gradient-echo fMRI with short echo times”. In: *Magnetic resonance imaging* 19.6, pp. 827–831.
- Sun, Phillip Zhe, Jerry S Cheung, et al. (2011). “Association between pH-weighted endogenous amide proton chemical exchange saturation transfer MRI and tissue lactic acidosis during acute ischemic stroke”. In: *Journal of Cerebral Blood Flow & Metabolism* 31.8, pp. 1743–1750.
- Sun, Phillip Zhe, Peter CM Van Zijl, and Jinyuan Zhou (2005). “Optimization of the irradiation power in chemical exchange dependent saturation transfer experiments”. In: *Journal of magnetic resonance* 175.2, pp. 193–200.
- Sun, Phillip Zhe, Jinyuan Zhou, et al. (2007). “Detection of the ischemic penumbra using pH-weighted MRI”. In: *Journal of Cerebral Blood Flow & Metabolism* 27.6, pp. 1129–1136.
- Swanson, SD and Y Pang (2003). “MT is symmetric but shifted with respect to water”. In: *Proc 11th Annual Meeting ISMRM*, p. 660.
- Tiedje, KE et al. (2010). “ $\beta$ -Alanine as a small molecule neurotransmitter”. In: *Neurochemistry international* 57.3, pp. 177–188.
- Tietze, Anna et al. (2014). “Assessment of ischemic penumbra in patients with hyperacute stroke using amide proton transfer (APT) chemical exchange saturation transfer (CEST) MRI”. In: *NMR in biomedicine* 27.2, pp. 163–174.
- Tkáč, Ivan et al. (1999). “In vivo  $^1\text{H}$  NMR spectroscopy of rat brain at 1 ms echo time”. In: *Magnetic Resonance in Medicine: An Official Journal of the International Society for Magnetic Resonance in Medicine* 41.4, pp. 649–656.

- Togao, Osamu et al. (2014). “Amide proton transfer imaging of adult diffuse gliomas: correlation with histopathological grades”. In: *Neuro-oncology* 16.3, pp. 441–448.
- Triplett, William T et al. (2014). “Chemical shift-based MRI to measure fat fractions in dystrophic skeletal muscle”. In: *Magnetic resonance in medicine* 72.1, pp. 8–19.
- Turner, Robert et al. (1993). “Functional mapping of the human visual cortex at 4 and 1.5 tesla using deoxygenation contrast EPI”. In: *Magnetic resonance in medicine* 29.2, pp. 277–279.
- Van Zijl, Peter CM et al. (2007). “MRI detection of glycogen in vivo by using chemical exchange saturation transfer imaging (glycoCEST)”. In: *Proceedings of the National Academy of Sciences* 104.11, pp. 4359–4364.
- Vermathen, Peter, Aristides A Capizzano, and Andrew A Maudsley (2000). “Administration and 1H MRS detection of histidine in human brain: application to in vivo pH measurement”. In: *Magnetic Resonance in Medicine: An Official Journal of the International Society for Magnetic Resonance in Medicine* 43.5, pp. 665–675.
- Wada, Tatsuhiro et al. (2017). “Glycosaminoglycan chemical exchange saturation transfer in human lumbar intervertebral discs: Effect of saturation pulse and relationship with low back pain”. In: *Journal of Magnetic Resonance Imaging* 45.3, pp. 863–871.
- Walker-Samuel, Simon et al. (2013). “In vivo imaging of glucose uptake and metabolism in tumors”. In: *Nature medicine* 19.8, pp. 1067–1072.
- Wang, Rui et al. (2015). “Amide proton transfer magnetic resonance imaging of Alzheimer’s disease at 3.0 Tesla: a preliminary study”. In: *Chinese medical journal* 128.05, pp. 615–619.
- Wansapura, Janaka P et al. (1999). “NMR relaxation times in the human brain at 3.0 tesla”. In: *Journal of Magnetic Resonance Imaging: An Official Journal of the International Society for Magnetic Resonance in Medicine* 9.4, pp. 531–538.
- Warburg, Otto, Franz Wind, and Erwin Negelein (1927). “The metabolism of tumors in the body”. In: *The Journal of general physiology* 8.6, p. 519.
- Ward, KM, AH Aletras, and Robert S Balaban (2000). “A new class of contrast agents for MRI based on proton chemical exchange dependent saturation transfer (CEST)”. In: *Journal of magnetic resonance* 143.1, pp. 79–87.
- Wei, Wenbo et al. (2014). “Chemical exchange saturation transfer MR imaging of articular cartilage glycosaminoglycans at 3 T: accuracy of B0 field inhomogeneity corrections with gradient echo method”. In: *Magnetic resonance imaging* 32.1, pp. 41–47.
- Wen, Zhibo et al. (2010). “MR imaging of high-grade brain tumors using endogenous protein and peptide-based contrast”. In: *Neuroimage* 51.2, pp. 616–622.
- Wermter, Felizitas C, Christian Bock, and Wolfgang Dreher (2015). “Investigating GluCEST and its specificity for pH mapping at low temperatures”. In: *NMR in Biomedicine* 28.11, pp. 1507–1517.

- Williamson, A., O. Petroff, and D. Spencer (2007). “Homocarnosine effects on synchronous activity in the human hippocampus”. In: *Epilepsia* 48.s6, pp. 248–380.
- Windschuh, Johannes et al. (2015). “Correction of B1-inhomogeneities for relaxation-compensated CEST imaging at 7 T”. In: *NMR in biomedicine* 28.5, pp. 529–537.
- Woessner, DE (1961). “Nuclear transfer effects in nuclear magnetic resonance pulse experiments”. In: *The Journal of Chemical Physics* 35.1, pp. 41–48.
- Woessner, Donald E et al. (2005). “Numerical solution of the Bloch equations provides insights into the optimum design of PARACEST agents for MRI”. In: *Magnetic Resonance in Medicine: An Official Journal of the International Society for Magnetic Resonance in Medicine* 53.4, pp. 790–799.
- Wolff, Steven D and Robert S Balaban (1989). “Magnetization transfer contrast (MTC) and tissue water proton relaxation in vivo”. In: *Magnetic resonance in medicine* 10.1, pp. 135–144.
- (1990). “NMR imaging of labile proton exchange”. In: *Journal of Magnetic Resonance (1969)* 86.1, pp. 164–169.
- Xu, Xiang, Kannie WY Chan, et al. (2015). “Dynamic glucose enhanced (DGE) MRI for combined imaging of blood–brain barrier break down and increased blood volume in brain cancer”. In: *Magnetic resonance in medicine* 74.6, pp. 1556–1563.
- Xu, Xiang, Jae-Seung Lee, and Alexej Jerschow (2013). “Ultrafast scanning of exchangeable sites by NMR spectroscopy”. In: *Angewandte Chemie* 125.32, pp. 8439–8442.
- Xu, Xiang, Akansha Ashvani Sehgal, et al. (2020). “d-glucose weighted chemical exchange saturation transfer (glucoCEST)-based dynamic glucose enhanced (DGE) MRI at 3T: early experience in healthy volunteers and brain tumor patients”. In: *Magnetic resonance in medicine* 84.1, pp. 247–262.
- Yacoub, Essa et al. (2001). “Imaging brain function in humans at 7 Tesla”. In: *Magnetic Resonance in Medicine: An Official Journal of the International Society for Magnetic Resonance in Medicine* 45.4, pp. 588–594.
- Yan, Kun et al. (2015). “Assessing amide proton transfer (APT) MRI contrast origins in 9 L gliosarcoma in the rat brain using proteomic analysis”. In: *Molecular imaging and biology* 17.4, pp. 479–487.
- Yang, Yonggui et al. (2020). “Preliminary application of 3.0 T magnetic resonance chemical exchange saturation transfer imaging in brain metastasis of lung cancer”. In: *BMC Medical Imaging* 20.1, pp. 1–8.
- Zaiß, Moritz, Benjamin Schmitt, and Peter Bachert (2011). “Quantitative separation of CEST effect from magnetization transfer and spillover effects by Lorentzian-line-fit analysis of z-spectra”. In: *Journal of magnetic resonance* 211.2, pp. 149–155.
- Zaiss, Moritz, Goran Angelovski, et al. (2018). “QUESP and QUEST revisited—fast and accurate quantitative CEST experiments”. In: *Magnetic resonance in medicine* 79.3, pp. 1708–1721.

- Zaiss, Moritz, Philipp Ehse, and Klaus Scheffler (2018). "Snapshot-CEST: optimizing spiral-centric-reordered gradient echo acquisition for fast and robust 3D CEST MRI at 9.4 T". In: *NMR in Biomedicine* 31.4, e3879.
- Zaiss, Moritz, Johannes Windschuh, et al. (2015). "Relaxation-compensated CEST-MRI of the human brain at 7 T: unbiased insight into NOE and amide signal changes in human glioblastoma". In: *Neuroimage* 112, pp. 180–188.
- Zhang, Shanrong and A Dean Sherry (2003). "Physical characteristics of lanthanide complexes that act as magnetization transfer (MT) contrast agents". In: *Journal of solid state chemistry* 171.1-2, pp. 38–43.
- Zhang, Shanrong, Patrick Winter, et al. (2001). "A novel europium (III)-based MRI contrast agent". In: *Journal of the American Chemical Society* 123.7, pp. 1517–1518.
- Zhao, Xuna, Zhibo Wen, Fanheng Huang, et al. (2011). "Saturation power dependence of amide proton transfer image contrasts in human brain tumors and strokes at 3 T". In: *Magnetic resonance in medicine* 66.4, pp. 1033–1041.
- Zhao, Xuna, Zhibo Wen, Ge Zhang, et al. (2013). "Three-dimensional turbo-spin-echo amide proton transfer MR imaging at 3-Tesla and its application to high-grade human brain tumors". In: *Molecular imaging and biology* 15.1, pp. 114–122.
- Zhou, Jinyuan, Jaishri O Blakeley, et al. (2008). "Practical data acquisition method for human brain tumor amide proton transfer (APT) imaging". In: *Magnetic Resonance in Medicine: An Official Journal of the International Society for Magnetic Resonance in Medicine* 60.4, pp. 842–849.
- Zhou, Jinyuan, Bachchu Lal, et al. (2003). "Amide proton transfer (APT) contrast for imaging of brain tumors". In: *Magnetic Resonance in Medicine: An Official Journal of the International Society for Magnetic Resonance in Medicine* 50.6, pp. 1120–1126.
- Zhou, Jinyuan, Jean-Francois Payen, et al. (2003). "Using the amide proton signals of intracellular proteins and peptides to detect pH effects in MRI". In: *Nature medicine* 9.8, pp. 1085–1090.
- Zhou, Jinyuan, Erik Tryggstad, et al. (2011). "Differentiation between glioma and radiation necrosis using molecular magnetic resonance imaging of endogenous proteins and peptides". In: *Nature medicine* 17.1, pp. 130–134.
- Zhou, Jinyuan, David A Wilson, et al. (2004). "Quantitative description of proton exchange processes between water and endogenous and exogenous agents for WEX, CEST, and APT experiments". In: *Magnetic Resonance in Medicine: An Official Journal of the International Society for Magnetic Resonance in Medicine* 51.5, pp. 945–952.
- Zhou, Jinyuan and Peter CM van Zijl (2006). "Chemical exchange saturation transfer imaging and spectroscopy". In: *Progress in Nuclear Magnetic Resonance Spectroscopy* 48.2-3, pp. 109–136.
- Zhu, Xiao-Hong, Ming Lu, and Wei Chen (2018). "Quantitative imaging of brain energy metabolisms and neuroenergetics using in vivo X-nuclear  $^2\text{H}$ ,  $^{17}\text{O}$  and  $^{31}\text{P}$  MRS at ultra-high field". In: *Journal of Magnetic Resonance* 292, pp. 155–170.

**Titre:** Développement de techniques CEST à ultra-haut champ pour l'étude du métabolisme cérébral  
**Mots clés:** CEST, métabolisme cérébral, IRM, IRM fonctionnelle, ultra-haut champ

L'imagerie RMN de transfert de saturation par échange chimique (IRM CEST) est un outil puissant pour l'imagerie métabolique. L'IRM CEST permet de détecter indirectement des métabolites avec une sensibilité et des résolutions temporelle et spatiale accrues par rapport à la spectroscopie RMN (SRM), via la réduction du signal de l'eau après l'application d'un module de présaturation à la fréquence du métabolite. Grâce à l'avènement des champs magnétiques intenses pour l'IRM, l'IRM CEST suscite un intérêt croissant. Des avancées significatives ont été rapportées aussi bien dans les stratégies d'acquisition que les chaînes de traitement permettant la détection de nombreux métabolites dont le glucose, le glutamate, le myo-inositol, le lactate ou la créatine, et des applications prometteuses dans différentes disciplines (oncologie, sciences musculo-squelettiques, physiologie ou neurosciences) ont été proposées. Cependant, il reste difficile d'étudier les effets CEST plus faibles provenant de métabolites moins concentrés, en échange lent ou de détecter des changements CEST rapides. Cette thèse de doctorat visait à développer des techniques CEST à ultra-haut champ pour étudier le métabolisme cérébral *in vivo*. D'abord, l'avantage des ultra-hauts champs magnétiques pour l'imagerie CEST a été démontré *in vitro* par l'étude de trois neurométabolites majeurs : glucose, lactate et glutamate à différents champs magnétiques (9.4, 11.7 et 17.2 T). L'influence des changements de température et de pH sur la réponse CEST a également été étudiée. Puis, le développement et l'implémentation d'une nouvelle approche d'IRM CEST ultra-rapide sont présentés : la séquence "CEST-linescan". Cette méthode est adaptée à la détection des effets CEST ténus générés par des métabolites moins concentrés ou en échange lent. Grâce à sa rapidité, ce protocole d'acquisition offre une meilleure stabilité du signal tout en maintenant un rapport contraste/bruit similaire aux séquences CEST standards. Pour le traitement des

données, un outil d'analyse (PEAKIT) spécifiquement dédié à la caractérisation de contributions CEST a été développé au sein de notre équipe. PEAKIT estime la hauteur, la surface et la significativité statistique du pic CEST en se basant sur l'estimation de la ligne de base locale autour de la contribution CEST d'intérêt et est donc peu affecté par la forme globale des données CEST. Ces deux outils dédiés ont permis, pour la première fois, la détection *in vivo* (dans le muscle squelettique et dans le cerveau du rat) de la carnosine, un dipeptide endogène doté d'importantes fonctions antioxydantes et connu pour être impliqué notamment dans la réponse cellulaire à des niveaux élevés d'inflammation. Deux autres dérivés de la carnosine (anserine et homocarnosine) ont également été étudiés. Enfin, nous avons adapté le CEST-linescan ultrarapide afin d'étudier les changements métaboliques dynamiques dans le cerveau du rat. Une étude préliminaire a consisté à détecter les changements du contraste CEST induits par une variation contrôlée du pH. Nous avons ensuite étudié les changements métaboliques induits par l'activation neuronale déclenchée par une stimulation électrique de la patte avant chez le rat. Nous avons adapté la séquence et mis en œuvre diverses stratégies d'acquisition afin de minimiser les effets BOLD et maintenir la sensibilité et la spécificité (biochimique) du contraste CEST fonctionnel. Même si les résultats obtenus ne nous ont pas permis de détecter des changements significatifs dans les contributions CEST spécifiques pendant la tâche fonctionnelle, nous concluons que les protocoles d'imagerie développés demeurent prometteurs. En employant des paradigmes de stimulation optimisés pour des réponses d'activation plus stables et en augmentant le nombre d'animaux pour une plus grande puissance statistique, nous espérons être en mesure d'identifier les changements métaboliques transitoires induits par l'activité neuronale.

**Title:** Development of ultra-high field CEST technics for studying brain metabolism  
**Keywords:** CEST, cerebral metabolism, MRI, functional MRI, ultra-high field

Chemical exchange saturation transfer Magnetic Resonance Imaging (CEST MRI) is a powerful tool for metabolic imaging. Detection of specific neurometabolites can be performed using CEST MRI with enhanced sensitivity, and temporal and spatial resolution compared to NMR Spectroscopy (MRS), by measuring the reduction in bulk water signal after application of a dedicated presaturation module. With the increased availability of high and ultra-high magnetic fields, CEST MRI techniques gained a lot of attention. Significant advancements have been reported in both the acquisition strategies and processing pipelines which allowed the *in vivo* detection of numerous brain metabolites including glutamate, glucose, myo-inositol, lactate, creatine and promising applications in different disciplines (e.g. oncology, musculoskeletal sciences, physiology or neurosciences) have been demonstrated. Yet, it remains challenging to investigate weaker CEST effects from molecules with lower concentrations or slower exchange rates or detect rapid CEST changes. This PhD thesis aimed at the development of ultra-high field CEST technics for studying brain metabolism *in vivo*. In this project, the advantage of ultra-high magnetic fields for CEST imaging was first demonstrated *in vitro* through an investigation of the CEST detection of three major neurometabolites: glucose, lactate and glutamate at different high magnetic fields (9.4, 11.7 and 17.2 T). The influence of temperature and pH changes on the CEST response was also investigated. In the second part of this thesis, the development and implementation of a new ultrafast CEST MRI approach are presented: the "CEST-linescan" sequence. This method is adapted to the detection of the tenuous CEST effects generated by metabolites with very low concentrations and very low exchange rates. Due to its rapidity, this acquisition protocol is offering a better signal stabil-

ity while maintaining a contrast-to-noise ratio similar to that of standard CEST sequences. For processing, we used an analysis tool (PEAKIT) developed in our team specifically for characterizing CEST contributions. PEAKIT estimates the CEST peak height, area and statistical significance based on the estimation of the local baseline around the CEST contribution-of-interest and is therefore minimally impacted by the global shape of the CEST data. These two CEST-related tools enabled, for the first time, the *in vivo* detection (in the skeletal muscle and in the brain of rats) of carnosine, an endogenous dipeptide with important antioxidant functions known to be involved notably in the cellular response to high levels of inflammation. Two other derivatives of carnosine (anserine and homocarnosine) were also studied. In the last part of the project, we focused on adapting the ultrafast CEST-linescan sequence for the investigation of dynamic metabolic changes in the rat brain. A preliminary study consisted in detecting changes in the CEST contrast induced by a controlled pH decrease. We were then focused on monitoring metabolic changes induced by neuronal activation triggered by an electrical forepaw stimulation in rats. We made several sequence modifications and implemented various acquisition strategies in order to minimize the BOLD effects and maintain the sensitivity and (biochemical) specificity of the CEST signal changes. Even though the results obtained did not allow us to detect significant changes in specific CEST contributions during the functional task, we conclude that the imaging protocols developed are promising. By employing stimulation paradigms optimized for stable activation responses and increasing the number of animals for higher statistical power, we expect to be able to pinpoint transient metabolic changes driven by neuronal activity.

